A N N U A L R E P O R T

2004

and list of publications

Bayerisches Forschungsinstitut
für Experimentelle Geochemie und Geophysik
Universität Bayreuth

Bayerisches Geoinstitut
Universität Bayreuth
D-95440 Bayreuth
Germany

Telephone: +49-(0)921-55-3700
Telefax: +49-(0)921-55-3769
e-mail: bayerisches.geoinstitut@uni-bayreuth.de
www: http://www.bgi.uni-bayreuth.de

Editorial compilation by: Stefan Keyssner and Petra Ständner
Section editors: Tiziana Boffa Ballaran, Natalia Dubrovinskaia, Leonid Dubrovinsky, Dan Frost, Florian Heidelbach, Catherine McCammon, David Rubie, Friedrich Seifert, Gerd Steinle-Neumann, Michael Terry

Staff and guests of the Bayerisches Geoinstitut in **July 2004**:

Die Mitarbeiter und Gäste des Bayerischen Geoinstituts im **Juli 2004**:

First row, from left (1. Reihe, v. links) Martine Vernooij, Lydia Kison-Herzing, Sylvie Demouchy, Hélène Couvy, Tiziana Boffa Ballaran, Anastasia Kantor, Christina Schneider, Gerti Gollner, Yuki Asahara, Petra Ständner, Jun Liu

Second row, from left (2. Reihe, v. links) Catherine McCammon, Holger Kriegl, Heinz Fischer, Oskar Leitner, Sven Linhardt, Geoffrey Bromiley, Kiyoshi Fujino, Hidenori Terasaki, Marco Pistorino, Wolfgang Böss

Third row, from left (3. Reihe, v. links) Dave Rubie, Friedrich Seifert, Roman Skàla, Gerd Ramming, Martin Rigby, Bernhard Steinberger, Alexei Kuznetsov, Fiona Bromiley, Stefan Keyssner

Fourth row, from left (4. Reihe, v. links) Florian Heidelbach, Gerd Steinle-Neumann, Innokenty Kantor, Detlef Krauße, Christian Liebske, Kurt Klasinski, Dan Frost, Antonio Piazzoni, Mike Terry

Absent (Es fehlten) Matthias Bechmann, Ulrich Bläß, Ulrich Böhm, Natalia Dubrovinskaia, Leonid Dubrovinsky, Fabrice Gaillard, Giacomo Diego Gatta, Georg Herrmannsdörfer, Falko Langenhorst, Fred Marton, Fabrizio Nestola, Oliver Rausch, Bettina Schmickler, Hubert Schulze, Angelika Sebald, Andrei Shiryaev, Joseph Smyth, Emil Stoyanov, Iona Stretton

Contents

Foreword

The Bayerisches Geoinstitut is a research institute that is dedicated to experimental studies of Earth materials at high pressures and temperatures. The broad aims of the institute are centred primarily on understanding the structure, composition and dynamics of the Earth's interior through investigations of the physical and chemical properties of materials under the relevant pressure-temperature conditions. The methods used, especially for the characterization of materials, overlap strongly with those of other disciplines such as physics, chemistry and materials science.

The contributions in this annual report encompass a wide range of research topics related to the Earth and material sciences. Some of these contributions have only been possible as the result of technological developments and the availability of state of the art experimental facilities. Examples of such facilities include an ultra-high intensity X-ray diffraction system for studying the atomic structure of materials *in situ* up to megabar pressures. An understanding of the elastic properties of Earth materials at high pressures and temperatures is essential for interpreting seismic velocity data in terms of mineralogical models of the Earth's interior; new results in this fundamental research area are now being provided by the *in situ* technique of gigahertz ultrasonic interferometry through which extremely small single crystals can be studied at high pressure. Furthermore, a new deformation multianvil apparatus is now providing new data on deformation mechanisms and the rheological properties of minerals of the Earth's interior; such data are required in order to understand the solid-state convective flow of the Earth's mantle that is the driving force for plate tectonics.

Research activities involve both short-term projects and those that have been ongoing for a number of years. An example of a long-term project concerns the distribution of water in the Earth's interior. It has been known for more than 20 years that small amounts of water can dissolve into the common minerals of the Earth's mantle, at least down to a depth of 660 km. The conventional view that has developed is that the upper mantle, consisting mainly of the mineral olivine, can contain only a relatively small amount of water, whereas in the transition zone (410-660 km depth) as much as 3 wt.% water could be contained in the dominant minerals. New experimental results presented in this report show that, because of the dependence of water solubilities on temperature, the difference between the water contents of the upper mantle and transition zone is likely to be much smaller than formerly believed. The new results have a number of important implications, for example for understanding the cycling of water between the surface and the deep interior.

In 2004, funding from the State of Bavaria was granted to set up an International Graduate School under the Elitenetzwerk Bayern programme on the theme "Structure, Reactivity and Properties of Oxide Materials". The partners involved in this interdisciplinary Graduate School are the Bayerisches Geoinstitut, the Institute for Inorganic Chemistry (University of Bayreuth) and the Fraunhofer-Institut für Silicatforschung ISC in Würzburg. The Graduate

School is funded initially for four years, starting January 2005, and will provide positions for at least 12 graduate students.

From 1994 to 2004, the Bayerisches Geoinstitut was financed by the EU under the "Large Scale Facility" and "Access to Research Infrastructures" programmes. This funding enabled a large number of scientists from states and associate states of the EU to visit in order to use our experimental and analytical facilities. This funding is now being continued for the period 2005-2008 during which access of 324 mandays per year will be provided. The programme is open to scientists from the Earth sciences, physics, chemistry and material science.

Late in 2002, the Professorship for *Experimental Geophysics of the Solid Earth* at the Bayerisches Geoinstitut became vacant due to the move of Prof. Stephen Mackwell to the Lunar and Planetary Institute (Houston, USA). This Professorship was offered to Prof. Hans Keppler (Universitaet Tübingen) in 2004. It is a pleasure to report that he subsequently accepted the position and started at the Bayerisches Geoinstitut in December 2004.

As in previous years, and also on behalf of my colleagues, I would like to thank the *Free State of Bavaria* as represented by the *Bayerisches Staatsministerium für Wissenschaft, Forschung und Kunst* as well as the *Kommission für Geowissenschaftliche Hochdruckforschung* for their continuing support and strong commitment to the Bayerisches Geoinstitut. We also gratefully acknowledge generous support from external funding agencies, in particular the *Alexander von Humboldt Foundation*, the *European Union*, and the *German Science Foundation*, which have also contributed greatly to the development and success of the Institute.

Bayreuth, February 2005 David C. Rubie

Vorwort

Das Bayerische Geoinstitut ist ein Forschungsinstitut auf dem Gebiet der experimentellen Untersuchung der Erdmaterie unter hohen Drücken und Temperaturen. Im Mittelpunkt der weitgefassten Forschungsziele des Instituts steht in erster Linie das Verständnis der Struktur, der Zusammensetzung und der dynamischen Abläufe im Erdinneren. Dazu dienen die Untersuchungen der physikalischen und chemischen Materialeigenschaften unter entsprechenden Druck-/Temperaturbedingungen. Die für die Bestimmung eingesetzten Verfahren überlappen weitgehend mit Methoden anderer Disziplinen wie Physik, Chemie und Materialwissenschaften.

Die Beiträge des vorliegenden Jahresberichtes überspannen eine große Themenbreite in den Geo- und Materialwissenschaften. Einige Beiträge konnten nur aufgrund neuer technischer Entwicklungen und der Zugriffsmöglichkeit auf modernste experimentelle Einrichtungen geschrieben werden. Zu diesen Einrichtungen gehört ein hoch-intensives Röntgendiffraktometrie-System mit dem *in situ* die Atomstruktur von Materie unter Drücken im Megabar-Bereich untersucht werden kann. Kenntnisse über elastische Eigenschaften der Erdmaterie unter hohen Drücken und Temperaturen sind notwendig, um Ergebnisse aus Messungen seismischer Laufzeiten zu interpretieren und Modelle über den Aufbau des Erdinneren zu entwickeln. Durch die jetzt verfügbare neue *in situ*-Technik in der Gigahertz-Interferometrie lassen sich die elastischen Eigenschaften an extrem kleinen Proben unter hohen Drücken bestimmen. Weiterhin ermöglicht eine neue Verformungs-Vielstempelpresse die Bestimmung von Verformungsmechanismen und rheologischen Eigenschaften von Mineralen des Erdinneren. Diese Daten sind erforderlich, um zum Beispiel die Konvektion von Materie im Erdmantel, die Antriebskraft für die Plattentektonik, zu verstehen.

Forschungsaktivitäten des Bayerischen Geoinstituts beinhalten sowohl kurzzeitig befristete Projekte als auch Programme, die über einige Jahre fortgeführt werden. Beispiel für ein langfristiges Projekt sind Untersuchungen zur Verteilung von Wasser im Erdinneren. Bereits seit mehr als 20 Jahren wissen wir, dass kleine Mengen an Wasser in den Hauptmineralen im Erdmantel gelöst werden können, zumindest bis in eine Tiefe von 660 km. Es ist allgemein anerkannt, dass der obere Erdmantel, der hauptsächlich aus dem Mineral Olivin aufgebaut ist, nur relativ geringe Mengen an Wasser aufnehmen kann, während die Hauptminerale der Übergangszone (410-660 km Tiefe) bis zu 3 Gew.-% Wasser aufnehmen können. Nun werden in diesem Jahresbericht neue Ergebnisse zur Temperaturabhängigkeit der Wasserlöslichkeiten vorgestellt, die aufzeigen, dass die Differenz zwischen dem Wassergehalt des Oberen Mantels und dem der Übergangszone wahrscheinlich viel geringer ist, als bisher angenommen wurde. Diese neuen Ergebnisse haben eine Reihe weitreichender Konsequenzen für das Verständnis des Wasserkreislaufs zwischen Erdoberfläche und dem tiefen Erdinneren.

Im Jahr 2004 stellte der Freistaat Bayern Mittel für ein Internationales Graduiertenkolleg im Rahmen des Elitenetzwerks Bayern unter dem Titel „*Structure, Reactivity and Properties of*

Oxide Materials“ zur Verfügung. Partner in diesem multi-disziplinären Graduiertenkolleg sind das Bayerische Geoinstitut, das Institut für Anorganische Chemie (Universität Bayreuth) und das Fraunhofer-Institut für Silicatforschung (ISC) in Würzburg. Die Förderung beginnt im Januar 2005 für zunächst 4 Jahre und bietet Stellen für mindestens 12 Doktoranden.

In den Jahren 1994 bis 2004 war das Bayerische Geoinstitut Empfänger von Mitteln der EU im Rahmen der Programme „*Large Scale Facility*“ und „*Access to Research Infrastructure*“. Durch diese Förderung konnten zahlreiche Wissenschaftler aus den EU-Ländern und den „*Associated States*“ die experimentellen und analytischen Einrichtungen am Geoinstitut nutzen. Diese Förderung wird auch in den Jahren 2005-2008 fortgesetzt werden. In diesem Zeitraum werden jeweils 324 Wissenschaftler-Tage pro Jahr gewährt werden. Das Förderprogramm steht Wissenschaftlern aus den Geo- und Materialwissenschaften sowie aus der Physik und der Chemie offen.

Zum Jahresausgang 2002 wurde der Lehrstuhl für Experimentelle Geophysik der Festen Erde frei, als der Inhaber Prof. Stephen Mackwell einen Ruf an das *Lunar and Planetary Institute* in Houston/Texas annahm. Der Lehrstuhl wurde im Jahr 2004 Prof. Hans Keppler von der Universität Tübingen angeboten. Es freut mich berichten zu können, dass Herr Keppler die Stelle angenommen und seine Arbeit im Bayerischen Geoinstitut im Dezember 2004 aufgenommen hat.

Wie in den vorangegangenen Jahren möchte ich auch im Namen meiner Kollegen dem *Freistaat Bayern*, vertreten durch das *Bayerische Staatsministerium für Wissenschaft, Forschung und Kunst*, als auch der *Kommission für Geowissenschaftliche Hochdruckforschung* der *Bayerischen Akademie der Wissenschaften* meinen Dank für ihre fortwährende Unterstützung und ihre enge Verbundenheit mit dem Bayerischen Geoinstitut aussprechen. Wir sind auch für die großzügige Förderung durch externe Geldgeber, insbesondere durch die *Alexander von Humboldt-Stiftung*, die *Europäische Union* und die *Deutsche Forschungsgemeinschaft*, die ebenfalls wesentlich zur Entwicklung und zum Erfolg des Bayerischen Geoinstituts beigetragen hat, sehr dankbar.

Bayreuth, im Februar 2005 David C. Rubie

1. Advisory Board and Directorship

1.1 Advisory Board

The *Kommission für Geowissenschaftliche Hochdruckforschung* der *Bayerischen Akademie der Wissenschaften* advises on the organisation and scientific activities of the Institute. Members of this board are:

Prof. Dr. Drs. h. c. E. ALTHAUS	Emeritus, Mineralogisches Institut der Universität Karlsruhe
Prof. Dr. U. CHRISTENSEN	Max-Planck-Institut für Aeronomie, Katlenburg-Lindau
Prof. Dr. Drs. h. c. E. U. FRANCK[†)]	Emeritus, Institut für Physikalische Chemie der Universität Karlsruhe
Prof. Dr. H. PALME	Institut für Mineralogie und Geochemie der Universität zu Köln
Prof. Dr. R. RUMMEL	Institut für Astronomische und Physikalische Geodäsie der TU München
Prof. Dr.-Ing. G. SACHS (Chairman)	Lehrstuhl für Flugmechanik und Flugregelung der Technischen Universität München
Prof. Dr. E. SALJE	Department of Earth Sciences, University of Cambridge
Prof. Dr. Drs. h. c. W. SCHREYER	Emeritus, Institut für Mineralogie der Ruhr-Universität Bochum
Prof. Dr. H. SOFFEL	Emeritus, Institut für Allgemeine und Angewandte Geophysik der Universität München

[†)] deceased December 21, 2004

The Advisory Board held meetings in Bayreuth (22.-23.04.2004) and in Munich (19.11.2004).

1.2 Leadership

Prof. Dr. David C. RUBIE (Director)
Prof. Dr. Hans KEPPLER
Prof. Dr. Friedrich SEIFERT

2. Staff, Funding and Facilities

2.1 Staff

At the end of 2004 the following staff positions existed in the Institute:

- Scientific staff: **12**
- Technical staff: **12**
- Administrative staff: **2**
- Administrative officer: **1**

During 2004, 14 scientific (107 months) and 1 technical (2 months) positions were funded by grants raised externally by staff members of the institute.

In addition 13 long-term scientific positions (86 months) were funded by the resources of the BGI Visiting Scientists' Program (see Sect. 5) which also supported short-term visits for discussing future projects or presenting research results (see Sect. 4.6). 9 scientists (79 months) were funded by personal grants (stipends).

2.2 Funding

In 2004, the following financial resources were available from the Free State of Bavaria:

- Visiting Scientists' Program: 382.000 €
- Consumables: 442.000 €

The total amount of national/international external funding („*Drittmittel*") used for ongoing research projects in 2004 was 722.000 € (Positions: 407.000 €; equipment, consumables and travel grants: 315.000 €).

	positions	**equipment, consumables, travel grants**	**total**
• AvH	174.000 €	191.000 €	365.000 €
• DAAD		6.000 €	6.000 €
• DFG	222.000 €	72.000 €	294.000 €
• EU	11.000 €	42.000 €	53.000 €
• Others		4.000 €	4.000 €
			722.000 €

(AvH = Alexander von Humboldt Foundation; DAAD = German Academic Exchange Program; DFG = German Science Foundation; EU = European Union)

In the following list only the BGI part of the funding is listed in cases where joint projects involved other research institutions. Principal investigators and duration of the grants are listed in brackets.

Funding institution	**Project, Funding**	**Total Project Funding**
AvH	Sofia-Kovalevskaja-Programm (T. Boffa Ballaran – 8.01 - 7.04) Positions, consumables, equipment, travel:	843.740 €
DAAD	PROCOPE (F. Langenhorst – 1.04 - 12.05) Travel funding:	8.000 €
DAAD	PPP Schweden (L.S. Dubrovinsky – 1.04 - 12.04) Travel funding:	3.500 €
DFG	DU 393/1-1 (L.S. Dubrovinsky – 5.02 - 4.05) Investment money:	555.000 €
DFG	Fr 1555/1-2 (D.J. Frost, D.C. Rubie – 9.03 - 8.04) Positions: BAT IIa/2, 12 months Consumables and travel funding:	6.125 €
DFG	Fr 1555/2-1 (D.J. Frost, F. Heidelbach, F. Langenhorst, D.C. Rubie – 1.04 - 12.04) Positions: BAT IIa/2, 12 months Consumables and travel funding:	5.000 €
DFG	Ja 1122/1-1 (S.D. Jacobsen, L.S. Dubrovinsky – 2.04 - 1.06) Positions: BAT IIa/2, 24 months Consumables and travel funding:	21.000 €
DFG	Gottfried Wilhelm Leibniz-Preis Ke 501/6-1 (H. Keppler – 12.04 - 9.06) Positions, consumables, equipment, travel:	240.000 €
DFG	La 830/4-5 (F. Langenhorst – 1.04 - 12.04) Consumables and travel funding:	9.200 €
DFG	La 830/4-6 (F. Langenhorst – 3.04 - 2.05) Positions: BAT IIa, 12 months Consumables and travel funding:	6.900 €
DFG	La 830/6-1 (F. Langenhorst, G. Steinle-Neumann, D.J. Frost – 6.04 - 5.06) Positions: BAT IIa, 24 months Consumables and travel funding:	11.800 €

DFG	Ma 801/7-1 (A. Magerl and M. Göbbels/Erlangen, F. Seifert/ Bayreuth) Positions: BAT IIa, 24 months Consumables and travel funding: 18.400 € (Erlangen)	
DFG	Mc 3/13-1 and Mc 3/13-2 (C.A. McCammon, L.S. Dubrovinsky – 1.04 - 12.04) Positions: BAT IIa/2, 12 months Consumables and travel funding:	9.321 €
DFG	Ru 437/6-1 (D.C. Rubie, D.J. Frost, F. Langenhorst, A. Holzheid – 4.02 - 3.04) Positions: BAT IIa/2, 24 months Consumables and travel funding:	13.800 €
DFG	Ru 437/6-2 (D.C. Rubie, D.J. Frost, F. Langenhorst, A. Holzheid – 4.04 - 3.06) Positions: BAT IIa, 24 months Consumables and travel funding:	12.100 €
DFG	Ru 437/7-1 (D.C. Rubie, B.T. Poe – 2.02 - 1.04) Positions: BAT IIa/2, 24 months Consumables and travel funding:	22.500 €
DFG	Ru 437/7-2 (D.C. Rubie – 2.04 - 1.05) Positions: BAT IIa, 12 months Consumables and travel funding:	18.200 €
DFG	Wr15/20-2 (A. Sebald, B. Wrackmeyer/Bayreuth, joint project – 7.02 - 5.04) Positions: BAT IIa, 12 months, BAT IIa/2, 12 months Consumables and travel funding:	4.000 €
DFG	Wr15/20-3 (A. Sebald, B. Wrackmeyer/Bayreuth, joint project – 5.04 - 4.06) Positions: BAT IIa, 12 months, BAT IIa/2, 12 months Consumables and travel funding:	11.000 €
EU	"Access to Research Infrastructures" Programme (D.C. Rubie – 5.00 - 1.04) Positions, consumables, equipment, travel:	825.000 €
EU	Hydrospec-Network (H. Keppler – 9.00 - 8.04) Positions/Consumables:	181.000 €
EU	Marie Curie Fellowships (Training Center) (S. Mackwell/D. Rubie – 01.02. - 01.06) Positions, consumables, equipment, travel:	150.000 €
	Collaboration with Fa. Anzaplan, Hirschau (F. Heidelbach)	2.500 €

2.3 Laboratory and office facilities

The institute occupies an area of

ca. 1200 m^2	laboratory space
ca. 480 m^2	infrastructural areas (machine shops, computer facilities, seminar room, library)
ca. 460 m^2	office space

in a building which was completed in 1994.

2.4 Experimental equipment

The following major equipment is available at Bayerisches Geoinstitut:

I. High-pressure apparatus

5000 tonne multianvil press (25 GPa, 3000 K)
1200 tonne multianvil press (25 GPa, 3000 K)
1000 tonne multianvil press (25 GPa, 3000 K)
500 tonne multianvil press (20 GPa, 3000 K)
500 tonne press with a deformation DIA apparatus
3 piston-cylinders (0.5" and 0.75"; 4 GPa, 2100 K)
Cold-seal vessels (700 MPa, 1000 K, H_2O), TZM vessels (300 MPa, 1400 K, gas), rapid-quench equipment
Internally-heated autoclave (1 GPa, 1600 K)

II. Structural and chemical analysis

2 X-ray powder diffractometers
1 X-ray powder diffractometer with furnace and cryostat
X-ray powder microdiffractometer
Single-crystal X-ray cameras
3 automated single-crystal X-ray diffractometers
2 Mössbauer spectrometers (1.5 - 1300 K)
Mössbauer microspectrometer
FTIR spectrometer with IR microscope
FEG transmission electron microscope, 200 kV analytical, with EDS and PEELS
FEG scanning electron microscope with BSE detector, EDS, EBSD and CL
2 Micro-Raman spectrometers

JEOL JXA-8200 electron microprobe; fully-automated with 14 crystals, 5 spectrometer configuration, EDX, capability for light elements
Cameca SX-50 electron microprobe
ICP-AES sequential spectrometer
Water content determination by Karl-Fischer titration

III. *In situ* determination of properties

1 calorimeter (77 - 1000 K) scanning
Diamond anvil cells for powder and single crystal X-ray diffraction, Mössbauer, IR, Raman, optical spectroscopy and electrical resistivity measurements up to at least 100 GPa
Facility for *in situ* hydrothermal studies in DAC
Externally electrically heated DACs for *in situ* studies at pressures to 100 GPa and 1200 K
1-atm furnace (to 1873 K, gas mixing) equipped with zirconia fO_2 probes
Paterson HP/HT deformation apparatus
1-atm high-temperature creep apparatus
Gigahertz ultrasonic interferometer with interface to resistance-heated diamond-anvil cells
Heating stage for fluid inclusion studies
Impedance/gain-phase analyser for electrical conductivity studies
Apparatus for *in situ* measurements of thermal diffusivity at high P and T

The Geoinstitut is provided with well equipped machine shops, electronic workshop and sample preparation laboratories. It has also access to the university computer centre.

Piston cylinder laboratory

Stempel-Zylinder-Pressen-Labor

Deformation laboratory

Verformungslabor

7th International Short Course/"Doktorandenkurs" at Bayerisches Geoinstitut,
"High-Pressure Experimental Techniques and Applications to the Earth‘s Interior"
14.-18. February 2005

Theoretical and practical sessions and demonstrations in the laboratories
Theoretische und praktische Einweisungen in den Labors

3. Forschungsprojekte

Es wird an dieser Stelle nur über die wichtigsten, derzeit laufenden Projekte berichtet. Informationen über abgeschlossene Teilprojekte sind in den Abschnitten 4.1 und 4.2 in Form von Literaturzitaten angegeben. Die Beiträge des Kapitels 3 sollen nicht zitiert werden.

3.1 Rheologie

Das Erdinnere wird von dynamischen Prozessen beeinflusst, die ihren Ausdruck an der Erdoberfläche in Erdbeben oder Vulkanausbrüchen sowie in der Bewegung der Lithosphärenplatten und der Bildung von Gebirgsketten finden. Das dynamische Verformungsverhalten der Erdmaterie wird durch deren rheologische Eigenschaften bestimmt, d. h durch ihre Reaktion auf mechanische Spannung. Die Rheologie von Mineralen und Gesteinen wird durch Fließgesetze beschrieben, die die aufgebrachte Spannung zu der Verformungsrate in Beziehung setzen. Fließgesetze können in mechanischen Testverfahren ermittelt werden, jedoch wird man mit verhältnismäßig vielen Variablen konfrontiert. Neben äußeren Einflussgrößen wie Temperatur, Druck, Fugazität/Aktivität verschiedener chemischer Komponenten müssen auch intrinsische, probenspezifische Materialeigenschaften wie Kristalldefekte und kristallographische Vorzugsrichtungen (Textur) in Betracht gezogen werden. Auch die plastische Materialverformung selbst beeinflusst diese spezifischen Eigenschaften. In den Geowissenschaften wird die Mikrostruktur verformter Gesteine daher häufig ausgewertet, um daraus ihre Deformationsgeschichte zu abzuleiten. Während sich der eigentliche Deformationspfad natürlicher Gesteine oft relativ erfolgreich rekonstruieren lässt, bleibt die Bestimmung der Spannung, die zur Verformung führte, weiterhin extrem schwierig. Hier bietet bisher zumeist nur die Messung und Extrapolation von Daten aus mechanischen Versuchen eine Möglichkeit, quantitative Ergebnisse zu erzielen.

Für das Verständnis der Konvektionsprozesse im oberen Erdmantel sind Kenntnisse über die plastische Verformung von Olivin ausschlaggebend. Seitdem ein neuer Typ Verformungs-apparatur (‘D-DIA’-Typ) für kontrollierte Hochdruck-Verformungsexperimente verfügbar geworden ist, können experimentell die Spannungen erzeugt werden, die für die plastische Deformation des Olivins unter den Bedingungen des oberen Erdmantels nötig sind. In Kombination mit einer Synchrotron-Strahlenquelle sind *in situ*-Bestimmungen von Spannung und elastischer Verformung unter hohen Drücken realisierbar geworden. Erkenntnisse über den Einfluss einer Zugabe von basaltischer Schmelze auf die Verformung von Olivin sind von Bedeutung, da der oberste Erdmantel unter den mittelozeanischen Rücken und über abtauchenden Krustenplatten wahrscheinlich bis zu 10 % Schmelze aufweist. Die Anwesenheit einer Schmelze führt zu einer Verformungstextur, die sich drastisch von einer Olivinprobe ohne Schmelze unterscheidet, und damit auch zu einem sehr unterschiedlichen Muster in der physikalischen Anisotropie (z. B. seismische Wellengeschwindigkeiten). In ähnlicher Weise führt bei monophasem Gestein die Zugabe von Partikeln einer zweiten Phase zu einem drastisch veränderten Verformungsverhalten. Die Anteile der plastischen Verformung in beiden Phasen sind dann stark von der Temperatur und vom rheologischen Kontrast abhängig.

Die Rheologie von Eklogit bestimmt sowohl das Verhalten abtauchender Platten als auch die Bildung von Hochdruck-Terranes, die in Gebirgsgürteln auf der ganzen Erde auftreten. Die Festigkeit von Eklogit wird durch das mechanische Verhalten der Minerale Omphazit und Granat gesteuert, wobei sich der Granat als überraschend stark deformierbar erweist, wenn seine Korngröße klein genug ist, um durch Diffusionskriechen und Korngrenzengleiten verformt zu werden. Die Obduktion von Eklogitgesteinen auf kontinentale Kruste bleibt rätselhaft, da die Dichte von Eklogit im allgemeinen deutlich über der der umgebenden Gesteine liegt. Tektonische Modelle, die diese Diskrepanz zu erklären versuchen, müssen daher sorgfältig im Hinblick auf die Deformationsmerkmale in den obduzierten Gesteinen selbst überprüft werden.

Feldspat und Quarz sind die Hauptbestandteile von Krustengesteinen und daher die wichtigsten Minerale für die Untersuchung des Deformationsverhaltens der Erdkruste. Das rheologische Verhalten dieser Minerale ist daher von großer Bedeutung sowohl für Hochtemperatur-Mylonite der tieferen Erdkruste als auch beim Einsetzen bruchhafter Verformung bei niedrigeren Temperaturen, und sogar bei der Verformung von Sandsteinen in direktem Kontakt mit Eis unter einem Gletscher. Im letzteren Beispiel deuten Mikrostrukturen an, dass die durch die Gletscherbewegung verursachte Reibungshitze unerwartet hohe Temperaturen erreicht hat, die möglicherweise sogar zur Schmelzbildung ähnlich wie in Pseudotachyliten geführt hat. Sogenannte 'PDFs' (planar deformation features) in Quarz werden als Anzeichen einer Schockmetamorphose unter hohen Drücken (z. B. durch ein Impaktereignis) interpretiert; sie müssen jedoch sorgfältig von regulären Deformations-lamellen unterschieden werden, die sich bereits bei niedrigen Spannungen bei der Verformung von Quarz bilden.

3.2 Physikalische Eigenschaften von Mineralen

Die Beziehung zwischen Struktur (sowohl im atomistischen als auch im mesoskopischen Maßstab) und physikalischen Eigenschaften von Materialien steht in zahlreichen wissenschaftlichen Fachgebieten im Mittelpunkt der Forschung. Minerale sind in diesem Zusammenhang von doppelter Bedeutung, da sie einerseits das Material repräsentieren, aus dem sich die feste Erde aufbaut und andererseits die Template für oxidische Materie darstellen, die für die Materialforschung von Interesse ist. Für das Verständnis von Materialeigenschaften unter Bedingungen des Erdinneren, wo hohe Drücke und Temperaturen vorherrschen, ist Kompression offensichtlich der zentrale Parameter. Druck kann jedoch auch als Werkzeug verwendet werden, um die interatomaren Abstände zwischen elementaren Bausteinen so zu verändern, dass damit drastische Änderungen in den physikalischen Eigenschaften hervorgerufen werden.

Sowohl in den Geo- als auch in den Materialwissenschaften stehen Übergangsmetalloxide im Mittelpunkt des Interesses: Sie spielen eine wichtige Rolle als Träger von paläomagnetischer Information, stellen einen Hauptbestandteil des Erdinneren dar (und liefern Aufzeichnungen über dessen Oxidationszustand) und sie können als magneto-optische Bausteine sowie als

magnetische Nano-Partikel Einsatz finden. Daher stehen sie auch im Bayerischen Geoinstitut im Zentrum vieler experimenteller Arbeiten. In diesem Berichtsjahr konzentriert sich die Forschung im Diamantstempelzellen-Labor auf die Magnetismus/Struktur-Beziehungen in FeO-Wüstit. Zwei Beiträge des Kapitels befassen sich damit. Diese Beiträge werden durch einen weiteren Artikel zu Struktur-/Eigenschaftsbeziehungen in Wüstit/Periklas-Mischkristallen für $(Mg_{0.8}Fe_{0.2})O$ ergänzt.

Zwei weitere Beiträge haben die thermische Ausdehnung von Ti-Verbindungen zum Thema. Die Untersuchungen von Hochdruckphasen von TiO_2 in der α-PbO_2-Struktur und TiS werden hier dargestellt. Die Ergebnisse liefern wichtige Daten zum thermodynamischen Stabilitätsfeld dieser Minerale im Vergleich mit ihren Niedrigdruck-Polytyp (im Fall TiO_2), als auch zur Mischbarkeit von TiS mit Troilit (FeS).

Ein Beitrag nimmt die Untersuchungen zum Kompressionsverhalten eines Mitglieds der Pyroxengruppe mit Si in teilweise sechsfacher Koordination wieder auf. Es wird festgestellt, dass dieser Pyroxen die geringste Kompressibilität dieser Gruppe aufweist. Den Abschluss dieses Kapitels bildet ein Artikel über das Schmelzverhalten von Eis VII. Mit Hilfe der Raman-Spektroskopie konnte eine früher kontrovers debattierte Schmelzkurve bei relativ niedrigen Temperaturen bestätigt werden.

3.3 Mineralogie, Kristallchemie und Phasenübergänge

Kruste und Mantel der Erde liegen fast vollständig in festem, kristallinen Zustand vor. Aus diesem Grunde sind die Kristallstrukturen der Erdmaterie und die Beziehungen zwischen ihren mikroskopischen (d. h im atomistischen Maßstab) und makroskopischen Eigenschaften (wie z. B. Volumen oder Elastizität) von wesentlicher Bedeutung, sowohl in den Geowissenschaften, als auch in der Physik, Chemie und den Materialwissenschaften. Sowohl Strukturen als auch Eigenschaften reagieren auf Veränderungen der äußeren Parameter wie z. B. Temperatur, Druck, Fugazität der leichtflüchtigen Bestandteile. Die Reaktionen können kontinuierlich oder diskontinuierlich ablaufen. So steigen zum Beispiel die Wellengeschwindigkeiten im unteren Erdmantel durch die druckbedingte kontinuierliche Zunahme von Dichte und elastischen Konstanten an; plötzliche „Sprünge“ in den Wellengeschwindigkeiten sind an Diskontinuitäten wie bei 410 und 660 km Tiefe gebunden, wo polymorphe Phasenübergänge stattfinden (z. B. von Olivin nach Wadsleyit bei 410 km), oder wo durch den Zerfall von Ringwoodit in Silicat-Perowskit und Ferroperiklas ganz neue Verbindungen entstehen (wie bei 660 km). Durch Untersuchungen von Struktur-/Eigenschaftsbeziehungen als Funktion von Druck, Temperatur oder chemischer Zusammensetzung gewinnen wir somit Einblicke in sehr lokale, atomistische Mechanismen, die wir dann auf globale Fragestellungen anwenden dürfen. Sogar Extrapolationen in experimentell nicht zugängliche Druck- und Temperaturbereiche oder für bestimmte chemische Zusammensetzungen sind zu einem gewissen Maß erlaubt, wenn die Systematik der Struktur-/Eigenschaftsbeziehungen bekannt ist.

Prozesse und elastische Verformung im atomistischen Maßstab wurden in sogenannten „einfachen“ chemischen Verbindungen wie den Endgliedern $MgSiO_3$ oder Mg_2SiO_4 in den letzten Jahrzehnten erfolgreich untersucht. Nur wenige Informationen liegen jedoch über chemisch und strukturell komplexere Materie oder Mischkristalle vor. Das gilt sogar für lediglich binäre Systeme, in denen nur eine Atomart durch eine andere ersetzt wurde (z. B. Fe^{2+} gegen Mg in natürlichem Olivin) und in denen als zusätzliche Variable eine temperaturabhängige intrakristalline Ordnung/Fehlordnung auftaucht. Die so erzeugten lokalen Deformationen beeinflussen auch die Modelle im makroskopischen Maßstab zum thermodynamischen Mischungsverhalten, die für die Berechnung von Phasengleichgewichten chemisch komplexerer Minerale benötigt werden.

Die Beiträge dieses Kapitels gehen auf diese Entwicklungen ein. Sie bedienen sich weitgehend bekannter und verbreiteter Mineralgruppen (Pyroxene, Olivine, Amphibole, Karbonate) und beschreiben Struktur- und/oder Eigenschaftswechsel als Funktion von Druck, Temperatur und chemischer Zusammensetzung.

3.4 Geochemie

Viel von unserem Verständnis über Struktur und Geochemie des Erdinneren stammt aus der Kenntnis über die Gesamtzusammensetzung der Erde. Gleiches trifft offensichtlich für alle Planeten zu, und chondritische Meteoriten werden oft als Schlüssel zur Ursprungs-zusammensetzung der Planeten gepriesen. Das Verhältnis refraktärer lithophiler Elemente (wie z. B. Seltene Erden) im Erdmantel sowie die Verarmung an leichtflüchtigen Elementen in der Erde deuten darauf hin, dass sich die Erde aus einer Ur-Materie formte, die geochemisch mit der der meisten Chondrite übereinstimmt. Es bestehen jedoch auch eine Reihe von signifikanten Unstimmigkeiten beim Vergleich der Zusammensetzungen der Meteoriten mit dem oberen Erdmantel. Einige dieser Widersprüche sind auf die Differenzierung der Erde zurückzuführen, d. h die Abtrennung von Elementen in den Erdkern oder möglicherweise in nicht zugängliche Reservoire des silicatischen Erdmantels. Andererseits mögen zahlreiche Unterschiede die Tatsache widerspiegeln, dass keine meteoritische Zusammensetzung genau mit der chemischen Gesamtzusammensetzung der Erde übereinstimmt. Fraktionierungsexperimente, die unser Verständnis für die Art und die Bedingungen der Elementverteilung in der Erde mehren sollen, sind ausschlaggebend für eine Beantwortung dieser offenen Fragen. Das langfristige Ziel, die Gesamtzusammensetzung der Erde genauer zu bestimmen, ist Thema zahlreicher Beiträge dieses Kapitels.

Alle chondritischen Meteorite weisen niedrigere Mg/Si-Gesamtverhältnisse als der obere Erdmantel auf, wofür verschiedene Fraktionierungsprozesse verantwortlich sein könnten. Eine Erdkernbildung unter reduzierenden Bedingungen könnte zur Abtrennung von Silicium in den Kern geführt haben. Wenn andererseits signifikante Anteile der Erde zum Zeitpunkt ihrer Bildung im Schmelzzustand waren, könnte eine Kristallabtrennung von Si-reichen Silicatmineralen in den unteren Erdmantel hinein das Mg/Si-Verhältnis in der Restschmelze,

aus der sich bei der Abkühlung der obere Erdmantel entwickelte, erhöht haben. Anhand von Hochdruck-/Hochtemperaturexperimenten lassen sich diese Hypothesen überprüfen; es lassen sich auch Antworten auf die Frage finden, ob erhöhte Mg/Si-Verhältnisse im oberen Mantel das Ergebnis von Fraktionierungsprozessen darstellen, die den ganzen Planetenkörper betroffen haben, oder ein Artefakt der Gesamtzusammensetzung der Erde darstellen.

Der äußere Erdkern enthält bis zu 10 % eines bisher nicht identifizierten leichten Elements bzw. eines Gemenges leichter Elemente. Falls wir die Bedingungen der Kernbildung sicher bestimmen könnten und die Mechanismen kennen würden, die zur Elementfraktionierung aus dem Erdmantel führen, kämen wir einer Bestimmung der chemischen Zusammensetzung des Erdkerns ein großes Stück näher. Die leichten Elemente im Kern könnten zum Beispiel den Durchgang einer Metallschmelze durch einen festen silicatischen Mantel begünstigt haben, indem sie die Benetzungswinkel zwischen Metall und Silicat verringert haben und damit Fließen durch den Porenraum ermöglichten. Die Bestimmung des Einflusses verschiedener leichter Elemente auf die Metall/Silicat-Benetzungswinkel könnte somit Hinweise auf das im Kern vorhandene leichte Element liefern. In ähnlicher Weise könnten hohe Drücke die Löslichkeit leichter Elemente in dem Metall des Erdkerns beeinflussen.

3.5 Geodynamik

Geophysikalische Beobachtungen, insbesondere Seismologie und Untersuchungen zum Gravitationsfeld der Erde, liefern uns ein immer besseres Bild der physikalischen Eigenschaften im Inneren unseres Planeten. Hypothesen zum dynamischen Zustand des Erdmantels lassen sich jetzt durch die Kombination von Berechnungen des viskosen Fließens mit unserem derzeitigen Kenntnisstand über entsprechende physikalische Eigenschaften der Erdmaterie unter hohen Drücken und Temperaturen überprüfen.

Während der größte Teil der Hochdruckforschung am Bayerischen Geoinstitut auf diesen zweiten Aspekt der Geophysik der tiefen Erde abzielt, stellen Ergebnisse aus der Geodynamik eine wichtige Verbindung zur beobachtenden Geophysik (und Geochemie) dar. Die Geodynamik verwendet vermehrt Informationen aus solchen Beobachtungen in ihren Modellen zur plastischen Verformung des Erdmantels.

In den vergangenen Jahren wurden zunehmend Aspekte der Mineralphysik in geodynamische Berechnungen integriert. Ein Beitrag dieses Kapitels befasst sich mit der Erkundung der viskosen Struktur des Erdmantels durch die Kombination von Beobachtungen des Geoids mit durchschnittlichen Wärmeflussdaten, anomalen seismischen Laufzeiten und mineral-physikalischen Eigenschaften. Ein weiterer Beitrag beschäftigt sich mit dem Einfluss der Freisetzung von latenter Wärme als Folge von Phasenübergängen sowohl auf die Topographie der entsprechenden seismischen Diskontinuitäten als auch auf die dynamische Topographie der Erde.

3.6 Metamorphose in unterschiedlichen Zeitskalen

Metamorphe Gesteine nehmen ungefähr 85 % des Erdvolumens ein. Fast alle diese Gesteine wurden in der unteren Erdkruste und im Erdmantel gebildet. Sie stellen das Produkt tektonischer Prozesse dar, zu denen Subduktion an Plattengrenzen, Krustenverdickung unter kontinentalen Gebirgsgürteln, Grabenbrüche bei der Entstehung neuer Plattengrenzen zählen. Auch Konvektionsprozesse im Erdmantel spielen eine Rolle. Metamorphe Gesteine entstehen dadurch, dass ältere Ausgangsgesteine durch veränderte tektonische Umgebungsbedingungen überprägt werden und von physikalischen und chemischen Veränderungen im festen Zustand betroffen werden. Physikalische Änderungen beruhen auf Verformung und Mineral-Neubildungen, chemische resultieren aus kontinuierlichen und diskontinuierlichen metamorphen Reaktionen, die zu neuen stabilen Mineralen oder neuen Mineralzusammensetzungen führen.

Während ihrer Entstehung in einem veränderten tektonischen Umfeld wird in den metamorphen Gesteinen doppelte Information gespeichert. Zum einen werden Einblicke in den tektonischen Rahmen und in beteiligte Prozesse ermöglicht, woraus sich zum Beispiel durch das Studium der Mineralparagenesen die Bildungsbedingungen ableiten lassen, während die rheologischen Eigenschaften von Kruste und Mantel aus Verformungsmerkmalen stabiler Minerale abgeleitet werden können. Auf die Dauer der beteiligten Prozesse lässt sich durch Altersdatierungen der metamorphen Minerale schließen. Der andere Bereich der gespeicherten Informationen umfasst Einblicke in den Metamorphoseprozess, einschließlich z. B. der Keimbildung und des Wachstums metamorpher Minerale und betrachtet die Rolle von Verformung und Fluiden als Beschleuniger metamorpher Reaktionen. Die Beiträge dieses Kapitels fallen in beide Bereiche und stellen neue Erkenntnisse über tektonische und metamorphe Prozesse dar. Dabei werden neue Daten für die Bildungsbedingungen von Hochdruck-Mineralvergesellschaftungen und neue experimentelle Untersuchungen über die Rolle der Deformation für die Kinetik metamorpher Reaktionen aufgeführt.

3.7 Fluide und ihre Wechselwirkung mit Schmelzen und Mineralen

Ohne Fluide wäre die Erde heute anders beschaffen. Abgesehen davon, dass sich ohne Ozeane möglicherweise kein Leben entwickelt hätte, würden auch Prozesse, die jetzt auf der Oberfläche und im Inneren der Erde ablaufen, entweder gar nicht stattfinden oder sich ziemlich unterschiedlich vollziehen. Fluide sind seit der frühen Erdgeschichte präsent und finden sich vom Kern bis zur Kruste. Seitdem entdeckt wurde, dass „trockene“ bzw. nominell wasserfreie Minerale tatsächlich relativ große Mengen an Wasserstoff in ihrem Gitter einbauen können, ist davon auszugehen, dass die Ozeane wohl lediglich einen kleinen Teil der Wassermenge repräsentieren, die in der Erde gespeichert ist. Daraus folgt, dass Wasser aus den Ozeanen und der Atmosphäre, das entlang von Subduktionszonen in den Erdmantel transportiert wird, über lange Zeiträume im Erdinneren verbleiben kann. Da gelöster

Wasserstoff signifikante Auswirkungen auf die physikalischen und chemischen Eigenschaften des Erdmantels hat, ist die Frage nach der Löslichkeit und dem Lösungsmechanismus von Wasserstoff in Mantelphasen ausschlaggebend.

Fluide stellen eine Hauptkomponente bei der Bildung von zahlreichen mineralischen Rohstoffen auf und in der Erde dar. Einer der seltensten, jedoch wirtschaftlich hoch attraktiven Rohstoffe – Diamanten – wird ebenfalls unter dem Einfluss von Fluiden gebildet. Noch immer liegen viele Details der Bildungsgeschichte natürlicher Diamanten im Dunkeln. Deren Untersuchung liefert genauere Hinweise zum Chemismus der Fluide, aus denen sich die Diamanten bildeten. Komplementäre Studien an synthetischen Diamanten unterstützen die Modellierung der Bildungsprozesse.

3.8 Physikalische Eigenschaften von Schmelzen und Magmen

Die chemische Zusammensetzung der Erde entwickelte sich vor allem über Bildung von Magmen (im Sinne von teilgeschmolzenen Gesteinen) durch Aufschmelzung in der Tiefe, Transport der Magmen und ihre anschließende Kristallisation. Experimentelle Untersuchungen zu magmatischen Prozessen sowohl hinsichtlich der Schmelz-/Kristallisationsbeziehungen als auch der physikalischen und chemischen Eigenschaften von Schmelzen und Magmen sind daher besonders wichtig. Dadurch gewinnen wir klarere Vorstellungen, wie sich der Chemismus und die Struktur der Erde entwickelt haben und sich noch heute weiterentwickeln.

Magmatische Prozesse spielten in der sehr frühen Entwicklungsgeschichte der Erde und anderer erdähnlicher Planeten eine wichtige Rolle. Während der Akkretion aus solarem Nebel bewirkten Bombardements durch kleine asteroidengroße Körper („Planetesimale“) auf der jungen Erde wahrscheinlich einen derartig hohen Temperaturanstieg, dass der Planet in einem globalen Maßstab aufgeschmolzen wurde. Ein „Magma-Ozean“ bildete sich aus. Es ist auch wahrscheinlich, dass unser Mond als Resultat einer Kollision der Erde mit einem marsgroßen Körper aus der Erdmasse herausgeschleudert wurde. Allein dieses Impakt-Ereignis hätte möglicherweise für die Ausbildung eines Magma-Ozeans auf der Erde mit einer Tiefe von 1500-2000 km oder mehr ausgereicht. Ein frühgeschichtlicher Magma-Ozean förderte eine früh einsetzende chemische Differenzierung des Erdkörpers. Erstens konnte geschmolzenes, eisenreiches Metall sich sehr leicht von einer silicatischen Schmelze abtrennen und unter dem Einfluss der Schwerkraft absinken, und so den Erdkern bilden. Zweitens könnte die Kristallisation der Silicatschmelze durch eine Abtrennung der Kristalle (absinkend oder aufschwimmend) zu einer frühen Differenzierung geführt haben. Die Dynamik von Konvektion, Abkühlung und Auskristallisation in dem Magma-Ozean wird von den Transporteigenschaften der Silicatschmelze unter hohen Drücken beeinflusst. Zwei Artikel in diesem Kapitel stellen neue Ergebnisse aus Untersuchungen zu Transporteigenschaften (Viskosität und Diffusion) einer Peridotitschmelze bei Drücken bis 16 GPa und Temperaturen bis 2500 K vor.

Untersuchungen über die Eigenschaften von Magmen sind für das Verständnis von heutigen Vulkanausbrüchen unerlässlich. Diese Studien sind für Vorhersagen zur Beschaffenheit des Vulkanismus notwendig – zum Beispiel für Abschätzungen, ob erwartete Ausbrüche einen explosiven Charakter aufweisen werden. Ein wesentlicher Faktor ist in dieser Hinsicht das Maß, in dem gelöste, leicht flüchtige Stoffe (z. B. Wasser und Kohlendioxid) während des Magmenaufstiegs freigesetzt werden können. Hier kann eine Entgasung unter Ungleichgewichtsbedingungen eine wichtige Rolle spielen, wie in diesem Kapitel am Beispiel von Magmen des Vesuvs gezeigt wird. Zusätzlich zur Differenzierung durch Kristallisation kann die chemische Zusammensetzung von Magmen durch Kontamination verändert werden. Dies geschieht durch Auf- bzw. Anschmelzung von Gesteinen, die das aufsteigende Magma auf dem Weg an die Erdoberfläche passiert. In einem Beitrag wird gezeigt, wie die Reaktion von Magmen mit Kalksteinen und Marmoren der kontinentalen Kruste die Zusammensetzung der kalkalkalischen Gesteine in Italien beeinflusst hat. Die beschriebenen Reaktionen liefern auch eine Erklärung für die erheblichen Kohlendioxid-Emissionen, die in der Umgebung der italienischen Vulkane beobachtet wurden.

Eine wichtige Methode der Geophysik, um in der Tiefe vorhandenes Magma in der Erdkruste aufzuspüren ist die Messung der elektrischen Leitfähigkeiten. Um Ergebnisse aus Geländemessungen interpretieren zu können, sind Laboruntersuchungen zur elektrischen Leitfähigkeit von Magmen als Funktion der chemischen Zusammensetzung und des Grads der Kristallisation erforderlich. Daten dieser Art werden hier für basaltische Magmen präsentiert. Dabei wird die Bedeutung der chemischen Zusammensetzung der Restschmelze während des Kristallisationsprozesses hervorgehoben. Ein weiterer Beitrag zeigt anhand experimentell gewonnener Daten auf, dass wahrscheinlich eine Magmenkammer unter dem tibetanischen Plateau existiert.

Schließlich befasst sich ein Beitrag mit der Rolle des Eisens bei der Beeinflussung von Struktur und chemischen/physikalischen Eigenschaften von Silicatschmelzen. In diesen Studien wurden abgeschreckte Gläser untersucht, da entsprechende spektroskopische Messungen in Schmelzen nur schwer oder gar nicht durchzuführen sind.

3.9 Materialwissenschaften

Die Hochdruck-/Hochtemperatur-Forschung ist mehr denn je an der Entwicklung neuer Materialien beteiligt, wobei das Geoinstitut durch seine Aktivitäten auch auf diesem Fachgebiet in einer starken Position ist. Die einzelnen Forschungsarbeiten decken einen weiten Bereich an Materialien ab, von einfachen Metallen bis hin zu komplexen Verbindungen. Die Eigenschaften von Ce, Pr, Ge und Sn sowie die ihrer Legierungen sind temperatur- und druckabhängig, wodurch sich neue Möglichkeiten in der Synthese von Materialien mit einzigartigen und nützlichen Eigenschaften ergeben. Im Mittelpunkt der Untersuchungen stehen weiterhin superharte Stoffe: Der Einsatz der 5000 Tonnen-Multianvil-

Presse am Bayerischen Geoinstitut ermöglichte die Synthese eines neuartigen superharten Verbundmaterials aus Borcarbid und Bor-dotiertem Diamant. Geräte, bzw. Bausteine aus diesem Material ermöglichen eine Verwendung in Temperaturbereichen, in denen konventionelle Elektronik auf Silizium-Basis versagt. Oxide wurden sowohl mit theoretischen als auch experimentellen Ansätzen untersucht, um ihren Einsatz in zahlreichen technologischen Anwendungsbereichen zu optimieren. Die Hochdruck-Synthese von Doppel-Perowskiten führte zu neuen Erkenntnissen über die Physik der Kationen-Fehlordnung und über die Ursache bemerkenswerter Eigenschaften wie sehr starkem magnetischen Widerstand. Lagenförmiges Zirkon-Phosphat und -Phosphonat liefern die Basis zur Vorbereitung maßgeschneiderter Verbindungen mit Strukturen und Reaktivitäten für zahlreiche feinabgestimmte Anwendungen.

3.10 Methodische Entwicklungen

Die Entwicklung neuer experimenteller Techniken und die Erkundung ihre Leistungsfähigkeit stellt eine faszinierende wissenschaftliche Herausforderung dar, die zu unerwarteten, bahnbrechenden Ergebnissen führen kann. Daher sollten keine Mühen und Kosten im Zusammenhang mit zeitraubenden Neuentwicklungen gescheut werden. Die Ergebnisse machen den Einsatz lohnenswert.

Im Bayerischen Geoinstitut ist eine Vielzahl von modernsten Hochdruck-Apparaturen und analytischen Techniken verfügbar, mit denen *in situ* und *ex situ* Mikroanalysen durchgeführt werden (Raman-, IR- und Mössbauer-Spektroskopie, elektrische Leitfähigkeitsmessungen, Mikrosonde und ein hochauflösendes analytisches Transmissionselektronenmikroskop (ATEM), etc.). Konventionelle Röntgendiffraktometrie lässt sich leider nicht für *in situ*-Beugungsmessungen in Diamantstempelzellen im Megabar-Bereich einsetzen. Hierfür ist zwar die Synchrotron-Technik gut geeignet; jedoch ist eine Verknüpfung von Synchrotronstrahlung mit anderen experimentellen Erfordernissen oft problematisch. Zahlreiche Phasenübergänge, speziell die in komplexen Systemen, erfordern einen chemischen Transport über Abstände von einigen Mikrometern (z. B. Auflösungsreaktionen). Derartige Prozesse werden thermisch aktiviert, sind jedoch aufgrund des niedrigen Diffusionsvermögens in Hochdruck-Phasen recht langsam. Verlässliche Ergebnisse können somit nur bei ausreichend langer Versuchsdauer gewonnen werden (bis zu 12 Std. oder länger pro Druck/Temperatur-Stufe). Weiterhin erfordern die Untersuchungen in bestimmten Intervallen zusätzliche Messmethoden wie z. B. Mössbauer-, Raman-, Infrarot-Spektroskopie oder Messungen der elektrischen Leitfähigkeit, die nicht an Synchrotron-Einrichtungen, jedoch am Bayerischen Geoinstitut parallel verfügbar sind. Ein kürzlich installiertes hochauflösendes Röntgensystem ermöglicht vor Ort Röntgenbeugungsmessungen bei Drücken bis in den Megabar-Bereich.

Die Fortschritte in der methodischen Entwicklung komplexer Hochdruck-/Hochtemperatur-Experimente werden in zwei Beiträgen vorgestellt: der erste betrifft die Mössbauer-Apparatur

für Messungen unter hohen Drücken und Temperaturen, der zweite eine Methode, gleichzeitig Röntgenbeugungsmessungen und Bestimmungen des elektrischen Widerstands an Metallen vorzunehmen. Zum Abschluss des Kapitels werden neue analytische Entwicklungen in der Festkörper-NMR (Nuclear Magnetic Resonance) vorgestellt.

3. Research Projects

In this section an overview of the most important ongoing projects is given. Information concerning recently-completed projects can be obtained from the publication lists of sections 4.1 and 4.2. Please note that the following contributions should not be cited.

3.1 Rheology

The interior of the Earth is governed by dynamic processes which find their most prominent expression in phenomena like earthquakes or volcanic eruptions as well as the movement of lithospheric plates or the formation of mountain chains. The dynamic deformation behaviour of Earth materials is determined by their rheology, that is, their response to mechanical stresses. The rheology of minerals and rocks are described by flow laws which relate the applied stress to the deformation rate. Flow laws can be determined in mechanical tests in the laboratory, but the number of variables is rather large. Besides external parameters such as temperature, pressure, and fugacity/activity of various chemical components also intrinsic materials properties such as crystalline defects and crystallographic preferred orientations (texture) have to be taken into account. In addition, plastic deformation of a material will also change its intrinsic properties. In the geosciences the microstructures of deformed rocks are therefore often used to reconstruct their deformation history. Whereas the reconstruction of the deformation path itself can be quite successful in natural rocks, the determination of the stresses that caused the deformation still remains extremely difficult. Here the measurement and extrapolation of data from mechanical tests offer in most cases the only possibility to achieve quantitative results.

The plastic deformation of olivine is of crucial importance for the understanding of convection processes in the upper mantle. The stresses necessary to deform olivine plastically at upper mantle conditions are becoming only now accessible, since a new type of deformation apparatus (‘D-DIA’) allows controlled deformation experiments to be performed at high pressure. In combination with synchrotron radiation sources, *in situ* measurements of stress and strain at high pressures (< 10 GPa) are feasible. The influence of added melt on olivine deformation is rather important since the uppermost mantle beneath mid ocean ridges and above subducting slabs most likely contains up to 10 % melt. It appears that the addition of melt leads to a very different texture and consequently to a very different pattern of physical anisotropy. Similarly, the addition of second phase particles to a single phase rock may also change the deformation behaviour drastically. Partitioning of strain between the two phases is then dependent on temperature and the rheological contrast between them.

The rheology of eclogite is critical for the behaviour of subducting slabs as well as for the formation of high-pressure terranes which are found in mountain belts around the world. The strength of eclogite is governed by the mechanical behaviour of omphacite and garnet, whereby garnet may be rather weak, if its grain size is small enough to deform by diffusional

creep and grain boundary sliding. The obduction of eclogite remains a puzzling problem since its density is generally significantly higher than that of the surrounding rocks. Tectonic models that attempt to explain this problem have to be carefully checked with respect to the deformational structures present in the rocks.

Feldspar and quartz are the main components of crustal rocks and therefore the most important minerals when we try to understand the deformation behaviour of the crust. Their rheology is of critical importance in high-temperature mylonites, at the onset of semi-brittle deformation in a low temperature regime and even for the deformation of sandstone underneath a glacier. In the last case microstructures indicate that frictional heating due to glacial movement may cause unexpected high temperatures, possibly even up to the formation of melts similar to pseudotachylites. Planar deformation features in quartz finally are indicative of high-pressure shock metamorphism (*e.g.* during impact events), but have to be carefully distinguished from regular deformation lamellae induced already at low stresses.

a. *Using the D-DIA to measure the stress in forsterite at high pressure and temperature (H. Couvy, D.J. Frost and F. Langenhorst, in collaboration with Y. Wang/Chicago, W.B. Durham/Livermore, D. Weidner/Stony Brook and P. Cordier/Lille)*

A major challenge in mineral physics is the measurement of rheological properties at the high pressures and temperatures that correspond to the Earth's convecting mantle. A newly developed deformation apparatus, the deformation-DIA (D-DIA), allows stress and strain to be determined during deformation at high temperature (to 2000 °C) and pressure (to 10 GPa) using *in situ* synchrotron techniques. This apparatus is a modification of the DIA cubic anvil apparatus, which is used in solid-media compression experiments. The device compresses a cubic pressure assembly quasi-hydrostatically by the advancement of 6 cBN or WC anvils. In the D-DIA, once pressure and temperature are achieved, the top and bottom anvils can be driven independently thus applying a compressive stress in the vertical direction while the four side anvils are retracted to allow the pressure to remain constant. Very low strain rates can be achieved, similar to those attainable with a Paterson type deformation apparatus.

In this study, we are using the D-DIA to measure the stress and strain rate in a sample of polycrystalline forsterite (Mg_2SiO_4) during deformation. As a first step, a cell design was developed that could sustain high temperatures for relatively long periods of time and in which sample strain was minimal during hydrostatic compression. This development was performed off-line using the D-DIA press installed at the Bayerisches Geoinstitut. A 1 mm long sample of hot pressed forsterite was used. The sample was heated using a graphite furnace and stress on the sample was transmitted using hard alumina pistons. Softer crushible alumina was also used in the sample column in order to minimise sample strain during compression. A 6 mm edge length cubic pyrophyllite assembly was employed with 4 mm WC truncations.

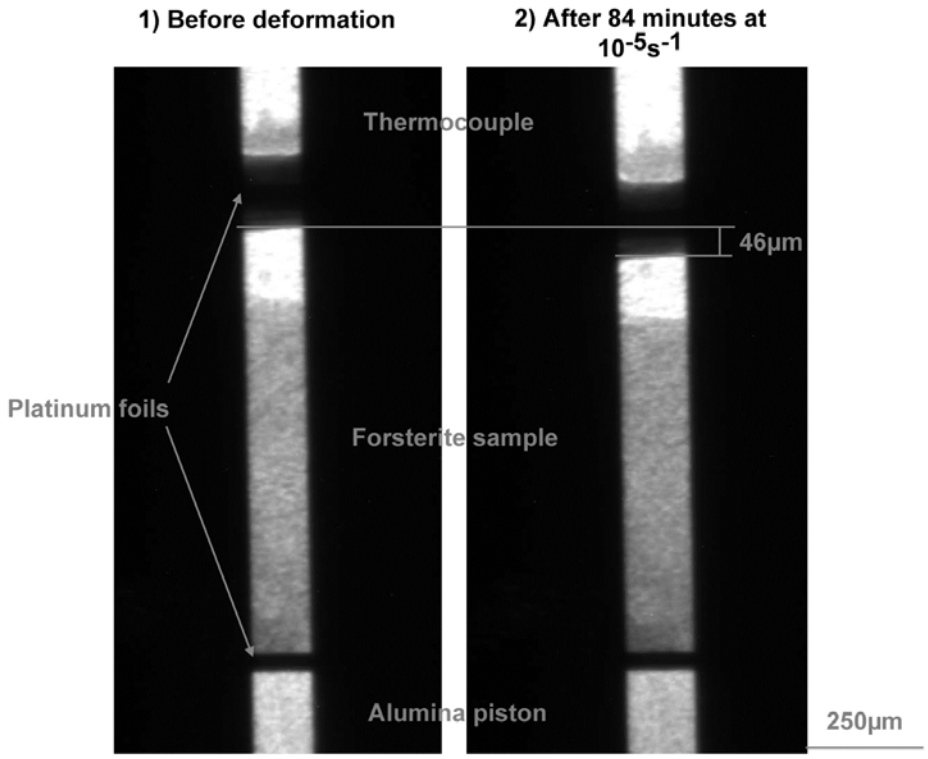

Fig. 3.1-1: Radiographic images of a D-DIA experiment performed at APS (60 t and 1300 °C). Shadows created by platinum foils on the top and bottom of the sample allow sample strain to be measured from the images. Black shadows on the left and right are from the anvils.

In situ experiments were performed using synchrotron facilities at the Advanced Photon Source (APS) and at National Synchrotron Light Source (NSLS). Sample stress and pressure were determined from the lattice strain using X-ray diffraction and sample strain was measured using *in situ* X-ray radiography (*e.g.* Fig. 3.1-1). At APS, samples were deformed by 6 % at about 3 GPa and 1300 °C, with a strain rate of approximately $10^{-5}s^{-1}$. At NSLS, a sample was deformed by 10 % at about 4 GPa and 1300 °C with a strain rate of about $10^{-5}s^{-1.}$ For an applied load of 50 tonnes the sample pressure was determined to be approximately 4.5 GPa at room temperature and the differential stress was approximately 1.5-2 GPa. As the sample was heated to 1000 °C the differential stress decreased drastically to below 0.5 GPa. The differential stress stayed below 0.5 GPa during deformation at 1300 °C and a strain rate of $2.5\times10^{-5}s^{-1}$. The hydrostatic pressure decreased to 4 GPa and stayed constant during deformation (Fig 3.1-2). Microstructures of the recovered samples will be investigated to determine the dominant deformation mechanisms under these high-pressure conditions.

The D-DIA coupled with a synchrotron X-ray source allows rheological properties of minerals to be accurately determined under high pressure and temperature and, hence, offers a new opportunity to better understand dynamic processes of the Earth's mantle.

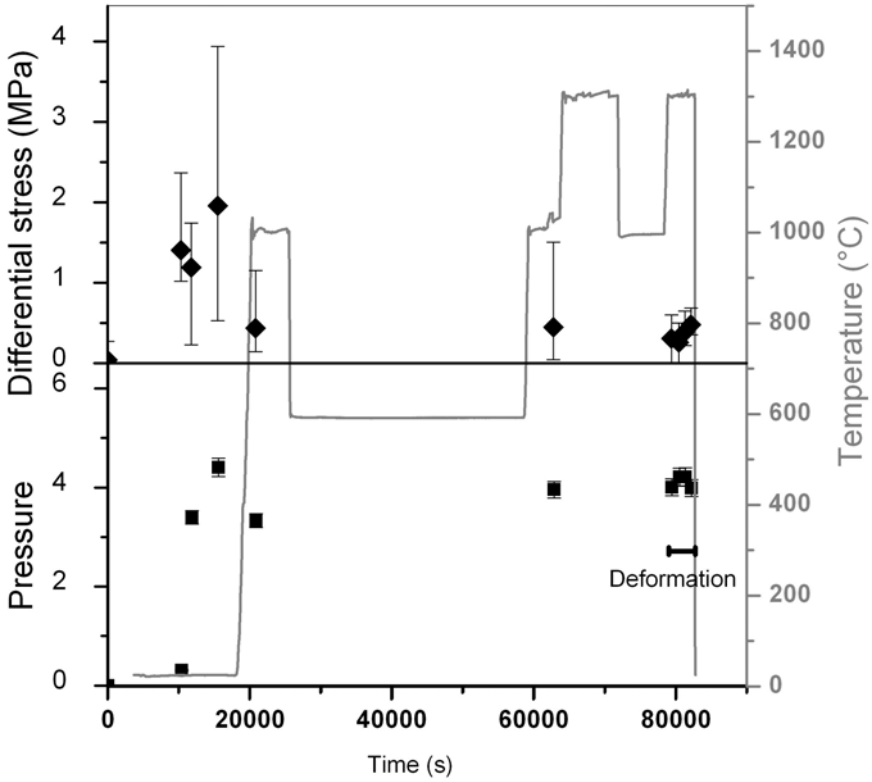

Fig. 3.1-2: Pressure and differential stress calculated from lattice strain of the forsterite sample. Hydrostatic pressure: black squares. Differential stress: black diamonds. The temperature path is indicated in grey. The plotted values of stress are an average of the calculated values from the different diffraction peaks. The error bars represent the range of the values from these peaks.

b. *The influence of melt on olivine LPO (B. Holtzman, M. Zimmerman, D. Kohlstedt/ Minneapolis and F. Heidelbach)*

Understanding the origins of seismic anisotropy is essential to interpret mantle convection patterns from measurements of seismic data. This problem is especially difficult and important in regions such as mid-ocean ridges and subduction zones where large amounts of melt are being produced and continental and oceanic crust is being created. Thus, we are studying the influence of melt and the organization of melt on the seismic properties of mantle rocks. It is well known that solid state deformation that is partly or wholly occurring in the dislocation creep regime will tend to align the easiest slip system of the deforming crystals in the direction of flow, creating a lattice preferred orientation (LPO) in the rock. For seismically anisotropic minerals like olivine, this alignment causes a bulk seismic anisotropy in the rock. For olivine, it has long been assumed that the dominant anisotropy in high-temperature (asthenospheric) conditions is produced by the slip system (010)[100], such that a-axes [100] align parallel to the shear direction. This assumption, based on numerous field and experimental studies, seems valid over large regions of the upper mantle, but tends to cause

complications in the interpretation of seismic anisotropy in partially molten regions in the upper 200 km of the Earth.

In a recent study, we demonstrated that melt causes significant changes to olivine LPO, in synthetic samples deformed in a Paterson gas medium apparatus at the University of Minnesota. The fabric depends strongly on the geometry of the melt. We painted a very simple picture of three fabrics, as shown in Fig. 3.1-3.

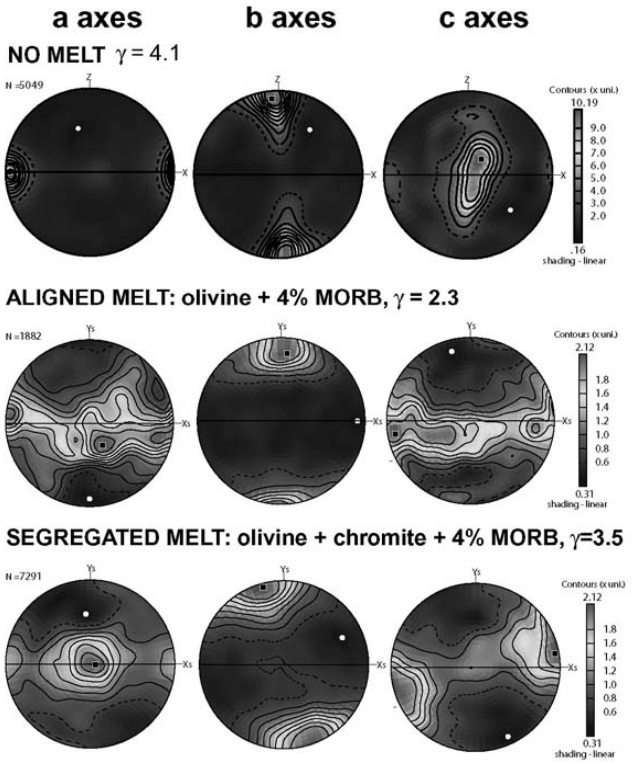

Fig. 3.1-3: Olivine pole figures for three samples deformed in simple shear (top-to-the-right).

If no melt is present, olivine a-axes are aligned parallel to the shear direction. If melt pockets are aligned, but are distributed homogeneously at length scales longer than the grain scale, then olivine a-axes form a girdle, as in Fig. 3.1-3. When melt is distributed on a length scale longer than the grain scale and melt-rich channels form, then a-axes form concentrations in the shear plane, 90° to the shear direction. Normally, this pattern would be interpreted as deformation dominated by the (010)[001] slip system. We attributed the change instead to the effect of strain partitioning and a consequent rotation of the local stress tensors felt by the melt-depleted lenses. Thus, the deformation is still dominated by the (010)[100] slip system, because there is no thermodynamic reason to suspect a change in the dislocation dynamics.

We have continued to explore this story in several ways, in order to better understand the nature of the transition between these fabric types. We vary primarily the melt fraction, the

length scale of variations in the melt distribution (from the grain scale to tens of times that distance), finite shear strain, boundary conditions of deformation geometry, and the applied shear stress or strain rate. Here, we present two simple trends that illustrate the complexity of the problem.

1. Olivine + MORB and the onset of the a-axis rotation. Increasing strain on a sample with no long wavelength melt fraction variations (olivine + MORB) actually causes a transition from the fabric shown in Fig. 3.1-3 (center) to that in 3.1-3 (bottom). It is the aligned melt pockets with variations at any length scale that cause the destruction of a-axis point maxima in the shear direction. However, with increasing shear strain, those maxima continue to cluster 90° to the shear direction. In samples with long wavelength variations in melt distribution, this transition probably also happens, but at very low strain. While we had previously thought that the longer wavelengths of melt segregation were required to cause the a-axis rotation, it now seems that the processes that cause this rotation also work for small wavelength variations in the melt distribution (*i.e.* melt pockets separated by one to several grain diameters). It appears that the kinetics of the processes that cause the rotation are slower when the melt distribution variations are at smaller wavelengths.

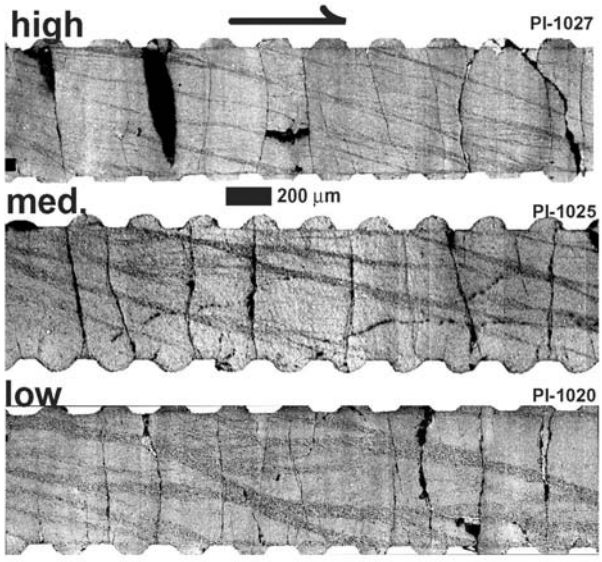

Fig. 3.1-4: Three samples of olivine + chromite + MORB deformed to shear strains of ~ 3.5, to three different final stress values, 30 MPa, 110 MPa, and 175 MPa. The melt rich bands are the grey features oriented at ~ 10-20 degrees to the shear direction. The vertical lines are quench cracks.

2. The effect of stress on olivine LPO. Another closely related set of experiments and questions concern the influence of stress on the melt distribution in the sample and LPO of olivine. As shown in Fig. 3.1-4, as the shear stress applied to the sample increases (in samples deformed to constant shear strain of 3.5), the dominant frequencies in the melt distribution decrease (*i.e.* the largest spacing between the largest bands decreases). Also, as stress

increases, the strength of the fabric remains the same, but the strength of that fabric increases significantly, as shown in Fig. 3.1-5, especially in the a- and c- pole figures.

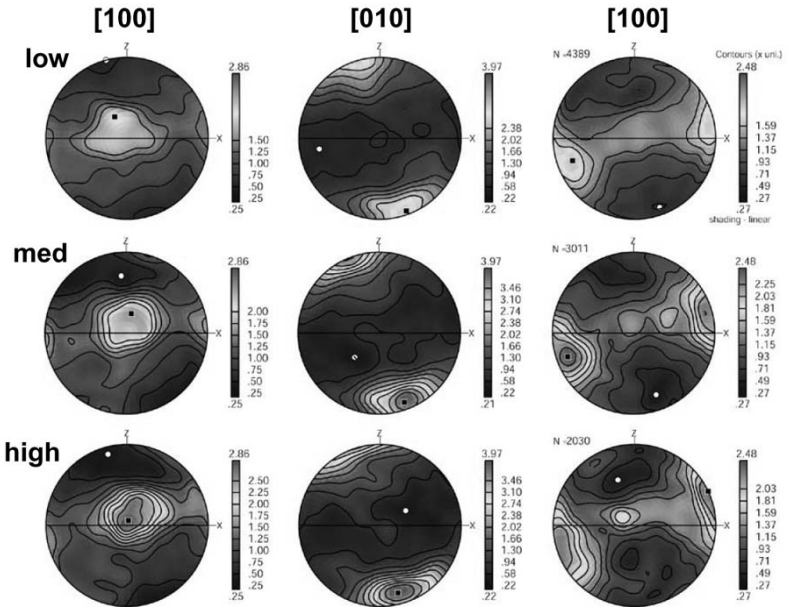

Fig. 3.1-5: Olivine pole figures for the three samples shown above. All pole figures for each plane are plotted on the same gray scale.

Thus, we see a conundrum: if we extend the trend in #2 down to the scale of melt bands distributed down to the grain size (*i.e.* a uniform distribution of pockets), we would expect even stronger fabrics with rotated a-axis maxima. However, this prediction is in conflict with the observations of the olivine + MORB samples with girdles slowly becoming point maxima, discussed in #1, above. Thus the length scale of variations in melt distribution (related to the compaction length) is not the only controlling parameter; shear stress is also important in determining the fabric type.

In conclusion, we are making progress towards understanding the transitions between the fabrics illustrated in Fig. 3.1-3, but we have several aspects of parameter space left to explore. Understanding these transitions in fabric patterns will be important in understanding the conditions at which naturally observed fabrics formed and interpreting patterns of seismic anisotropy in partially molten regions of the Earth.

c. *Large strain deformation of two-phase aggregates (M. Bystricky/Zurich, S.J. Mackwell/ Houston and F. Heidelbach)*

Although natural rocks are typically composed of several phases, most experimental deformation studies have focused on the rheological properties of monomineralic aggregates.

Low-strain experiments in compression have permitted the identification of deformation mechanisms and the formulation of constitutive equations. More recently, experimental studies using a torsion apparatus have investigated the effect of strain on the deformation properties of monomineralic rocks. Typically, deformation by dislocation creep to large strain results in weakening or in steady mechanical behaviour along with progressive recrystallization of the microstructure and the formation of strong crystallographic preferred orientations (CPO). Though attempts to model the behaviour of polyphase systems with properties of the end-members exist, little is known on the effect of secondary phases on the evolution of microstructures and hence strength and texture development at large strains. We have started an experimental investigation of the deformation properties of a model aggregate comprised of olivine (strong phase) and magnesiowüstite (Mg,Fe)O (weak phase), two minerals that have previously been studied extensively both in compression and in torsion.

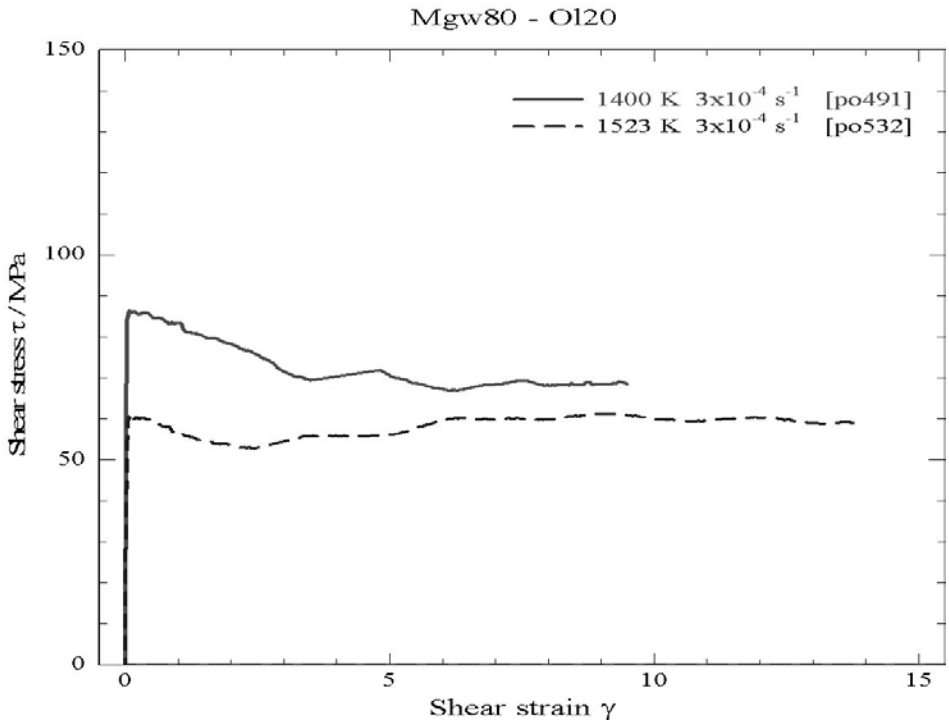

Fig. 3.1-6: Magnesiowüstite-olivine samples deformed at 1400K and 1523K to shear strains up to 14.

Two-phase aggregates with ~ 20 vol.% olivine (simulating hard inclusions in a weak matrix) were deformed in torsion in a gas-medium vessel at 1400K and 1523K, 300 MPa confining pressure and strain rates of 1-3 x 10^{-4} s^{-1} to shear strains up to 14. At low strains, the measured strengths are consistent with the ones predicted by theoretical models for strengthening due to a hard second phase. At large strains, we observed ~ 25 % of weakening at 1400K, and an approximately steady behaviour at 1523K. Stress exponents of 4 at both intermediate and large strains suggest deformation remained controlled by dislocation creep in (Mg,Fe)O throughout the experiments.

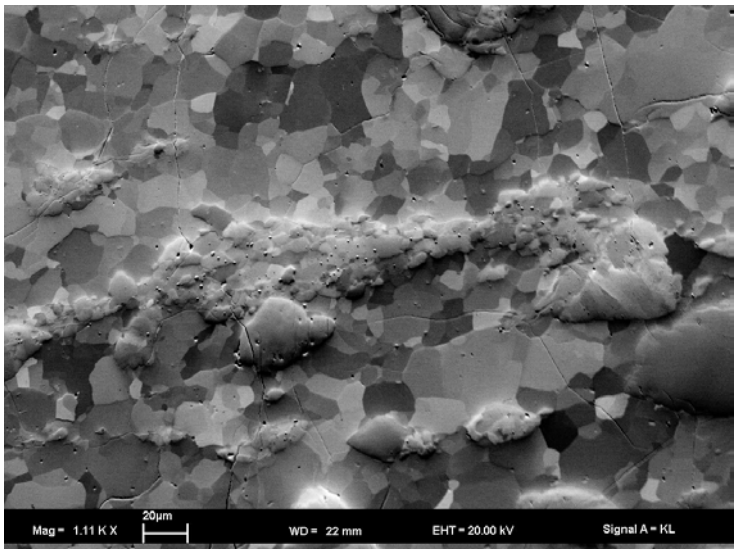

Fig. 3.1-7: Recrystallized olivine grain (center) in a magnesiowüstite matrix; sample deformed at 1523K to a shear strain of 14. SEM orientation contrast image.

Microstructural analysis using SEM reveals an equigrained starting microstructure with homogeneously distributed olivine grains in the (Mg,Fe)O matrix. Deformation leads to grain size refinement of (Mg,Fe)O by dynamic recrystallization. The recrystallized (Mg,Fe)O grains remain equant, suggesting high grain boundary mobility. Electron backscatter diffraction (EBSD) measurements show a texture with a weak alignment of <110> in the shear direction and a preferred orientation of {100} oblique to the shear plane and the shear direction. The somewhat weak texture and the lack of shape preferred orientations of the magnesiowüstite grains point to deformation by dislocation creep with an important contribution of diffusional processes. By contrast, many of the olivine grains appear relatively undeformed and have a slight shape preferred orientation, confirming that most of the strain is accommodated by the (Mg,Fe)O matrix. Internal deformation features are visible in some olivine grains and a few grains are fully recrystallized and highly sheared. At high temperature, fully recrystallized olivine grains are more numerous and create a foliation in agreement with the total bulk shear. CPOs consistent with the main slip systems for pure olivine at these conditions confirm that dislocation creep is active in the olivine inclusions at both temperatures. This study provides one of the first experimental data sets that allows direct testing of models of creep in two-phase aggregates with a large viscosity contrast.

d. *The rheology of high-pressure shear zones, Western Gneiss Region, Norway (M.P. Terry and F. Heidelbach)*

Ductile faults or shear zones have the potential to allow large displacements of metamorphic rocks and have played a crucial role in subduction and exhumation processes in many HP and UHP terrains. The strength of these zones may control that rates at which material can be

transported to the surface of the Earth. In this study, we examine the shear zones that were formed during continental subduction. The rheologic properties of polyphase materials are difficult to determine since the mixing behaviour and its effect on the strength of the rock are generally unknown. However, the presence of monomineralic to nearly monomineralic layers of garnet, plagioclase, and omphacite in the strained samples and their deformation without necking or breaking indicates that, as a first approximation, the flow laws for these minerals can be applied separately. The similar strengths of these layers suggest that the flow laws for the different minerals might converge at a common differential stress and strain rate.

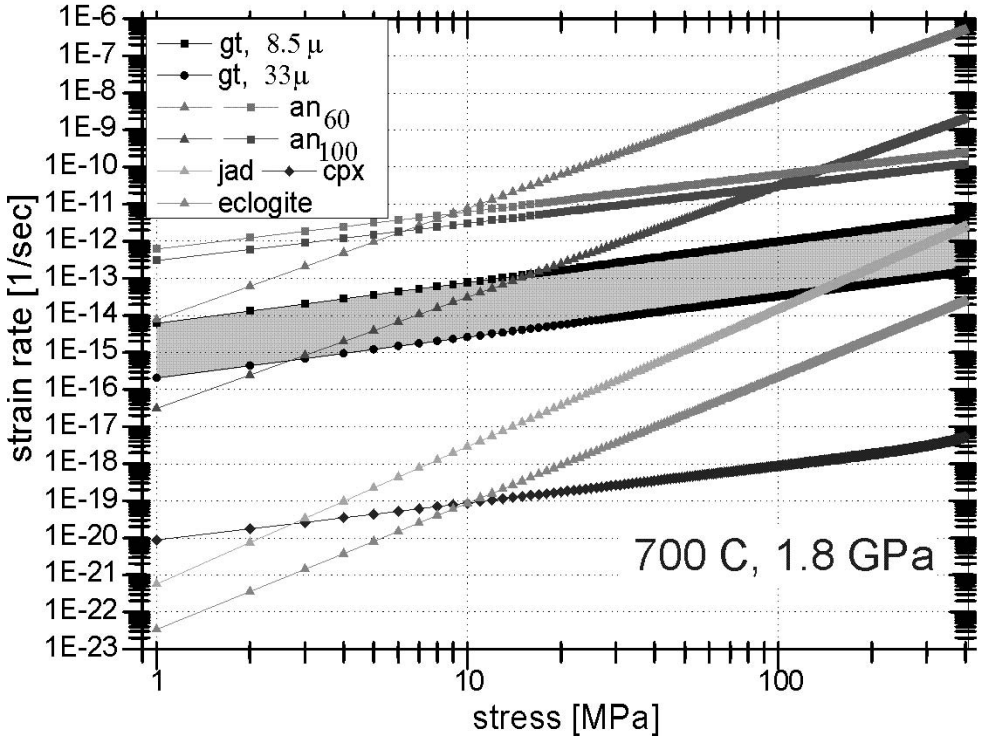

Fig. 3.1-8: Stress-strain rate plot showing experimental flow laws for garnet (gt 8.5µ and gt 33µ), plagioclase with 60 and 100 % anorthite content (an60 and an100), clinopyroxene, jadeite and eclogite. All calculations were carried for a temperature of 700 °C. Symbols indicate diffusion creep (squares, circles), dislocation creep (triangles) and combined dislocation-diffusion creep (diamonds).

In Figure 3.1-8, the available previously published rheological data applying to our case are displayed for the relevant stress-strain rate region. A temperature of 700 °C was assumed and grain sizes of 8.5 and 33 µm for garnet, and 50 µm for plagioclase and omphacite were used in the calculations. For stresses between 10 and 100 MPa, the flow laws of fine grained garnet give strain rates between 10^{-13} and 10^{-12} sec^{-1} for deformation by diffusional creep. Increasing the grain size of garnet from 8.5 to 33 µm reduces the strain rate by about 1.5 orders of magnitude (at constant stress), which may reflect realistically the different deformation rates in different parts of the shear zone.

The combination of flow laws makes stresses of 100 to 150 MPa and strain rates of 10^{-12} to 10^{-13} sec^{-1} the most likely deformation conditions for the shear zones in the Haram gabbro. The relatively high stresses are mainly needed for the deformation of jadeite/omphacite; the mechanical data for the pyroxenes are still very scarce, and none exist for diffusional creep, which becomes more important at lower stresses. The influence of pressure on the flow laws was neglected here since there are no systematic studies; the flow laws presented were measured at confining pressures between 300 MPa (plagioclase, clinopyroxene) and 3 GPa (eclogite), indicating that for the pressure range in question (< 1.8 GPa) large effects are unlikely. Another unknown is the water content of the minerals at the time of deformation; from the absence of water bearing phases it is clear that there was no free water, but the amount of water dissolved in the minerals is not constrained. With the exception of plagioclase, the flow laws were derived at 'dry' conditions, which mean that they give upper bounds in strength. Additional water is most likely to decrease the stresses and to increase the strain rates. Keeping also in mind that all of the flow laws above had to be extrapolated considerably to match natural conditions (especially in strain rate, temperature and, to a lesser extent, in grain size and composition) the resulting stress-strain rate conditions of the Haram gabbro seem at least realistic for the prograde deformation of a subducting slab.

e. *Electron Backscattered Diffraction studies on omphacite in eclogites of the Tauern Window (Austria): Implications for the exhumation of eclogites in extrusion wedges (K. Neufeld and U. Ring/Mainz; F. Heidelbach)*

The question how extremely dense eclogites are exhumed in orogens remains a lively debated controversy in tectonics. A widely held opinion is that buoyancy is the main driving mechanism and that buoyancy forces lead to the formation of an extrusion wedge which is bounded by a lower thrust and an upper normal fault. We have tested this model by studying the deeply exhumed Eclogite Zone in the Tauern Window of the Austrian Alps. The Eclogite Zone is part of the Pennine nappe edifice of the Tauern Window and is sandwiched between metasedimentary rocks of the Venediger Nappe as the footwall and ophiolitic rocks of the Glockner Nappe as the hanging wall. Inside the Eclogite Zone the eclogitic rocks occur in lenses with a maximum size of 1000 m by 700 m and are embedded mainly in garnet mica schists. The eclogites can be divided in two different types; a coarse grained type with only partly layered garnets of up to 5 mm size and a fine grained type with continuous garnet layers in an omphacite groundmass. Both eclogite types are uniformly distributed over the whole Eclogite Zone, with the coarse grained variation being much more common. While maximum pressures of the surrounding units were 10-12 kbar, the Eclogite Zone was subjected to pressures of up to 20-25 kbar. The preserve of adjacent lower pressure rocks leads to the assumption of an extrusion wedge, bounded by a top-N thrust fault below and a top-S normal fault above.

The validity of this model can be tested by (micro)structural analysis of the kinematics inside the Eclogite Zone. The extrusion wedge model predicts a change in asymmetry of the fabrics

in profiles across the Eclogite Zone between footwall (top N movement) and hanging wall (top S movement). Electron Backscattered Diffraction (EBSD) and orientation contrast (OC) imaging were used to analyse microstructures and lattice preferred orientation (LPO) of the eclogites in the SEM. The garnets in the Eclogite Zone do not show any features typical for strong intracrystalline deformation except for large subgrains in the coarse grained type eclogites. These subgrains are generally elongated with the long axis being parallel to the lineation. Only close to the hanging wall (Glockner Nappe) the long axes of these subgrains are oriented largely perpendicular to the lineation. Apart from this garnet microstrucutres are rather homogeneous throughout the Eclogite Zone. No LPOs of garnet could be detected in either coarse or fine grained eclogite types. The LPOs of omphacite do not seem to change significantly between hanging wall and footwall along Eclogite Zone profiles. Omphacite textures are characterized by an alignment of {010} and to a lesser degree {110} with the foliation plane and a maximum of <001> close to the lineation (Fig. 3.1-9). This LPO is indicative of deformation by intracrystalline glide on the (010)[001] and (110)[001] slip systems. The slight asymmetry of the fabric also does not seem to change in any systematic fashion across the Eclogite Zone.

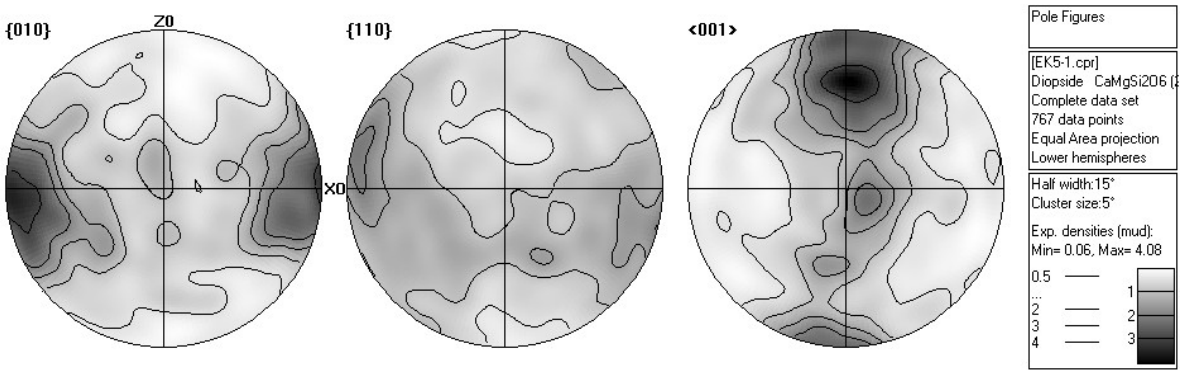

Fig. 3.1-9: LPO pattern of omphacite in a Tauern Window eclogite located close to the hanging wall contact; pole of foliation plane is marked with X0, lineation is vertical (Z0); equal area projection.

Our preliminary results are not compatible with the extrusion wedge model but rather point to a different kinematic model in which the Eclogite Zone is bound by a top-N thrust fault below and a top-N out-of-sequence thrust above; the latter would also explain the occurrence of the lower pressure Glockner Nappe above the Eclogite Zone.

f. *Origin and orientation of microporosity in eclogites of different microstructure (M. Machek, S. Ulrich and P. Špaček/Prague; F. Heidelbach)*

Crystalline rocks of metamorphic and magmatic origin are usually of very low porosity (below 1 %). Porosity corresponds to grain boundaries, cleavage planes of rock forming

minerals and microfractures of different length that can be either sealed or open. Orientation and connectivity of microporosity in these rocks and its closure with respect to increasing confining pressure is of great interest as they are suitable for dangerous waste disposal. However, there is limited number of methods how to measure it. In this work, we examine origin and spatial orientation of microporosity in two eclogites of similar lattice preferred orientation (LPO) of omphacite, but different microstructure and grain size using 1) subtraction of velocities of acoustic P-waves ($\Delta vP/\Delta p$) experimentally measured in 132 directions at different confining pressures on spherical sample (pulse transmission technique), 2) measurement of lattice preferred orientation using SEM-EBSD method and 3) quantitative microstructural analysis of grain boundaries orientation in three thin sections that are oriented parallel to xz, xy and yz planes of finite strain ellipsoid. We choose eclogites as a relatively simple bi-mineralic rock type composed of omphacite and garnet as cleavage-bearing anisotropic and cleavage-free isotropic minerals, respectively.

The first sample (JK1b) is dynamically recrystallized crustal eclogite having fine-grain omphacite matrix of 0.07mm in average size and shows elongated grains (axial ratio between 10 and 20) that define mylonitic foliation. Garnet grains have idiomorphic shapes with the size ranging between 0.05 to 0.3 mm. The second sample (SNW3) belongs to the population of mantle xenoliths and is coarse-grained with equilibrated microstructure and slightly elongated garnet and omphacite grains having size between 0.5 and 1.0 cm.

In the sample JK1b, two main fields (A and B) of directions of high values of $\Delta vP/\Delta p$ characterize spatial distribution of microporosity (Fig. 3.1-9a). The third less significant field of directions of high values of $\Delta vP/\Delta p$ (field C) occurs in the foliation plain at the eastern pole of diagram. Partial subtractions after every hydrostatic pressure step shows that the set of microporosity corresponding to the field A close down already at 20 MPa, whereas fields B and C disappeared above 50 MPa. The electron backscattered diffraction (EBSD) method showed that poles (110) of omphacite cleavage planes fit well with fields A and B (Fig. 3.1-10 top). Comparison of results from all three applied methods showed that 1) oriented microporosity characterised by field A maximum corresponds mainly to grain boundaries, but also to omphacite cleavage planes, 2) field B maximum corresponds to omphacite cleavage planes and 3) field C maximum corresponds very likely to intersection between two sets of cleavage planes or grain boundaries in the strongly linear microstructure of the sample JK1b. In the sample SNW3 (Fig. 3.1-10 bottom), the subtraction of P-wave velocities measured at individual pressure levels shows neither clear concentration of directions of high values of $\Delta vP/\Delta p$ nor systematic progressive closure of microporosity in any direction. Hence, applied method does not indicate any preferred orientation of microporosity in this sample. This is supported by the texture data that showed weak and very scattered distribution of omphacite (110) cleavage planes.

The results show that experimental pulse transmission technique is useful tool for visualization of oriented microporosity in 3D and provide important basis for further study of permeability anisotropy through studied rocks.

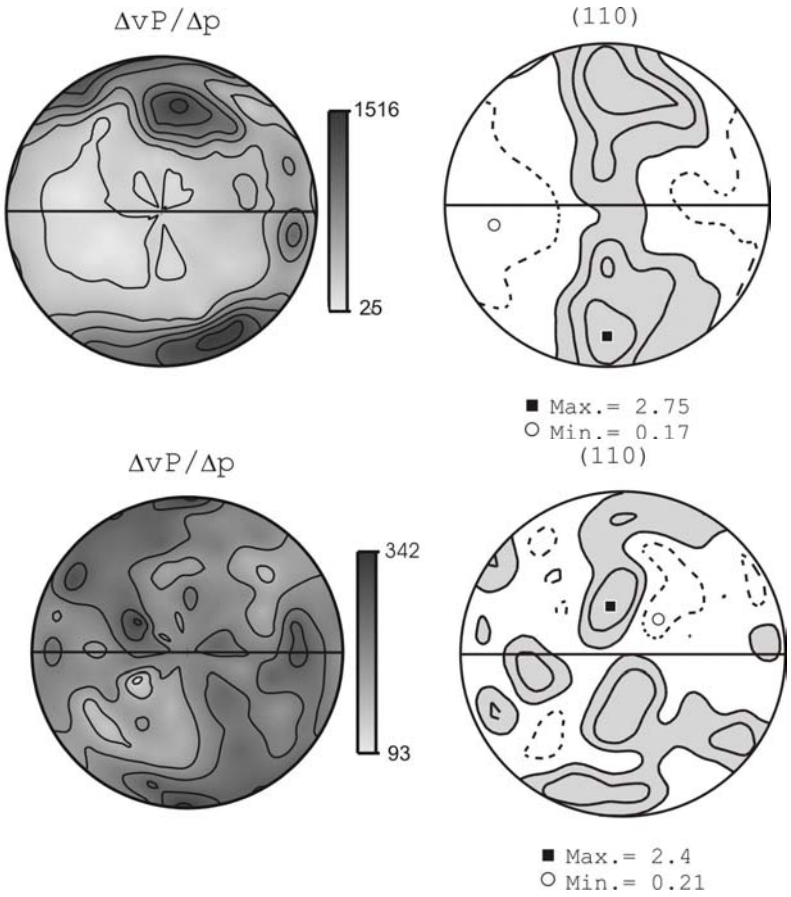

Figure 3.1-10: Contour diagrams of differential values of P-wave velocities measured at 400 MPa and 0.1 MPa (left) and contour diagrams of (110) cleavage planes of omphacite (right) for samples JK1b (top) and SNW3 (bottom). Equal area projections with the trace of the foliation horizontal.

g. *EBSD study of feldspar and quartz textures in an amphibolite facies shear zone from the Bolangir massif-type anorthosite complex, India (C. Dobmeier/Berlin and F. Heidelbach)*

This study is part of a project that investigates possible mechanisms for the formation of shear zones in the lower crust. Study object is a high-temperature shear zone with intricate internal fabrics and petrologic and structural evidence for repeated reactivation. The last stage of deformation led to the formation of a protomylonite with antiperthite porphyroclasts and a fine grained matrix with an average grain size of 400 μm for plagioclase, < 100 μm for potassium feldspar, and 200 μm for quartz. The small grain sizes prohibit the determination of the lattice orientation of feldspar grains by optical methods, which requires the observability of the (010) twin axis and the (001) cleavage plane. Further, the chemical composition of the mineral has to be known as the lattice orientation has to be inferred from the measured optical indicatrix axes, which depend on mineral composition in feldspar. In difference, electron backscattering diffraction (EBSD) allows to determine the orientation of the crystal lattice directly. The required area approximates the size of the electron beam-sample interaction volume.

The mylonite matrix consists of ellipsoidal plagioclase grains (x:z 1.5-2.5), individually interspersed and irregularly shaped potassium feldspar grains, and quartz, which is concentrated in lenticular monomineralic domains. The EBSD analysis yielded a strong lattice preferred orientation (LPO) for plagioclase (Fig. 3.1-11). {010} shows a great circle distribution, with a projection pole close to the maximum of {001}, and a weak maximum close to the projection pole of the mylonitic foliation. <001> trends to parallelism with the stretching lineation. The maxima positions are consistent with recrystallisation of plagioclase at medium to high-grade metamorphic conditions. The great circle distribution of {010} and the overall monoclinic symmetry of the LPO, which is best imaged by {001} and <100>, argue for progressive misorientation of subgrains during non-coaxial deformation as major deformation mechanism.

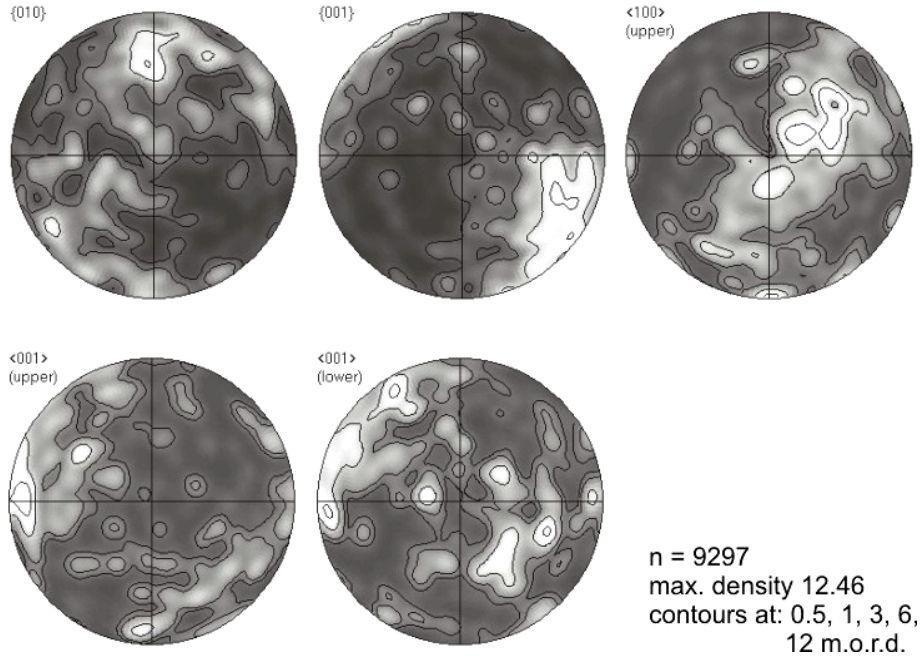

Fig. 3.1-11: Preferred orientation of plagioclase in mylonite matrix, shown in XZ sections, Schmidt net, lower hemisphere; trace of mylonitic foliation is horizontal.

In contrast to plagioclase, potassium feldspar does not show a strong LPO (Fig. 3.1-12). This results most likely from the isolated occurrence of the grains between plagioclase grains and the small grain size, which did not allow the evolution of a coherent LPO for the potassium feldspar population due to grain boundary effects. The grains nevertheless show recrystallization features with progressive misorientation of subgrains as deformation mechanism. Strong <001> maxima for quartz indicate the dominance of prism <a> slip and the dominance of non-coaxial deformation. At the same time, the a-axes show a symmetric distribution with six maxima, two of them being parallel to the mylonitic foliation. In difference to feldspar, there is no evidence for progressive misorientation of subgrains. This suggests static recrystallization of the quartz LPO following deformation.

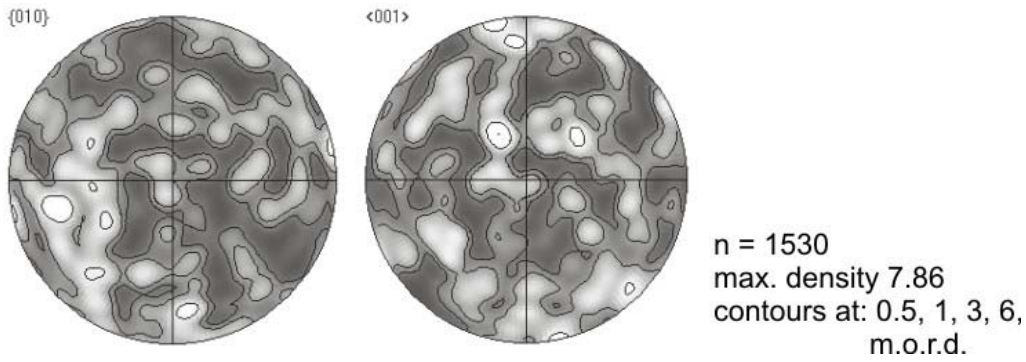

Fig. 3.1-12: Preferred orientation of potassium feldspar in mylonite matrix, shown in XZ sections, Schmidt net, lower hemisphere;trace of mylonitic foliation is horizontal.

Two-feldspar thermometry using potassium feldpar epipedes and plagioclase host compositions from mantled antiperthite porphyroclasts suggests temperatures of 600 to 620 °C as minimum temperature for the exsolution process. The mantle consists of plagioclase and potassium feldspar and is interpreted to have formed during exsolution. No boundary exists between the mylonite matrix and the dynamically recrystallized porphyroclast mantle. Further, both feldspars have the same composition and occur in the same modal proportion in mantle and matrix. The mylonite matrix is interpreted as completely recrystallized magmatic feldspars of the anorthositic precursor. Mantles and matrix formed and were deformed together, and the temperature estimates of the two-feldspar thermometry are also representative for the deformation of the mylonite matrix.

h. *Texture analysis of a deformed granite dyke from the Bavarian Forest, Central European Variscides (E. Galadi-Enriquez and G. Zulauf/Frankfurt; F. Heidelbach)*

In the present study we are trying to elucidate the deformation history along a major deformation zone of the variscan orogen, the so-called Bavarian Lode. The NW—SE trending shear zone is located in the Moldanubian subunit of the Central European Variscides, and samples were taken from a variably deformed granite dyke just south of the Bavarian Lode shear zone. The granite dyke intrudes so-called diatexites which have a variable, mostly granodioritic composition with a high content of mafic minerals and large K-feldspar phenocrysts (location Saunstein quarry) and were affected by Variscan anatexis. The dark-coloured diatexites extend over 50 km along the Bavarian Lode and show a foliation which parallels the steeply dipping NW—SE striking mylonitic foliation of the Bavarian Lode shear zone which results from dextral simple shear. This foliation is thought to have formed during the main variscan deformation event at high temperature. The diatexites are cut by the subvertical, E-W trending granite dyke, the thickness of which is about 50 m. The magmatic age of both rock types are respectively 334 ±3 und 326 ±9 Ma. The E-W trending foliation of the granite dyke is parallel to the contact to the host rock (Fig. 3.1-13).

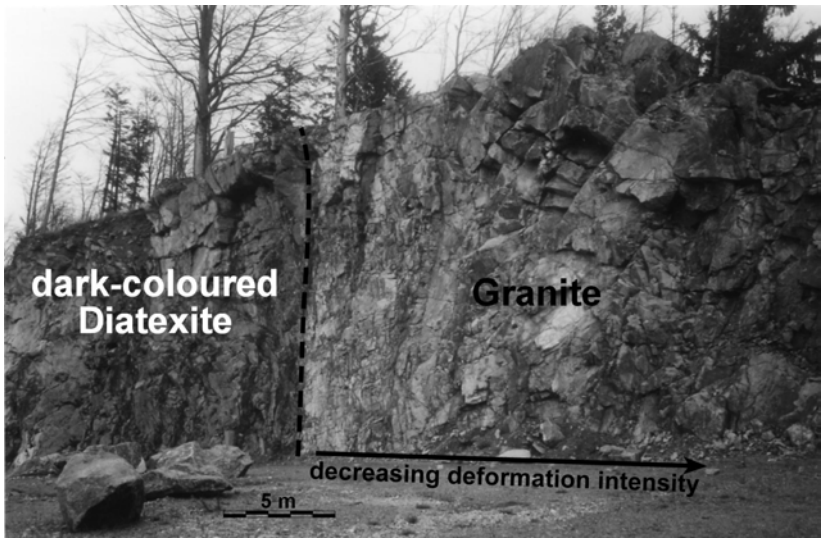

Fig. 3.1-13: View of the contact between dark-coloured diatexite and granite dyke.

Apart from the orientation of the foliation, the sinistral sense of shear of the deformed dyke also differs from the kinematics of the Bavarian Lode shear zone and the diatexites. The foliation of the dyke is particularly well developed adjacent to the contact to the host rock and becomes gradually weaker towards the dyke centre. It is important to note that dextral displacement along NW-SE trending planes of the dark-coloured diatexite and sinistral displacement along E-W trending planes of the granite cannot result from one single deformation phase. The aim of this study is therefore to use the microstructures and textures of the granite dyke to constrain the conditions and timing of deformation.

The microstructure of the deformed granite dyke is characterized by equigranular polycrystalline quartz ribbons (Fig. 3.1-14) in a fine grained matrix of feldspar and mica.

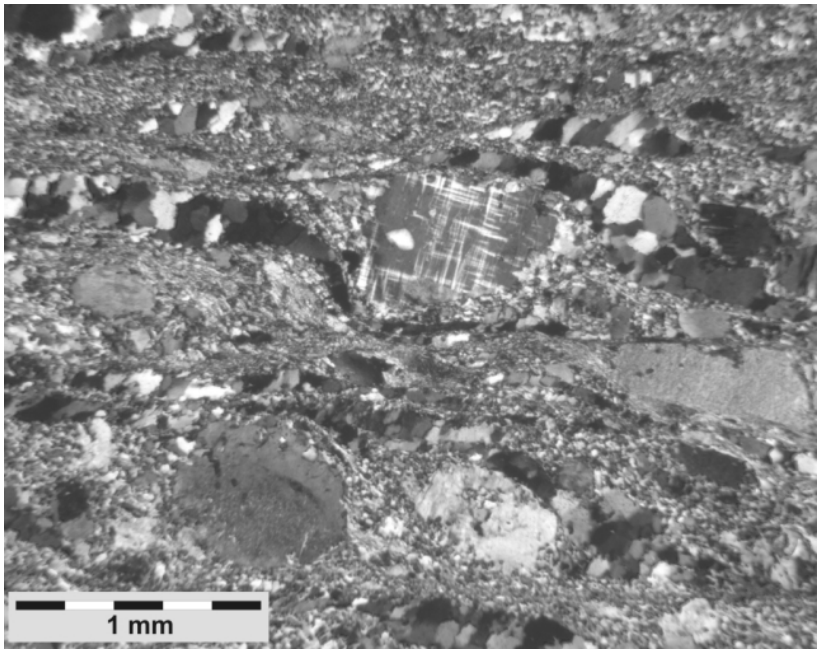

Fig. 3.1-14: Optical micrograph of deformed granite dyke (sample 607); white mica and feldspar porphyroclasts are embedded in a matrix of alternating fine grained feldspar layers and polycrystalline quartz ribbons; section is perpendicular to the foliation and parallel to horizontal lineation; shear sense is sinistral; crossed nicols.

Grain boundaries are mostly irregular and a lattice preferred orientation (LPO) is present. Some grains appear to be strain-free, *i.e.* without internal substructure, others show prism parallel subgrains or deformation bands. Grain boundary migration and progressive subgrain rotation appear to have been the dominant recrystallization mechanisms.Feldspar is largely recrystallized, forming fine grained layers that surround remnant σ clasts (core and mantle structure). Newly formed recrystallized feldspar grains are generally more Na-rich, whereas the feldspar clast have high K content. Some of the porphyroclasts are transected by synthetic of antithetic microfaults. Primary igneous feldspars are partilly converted to sericite. White mica typically forms mica-fishes and kink-folds.

Four granite samples with different deformation intensities were analysed by means of EBSD. In order to study the microfabrics of quartz, the samples were cut parallel to the XZ plane of the finite strain ellipsoid. A typical LPO pattern (Fig. 3.1-15) shows a clustering of quartz *c*-axes parallel to the intermediate *Y*-axis of the finite strain ellipsoid, a maximum of prism planes parallel to the foliation plane and a concentration of *a*-axes in the parallel to the lineation. This LPO is diagnostic for prism <*a*> slip in quartz, which is known to be dominant at middle to high-temperature conditions, that is, at upper greenschist to amphibolite facies conditions. This fabric is developed in all samples, but the strength of the LPOs is not correlated with the deformation intensity deduced from microstructural observations. Especially in one of the most fine-grained samples the texture is more poorly developed than in the others. This could be a result of operating deformation mechanisms that do not promote or even prevent the development of LPO, such as grain boundary sliding or solid-state diffusion creep. The pole figures show a monoclinic symmetry originated as a result of non-coaxial progressive deformation. This symmetry can be used to infer the sinistral shear sense consistent with the kinematic indicators visible under the microscope and in hand specimen.

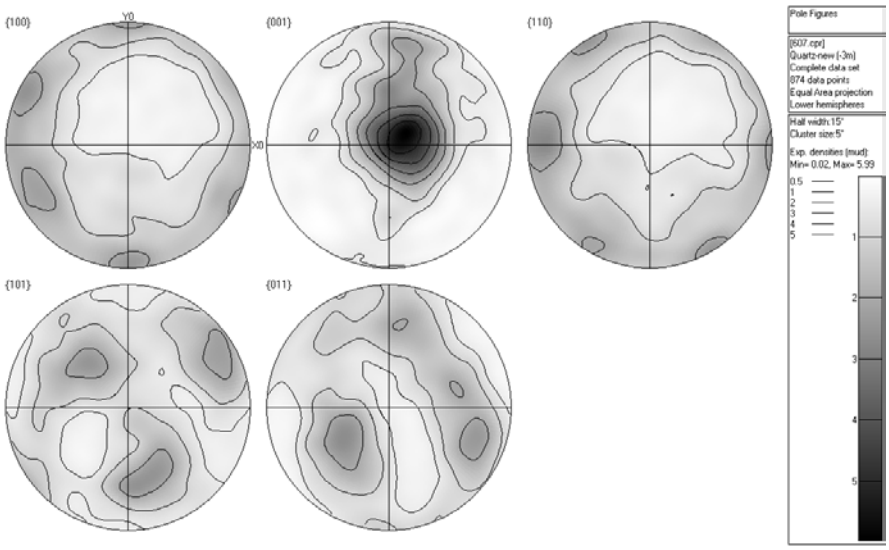

Fig. 3.1-15: Lattice preferred orientation of quartz in sample 607 located 6.6 m away from the granite-diatexite contact; equal area projections, trace of foliation and lineation are horizontal.

i. *Nucleation of dynamic recrystallization along microcracks in quartz (M. Bestmann and B. Grasemann/Vienna; F. Heidelbach)*

The nucleation process of dynamic recrystallization during rock deformation is still not fully understood. In relatively low strained rocks, deformation and recrystallization are restricted to grain boundaries and to shear zones that cut through individual grains. Here we present results from a quartzite vein (Schober Group, Austria) deformed under semi-brittle conditions. Within coarse quartz grains (1-3 mm), small grains (5-10 μm) recrystallized at conjugated sets of microcracks (20-70 μm in length) (Fig. 3.1-16). The deformation feature around the microcracks show characteristic lattice distortion pattern of hyperbolic shaped stress contours.

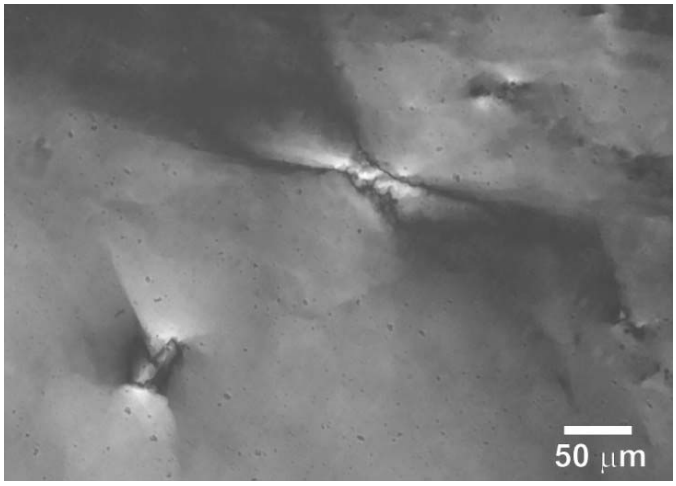

Fig. 3.1-16: Optical micrograph of low-temperature deformation microstructure in a quartz vein.

EBSD analysis reveals that recrystallized grains have two orientation populations; one disperses around the host orientation and the other one has a Dauphiné twin relation to the host (60° rotation around the *c*-axis). Misorientation profiles show a continuous lattice distortion towards the new grains. But when crossing subgrain (< 10° misorientation) or grain boundaries (> 10° misorientation) there is a slight deviation from the general dispersion trend. Also, the recrystallized grains with the Dauphiné twin orientation deviate slightly from the perfect twin symmetry operation with respect to their host grain. This indicates that subgrain rotation recrystallization is to some extent accompanied by grain boundary sliding. Blurred EBSD patterns give evidence of high dislocation densities around the microcracks. The characteristic lattice distortion pattern is comparable with the calculated deformation field around faults embedded in a non-linear ductile medium (Fig. 3.1-17). Increased tensional stresses that are set up around the micro-cracks favour the formation of secondary deformation zones, which are propagating from the crack tip. Stress concentration, which can cause an incease of stress of several orders of magnitude, commonly results in deformation zones oriented at 15°-35° angles oblique to the micro-crack. Their orientation can be predicted by continuum mechanics theory.

In summary, we can say that new grains nucleated in response to small displacements along local microcracks, even if we do not know the mechanism by which these microcracks nucleated. The nucleation of new grains is mainly related to subgrain rotation recrystallization, which might result in the Dauphiné twin orientation. Further TEM analysis is planned to relate dislocations densities and subgrain size to the modelled stress field distribution.

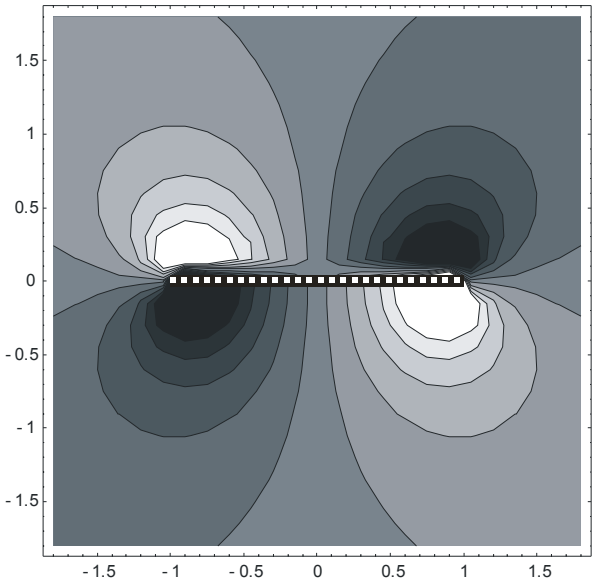

Fig. 3.1-17: Mean normal stress around a uniformly loaded dextral Mode II crack. The crack runs from (-1,0) to (1,0). Black: high (compressive), white low stresses. The plot was calculated using Westergaard Stress Functions using the software package Mathematica.

j. *Evidence for high temperatures in quartzitic sandstone deformed by rapid glacial flow at the base of a Neoproterozoic glacier? (M. Bestmann, H. Rice and B. Grasemann/Vienna; F. Heidelbach and F. Langenhorst)*

It is a well-known phenomenon that moving glaciers produce striations in the underlying bedrock. Low-porosity rocks, like quartzitic sandstones, may display polished striations where the fine-grained wear product has been removed by the continuing movement of the glacier. In contrast, the glacial striations of a Neoproterozoic quartzitic sandstone pavement show a pronounced topography developed from fragments of the abraded quartzite, in which an internal microstructure indicating a very high deformation has been preserved (Fig. 3.1-18a).

The polished glacial striation is underlain by a highly deformed zone up to 1 mm thick. The deformation gradient dies out rapidly downwards in this zone. The highly-deformed zone contains a mixture of fine-grained and strongly deformed coarse-grained crystal fragments. In the optical microscope, pronounced undulatory extinction occurs, with patchy grain

segmentation into domains of slightly different optical orientations. Low-angle subgrain boundaries, detected by EBSD orientation mapping and grain segmentation, are associated with microcracks visible in cathodoluminescence images. In fine-grained parts of the highly deformed zone, transmission electron microscopy (TEM) analysis revealed a compact fine-grained (0.2-1μm) microstructure, with frequent 120° grain boundary triple junctions. The grains are free of dislocation and interstitial voids are rare (Fig. 3.1-18b).

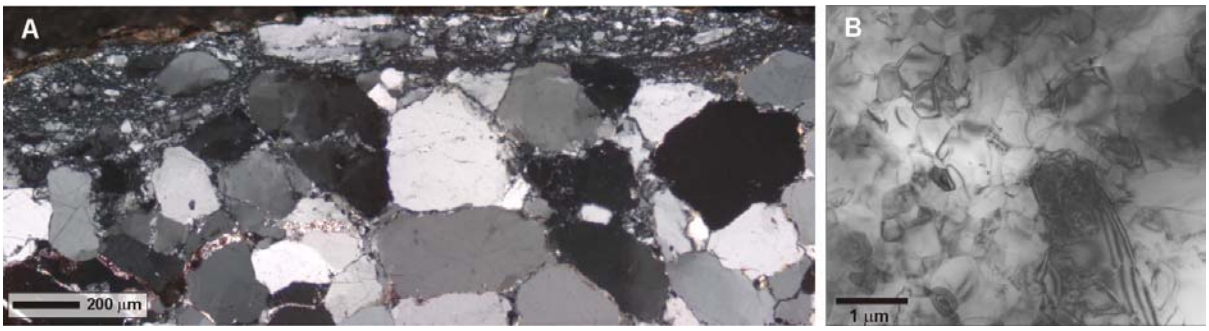

Fig. 3.1-18: a) Optical micrograph of deformed sandstone microstructure directly under striated surface. Note flow fabric in fine-grained deformation zone; b) TEM (bright field image) of microcrystalline quartz microstructure in highly deformed zone. Note compact grain boundary network with straight grain boundaries and approximately 120° triple junctions. Grains are free of dislocations except for the elongated grain.

It seems unlikely that the observed microstructure, with its 120° grain boundary fabric, reflects overgrowth of former fine-grained quartz fragments produced by crushing (cataclastic fracturing) during continuous slow sliding of pebbles across the sandstone bedrock. The very slow cementation rates at temperatures around the freezing point cannot account for the preservation of the deformed material *in situ*. Instead, the microstructure points to an equilibrium formation at elevated temperatures, either by instantaneous solid-state recrystallization or by crystallization from a silica melt. Only rapid solidification processes are able to preserve the observed topography and internally highly deformed microstructure along the polished striations during ongoing movement of the glacier. Calculations have shown that glacial sliding speeds of 0.1-0.3 m/s are able to produce short-term peak temperatures of 1500-2000 °C in the bedrock beneath an ice-loaded clast. These findings support recent speculations that the detection of glacially generated seismicity is attributed to episodic rapid shifts of substantial ice masses over the underground.

k. *Deformation lamellae and planar deformation features in quartz: A comparative TEM study (M. Vernooij/Zurich and F. Langenhorst)*

Planar deformation features (PDFs) in quartz are the most robust shock indicators in rocks because they are often preserved as last evidence for an impact event despite long-standing annealing and alteration. However, PDFs are not the only planar features that are observed at

the optical scale in quartz-bearing rocks. Despite their very different origins, tectonically induced deformation lamellae may sometimes resemble shock-induced PDFs. To address the microstructural differences between tectonic deformation lamellae and shock induced PDFs, we have produced extensive deformation lamellae during slow experimental deformation of quartz single crystals and compare them to PDFs, using optical and transmission electron microscopy (TEM).

A series of quartz single crystals were uniaxially deformed in a Griggs solid medium apparatus together with 1 vol.% added water at the ETH/Zurich. The initial orientation of crystals and the amount of strain were varied. The samples were deformed at a temperature of 800 °C, a confining pressure of 1200 MPa and a strain rate of ~ 10^{-6} s^{-1}, *i.e.* deformation occurred in the ductile regime. The synthetic deformation lamellae have been compared to natural PDFs in shocked quartz from the Ries impact crater, Germany.

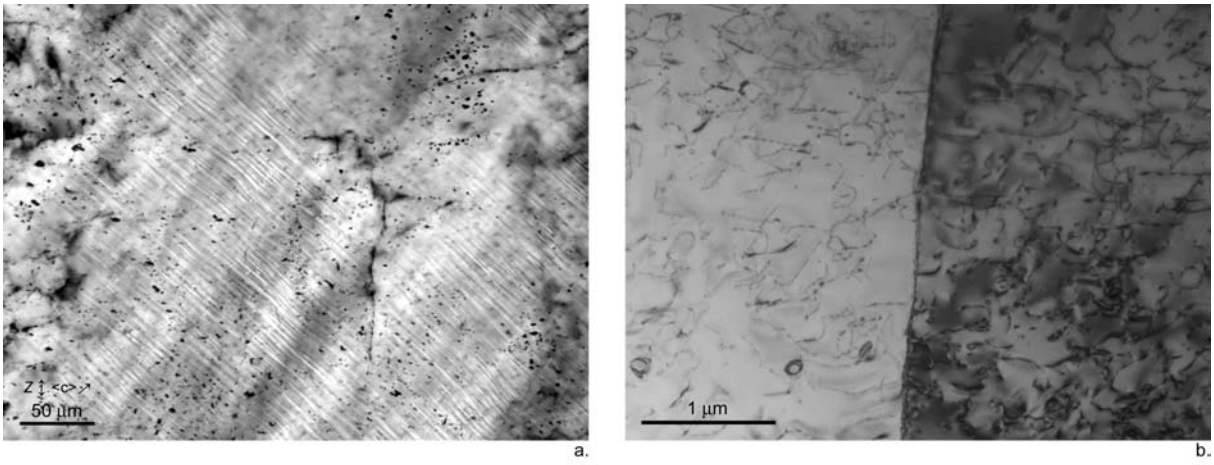

Fig. 3.1-19: Optical (a) and TEM (b) micrographs of experimentally produced deformation lamellae (GRZ28, finite strain 2.7 %, yield stress 0.3 GPa).

Under the optical microscope the deformation lamellae appear as gently curved planar features that are roughly parallel to the basal plane (Fig. 3.1-19a). They are always observed in areas with elongated bands of gradual undulatory extinction that are more or less parallel to the prism planes. A slight change in birefringence across the lamellae indicates that they are associated with a change in orientation. TEM reveals that this orientation change across the lamellae occurs along sub-grain walls that consist of well-organized and straight dislocations (Fig. 3.1-19b). The dislocations in the vicinity of the sub-grain walls are always curved and entangled, and sometimes contain tiny inclusions of water (density ~ 10^{10} cm^{-2}). The sub-grain walls occur in a sub-parallel fashion throughout the deformed quartz crystals.

Optically, the analysed PDFs in shocked quartz from the Ries crater appear as perfectly planar features that are decorated with tiny fluid inclusions as a result of post-shock annealing (Fig. 3.1-20a). There are no orientation changes across the PDFs and almost no free dislocations in

the vicinity of them (density ~ $0.2 \cdot 10^{10}$ cm^{-2}). TEM reveals furthermore that the PDFs consist of tiny dislocation loops, voids and bubbles, which have formed during post-shock recrystallisation of the originally amorphous PDFs (Fig. 3.1-20b). The orientations of the PDFs can be easily measured with the TEM. In our case two PDF sets developed with a rhombohedral orientation, $(10\bar{1}3)$ and $(\bar{1}013)$, indicating a shock pressure of ~ 20 GPa, and one set parallel to the prism plane, $(10\bar{1}0)$. In conclusion, TEM observations substantiate the clear difference in the nature of deformation lamellae and PDFs, reflecting their different geological formation processes.

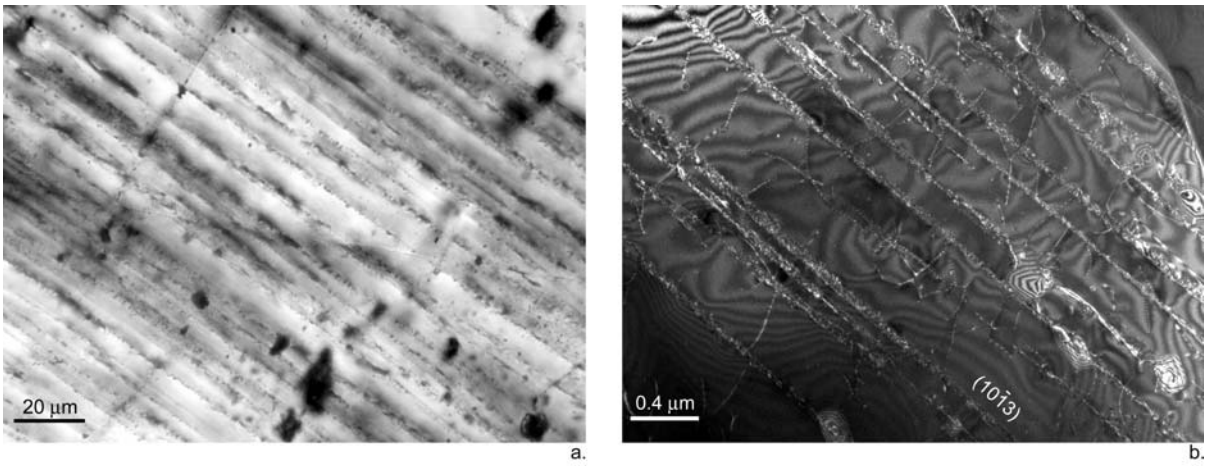

Fig. 3.1-20. Optical (a) and TEM (b) micrographs of natural PDFs in shocked quartz grains from the Ries Crater in Germany.

3.2 Physical Properties of Minerals

The relation between the structure (both atomic and mesoscopic) and physical properties of materials is at the center of a wide variety of scientific disciplines. In this context minerals are of importance as the materials that form the solid Earth and as templates for oxidic materials that are of interest in materials research. Compression is obviously of central importance in understanding material properties at conditions of the Earth's interior, where high pressures and temperatures prevail. However, pressure can also serve as a convenient way to change the interatomic distances among the elemental components of a material, potentially changing physical properties in drastic ways.

Materials that are of interest in both of these scientific areas are transition metal oxides: they play an important role as carrier of paleomagnetic information, are an important constituent of the Earth's interior (and can serve as a tracer for its oxidation state), and are candidate materials for use as magnetooptical devices and magnetic nanoparticles. So it is not surprising that they are also at the center of work at the Bayerisches Geoinstitut. This year the relation of magnetism and structure in FeO wüstite has been one of the focal points in the work of the diamond anvil cell group with two contributions in this section of the yearbook. Structure-property relations on the solid solution between wüstite and periclase for $(Mg_{0.8}Fe_{0.2})O$ complete the wüstite contributions in this section.

Thermal expansion of Ti-compounds is studied in the following two sections. The high-pressure α-PbO_2 structured TiO_2 and TiS are examined here. These data provide important constraints on the thermodynamic stability of these minerals compared to their low-pressure polytype (in the case of TiO_2) as well as the miscibility of TiS with troilite FeS.

The compression behaviour of a pyroxene with Si in six-fold coordination is revisited, and it is found that it is the least compressible pyroxene reported. In the final contribution of this section the melting of ice VII is examined by means of Raman spectroscopy, confirming a previously debated low-temperature melting curve.

a. *Pressure-induced magnetization in FeO: Evidence from elasticity and Mössbauer spectroscopy (A.P. Kantor, I.Yu. Kantor, L.S. Dubrovinsky and C.A. McCammon, in collaboration with S.D. Jacobsen/Washington DC and H.-J. Reichmann/Potsdam)*

The complete elastic tensor of $Fe_{0.94}O$ (wüstite) has been determined to 10 GPa using acoustic interferometry at GHz frequencies inside a diamond anvil cell (DAC). Single crystals of $Fe_{0.94}O$ were compressed in the DAC using a 16:3:1 methanol:ethanol:water mixture as a pressure transmitting medium. Measured single-crystal travel time data t_P<100>, t_S<100>, and t_S<111> were converted to sound wave velocities. The complete elastic tensor was obtained using the pure-mode solutions to the Christoffel equations and individual elastic constants are plotted in Fig. 3.2-1. The isotropic adiabatic bulk (K_S) and shear (G) moduli were calculated

using the variational approach of Hashin and Strikman and are also shown in Fig. 3.2-1. We observed a change in slope for both C_{11} and C_{12} elastic constants and for the isotropic moduli at 4.7 ± 0.2 GPa (Fig. 3.2-1). Mössbauer spectroscopy provides a possible explanation: At a pressure of 5.0 ± 0.5 GPa we observed the onset of magnetic ordering in polycrystalline ^{57}Fe-enriched $Fe_{0.94}O$. The remarkable coincidence in transition pressures suggests that magnetic ordering in FeO is manifested in changes of elastic properties detected by the high-precision ultrasonic data.

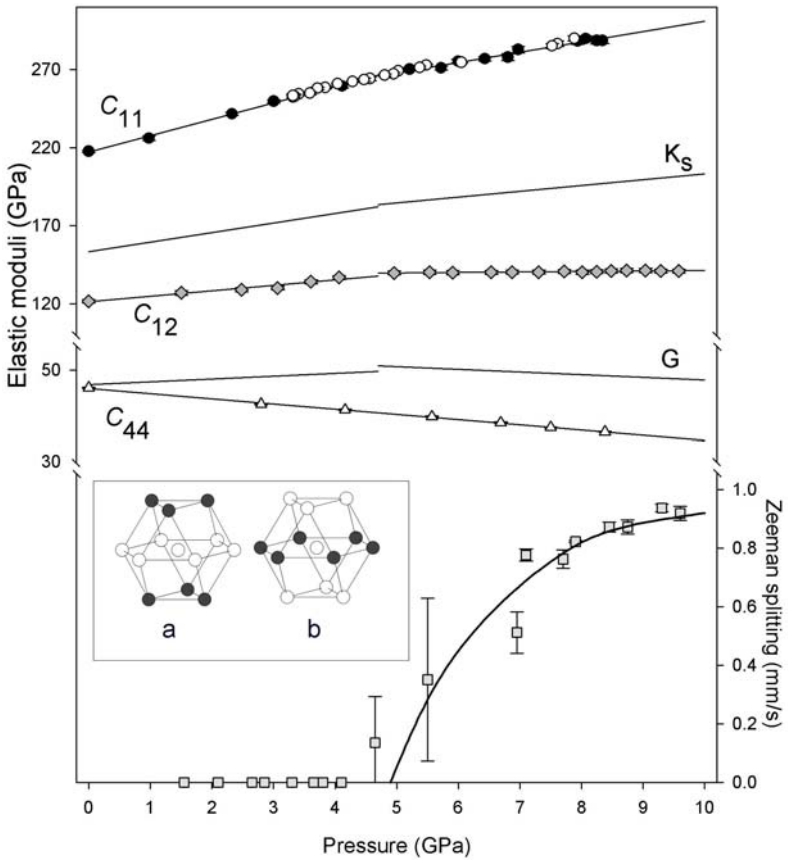

Fig. 3.2-1: The elastic constants (black and white circles for C_{11} indicate points measured on compression and decompression, respectively), isotropic adiabatic moduli, and hyperfine Zeeman splitting for $Fe_{0.94}O$ vs. pressure. Inset: a – AF-IIr magnetic structure, b – hypotetical AF-IIc structure. Ions with "+" spins are represented by open circles and ions with "-" spins are shown by filled circles.

Mössbauer spectra of the cubic and the rhombohedral magnetic phases differ in some ways: Mössbauer spectrum of a cubic phase consists of a broad magnetic part with unresolved lines and a "paramagnetic" doublet, which persists up to the structural phase transformation at ~ 17 GPa in hydrostatic conditions. Mössbauer spectra of the rhombohedral phase contain only a relatively well-resolved magnetic sextet. The hyperfine Zeeman splitting of a magnetic sub-spectral component appears in Mössbauer spectra after a magnetic transition at about 5 GPa. It increases with pressure rapidly, as expected for magnetic ordering transitions (Fig. 3.2-1).

Our new results combined with literature structural high P-T data suggest that there is a magnetic, although still cubic phase of FeO between ~ 5 and ~ 17 GPa. The classical antiferromagnetic structure of type-II (AF-IIr) is not consistent with our observations, because it possesses rhombohedral symmetry (Fig. 3.2-1, inset a). We proposed a slightly modified magnetic structure with a cubic symmetry (AF-IIc). In the AF-IIr structure the parallel spins form sheets within (111) planes of the lattice, where each adjacent sheet is antiparallel. Magnetic interactions between sheets give rise to a slightly attractive or repulsive force resulting in rhombohedral distortion of the lattice below Néel transition. In the AF-IIr structure, all the next-nearest neighbors (*nnn*) are antiparallel, and only a half of the nearest neighbors are antiferromagnetically coupled, while the other half being coupled ferromagnetically (Fig. 3.2-1, inset a). Assuming *nnn* interactions the same as in the AF-IIr type, we propose a structure where the spins are distributed in the first coordination shell in a different way: six *nn* with antiparallel spins lie in the same close-packing layer as the central ion, while six *nn* with parallel spins lie in upper and lower hexagonal layers (Fig. 3.2-1, inset b). The AF-IIc structure can be considered an intermediate step towards the AF-IIr structure since every hexagonal layer consists primarily of ions with parallel spins with only one quarter of ions having antiparallel spins.

b. *Phase diagram of $Fe_{1-x}O$: Discovery of a cubic antiferromagnetic phase (I.Yu. Kantor, L.S. Dubrovinsky, C.A. McCammon, N.A. Dubrovinskaia, A.P. Kantor and A.Yu. Kuznetzov, in collaboration with W.A. Crichton/Grenoble and I. Goncharenko/Saclay)*

$Fe_{1-x}O$ is fundamental to solid state physics and chemistry as a prototype strongly correlated transition metal monoxide, and to the Earth sciences as an endmember of (Mg,Fe)O, an important oxide in the lower mantle. It has long been known that $Fe_{1-x}O$ is antiferromagnetic, with a distorted rhombohedral structure below its Néel temperature. It has been generally believed that the rhombohedral distortion is a result of a magnetic ordering due to magnetoelastic coupling. High-pressure data of $Fe_{1-x}O$ show a rhombohedral distortion at room temperature and 10-18 GPa, which has been assumed to coincide with the Néel temperature by analogy with ambient pressure data. However there are no combined structural and magnetic studies of $Fe_{1-x}O$ to confirm this assumption.

We determined the phase diagram of $Fe_{1-x}O$ (where $0.06<x<0.08$) to 70 GPa and 1100 K using a resistively heated diamond anvil cell, with Mössbauer spectroscopy and neutron diffraction to determine the magnetic phase boundary, and with X-ray diffraction to determine the structural phase boundary. Mössbauer spectra indicate either paramagnetic or magnetic, and compilation of all data gave an apparently linear magnetic phase boundary with the Néel temperature given by $T_N(K) = 200(5) + 20.8(5)P$ (GPa) (Fig. 3.2-2). Note that the extrapolation of the magnetic phase boundary to ambient pressure gives a Néel temperature (200 K) that is in good agreement with all previous studies. We studied the low-temperature part of the magnetic phase boundary using neutron diffraction at Laboratoire Léon Brillouin

up to 5 GPa. Néel temperatures at three different pressures were determined by appearance of the (3/2 1/2 1/2) magnetic peak and are shown as diamonds in Fig. 3.2-2. Note that the neutron diffraction data (which are sensitive to long-range magnetic order) are in perfect agreement with Mössbauer data (which are sensitive to the local environment). The structural phase boundary was determined at ESRF by the observation of the splitting of diffraction lines that occurs due to the cubic-to-rhombohedral distortion. At room temperature the rhombohedral distortion was observed at 12(1) GPa, in good agreement with previous reports. The transition pressure as a function of temperature was determined to be P_{tr}(GPa) = -4.7(2) + 0.056(5) T(K), which differs slightly from previous data (grey line in Fig. 3.2-2), possibly due to non-hydrostatic environments in this study.

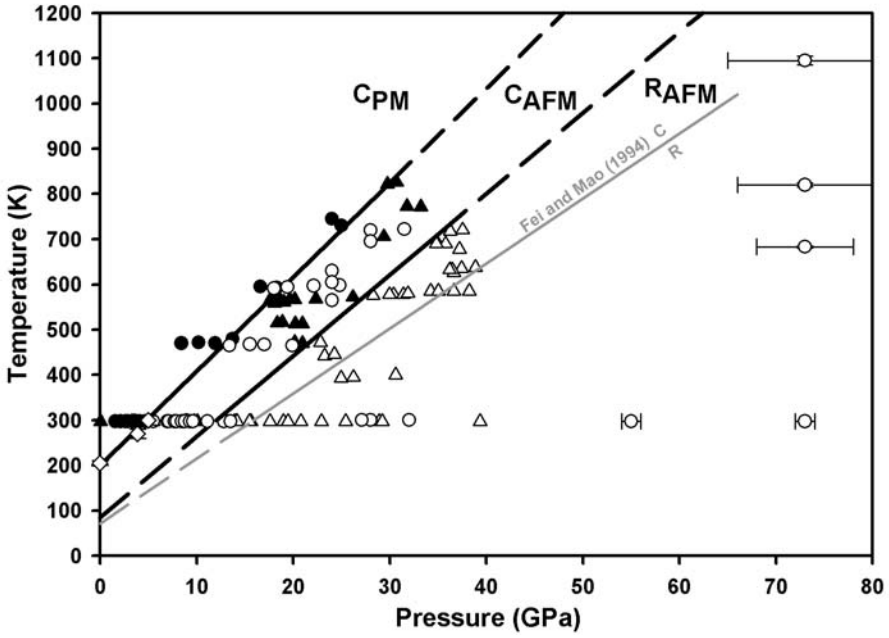

Fig. 3.2-2: Phase diagram of non-stoichiometric wüstite. Black lines – phase boundaries between cubic paramagnetic (C_{PM}), cubic antiferromagnetic (C_{AFM}), and rhombohedral antiferromagnetic (R_{AFM}) phases obtained in this study. Circles (Mössbauer data): solid – paramagnetic, open – magnetically ordered; triangles (X-ray diffraction data): solid – cubic, open – rhombohedral; diamonds (neutron diffraction data): observed Néel temperatures. A structural phase boundary from the literature [Y. Fei and H.-K. Mao, Science, 266, 1678 (1994)] is shown for comparison in grey.

The phase diagram of $Fe_{1-x}O$ presented in Fig. 3.2-2 shows a relatively wide stability range of a cubic antiferromagnetic phase, challenging the long accepted belief that the Néel temperature coincides with the rhombohedral distortion. A close examination of the literature shows that there are, in fact, no studies at ambient pressure that have shown this coincidence unequivocally; hence we are conducting further experiments on $Fe_{1-x}O$ to provide a basis upon which the fundamental coupling between crystal and magnetic structure can be elucidated.

c. *A study of the rhombohedral distortion of $Mg_{0.8}Fe_{0.2}O$ at high pressure (I.Yu. Kantor, L.S. Dubrovinsky, C.A. McCammon and A.P. Kantor, in collaboration with W.A. Crichton/ Grenoble)*

$(Mg_xFe_{1-x})O$ ferropericlase with $x \sim 0.8$ is probably the second most abundant phase in the Earth's lower mantle after $(Mg,Fe)SiO_3$ perovskite, and therefore its properties and stability field are important for geophysical and geochemical models of the Earth's deep interior. Previous studies have reported the presence of a rhombohedral distortion in ferropericlase at high pressure, although results from different groups are not consistent. Since a rhombohedral distortion could dramatically affect properties of the Earth's lower mantle, for example due to rapid C_{44} mode softening and a decrease of sound wave velocities at the transition, we undertook a detailed study of the structure of ferropericlase at high pressure.

We have performed an *in situ* investigation of the behaviour of $(Mg_{0.8}Fe_{0.2})O$ in the diamond anvil cell (DAC) using Mössbauer spectroscopy (MS), X-ray powder diffraction (XRD), and X-ray Fe K_α-edge absorption spectroscopy (XANES). Two samples of ferropericlase, FP-1 and FP-2 were used in this study, both with the same Mg/Fe ratio, but with different ferric iron content. Mössbauer spectra of FP-1 and FP-2 were collected up to 56 GPa. A typical Mössbauer spectrum of the FP-1 sample at 47 GPa is shown in Fig. 3.2-3 (inset). The isomer shift of the main doublet depends linearly on pressure with a slope of about -0.003 mm/s per GPa within the pressure range considered. We observed a strong non-monotonous pressure dependence of the quadrupole splitting: it increases up to pressures of about 36-37 GPa and decreases at higher pressures (Fig. 3.2-3). Quadrupole splitting is a sensitive indicator of the distortion of the local iron environment; hence we infer that the changes in quadrupole splitting of samples FP1 and FP2 could be due to the distortion of the Fe^{2+} octahedra in the structure. No evidence of magnetic ordering or line broadening in MS was observed up to the highest pressure reached in this study (56 GPa).

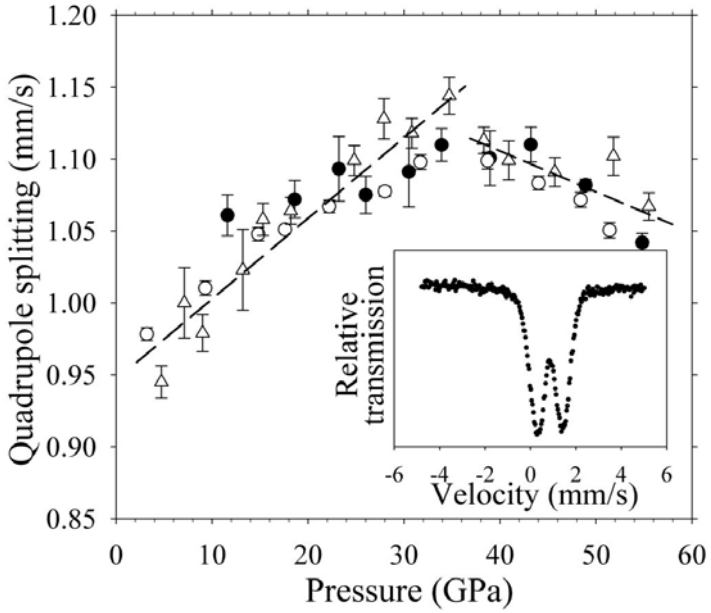

Fig. 3.2-3: Quadrupole splitting of the main Fe doublet as a function of pressure. Solid circles – compression path of sample FP-1, open circles – decompression path of sample FP-1, triangles – compression path of sample FP-2. Dashed lines are guides for the eye. Inset: Mössbauer spectra of sample FP-1 at 47(1) GPa. The velocity scale is relative to α-Fe.

X-ray absorption spectra were collected from 0 to 64 GPa at room temperature on beamline ID24 at ESRF. The XANES spectra collected for sample FP-1 show changes at 36 GPa that can be seen in δμ/δE derivatives or edge position, providing further evidence of local structural changes and/or chemical bonding of Fe ions in ferropericlase at about 35-36 GPa.

In order to examine the long-range crystallographic structure and to obtain an isothermal equation of state, we performed an X-ray diffraction study of sample FP-1 on beamline ID30 at ESRF. The XRD pattern of sample FP-1 fits perfectly to a cubic rock-salt structure up to 35 GPa; however at higher pressures some of the diffraction peaks broaden. The transition from the rocksalt to a rhombohedral structure should cause a the splitting of $(111)_c$ and $(220)_c$ cubic reflections, while the most intense $(200)_c$ cubic reflection should remain unsplit (hereafter we use subscripts c and r for the Müller index of cubic and rhombohedral structures, respectively). From the X-ray diffraction images we clearly see the splitting of the $(220)_c$ reflection (Fig. 3.2-4). Also, the full width at half maximum (FWHM) of the $(200)_c$ peak remains constant with pressure, while rapid broadening of the $(220)_c$ reflection starts at 35 GPa. These features are all typical of the rhombohedral distortion of the fcc lattice, well known in FeO and magnesiowüstites with high iron concentration. Refinement of all split reflections at 42 GPa (which is above the transition pressure) shows that they are fully consistent with a rhombohedral structure with α (rhombohedral angle) equal to 60.45°. From the XRD data the transition pressure was determined to be 35(1) GPa. P-V data were fitted to a second-order Birch-Murnagham isothermal equation of state with values K_{300}=158(5) GPa and V_0=11.53(1) cm^3/mol for the cubic structure and K_{300}=170(7) GPa and V_0=11.21(1) cm^3/mol for the rhombohedral structure.

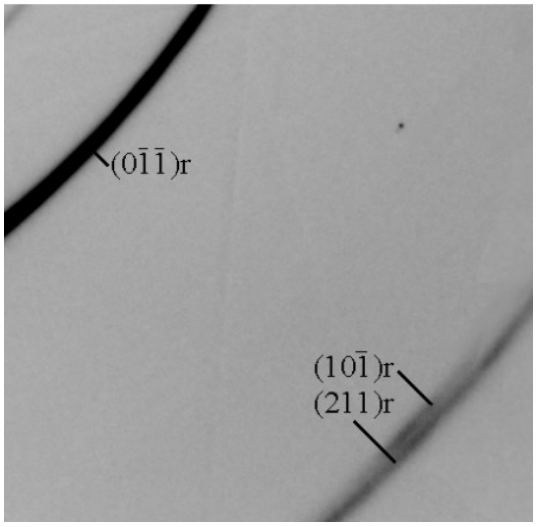

Fig. 3.2-4: Part of the MAR345 diffraction image of sample FP-1 at 44(1) GPa. Reflection indicies are for a rhombohedral lattice ($a = b = c$, $\alpha = \beta = \gamma \neq 60°$).

Although the minimum iron content that can induce a rhombohedral distortion is not yet clear, we can confidently state on the basis of the present study that 20 mol.% FeO is sufficient. It is clear that the rhombohedral distortion of ferropericlase is not associated with changes in magnetic ordering as observed from Mössbauer spectroscopy. The nature of this transition

could be explained by the appearance of exchange interactions, due to short-range ordering of the magnetic moments of Fe atoms in a paramagnetic state. Therefore, the well-known structural distortions in transition metal monoxides may not necessarily result from magnetic ordering, which is explored for $Fe_{1-x}O$ in the two previous contributions of this Annual Report.

d. *High-temperature X-ray diffraction on the α-PbO_2 structure of TiO_2 (D.J. Frost, T. Boffa Ballaran and F. Langenhorst)*

The accessory mineral rutile, which occurs in many types of metamorphic rocks, has a high-pressure orthorhombic polymorph with the α-PbO_2 structure (HP-TiO_2) that has been identified in ultrahigh-pressure assemblages and impact rocks. The phase boundary between rutile and HP-TiO_2 has been determined in laboratory experiments and has a positive Clapeyron slope in the range 5-9 GPa at temperatures between 400 and 1600 °C (see yearbook 2003). In order to determine thermodynamic properties of HP-TiO_2 from the experimentally determined phase relations, heat capacity, thermal expansion and compression data on both phases are required. Here we have attempted to measure the thermal expansion of HP-TiO_2 for which data were previously unavailable. The thermal stability of this polymorph is also of interest in relation to its preservation in natural mineral assemblages.

Several samples of HP-TiO_2 were synthesised between 9 GPa and 14 GPa at 1200-1400 °C in the 5000 tonne multianvil press. The unit cell volume of HP-TiO_2 synthesised at 14 GPa was found to be approximately 0.1 % larger than samples recovered at 9 GPa as a result of an elongation of the b-axis. When recovered samples were examined on the heating stage of the Philips powder diffractometer, a back transformation to rutile commenced at temperatures above 300 °C and went to completion during 5 hour heating to 500 °C.

All samples of HP-TiO_2 showed changes in lattice parameters after returning from high temperature to 25 °C. These changes were most pronounced in the sample synthesised at 14 GPa. As shown in Fig. 3.2-5 the b-axis increases linearly with temperature up to 125 °C then decreases sharply up to 200 °C. The room temperature b-axis after returning from 200 °C (*i.e.* where cycle 3 begins) is significantly lower than the original sample. The lattice parameter varies linearly with temperature in the subsequent heating cycle up to 275 °C where a second smaller decrease occurs. A similar decrease occurs over 370 °C. After heating to 400 °C the recovered b-axis lattice parameter is approximately 0.15 % smaller than in the original sample. The c-axis shows a similar but slightly smaller decrease while the a-axis increases slightly. Overall the volume decreases during annealing by 0.1 %.

Several samples were ramped a number of times up to 300 °C and back. After an initial change in the lattice parameters on the first heating cycle they remained constant after being recovered from the subsequent cycles. The thermal expansion of HP-TiO_2 determined during these cycles is $2.8(4)\times10^{-5}$ which is, within error, identical to that of rutile.

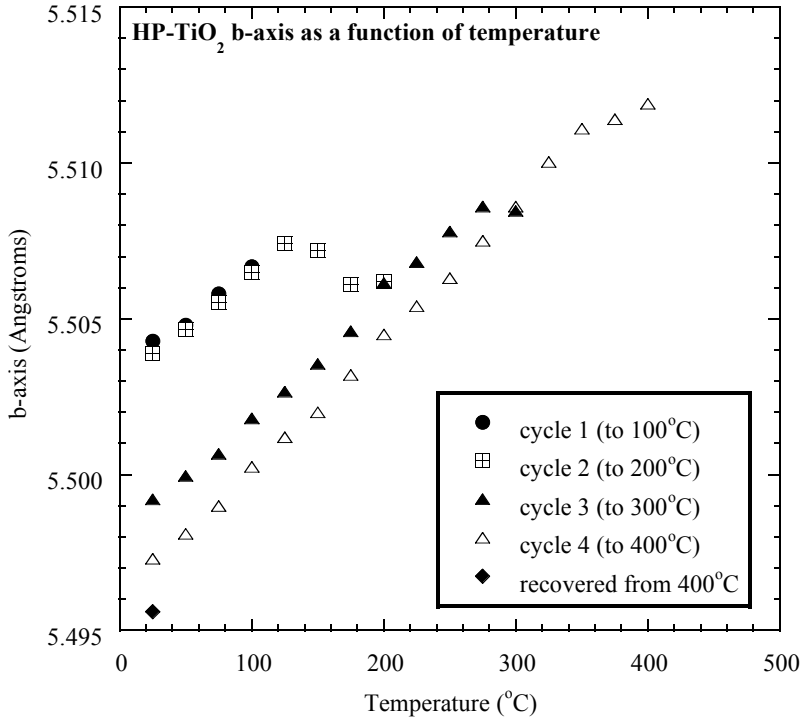

Fig. 3.2-5: The b-axis of HP-TiO_2 measured on the Philips powder diffractometer heating stage. The sample was initially synthesised at 14 GPa and 1400 °C. Four cycles of heating were performed with intermittent cooling to room temperature.

There are several reasons that can be entertained as to why the lattice parameters of HP-TiO_2 may change during annealing at room pressure. Lattice strain caused by the back transformation to rutile might be a possibility. However, strain broadening of diffraction lines is absent and preliminary TEM investigation of an annealed grain revealed no evidence of rutile stacking faults. Annealing out of high-pressure defects is quite plausible, however, possibly resulting from oxidation of Ti^{3+} interstitials. If this is the case it implies that Ti^{3+} defects may increase in concentration with pressure, as the sample synthesised at the highest pressure had, paradoxically, the largest unit cell volume. Examining the effect of synthesis pressure on the bulk modulus of recovered HP-TiO_2 may help to explain these observations.

e. *Thermal expansion of TiS: Assessment of miscibility with troilite (FeS) (R. Skála, M. Drábek/Prague and T. Boffa Ballaran)*

In aubrites, in which otherwise lithophile elements behave as siderophiles due to strongly reducing conditions, titanium-rich iron monosulfides were reported in literature. For example, in the Bustee aubrite, the titanium-bearing troilite, associated with osbornite (TiN), heideite ($FeTi_2S_4$) and oldhamite (CaS), was found to contain 17.2 to 25.2 wt.% Ti. In the Bishopville aubrite, the content of titanium in troilite is reported to be up to 5.7 wt.%. The crystal

structures of troilite and TiS are not identical under ambient conditions. While troilite is hexagonal with space group $P\bar{6}2c$ and unit-cell dimensions a ~ 5.97 Å, c ~ 11.76 Å, V ~ 362 Å^3, TiS adopts NiAs-type structure (space group $P6_3/mmc$) and the unit cell parameters of a ~ 3.31 Å, c ~ 6.34 Å, V ~ 60.2 Å^3. At elevated temperatures, however, the troilite structure transforms to NiAs-type structure. Consequently, increased solubility can be expected between FeS and TiS at temperatures above this phase transition. To evaluate the crystallographic limits for the TiS miscibility in FeS we carried out a series of high-temperature unit-cell refinements for the former phase. Here we present preliminary results for temperature range from 20 to 400 °C (Fig. 3.2-6). Further experiments at higher temperatures are planned.

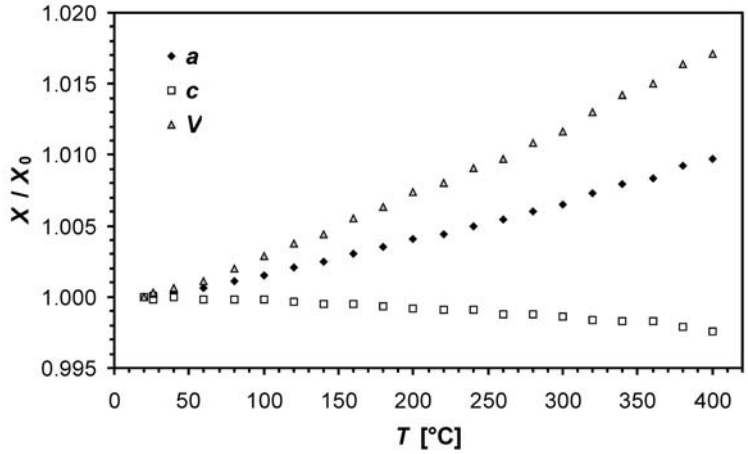

Fig. 3.2-6: Relative changes of unit-cell dimensions in TiS at elevated temperatures.

f. *Structure and elastic behaviour of pyroxenes with 6-coordinated silicon (J. Konzett/ Innsbruck, H. Yang/Florida and D.J. Frost)*

It had long been assumed that clinopyroxene (cpx) – in spite of its high-pressure stability to approximately 18 GPa – contains silicon exclusively in tetrahedral coordination. However, Angel *et al.* (Nature, 335, 156, 1988) described a pyroxene with a stoichiometry $Na(Mg_{0.5}Si_{0.5})Si_2O_6$ (NaPx) that contains silicon both in tetrahedral and octahedral coordination. This pyroxene was synthesized at 10 and 15 GPa and a temperature of 1600 °C. Its major structural feature is the presence of Si on *M1*-sites. Due to the large difference in size and charge between Mg and Si the two cations are completely ordered, resulting in reduction of symmetry from *C2/c* to *P2/n*. The discovery that cpx can accommodate 6-coordinated silicon is of fundamental importance for an understanding of crystal chemistry of chain silicates at high P and T in particular, and high-P minerals in general. This is because phase transitions involving a change in coordination of silicon from fourfold to sixfold have significant effects on material properties such as density, bulk modulus and elastic moduli and, consequently, on the P-(T) stability fields of these phases. Thus, in order to gain insight into the crystal chemical effects of $^{[6]}$Si-substitution in cpx, we attempted to study the crystal

structures and elastic behaviour of Na-pyroxene (NaPx) and its solid solutions with diopside and jadeite.

NaPx and NaPx solid-solutions were synthesized using a 1000t-multi anvil device at the Bayerisches Geoinstitut. NaPx and NaPx-Di_{ss} were examined with single-crystal X-ray diffraction at ambient conditions. NaPx was further studied at high pressure with a Mao-Bell type diamond anvil cell and synchrotron radiation at the Argonne National Laboratory up to 54 GPa. The powdered sample, placed between two pieces of aluminium foil, was packed in a 150 µm-diameter hole of a Re-gasket. High-purity aluminium not only acts as a pressure marker, but also a pressure medium by virtue of its low shear strength. All measurements were conducted at room temperature. Pressure was determined from the equation of state of Al. The unit-cell parameters were determined using least-squares refinement on individually-fitted peaks.

At 15 GPa and 1600 °C, a pure NaPx bulk composition did yield $Na_{0.98}Mg_{0.53}Si_{2.49}O_6$ ($NaPx_{98}En_{02}$) crystals of up to 100 µm in size with trace amounts of stishovite (Fig. 3.2-7) after a run duration of 17 hours. Single-crystal X-ray diffraction of the NaPx crystals yields a monoclinic unit cell with a_0 = 9.408(5), b_0 = 8.660(5), c_0 = 5.274(3) Å, b=108.18(2)°, V=408.2(6) $Å^3$, and the space group *P2/n*. The structure refinement shows that this pyroxene is comparable to that reported by Angel *et al.* (1988), with half the *M1*-site occupied by Si^{4+}. Preliminary high-P data suggest that NaPx undergoes three phase transformations under pressure: one between 4 and 9 GPa, one between 24 and 27 GPa, and one between 43 and 47 GPa. The structure after the first phase transformation probably possesses a C-centred lattice. The linear compressibilities for the structure below 4 GPa are b_a=0.00059, b_b=0.00199, b_c=0.00194/GPa, and the bulk modulus is 222(16) GPa, which is the largest value reported for a pyroxene to date (Fig. 3.2-8). The large bulk modulus and the stiffness along the *a*-axis may result from the occupation of Si^{4+} in the *M1*-site, indicating a governing role of the *M1*-octahedra in the high-pressure crystal chemistry of pyroxenes.

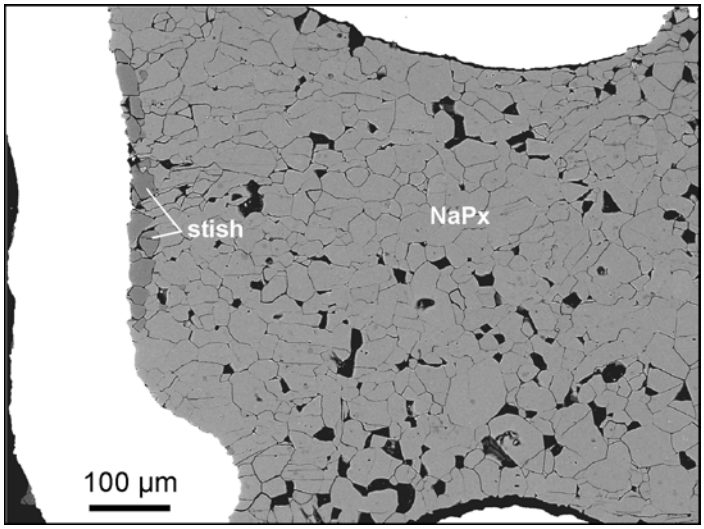

Fig 3.2-7: A Scanning electron microscope (BSE) image of an experimental capsule showing crystals of Na-pyroxene ($Na_{0.98}Mg_{0.53}Si_{2.49}O_6$) recovered from 15 GPa and 1600 °C. Crystals of stishovite can be seen growing on the left wall of the capsule.

A $NaPx_{70}Di_{30}$ bulk composition was found to be super-solidus at 15 GPa and 1600 °C, producing a ternary cpx solid-solution $NaPx_{56}Di_{36}En_{08}$ + stishovite + quenched melt. The structure of this cpx has space group *C2/c* with a_0 = 9.579(5), b_0 = 8.759(5), c_0 = 5.261(3) Å, b=107.20(2)°, V=421.7(6) $Å^3$ and a structural formula $(Ca_{0.36}Na_{0.56}Mg_{0.08})(Mg_{0.73}Si_{0.27})Si_2O_6$ which indicates that ordering of Si and Mg on the *M1*-site is incomplete, thus preventing the symmetry reduction from *C2/c to P2/n.*

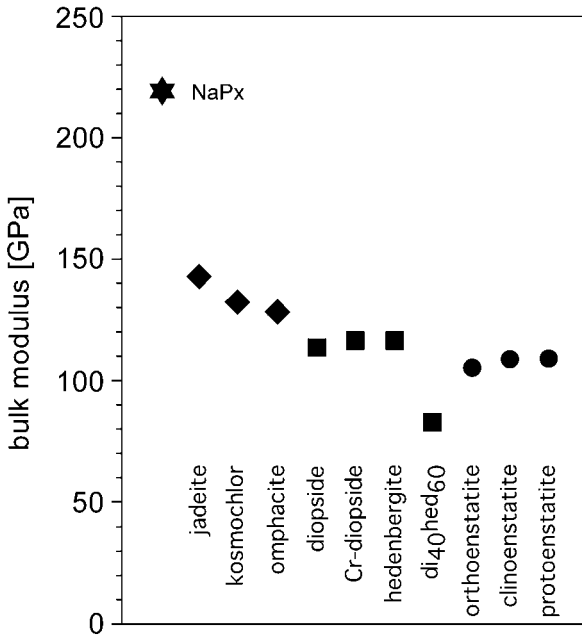

Fig. 3.2-8: A comparison of the bulk modulus of various pyroxene minerals with the $Na_{0.98}Mg_{0.53}Si_{2.49}O_6$ bulk modulus reported here. NaPx has by far the highest bulk modulus of any pyroxene reported.

g. *Melting of Ice VII from Raman spectroscopy to 50 GPa (N.A. Dubrovinskaia and L.S. Dubrovinsky)*

Properties of H_2O at elevated pressure and temperature are of fundamental importance in both condensed matter physics and planetary sciences. The pressure-temperature phase diagram of water ices is extremely complex and various solid forms of H_2O have been and still are the subject of intense experimental and theoretical investigations. Ice VII is a stable phase of water at room temperature and pressure above 2.3 GPa. Melting of Ice VII has been studied over last 40 years by different techniques. Fei *et al.* studied melting of Ice VII in externally electrically heated DAC to about 16 GPa by monitoring the disappearance of the (110) peak in the X-ray diffraction collected by an energy dispersive detector. Datchi *et al.* followed melting of water at pressure up to 13 GPa (temperatures about 750 K) by visual observations in externally heated DACs. We extended the studied pressure range up to 37 GPa employing the whole-cell heating assemblage for pressure and temperature generation and angle-dispersive synchrotron-based X-ray diffraction for detection of Ice VII melting event. Lin *et al.* applied Raman spectroscopy and visual observations in an externally heated DAC to detect melting of water and reached 22 GPa and 900 K. Keeping in mind that different techniques are used for the identification of melting and different standards for pressure characterization are applied (Au equation of state or fluorescence markers), there is fair agreement between

data obtained in electrically-heated DACs (Fig. 3.2-9): at 650 K the difference in pressure is less than 2 GPa. In contrast, the melting curve of H_2O measured in a laser-heated DAC with visual observation of the laser-speckle pattern is at odds with all data reported before: at 15 GPa the difference is ~ 250 K and increases with pressure). Resolving such a controversy requires further experimental studies with accurate *in situ* measurements of pressure and temperature in the DAC.

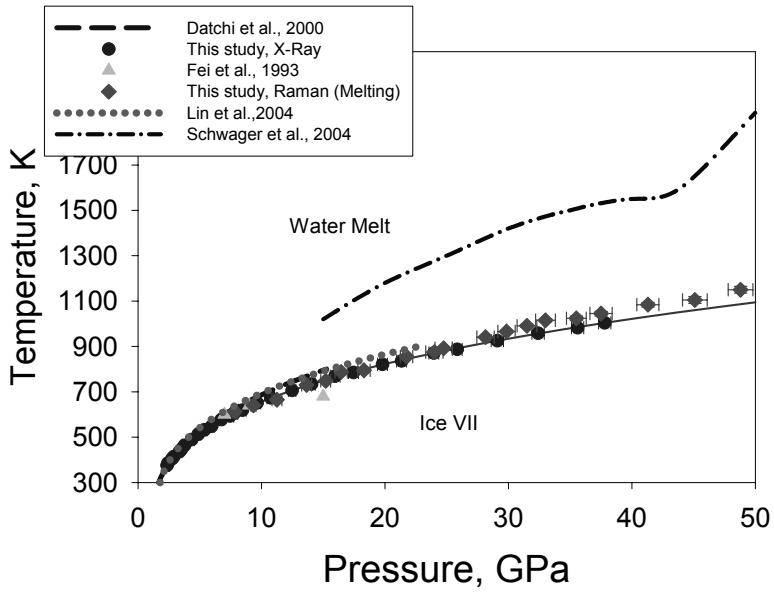

Fig. 3.2-9: Phase relations between Ice VII and liquid water. Circles represent X-ray data, diamonds – melting according to Raman and visual observations. The Solid line is the melting curve described by the equation given below.

In order to study the behaviour of pure doubly distilled deionised water at elevated pressures and temperatures we employed the external electrical heating diamond anvil cell technique. Pressure was determined from fluorescence sensors (Sm:YAG and ruby). Natural low-fluorescence type IIa and high-purity synthetic diamonds with 250 to 350 μm diameter culets were used. Re gaskets were used at temperatures up to 900 K. At higher temperatures with long-duration heating (dozens of minutes) Re starts to react with H_2O. Consequently, in experiments at temperatures of 900 K or higher, we used Ir gaskets which did not show any sign of reaction with water. Changes in the state of water were monitored by visual observations and Raman spectroscopy.

Raman spectra were recorded using Dilor XY (514 nm Ar laser, 1800 g/mm and 1200 g/mm grating, double-stage spectrometer, 1 cm^{-1} resolution) and LabRam (632 nm He-Ne laser, 1200 g/mm grating, ~ 2 cm^{-1} resolution) systems. High-pressure Raman studies of water ice is challenging due to weak signal from the sample, merging of Raman-active stretching mode of Ice VII into the second-order Raman signal from diamond anvils above 25 GPa, as well as stresses and pressure gradients developing in the ice. We have overcome the latter problems

by melting of samples and slow (~ 10 K/min) subsequent cooling to desired temperature. Even at pressures of ~ 50 GPa (highest pressure in this study) pressure variation in the sample cooled to room temperature is less than 1.5 GPa across the 130 μm diameter pressure chamber. In order to improve the signal-to-noise ratio and to collect especially weak Raman spectra of Ice VII and liquid water at high temperature, we used confocal optical configuration and spatial filtering with depth of focus down to 2 μm, as well as high purity thin (1.2 to 1.5 mm thickness) synthetic diamonds. The background spectra collected from the part of pressure chamber that was free of water (it was blocked by a particle of Au or Ir on the surface of the anvil) were subtracted.

Melting was indicated by translational modes in the Raman spectra and changes in the shape and reduction in intensity of OH-stretching modes (Fig. 3.2-10). The results on melting of Ice VII from Raman spectroscopy are summarized in Fig. 3.2-10, and can be describe by equation

$$P = 2.2 + 1.31\left[\left(T/364\right)^{3.3} - 1\right],$$

in agreement with X-ray diffraction data up to 37 GPa.

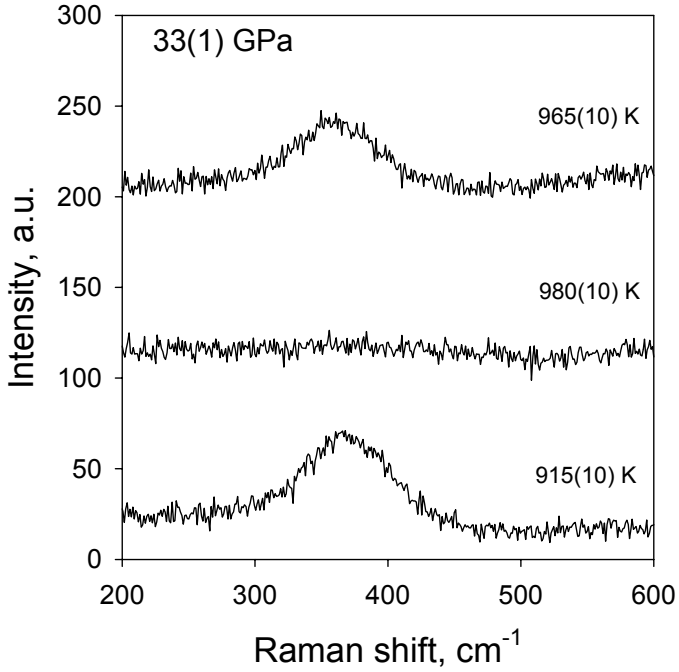

Fig. 3.2-10: Raman spectra of water collected at 33(1) GPa and different temperatures in low-frequency regions.

3.3 Mineralogy, Crystal Chemistry and Phase Transformations

Nearly all the Earth's crust and mantle is in the solid, crystalline state, and for this reason alone the crystal structures of the Earth's materials and the relationships between microscopic (i. e. on an atomistic scale) and macroscopic properties (as for instance volume or elasticity) are of fundamental importance in geosciences, and also in physics, chemistry and material sciences. Structures as well as properties respond to changes in external parameters (such as temperature, pressure, fugacity of volatile species), and this response may be continuous or discontinuous. For instance, the steady increase in seismic wave velocities in the lower mantle is explained by the continuous increase of density and elastic constants mostly due to increasing pressures, whereas the sudden "jumps" in velocity at the 410 and 660 km discontinuities are caused by polymorphic phase transitions (e. g. from olivine to wadsleyite at 410 km depth) or the formation of entirely new compounds (such as breakdown of ringwoodite to silicate perovskite and ferropericlase at 660 km depth). By studying structure-property relationships as a function of pressure, temperature or chemical composition we therefore gain insights into mechanisms on a very local, atomic scale, and have good reasons to apply these then on a global scale. Even extrapolations to experimentally inaccesible regions of pressure, temperature or composition are possible to some extent if the systematics are known.

Whereas the so-called chemically "simple" compounds such as the $MgSiO_3$ or Mg_2SiO_4 end members have been studied successfully over the last decades, there is still little information on processes and strains on an atomic scale in chemically and structurally more complex materials or in solid solutions of even binary systems, where one kind of atom is replaced by another (as for instance Fe^{2+} for Mg in natural olivines) and where temperature-dependent intracrystalline order/disorder comes in as another variable. These local strains eventually also control the macroscopic thermodynamic mixing models of solid solutions which are needed to calculate phase equilibria between chemically more complex minerals.

The contributions in this section illustrate this approach. They mostly relate to well-known and wide-spread mineral groups (pyroxenes, olivines, amphiboles, carbonates) and study the changes in structure and/or properties as a function of pressure, temperature and chemical composition.

a. *The effect of Ca substitution on the elastic and structure behaviour of orthoenstatite ($Mg_2Si_2O_6$) up to 10.2 GP (F. Nestola, T. Boffa Ballaran and G.D. Gatta)*

Orthopyroxenes, and in particular the orthoenstatite end-member ($Mg_2Si_2O_6$, space group *Pbca*), are among the most studied silicates in Earth Sciences. Such interest is due to their abundance in the Earth's lower crust and upper mantle, in volcanic rocks and in many kinds of meteorites. Knowledge of their thermodynamic properties allows us to determine correctly

the temperature and pressure conditions at which these minerals are formed and to constrain the formation conditions of rock assemblages in the Earth's deep interior. Several studies have been performed at high pressure by means of many investigation techniques, such as ultrasonic, X-ray diffraction, IR and Raman spectroscopy. One of the major controversies among all these studies is represented by the different values reported for the bulk modulus, K_0, (between 96 and 123 GPa) and by the anomalous high value of its pressure derivative, K', which ranges between 7 and 14.9. Such discrepancies are likely due to some difference in composition of the investigated samples, especially if they are from natural assemblages.

All compressibility data present in the literature for pure orthoenstatite have been reanalysed together with some new more accurate data in a recent study resulting in EoS coefficients: K_0 = 105.8(5) GPa and K' = 8.5(3). How cation substitution into the orthoenstatite structure can affect such EoS values is, however, still an open question. Ca atoms, for example, although present only in small amount in natural orthoenstatite, may play a major role in modifying its high-pressure and high-temperature behaviour. To test such hypothesis, high-pressure experiments were performed on a single-crystal of composition $Ca_{0.07}Mg_{1.93}Si_2O_6$ using a diamond anvil cell (DAC) loaded with a mixture of 16:3:1 water:methanol:ethanol as pressure transmitting medium and X-ray diffraction. We have measured the unit-cell parameters at 10 different pressures up to about 10.2 GPa. The pressure-volume data have been fitted by a third-order Birch-Murnaghan equation of state (BM3, Fig. 3.3-1) refining simultaneously unit-cell volume V_0, K_0 and K'. The refinement gave the following coefficients: V_0 = 838.26(8)Å^3, K_0 = 110(1) GPa, K' = 6.6(4).

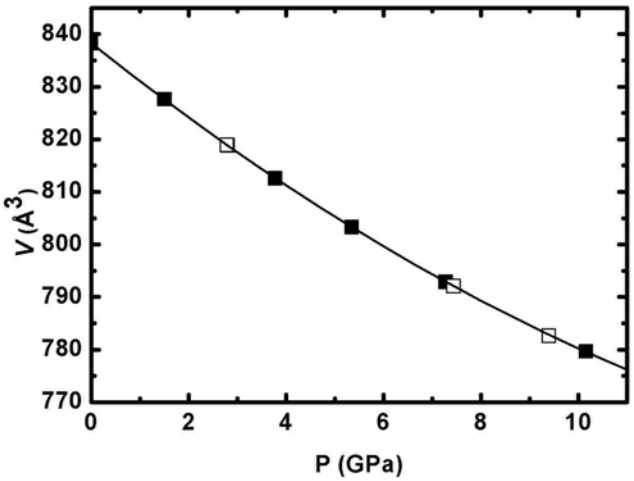

Fig. 3.3-1: Unit-cell volume variation as a function of pressure of $Ca_{0.07}Mg_{1.93}Si_2O_6$ orthopyroxene (filled squares indicate data point collected under compression, open squares those collected under decompression).

It appears, therefore, that the presence of a small amount of Ca slightly increases the bulk modulus of orthoenstatite but strongly decreases its first derivative. The linear axial

compressibilities [$\beta_d = -1/d_0(\partial d/\partial P)_{T,X}$, with $d = a$, b and c] are $\beta_a = 0.0018$ GPa^{-1}, $\beta_b = 0.0030$ GPa^{-1} and $\beta_c = 0.0023$ GPa^{-1}, with a resulting compressibility scheme $\beta_b > \beta_c > \beta_a$, similar to that of many other pyroxenes and in particular to orthoenstatite.

b. *Crystal structure and compressibility along the join jadeite ($NaAlSi_2O_6$)-acmite ($NaFeSi_2O_6$) (F. Nestola, T. Boffa Ballaran and C. Liebske)*

Jadeite ($NaAlSi_2O_6$, space group $C2/c$) is of crucial importance in understanding the conditions of formation of high-pressure metamorphic rocks like blueschist and eclogites. In fact, one of the most famous geobarometers is represented by the following reaction:

$$\text{albite } (NaAlSi_3O_8) = \text{jadeite } (NaAlSi_2O_6) + \text{quartz } (SiO_2) \qquad (1)$$

This reaction has been studied extensively and the results have been used to determine the maximum pressure at which albite is stable. However, very often natural jadeite is not perfectly pure but contains variable amount of diopside ($CaMgSi_2O_6$), hedenbergite ($CaFeSi_2O_6$) and acmite ($NaFe^{3+}Si_2O_6$) components. The effect of diopside (Di) on the reaction (1) has been determined and it has been found that diopside causes an increase of the stability field of albite. In contrast, only few studies have been performed on the effect of acmite and hedenbergite substitution on the reaction (1).

The aim of the present work is to investigate by means of single-crystal X-ray diffraction the join jadeite-acmite in order to quantify the structural behaviour of this solid solution both at ambient and high-pressure conditions and to provide accurate compressibility data. We have synthesised three samples with nominal composition $Jd_{75}Ac_{25}$, $Jd_{55}Ac_{45}$ and $Jd_{40}Ac_{60}$ at 1300-1500 °C and 6 GPa using a multianvil press. Oxygen fugacity was constrained by a Re/ReO_2 oxygen buffer to avoid reduction of Fe^{3+}. Complete intensity data collections have been measured for single-crystals having the three different compositions up to $2\theta = 80°$ using a Xcalibur four-circle diffractometer equipped with a graphite-monochromated $Mo_{K\alpha}$ radiation. Refinement of the structures gave an accord index factor R of 2.5 %, 2.3 % and 1.9 % for $Jd_{75}Ac_{25}$, $Jd_{55}Ac_{45}$ and $Jd_{40}Ac_{60}$, respectively. All crystals have space group $C2/c$. The unit-cell parameters as well as the Na-O and (Al,Fe)-O average bond distances increase linearly with increasing acmite content. The increase of (Al,Fe)-O distances is larger than that of Na-O distances (5 % and 2.5 % respectively) due to Al/Fe^{3+} cation substitution occurring at the M1 site. The average bond distances of the tetrahedral polyhedron are 1.625 Å for all the studied samples. The O3-O3-O3 kinking angle decreases in a non-linear manner as a function of acmite component.

The samples $Jd_{55}Ac_{45}$ and $Jd_{40}Ac_{60}$ have been loaded together in a diamond anvil cell for *in situ* X-ray high-pressure experiments. As pressure standard we used a crystal of quartz loaded together with the samples to be studied and a mixture of 16:3:1 water:methanol:ethanol as

pressure-transmitting medium. The measurements have been performed on a Huber four-circle diffractometer using the eight-position method for determining the unit-cell parameters at different pressures. Preliminary results up to about 6 GPa do not indicate significant stiffness differences (Fig. 3.3-2).

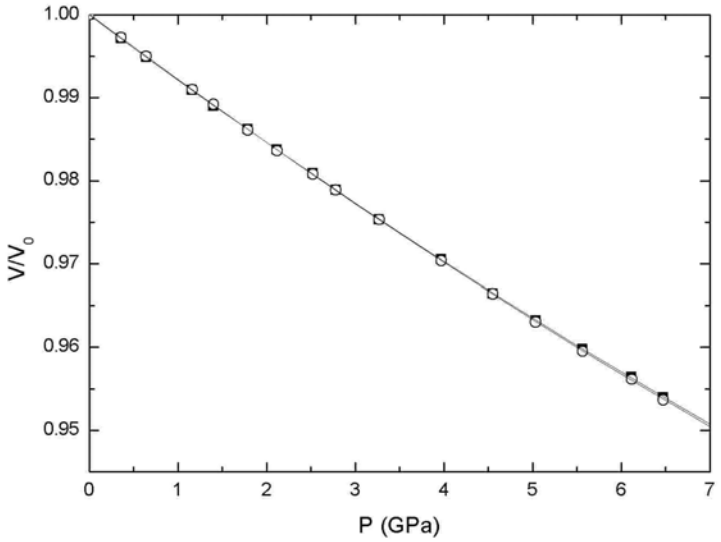

Fig. 3.3-2: Relative compression (V/V_0) as a function of pressure for the samples $Jd_{55}Ac_{45}$ (open squares) and $Jd_{40}Ac_{60}$ (filled circles)

c. *High-pressure $I\bar{1}$ - I2/c phase transition in $Ca_{0.2}Sr_{0.8}Al_2Si_2O_8$ ($An_{20}SrF_{80}$) feldspar: In situ structural investigation (P. Benna/Torino; F. Nestola and T. Boffa Ballaran; M. Tribaudino and E. Bruno/Torino)*

The Ca-Sr feldspars provide a suitable model for structural phase transitions occurring as a function of pressure and temperature in feldspars. A previous investigation at high pressure (see year book 2003) has shown the presence of a $I\bar{1}$ -*I*2/*c* phase transition and a transition from *I*2/*c* to a second monoclinic phase in a feldspar with composition $Ca_{0.2}Sr_{0.8}Al_2Si_2O_8$ ($An_{20}SrF_{80}$) at about P = 4.3 and 7.3 Gpa, respectively. In the present study, the structural behaviour of the $I\bar{1}$ -*I*2/*c* phase transition was detailed by the refinement of data collected for a single crystal of the same composition. Structural data were collected by X-ray *in situ* diffraction at P = 0.0001, 3.95 and 5.2 GPa, to follow the structural evolution through the $I\bar{1}$ - *I*2/*c* phase transition. The absorbance of the diamond anvil cell (DAC) strongly affected the measurement of the fainter *b*-type reflections, sensitive to Al-Si order, and tetrahedral oxygens bond distances. Therefore, in the refinements of the high-pressure data, the tetrahedral bond lengths were soft constrained to the room temperature values. The structure was refined with final residual indices R% = 3.5 at P = 0.0001 (without DAC) R% = 6.9 at 3.95 GPa and R% = 11.5 at 5.2 GPa.

The main changes at the transition involve the non-tetrahedral polyhedra as the Sr/Ca-O bond lengths go from 2.790 Å and 2.788 Å (average bond distances for Ca/Sr(0)-O and Ca/Sr(z)-O)

of the triclinic phase to 2.72 Å (average bond distances for Ca/Sr-O) of the monoclinic phase, with a variation of about 2.5 %.

In Figure 3.3-3 the partial projections along the *c* axis of the $An_{20}SrF_{80}$ feldspar structure at *P* = 0.0001 and at *P* = 5.2 GPa are shown. Some structural distances are superimposed on it in order to evidence the large differences between the two structures. A structural investigation is currently being performed on the monoclinic-monoclinic phase transition at $P \approx 7.3$ GPa.

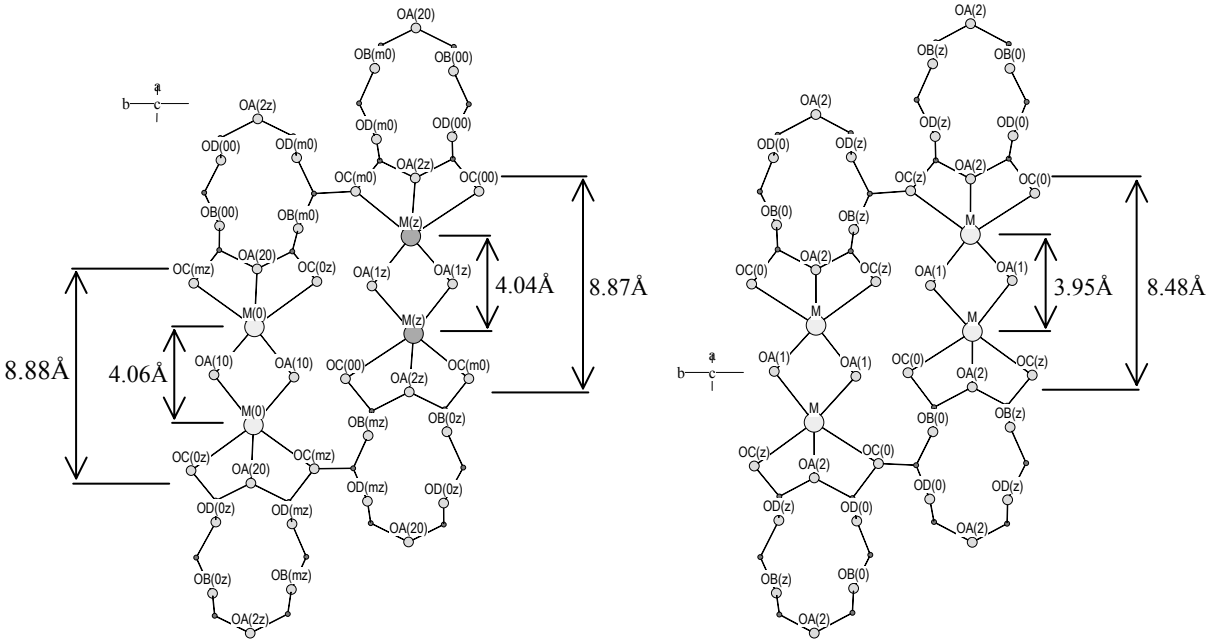

P = 1 atm Space group: $I\bar{1}$ *P* = 5.2 GPa Space group: *I*2/*c*

Fig. 3.3-3: Partial projection along the **c** axis of the $An_{20}SrF_{80}$ feldspar structure.

d. *Anomalous elastic behaviour and high-pressure structural evolution of zeolite levyne (G.D. Gatta and T. Boffa Ballaran, in collaboration with P. Comodi and P.F. Zanazzi/Perugia)*

Levyne is a rare zeolite with the ideal chemical formula: $(Ca_{0.5},Na,K)_6(Al_6Si_{12}O_{36})\bullet 18H_2O$, found as hydrothermal mineral in vugs of massive volcanic rocks. The synthetic Si/Al/P-counterparts of levyne, like SAPO-35 and AlPO-35, have many technological applications as molecular sieves. The framework of this zeolite can be described as a sequence of 6-membered double rings and 6-membered single rings of tetrahedra, which build up the so-called "levyne-cage" and is characterized by the presence of three equivalent channel systems perpendicular to the three-fold axis, confined by 8-membered rings (free diameters ~ 3.6 x 4.8 Å, Fig. 3.3.-4). The topological symmetry is $R\bar{3}m$ and corresponds to the general symmetry of the crystal structure. The extra-framework content, represented by Ca, Na, K and water molecules, lies in the cages. At least five independent cation sites have been located.

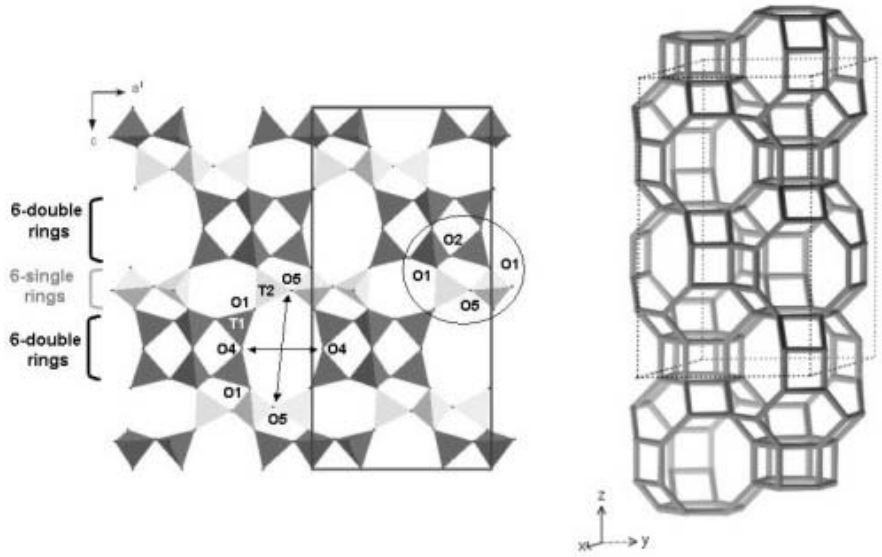

Fig. 3.3-4: Crystal structure of zeolite levyne (polyhedral representation on the left, "skeletal-model" on the right). The 6-single membered rings are shown in light gray, the 6-double membered rings in dark gray. The "joint-unit" between 6-double and 6-single membered rings is highlighted with a circle.

The elastic behaviour and the high-pressure (H*P*) structural evolution of a natural levyne have been investigated up to 5 GPa by means of *in situ* single-crystal X-ray diffraction with a diamond anvil cell using a non-penetrating pressure transmitting medium (glycerol). A peculiar elastic behaviour has been observed in the range 0-1 GPa: the *c* lattice parameter decreases between 0 and 0.2 GPa (Fig. 3.3.-5a), then increases up to 0.5-0.6 GPa. Above this *P*-value, the parameter decreases again as expected. An anomalous behaviour is also shown by the *a*-parameter, which first increases up to 0.2 GPa (Fig. 3.3.-5b), then decreases as expected. However, these anomalous lattice variations are only slightly reflected in the cell volume behaviour. The isothermal Equation-of-State (EoS) for $P > 1$ GPa, refined with a second-order Birch-Murnaghan EoS, yields the following parameters: $V_0 = 3539(3)$ Å^3 and $K_{T0} = 48(1)$ GPa. The axial anisotropy of levyne have been calculated as the ratio between the "linearized" bulk moduli along the *a* and *c*-axis for $P > 1$ GPa. A "linearized BM-EoS", truncated to the second-order, yields the following axial parameters: $a_0 = 13.305(4)$ Å and $K_{T0}(a) = 43.7(8)$ GPa; $c_0 = 23.079(8)$ Å and $K_{T0}(c) = 62(1)$ GPa. Thus, the lattice shows a strong anisotropy, being more compressible along the *a*-axis than along the *c*-axis with $K_{T0}(a):K_{T0}(c) = 1.00 : 1.42$. Unit-cell parameters measured during decompression show that the compressional changes are reversible.

Comparison of structural refinements performed at the University of Perugia (I) at 0.0001, 0.79(5) and 3.00(5) GPa highlights two distinct deformation mechanisms of the Si/Al-framework: one predominant at low pressures (0-1 GPa), with a cooperative anti-rotation of the tetrahedra belonging to the 6-membered double rings unit (Fig. 3.3-4), and one at high pressures (1-5 GPa), which acts on the "joint units" between the 6-membered rings with a

decrease of the distance O2-O5 (Fig. 3.3-4). The first mechanism (at $P < 1$ GPa) produces the [001]-elongation of the crystal lattice. At about 1 GPa, the 6-double ring achieves a geometrical configuration that cannot further expand along [001]. It is clear, therefore, that the unexpected H*P*-increase of the *c*-parameters at $P < 1$ GPa is due to the tetrahedral-tilting of the 6-membered double rings.

The extra-framework content does not show any evident modification within the pressure range investigated.

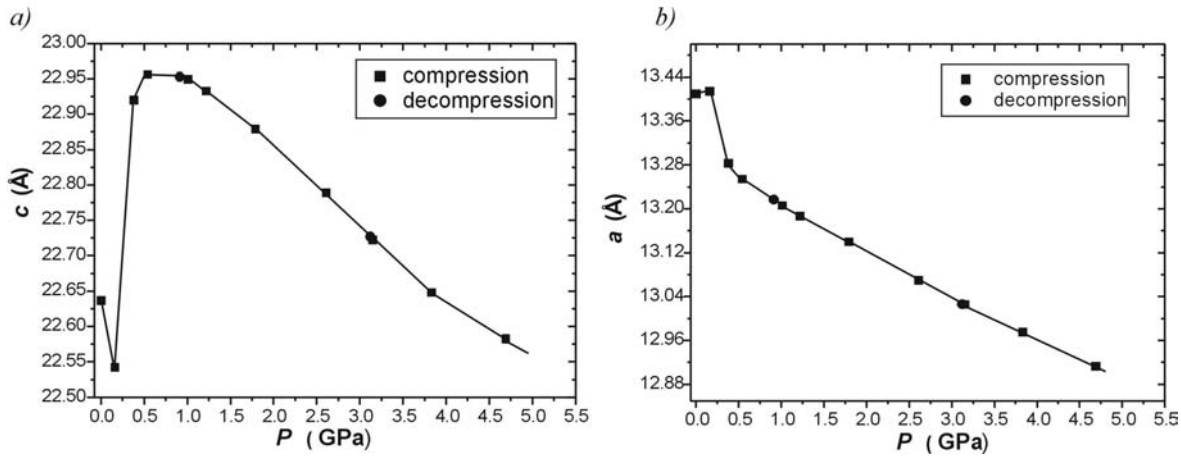

Fig. 3.3-5: Evolution of the *a* and *c* unit-cell parameters of levyne as a function of pressure

e. *The compressional behaviour of the columbite-group minerals along the $FeNb_2O_6$-$MnNb_2O_6$ solid solution (M. Pistorino/Pavia, F. Nestola and T. Boffa Ballaran, in collaboration with M.C. Domeneghetti/Pavia)*

Columbite-tantalite minerals are the predominant Nb-Ta phases found in rare-earth granite pegmatites. These minerals have general formula AB_2O_6 (where A = Fe^{2+}, Mn^{2+} and B = Nb^{5+}, Ta^{5+}, with other cations such as Mg^{2+}, Ca^{2+}, Sc^{3+}, Fe^{3+}, Ti^{4+}, Sn^{4+}, W^{6+} and rare-earth elements as minor substitutions). Columbites (samples with Nb as the dominant B cation) and tantalites (samples with Ta as the dominant B cation) crystallise in the orthorhombic system, space group *Pbcn*, with an α-PbO_2-type structure. A convergent order-disorder process occurs for samples at intermediate composition with Fe/Mn preferentially occupying the A site and Nb/Ta the B site. Minerals of the columbite group show a wide range of degrees of order; complete order can be experimentally achieved by annealing at high temperature, whereas completely disordered samples have never been found or synthesized.

The aim of this work is to study the high-pressure behaviour of the columbite-group minerals as a function of chemical composition and degree of order. In a first series of high-pressure experiments the effect of cation ordering on compressibility has been investigated. Two single-crystals from a natural sample of columbite from Raode, Africa, with same

composition, X_{Nb} = Nb/(Nb+Ta) = 0.973 and X_{Fe} = Fe/(Fe+Mn) = 0.800, but different degrees of order, $Q_{Raode\ 17}$ = 25 % and $Q_{Raode\ 15}$ = 100 %, have been loaded together in a diamond anvil cell with a quartz single-crystal as internal pressure standard and a 4:1 methanol:ethanol mixture as pressure medium. Unit-cell parameters were measured at room temperature as a function of pressure up to 7.1 GPa (Fig. 3.3-6). The reversibility of the experiments was checked by measuring lattice parameters releasing pressure at 5.9 and 3.1 GPa.

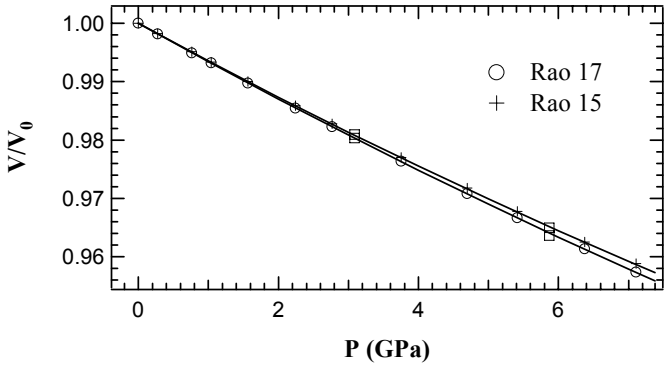

Fig. 3.3-6: Volume variation of two samples having the same composition, but different degrees of order as a function of increasing pressure (crosses and circles) and decreasing pressure (squares)

In a second series of experiments the compressibility as a function of the Fe/Mn substitution alone has been measured. Two totally ordered single-crystals of columbite from Ivigtuut, Greenland, (MM-13) and from Kragerve, Norway, (Kra 11), with composition X_{Nb} = 0.993, X_{Fe} = 0.750 and X_{Nb} = 0.923, X_{Fe} = 0.155 respectively, have been loaded together in a diamond anvil cell and studied by *in situ* high-pressure X-ray diffraction.

Cell parameters were measured at room temperature as a function of pressure up to 6.2 GPa and the reversibility of the experiments was checked by two measures of the lattice parameters releasing pressure at 4.2 and 1.7 GPa (Fig. 3.3-7).

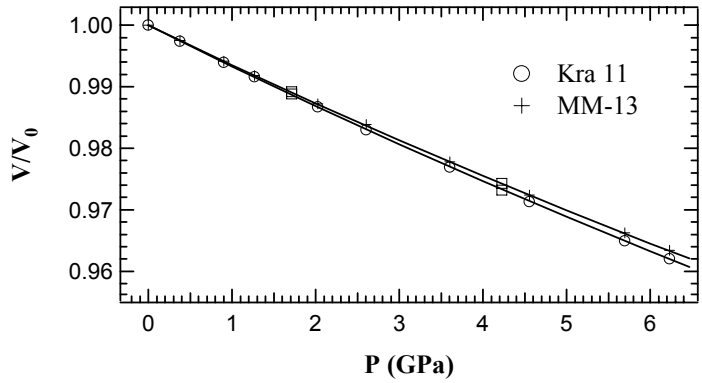

Fig. 3.3-7: Volume variation of two samples having different Fe/Mn ratios with increasing pressure (crosses and circles) and with decreasing pressure (squares)

No phase transitions were observed in the two series of experiments, as indicated by the continuous decrease of unit cell parameters.

EoS parameters calculated using a third order Birch-Murnaghan equation of state are V_0 = 413.89(2), K_0 = 152(1), K' = 4.8(3) for Raode 15, V_0 = 414.56(1), K_0 = 148.9(6), K' = 4.1(2) for Raode 17, V_0 = 415.03(5), K_0 = 152(3), K' = 4.9(8) for MM-13 and V_0 = 421.18(2), K_0 = 146(1), K' = 5.0(4) for Kra 11.

It can be noticed that there is a slight increase of compressibility with Mn substitution into the Fe columbite. Although the difference in K_0 values is minimal, the high accuracy of the unit-cell data suggests that ordered and relatively disordered samples (Raode) have a different compressional behaviour.

f. *Equation of state of beryl: A comparison between experimental measurements and first principle, quantum-mechanical computations (M. Prencipe/Torino and F. Nestola)*

The general aim of this work is the investigation of the high-pressure crystal-chemistry of minerals from the analysis of their *ab initio* calculated electron densities. Comparison of calculated properties (*e.g.*, geometry and elastic properties) with high quality experimental measurements is a crucial step in judging the quality of the calculated electronic wave function.

The equation of state of the mineral beryl ($Al_4Be_6Si_{12}O_{36}$; space group *P*6/*mcc*) has been experimentally determined by measuring the unit cell volume at different pressure values in the range 0.0001 – 6.3 GPa using a diamond anvil cell (DAC) loaded with a 16:3:1 water:methanol:ethanol mixture. Single crystal X-ray diffraction methods were employed for the measurement of the cell parameters and a HUBER four circle diffractometer was used. Pressures in the DAC were determined either by measuring the fluorescence frequency of a ruby crystal and by measuring the cell volume of quartz, as an internal diffraction pressure standard. The fitting of the *P*-*V* data, by using a third-order Birch-Murnaghan equation of state, gave an equilibrium volume V_0 = 675.66(3) Å^3 and a bulk modulus K_0 = 179(1) GPa, with K'= 3.7(3). The weighted χ^2 is 0.91 and the maximum ΔP ($|P_{obs} - P_{calc}|_{max}$) is 0.018 GPa, indicating a very high data quality.

An energy *vs* volume curve has also been determined by quantum-mechanical *ab initio* calculations, at the Hartree-Fock level, by using the CRYSTAL2003 code. At each different cell volume in the range 676-600Å^3, the *c/a* ratio and the atomic fractional coordinates were determined by minimizing the total energy of the unit cell. K_0 and V_0, determined by fitting of the *E*-*V* data with a Birch-Murnaghan equation of state (modified to express *P* as a function of E: $P = -dE/dV$), were 207.7(5) GPa and 675.1(1) Å^3, respectively (K' was kept fixed at the experimental value of 3.7). The error in the computed bulk modulus (+ 16 % with respect to the experimental value) is to be expected, due the increasing importance of electronic

correlation effects as the cell volume decreases; such effects are neglected at the Hartree-Fock level, thus producing an overestimation of the total energy at smaller cell volumes and therefore an higher bulk modulus. Further calculations, which include electronic correlation in the determination of the total energy, are in progress.

g. *High-pressure behaviour of $KAlSi_3O_8$ hollandite (J. Liu, T. Boffa Ballaran, L.S. Dubrovinsky and D.J. Frost)*

$KAlSi_3O_8$ feldspar is one of the abundant minerals in the Earth's crust and it can be subducted to a great depth. However, host minerals of potassium in the deep mantle have not yet been accurately characterized. Hollandite-type aluminosilicate materials with their dense structure, in which all Si and Al are in six-fold coordination, are considered as a possible repository of potassium in the Earth's lower mantle. In previous studies of quenched experiments, it has been found that the stability of $KAlSi_3O_8$ hollandite extends up to 95 GPa implying that such a phase could be the host for potassium down to the lower mantle. A previous *in situ* high-pressure single-crystal study of $KAlSi_3O_8$ hollandite has only been done up to pressures of 4 GPa, resulting in a high compressibility of the octahedral framework with respect to the related stishovite structure. This suggests a possible phase transformation of the hollandite structure at higher pressure. In our preliminary work we analysed a single-crystal of $KAlSi_3O_8$ hollandite by means of Raman spectroscopy up to 30 GPa in order to better constrain the behaviour of $KAlSi_3O_8$ hollandite at different depth intervals in the lower mantle and to investigate the possibility of non-quenchable phase transformations.

The $KAlSi_3O_8$ hollandite samples were synthesized at 1500 °C and 13 GPa in a multianvil press. A good single crystal was picked for the *in situ* high-pressure Raman experiment. The $KAlSi_3O_8$ hollandite sample was loaded into the DAC with argon as the pressure-transmitting medium, and a few small pieces of ruby as pressure calibrant. The sample was compressed up to 30.50 GPa at room temperature, and then decompressed slowly to ambient pressure. Raman spectra were collected both under compression and decompression (Fig. 3.3-8).

In the Raman spectrum at ambient pressure 5 peaks are easily recognizable. Peak 5 at 765 cm^{-1} can be assigned to Si-O stretching vibrations in the SiO_6 octahedra by comparison with a similar intense peak observed in the spectrum of stishovite (SiO_2). The peak at the lowest frequency may be mainly due to potassium vibrations, but it could not be followed as a function of pressure due to the high background. Peak 3 is broad and appears to be a combination of two peaks, as suggested by the fact that it separates into two peaks with increasing pressure. The other significant changes in the spectra are the intensities of peak 4 and peak 5. At ambient pressure, peak 5 is the most intense peak, and its intensity is higher than the intensity of peak 4. With increasing pressure, the intensity of peak 5 decreases and peak 4 becomes more intense. During decompression, the changes in peak 3, peak 4 and peak 5 are reversible. We are now working on the quantification of the peak shifts in order to

quantify the high-pressure behaviour of the Raman modes. Further high-pressure experiments including an X-ray study are also in progress, in order to compare the structural compressibility with the local structural behaviour obtained by Raman spectroscopy.

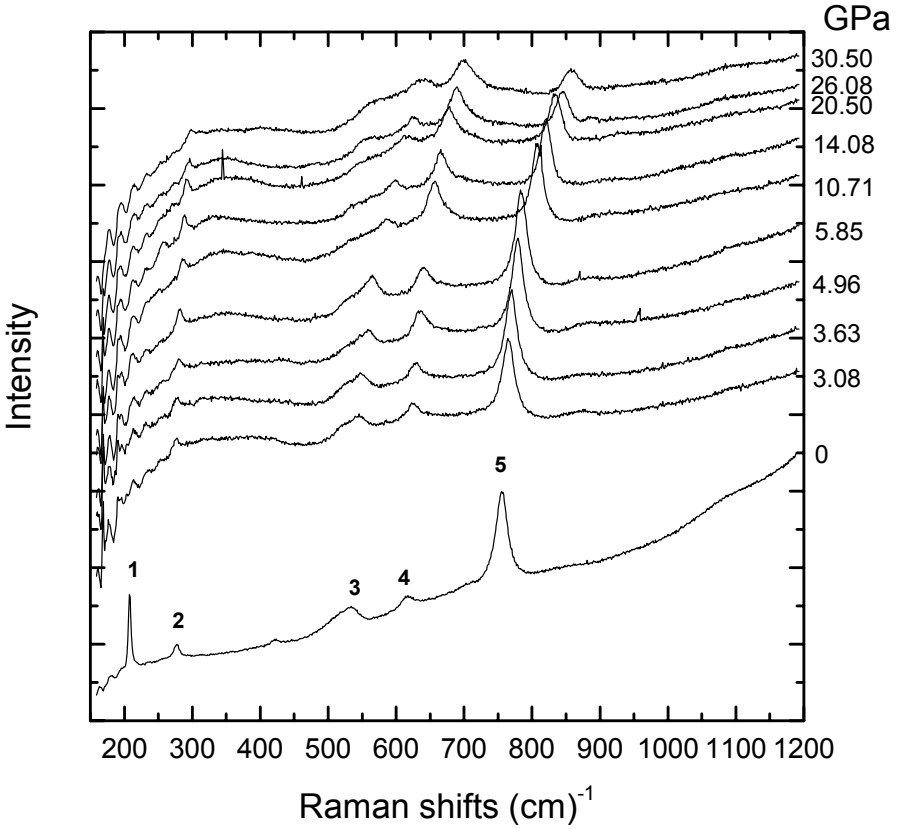

Fig. 3.3-8: Raman spectra of $KAlSi_3O_8$ hollandite collected at different pressures.

h. *Seifertite: A new natural very dense post-stishovite polymorph of silica (T.G. Sharp/Tempe, A. El Goresy/Mainz, L.S. Dubrovinsky, M. Chen/Guangzhou, B. Wopenka/St. Louis, P. Dera/Washington DC, C.T. Prewitt/Tucson, N.Z. Boctor/Washington DC and R.J. Hemley/Washington DC)*

In the last two decades, considerable interest has been devoted to the response of silica to extreme pressure conditions using both diamond anvil high-pressure devices and First Principles Calculations. This interest stems from the possibility of the existence of dense free silica in Earth's mantle. Silica is a major component of the Earth. Based on the chondritic model, SiO_2 makes up 50 wt.% of Earth's bulk. Possible natural polymorphs of silica denser than stishovite are also important for understanding the behaviour of SiO_2 in the Earth's interior and during natural dynamic events on planetary surfaces. High-pressure diamond anvil cell (DAC) experiments revealed that silica undergoes several phase transitions to "post-stishovite" (polymorphs denser than stishovite) phases above 48 GPa. Stishovite inverts displacively above 48 GPa to a $CaCl_2$ I -structured-polymorph (space group *Pnnm*), a

polymorph that contains silicon in distorted octahedrons. It has been shown experimentally and by First Principles Calculations that this polymorph is stable up to 78 GPa. Beyond that pressure the $CaCl_2$ polymorph transforms displacively to a denser species with the α-PbO_2-like structure with kinked chains of SiO_6 octahedra (space group *Pbcn* or *Pb2n*).

The Shergotty and Zagami SNC (possibly Martian in origin) meteorites contain silica grains with lamellar structure previously misidentified as PDF in quartz. Silica occurs as large (150-900 μm) prismatic grains, rhombic-or triangular shaped cross sections typical of orthorhombic β-tridymite morphology. The morphology of the cross sections is also consistent with cristobalite. Every silica grain consists of mosaics of domains (10-60 μm in size Fig. 3.3-9) each displaying two orthogonal sets of lamellae that have different brightness in Back Scattering Electron (BSE) mode in the Field-Emission Scanning Electron Microscope (FESEM). The brighter lamellae consist of a dense crystalline SiO_2 phase and the dark ones of dense SiO_2 glass (Fig. 3.3-10). Electron microprobe analyses with a defocused beam on the widest lamellae showed almost pure SiO_2 with minor concentrations in Na_2O (0.40 wt.%) and Al_2O_3 (1.14 wt.%). The lamellae are extremely sensitive to electron bombardment and are destroyed within a few seconds under a focused electron beam, despite the use of low sample current (< 5 nano-Amps). An attempt to determine the nature of the lamellae by laser microRaman spectroscopy failed due to the instantaneous vitrification under the focused laser beam, despite the use of low laser power.

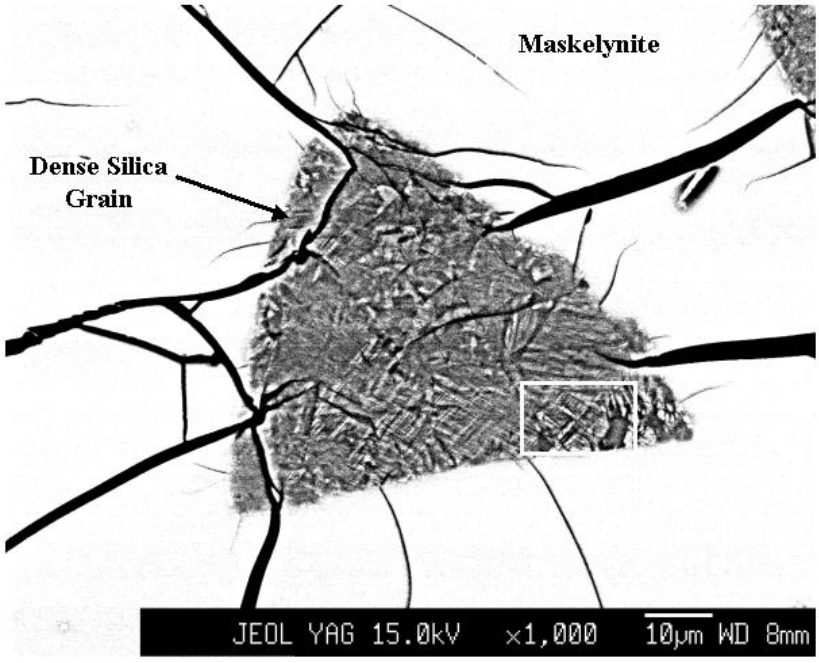

Fig. 3.3-9: A back scattered electron (BSE) photomicrograph of a triangular dense silica grain from the Shergotty meteorite. The grain consists of numerous domains of a maximum diameter of 60 μm. Each domain displays an orthogonal pattern of bright (seifertite) and dark (dense SiO_2 glass) lamellae.

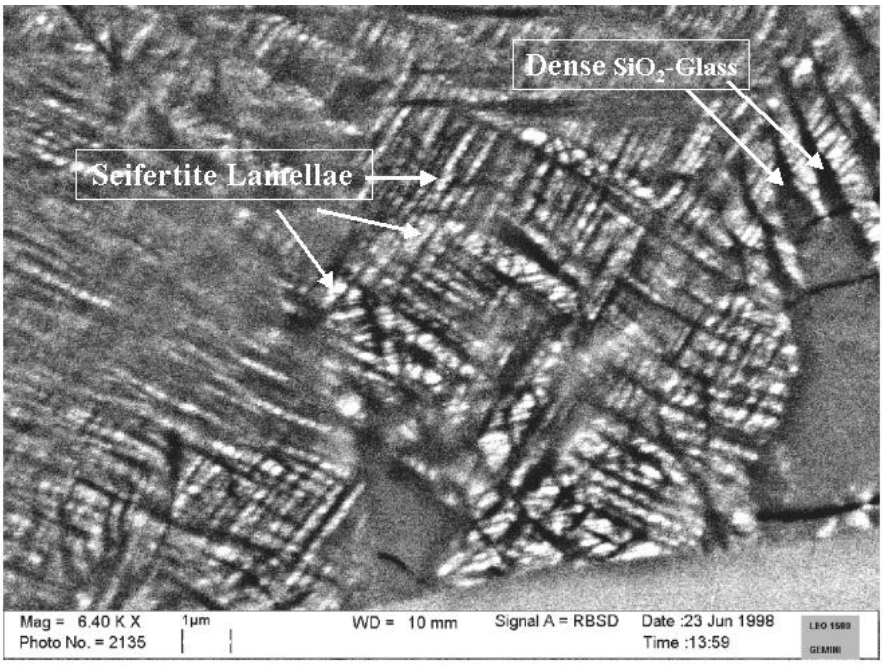

Fig. 3.3-10: A BSE-SEM detail of the area within the white box in Fig. 3.3-9. White lamellae are seifertite and the black lamellae consist of dense SiO_2 glass, probably formed by vetrification of another metastable post-stishovite silica plolymorph

X-ray diffraction and TEM investigations revealed that the dense crystalline silica in Shergotty is a new orthorhombic species (Space Group *Pbcn or Pb2n*) with the following cell parameters: *a* 4.097(1) Å, *b* 5.0462(9) Å, *c* 4.4946(8) Å, V 92.92 $Å^3$, Z = 4. Calculated density = 4.309 g/cm^3 (with empirical formula) and 4.294 gm/cm^3 (with pure SiO_2). High-pressure DAC experiments on cristobalite revealed a phase transformation above 40 GPa to the α-PbO_2-like structure. This strongly suggests that this species formed on the SNC parent body at peak-shock pressures slightly in excess of 40 GPa. The Commission of New Minerals and Mineral Names of IMA (International Mineralogical Association) approved the nomination of this very dense silica species after Friedrich Seifert (seifertite).

i. *Low-T neutron powder-diffraction and synchrotron-radiation IR study of synthetic amphibole* $Na(NaMg)Mg_5Si_8O_{22}(OH)_2$ *(G. Iezzi/Chieti, G.D. Gatta, R. Rinaldi/Perugia and G. Della Ventura/Roma)*

In comparison with framework silicates, phase transitions in chain silicates are relatively rare. Perhaps the best known are the *C*2/*m*-*P*2_1/*m* transition in cummingtonite and the *C*2/*c*-*P*2_1/*c* transition in pigeonite. Geometrical aspects of the structural changes involved in these transitions are well understood. In the *P* lattice, the facing chains of tetrahedra (generally labelled “A” and “B” chains) are non-equivalent; whereas in the *C*-centered lattice, the facing chains are symmetrically equivalent. Tetrahedra in the amphibole or pyroxene chains rotate to

produce changes in the coordination of cations at the M4 sites of cummingtonite or at the M2 sites of pigeonite. The M4 and M2 sites are relatively open in the *C*-face centered structures at high temperatures, but are significantly contracted in the *P* structures at low temperatures. Both transitions can be induced by changing pressure or temperature, depending on composition and on the degree of non-convergent order of cations between the M sites. Apart from cummingtonites, synthetic amphiboles with composition varying between $^{A}Na^{B}(NaMg)^{C}Mg_5Si_8O_{22}(OH)_2$ and $^{A}Na_{0.81}{}^{B}(Na_{0.81}Mg_{1.19})^{C}Mg_5Si_8O_{22}(OH)_2$ displays $P2_1/m$ symmetry at room conditions. This system differs signifincantly from cummingtonite for three different reasons: (1) the presence of mono- and di-valent cations at the M4 sites; (2) the nearly full occupancy of the A-sites; and (3) the impossibility of cation ordering between B- and C-sites.

The H*T*-behaviour of $Na(NaMg)Mg_5Si_8O_{22}(OH)_2$ has been recently investigated and a $P2_1/m \rightarrow C2/m$ second-order phase transition was observed at about 527 K. To complete the characterisation of the temperature behaviour of this amphibole, a structural refinement has been carried out for data collected at 8 K by means of neutron powder-diffraction.

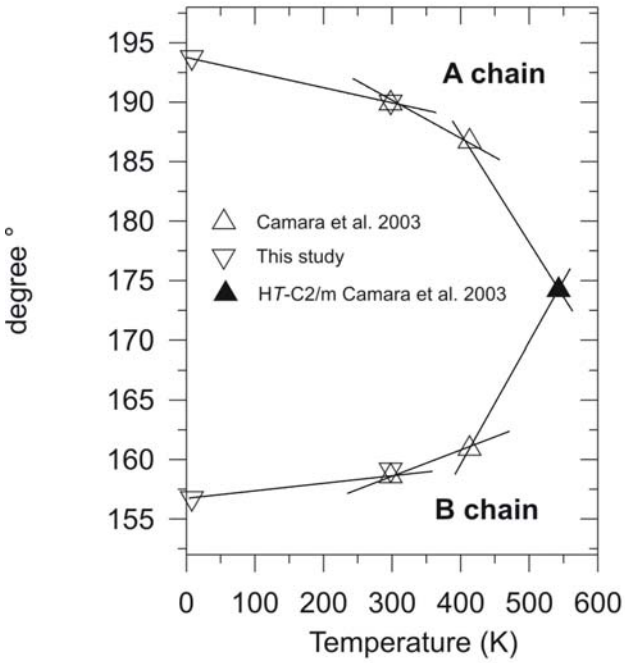

Fig. 3.3-11: Change in the O5-O6-O5 angles (A and B chains) between 8 and 573 K. Filled triangle: sample after the $P2_1/m \rightarrow C2/m$ phase transition (from Camara *et al.*, Phys. Chem. Minerals, 30, 570-581, 2003). The solid lines are drawn as a guide to the eye.

A partially deuterated amphibole with composition $^{A}Na^{B}(NaMg)^{C}Mg_5Si_8O_{22}(OH,D)_2$ was hydrothermally synthesised at 850 °C and 0.3 GPa. SEM, EPMA and X-ray powder-diffraction showed the run product to consist of a high amphibole yield (90-95 %), plus minor quartz and rare enstatite. Neutron powder-diffraction data were collected at room *T* and at 8 K using a time-of-flight diffractometer at the ROTAX instrument of the ISIS Facility of the Rutherford Appleton Laboratory, and structure refinement was carried out by the Rietveld method. The space group of the amphibole is $P2_1/m$ at both temperatures, as confirmed by the

presence of *b*-type reflections ($h+k=2n+1$). The unit-cell volume decreases less than 1 % from room *T* down to 8 K. Accurate structural positions for the hydrogen atoms were obtained and it was found than only less than 20 % of hydrogen was replaced by deuterium during the synthesis.

The O5A-O6A-O5A and O5B-O6B-O5B angles, describing the kinking of the A- and B-tetrahedral chains, are 190.0° and 159.2° at 293 K and 193.8° and 156.8° at 8 K, respectively (Fig. 3.3-11). At room *T*, the O5A-O6A-O5A and O5B-O6B-O5B angles obtained by neutron powder diffraction and SC-XRD refinement are virtually identical. At 573 K, the structure is *C*2/*m* and the double chains are equivalent and both extended, with the O5-O6-O5 angle ~ 174°.

j. *Thermoelastic and ordering behaviour in $CoMgSiO_4$ olivine: High temperature in situ neutron powder diffraction study (G.D. Gatta, in collaboration with R. Rinaldi/Perugia)*

Olivine, dominantly $(Mg,Fe)_2SiO_4$, is one of the most common constituent of the Earth's upper mantle and it is a fundamental component of igneous and metamorphic rocks of basaltic origin. Studies of the partitioning of divalent cations (*e.g.* Mg, Fe^{2+}, Co, Ni, Mn) between the two octahedral sites (M1 and M2) of the olivine structure as a function of *T*, *P* and composition yield essential information to constrain thermodynamic, petrological and geophysical properties of this important mineral. The solid solution of Mg and Fe^{2+} in the olivine structure is complete and there is virtually no ordering of the two cations between the M1 and M2 sites at room temperature, although there is a slight preference for Fe^{2+} to occupy the M1 site. Two competing forces have been suggested to determine the site partitioning in olivines: (1) preference of large cations for the M2 site and (2) strong covalent bonds of transition metals due to interactions between the *d*-orbitals with the ligands orbital of the M1 site. These two effects nearly neutralise each other in the case of Fe-Mg olivine, explaining the small degree of Fe-Mg order in this olivine. However, *in situ* neutron powder diffraction studies at high temperature on natural and synthetic Mg-Fe olivines, had revealed a tendency toward anti-order of the octahedral cations. With increasing temperature, Fe and Mg begin to disorder and then proceed towards a reverse ordering, with Fe^{2+} strongly segregating into site M2 (*i.e.* temperature has the effect of favouring force (1) with respect to force (2)).

Co^{2+} has a very different behaviour with respect to Fe^{2+} when substituted in the olivine structure. In this case force (2) is the dominat effect and in Co-Mg olivine Co has a very strong preference for the M1 site. The interesting question arising is whether also for these type of olivines increasing temperature would induce disorder and anti-order.

Neutron powder diffraction data were collected for a sample of composition $CoMgSiO_4$ at the POLARIS instrument of the ISIS Facility of the Rutherford Appleton Laboratory at 5 temperatures ranging from RT to 1000 °C. The melting point of this compound was found to be lower than 1200 °C. The degree of cation ordering was determined from direct

measurements of site occupancies in the two octahedral M sites. The refinements were very stable with no evident correlations between populations and thermal parameters in the octahedral sites. The evolution of the unit-cell volume of the $CoMgSiO_4$ with temperature is shown in Fig. 3.3-12.

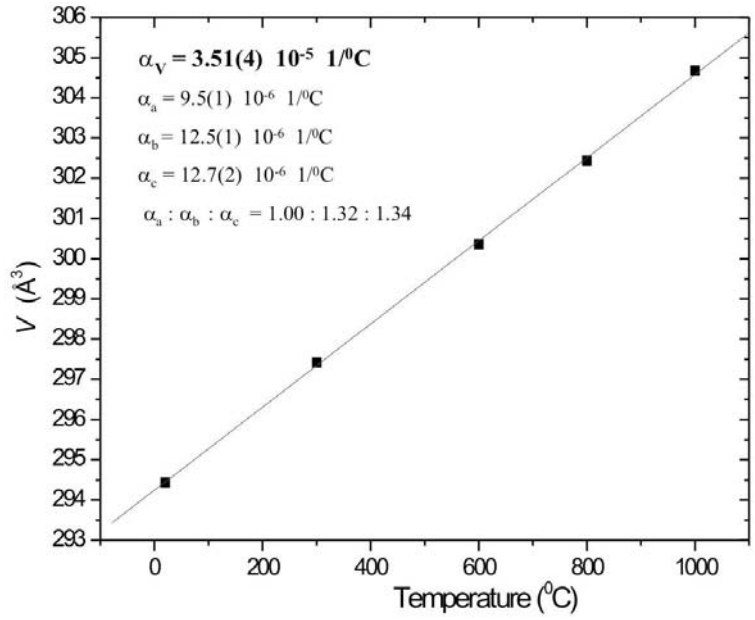

Fig. 3.3-12: Cell parameters behaviour with temperature. Volume and axial thermal expansion coefficients are reported

Axial and volume thermal expansion coefficient ($\alpha_j=l_j^{-1}\cdot\partial l_j/\partial T$, $\alpha_V=V^{-1}\cdot\partial V/\partial T$) have been calculated by weighted linear regression trough the data points at different temperatures, yielding the following values: α_a = 9.5(1)·10^{-6}, α_b = 12.5(1)·10^{-6}, α_c = 12.7(2)·10^{-6}, α_V = 3.51(4)·10^{-5} °C^{-1}. The thermal expansion of $CoMgSiO_4$, like that of Mg-Fe-olivines, is strongly anisotropic (α_a:α_b:α_c = 1.00 : 1.32 : 1.34).

Upon heating, the Co occupancy of site M1 shows an oscillatory behaviour , it decreases slightly at about 300 °C, it increases again until approximately 800 °C and it decreases once more at 1000 °C. This behaviour suggests that the Co-O covalent bonds at the M1 sites are so strong to prevent thermally induced disorder.

k. *An infrared investigation of the otavite-magnesite solid solution (F.A. Bromiley and T. Boffa Ballaran, in collaboration with M. Zhang/Cambridge)*

Infrared powder absorption spectroscopy can be used to quantitatively determine the local strains which arise when a cation is substituted for another with different size in a mineral structure. Silicate systems have been studied extensively using this technique, and it has been

shown that phase transitions are driven by a strain relaxation mechanism. This study aimed to investigate the solid solution and phase transformation mechanisms of one of the most important carbonate system [(Ca,Mg)CO_3]. The detailed configuration of the phase diagram is dependent on the nature of the order-disorder phase transition, but the difficult experimental conditions required make a precise analysis of this transition difficult. Therefore, the binary join within the magnesite ($MgCO_3$)-otavite ($CdCO_3$) system has been investigated as an analogue for the magnesite-calcite system because experiments can be carried out at significantly lower temperatures.

The samples studied have been synthesised in piston cylinder apparatus at 1GPa in the temperature range 500-800 °C for run durations of 1-120 hours. A complete, disordered solid solution, with $R\bar{3}c$ symmetry, was obtained at 800 °C, whereas ordered samples in the cadmium dolomite stability field, with $R\bar{3}$ symmetry, were obtained at intermediate compositions in the temperature range 500-650 °C.

Potassium bromide and polyethylene pellets were used as matrix materials for the measurements taken over three spectral regions; 50-350cm^{-1} (PE pellets), 350-500cm^{-1} (KBr pellets), 500-4000cm^{-1} (KBr pellets). Vibrational modes due to cations on the octahedral sites are present at the lowest frequency of the spectral regions investigated. All other vibrational bands can be assigned to vibrations of the carbonate group.

Phonon bands due to cadmium-oxygen translations (75-200cm^{-1}), and magnesium-oxygen translations (200-350cm^{-1}) were both observed in the IR spectra for samples of intermediate composition. A Lorentzian peak fitting routine was used to determine band positions for both sets of bands. Band positions for cadmium-oxygen translations remained constant as a function of composition, whereas band positions for magnesium-oxygen translations showed a decrease in wavenumber as a function of composition. This suggests that the magnesite-otavite solid solution displays a combination of one-mode and two-mode behaviour at low frequencies, which may be due to the difference in atomic weight between magnesium and cadmium atoms.

Vibrational bands in the spectral regions 350-550cm^{-1} (libration and translation of carbonate groups) and 650-900cm^{-1} (doubly degenetrate in-plane bending and out-of-plane bending of carbonate groups) vary linearly as a function of composition and no effect of order on band position is observed. In the region 1000-1800cm^{-1}, the phonon mode is due to doubly degenerate asymmetric stretching of the carbonate groups. The samples with $R\bar{3}c$ symmetry (800 °C series) show a linear shift in band position as a function of composition, whereas, samples in the cadmium dolomite stability field, with $R\bar{3}$ symmetry, show a marked increase in frequency compared to their $R\bar{3}c$ symmetry counterparts (Fig. 3.3-13). Since carbonate groups for samples with $R\bar{3}$ symmetry are slightly non-planar, as determined from Rietveld refinements, it appears that more energy is required for asymmetric stretching, with a

consequent shift in band position to higher wavenumbers with respect to the planar carbonate groups in samples with $R\bar{3}\,c$ symmetry.

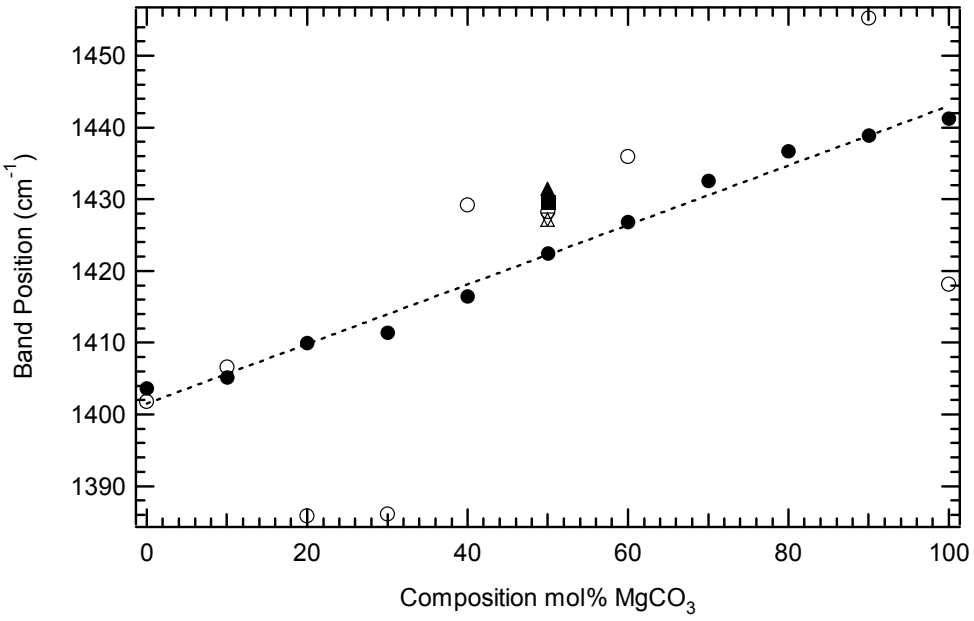

Fig. 3.3-13: Band position as a function of composition in the region 1000-1800cm^{-1}. The dashed line show a linear fit through the 800 °C series of data, given by, $\bar{\nu}$ = 1401.6 + 0.4146 mol.% $MgCO_3$. Symbols: open circle = 600 °C, 3 hrs, closed square = 600 °C, 19 hrs, open triangle = 600 °C, 86 hrs, inverted open triangle = 650 °C, 120 hrs, closed triangle = 500 °C, 96 hrs. Note that the ordered samples show an increase in wavenumber with respect to the disordered samples.

Cation substitution, or disordering causes broadening of IR vibrational bands for a given material. It is not always possible, however, to determine the line width of complex IR spectra using conventional fitting procedures. In this study an alternative method was used, which makes use of the autocorrelation function to establish average line widths for six spectral regions; 75-200cm^{-1}, 200-350cm^{-1}, 300-550cm^{-1}, 700-800cm^{-1}, 800-900cm^{-1} and 1000-1800cm^{-1}. The autocorrelation results, Δcorr, can be interpreted in terms of local strain fields present in the structure due to cation substitution and disordering.

In the low frequency region, the Δcorr values show a positive deviation from linearity as a function of composition. For samples of composition $Mg_{0.5}Cd_{0.5}CO_3$ the Δcorr values are virtually all the same, independent of the degree of order. This suggests that at a length scale of a few unit-cells the local heterogeneities within the samples due to cation substitution cannot be realised by cation ordering. In the region 800-900cm^{-1} and at a composition of $Mg_{0.5}Cd_{0.5}CO_3$, an effect of order is observed as a reduction in Δcorr values with respect to the sample with $R\bar{3}\,c$ symmetry (Fig. 3.3-14). That means that the heterogeneities around the carbonate groups and at a length scale of few Å are larger when Mg and Cd cations are

disordered among layers, probably because the carbon atoms have differently out-of-plane positions depending on what cations their oxygens are co-ordinating. The difference in Δcorr values between the ordered and disordered samples is proportional to the square of the local-order parameter, *q*, which scales linearly with the long-range order parameter, *Q*, determined by Rietveld refinement of X-ray powder diffraction data, suggesting that the ordering process is the same at both macroscopic and microscopic length scales.

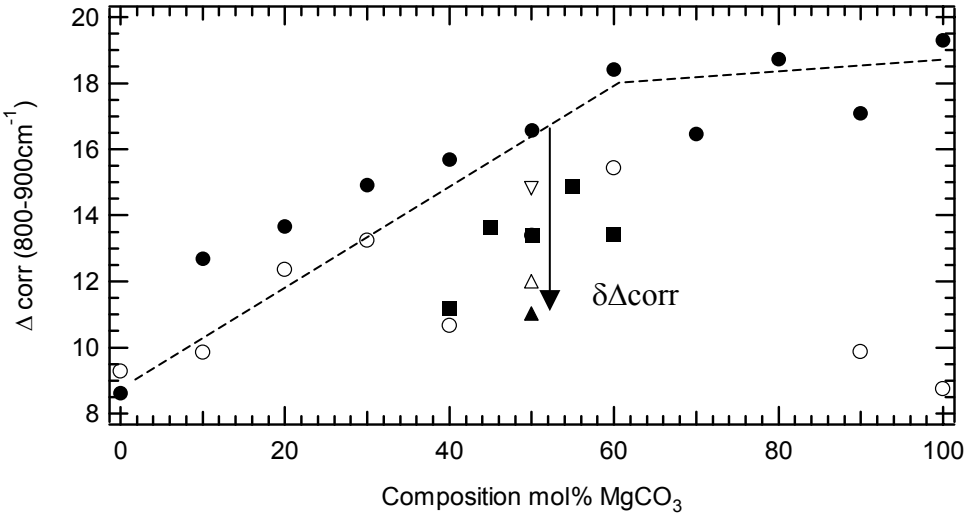

Fig. 3.3-14: Variation of Δcorr values with composition for the region 800-900cm^{-1}. Vibrations in this region are due to out-of-plane bending (ν_2) of the carbonate (CO_3) groups. Symbols: open circle = 600 °C, 3 hrs, closed square = 600 °C, 19 hrs, open triangle = 600 °C, 86 hrs, inverted open triangle = 650 °C, 120 hrs, closed triangle = 500 °C, 96 hrs. The dashed lines are a guide to the eye for the 800 °C series. Ordered samples have smaller Δcorr values than disordered ones.

I. *On the nature of Guinier-Preston zones in Johnstown orthopyroxene (F. Langenhorst and J.R. Smyth, in collaboration with H. Kroll/Münster)*

Pyroxenes are known to develop microscopic exsolution phenomena and cation ordering upon cooling in igneous host rocks. Consequently, the microstructure of pyroxenes carries substantial information on cooling parameters such as closure temperatures and cooling rates. As the cooling rate is commonly too fast to achieve thermodynamic equilibrium, pyroxenes often show stranded microstructures. The development of exsolution platelets in orthopyroxene from one to a few unit-cells in width - the so-called Guinier-Preston (GP) zones - is one such consequence of disequilibrium. GP zones lie parallel to the (100) plane of orthopyroxene and are enriched in calcium but differ structurally from monoclinic clinopyroxene. In a previous model, GP zones several unit cells wide were interpreted to possess $Pbc2_1$ symmetry and to consist of two half-unit cell layers with Wo0 and Wo50 compositions. This model assumes that the calcium cations have completely ordered in one half-unit layer of 9 Å width.

We have readdressed the question of the structure of GP zones, using transmission electron microscopy (TEM). The TEM observations have been performed on orthopyroxene from the Johnstown achondrite, containing GP zones parallel to (100) apparently a single unit cell in width (18 Å). Energy-dispersive X-ray analyses corroborate the enhanced calcium content within the GP zones but a quantitative determination of the Ca content across GP zones is impossible due to their small size.

To better constrain the structure of GP zones we therefore used electron diffraction and high-resolution TEM combined with numerical simulation. To determine the space group symmetry of GP zones and orthopyroxene host, the electron diffraction patterns have been taken along the three crystallographic axes ***a***, ***b*** and ***c***. The diffraction patterns of host orthopyroxene are fully compatible with the space group *Pbca*. However, the diffraction patterns taken from GP zones show a reduction of symmetry. Due to the limited periodicity of GP zones the electron diffraction patterns show streaks along the ***a***-axis, indicating a possible violation of the *c*-glide parallel to (010). In the (0*kl*) diffraction pattern of GP zones the *b*-glide parallel to (100) is clearly violated. These observations point to a space group with lower symmetry than the previously proposed $Pbc2_1$ symmetry.

High resolution TEM images taken along the ***c***-axis, *i.e.* in the direction of chains of SiO_4 tetrahedra, show that the GP zones are coherent with the orthopyroxene lattice but in fact are thinner than 18 Å (Fig. 3.3-15).

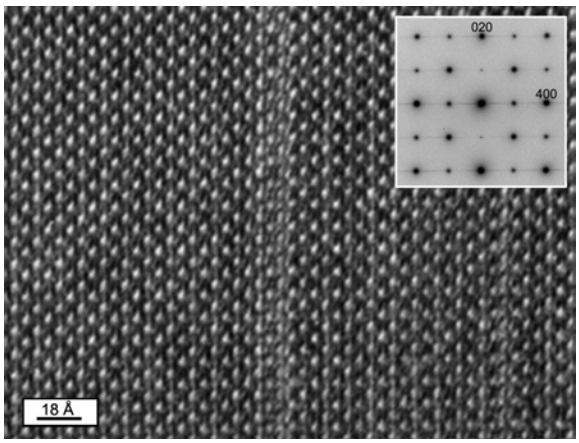

Fig. 3.3-15: (*hk*0) high-resolution TEM image of Johnstown orthopyroxene with a Guinier-Preston zone.

This observation suggests that calcium is concentrated within (100) sublayers of the unit cell. Numerical simulations of HRTEM images have been performed to test this hypothesis, employing various models for the distribution of Ca. These simulations confirm that ordering and enrichment of calcium in a coherent 9 Å layer would result in a contrast change similar to that observed. The ordering of calcium in sub-unit layers apparently results in an asymmetric distortion of the orthopyroxene lattice and a local reduction of symmetry.

m. *Ti $L_{2,3}$ electron energy loss near-edge structures of Ti_xO_y phases: Fingerprints to valence state and site geometry of titanium (E. Stoyanov and F. Langenhorst)*

Electron energy loss spectra (EELS) contain a wealth of element-specific information on the electronic and atomic structure of solids. In particular, the fine structure of ionization edges (ELNES) of transition metals is sensitive to their valence state, coordination, and site geometry. These fine structures are due mainly to covalent bonds by direct and/or indirect interactions between oxygen and transition metal atoms. To show the potential of the ELNES technique, we have carried out a series of Ti $L_{2,3}$ edge measurements on six titanium oxides (TiO, Ti_2O_3, TiO_2, Ti_3O_5, Ti_4O_7, Ti_5O_9), all containing titanium in octahedral coordination but in different distortion environments and valence states. These oxides represent a set of standards for titanium in three different valence states (Ti^{4+}, Ti^{3+}, Ti^{2+}, Ti^{4+}:Ti^{3+} ratios 3:2, 1:1, and 1:2). Their characterization is essential for the identification of titanium site location and coordination in minerals, cation ordering, and oxygen defect clustering in oxidic compounds.

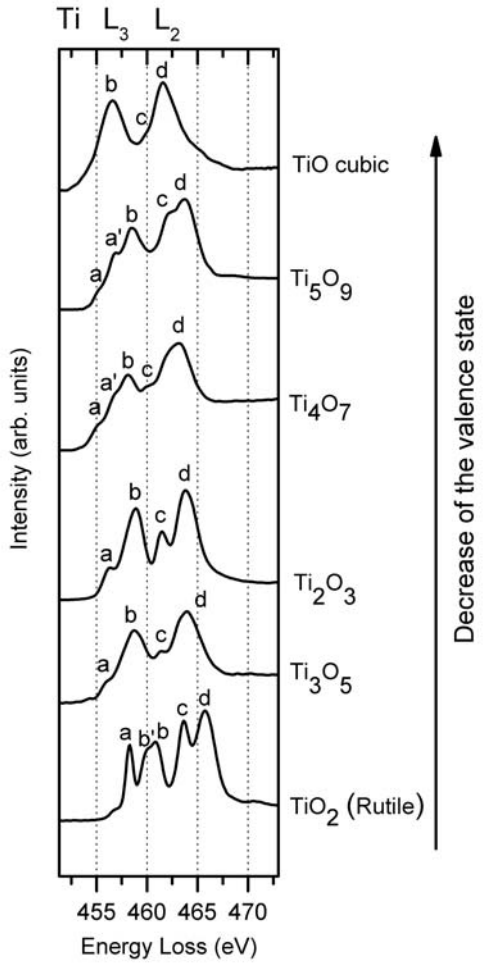

Fig. 3.3-16: EELS spectra of analyzed titanium oxides

The results of Ti $L_{2,3}$ ELNES measurements for the 6 titanium oxides are shown in Fig. 3.3-16. The spectra shift to lower energy losses with decreasing valence state of titanium. In perfect octahedral coordination the titanium *3d* orbitals split into three t_{2g} and two e_g levels. The Ti $L_{3,2}$ lines are due to transitions from the inner Ti *2p* levels to the titanium *3d* levels. The L_3 edge contains the peak *a*, which is due to transitions from the $2p_{3/2}$ Ti level to the $2t_{2g}$ molecular orbital level and the peak *b*, which is due to transitions from the $2p_{3/2}$ Ti level to the $3e_g$ molecular orbital level. In all analyzed titanium oxides (except TiO), the coordination octahedra are distorted. Ti_2O_3 shows trigonal distortion and the rest of the oxides show orthorhombic distortion. The orthorhombic distortion leads to further splitting of the t_{2g} and e_g levels, which can be seen in the spectra of rutile, Ti_4O_7, and Ti_5O_9. In the rutile spectrum the splitting of the e_g level is noticed by peaks b and b' and the observed splitting of the t_{2g} level in the Ti_4O_7 and Ti_5O_9 is labeled *a* and *a'*. In conclusion, our results demonstrate that the titanium $L_{2,3}$ ELNES spectra can be used as a sensitive fingerprint to the valence state and site geometry of titanium.

3.4 Geochemistry

A huge contribution to our understanding of the structure and geochemistry of the Earth's interior would come from knowledge of the Earth's bulk composition. The same obviously holds true for any planet. Chondritic meteorites are frequently championed as the key to terrestrial planet starting compositions. Upper mantle ratios of refractory lithophile elements – such as rare earths – and the depletion of volatile elements in the Earth indicate that the Earth formed from material that was geochemically quite similar to most chondrite meteorites. A number of significant inconsistencies exist, however, between any meteorite composition and the composition of the Earth's upper mantle. Some of these inconsistencies have been caused by the differentiation of the Earth *i.e.* partitioning of elements into the core or possibly into unsampled reservoirs of the Earth's silicate mantle. On the other hand, many differences probably reflect the fact that no meteorite composition exactly matches the bulk composition of the Earth. Experiments to understand how and under what conditions the Earth fractionated are a crucial aid in deciding between these two possibilities. This broader goal of determining the Earth's composition is a recurrent theme in many of the reports in this section.

All chondritic meterorites have bulk Mg/Si ratios that are lower than the Earth's upper mantle. Several fractionation processes could have been responsible for this. Core formation under relatively reducing conditions could have led to Si being partitioned into the Earth's core. Alternatively if significant portions of the Earth were molten during its formation, crystal fractionation of Si-rich silicate minerals into the lower mantle could have raised the Mg/Si ratio of the residual liquid, which later cooled to form the upper mantle. High pressure and temperature experiments can be used to test these possibilities and to examine if the elevated Mg/Si ratio of the upper mantle is a result of planetary fractionation processes or an artefact of the Earth's bulk composition.

The Earth's outer core contains up to 10 % of an unknown light element or mixture of elements. If we could ascertain the conditions at which core formation took place and determine the mechanism by which the fractionation from the silicate mantle occurred, we would be much closer to identifying the core's composition. The light element in the core might, for example, have aided the passage of the liquid metal though a solid silicate mantle by lowering the wetting angle between metal and silicate such that porous flow could occur. Identifying the influence of various light elements on liquid metal/silicate wetting angles might, therefore, provide a clue as to which light element is in the core. Similarly high pressures may affect the solubility of light elements in core forming metal.

a. *Redox controls on water in the primitive solar system (F. Gaillard, in collaboration with B. Scaillet and M. Pichavant/Orléans)*

Redox variations in the inner solar system are clearly indicated by the variable proportions of iron in the metallic form (Fe) over the oxidized form (FeO), as preserved in meteorites,

terrestrial planets and their satellites. The variable Fe/FeO ratios found in chondrites or predicted from conditions of core formation in terrestrial planets, reflect redox exchanges with other redox couples. A simple calculation based on the solar system abundance of the elements and combining oxygen with all potential oxygen acceptors excluding H_2 (*i.e.* SiO_2, MgO, FeO, Al_2O_3, Na_2O, K_2O, CO_2, CO…), indicates that Fe metal should only exist as a result of redox interactions between FeO and H_2. In a hydrogen-free solar system, metal Fe does not exist and O is in excess or at least, sufficiently abundant to make coexisting 100 % oxidized FeO with a gas mixture of 60-40 % of CO_2-CO ~ fO_2 =IW+1.5 at 1600 °C *i.e.* conditions that are several orders of magnitude higher than those required to saturate a chondritic or peridotitic melt in metal Fe (Fig. 3.4-1).

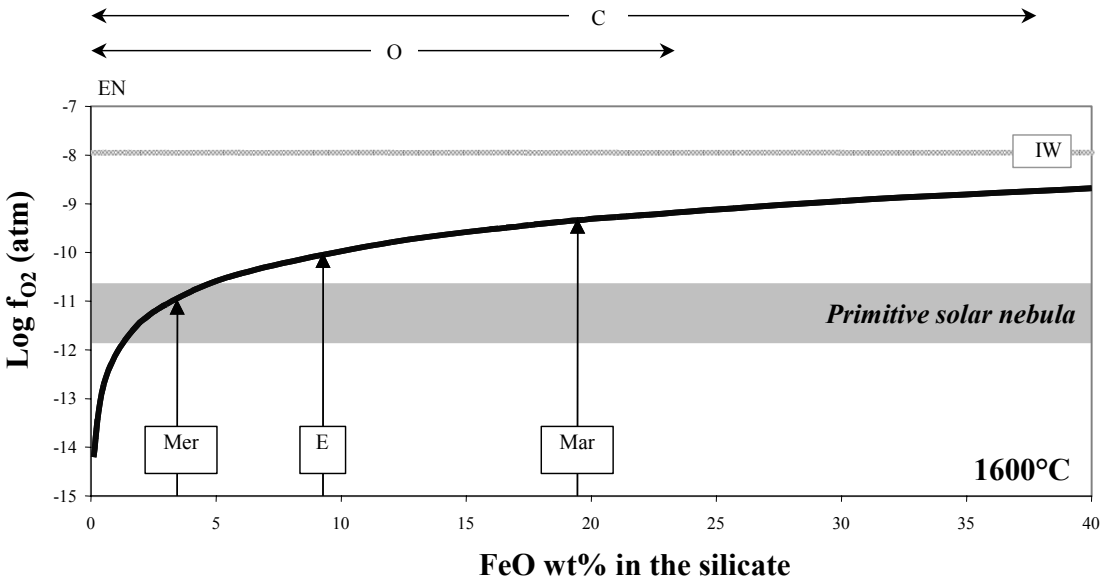

Fig. 3.4-1: Variation in the chemical potential of oxygen (fO_2) with changes in the FeO content of a molten silicate in equilibrium with metal Fe (core formation). Mer: Mercury; E: Earth; Mar: Mars. IW is the iron-wüstite redox buffer at 1600 °C. On top of the figure are shown the conditions of fO_2 encompassed by Enstatite (EN), ordinary (O) and carbonaceous (C) chondrites.

The existence of metallic Fe in the solar system seems, therefore, inexorably linked to redox exchanges between FeO and H_2. Interestingly, these redox exchanges also produce water via the hydrogen-wüsitite-iron-water (HWIW) reaction:

$$H_2 + FeO \Rightarrow Fe + H_2O \qquad \text{(HWIW)}$$

Recent studies have provided evidence that chondrites and the Earth were formed in the reducing chemical environment of the solar nebula (mainly H_2+He). However, CI chondrites, the most primitive chondrite, are completely oxidized and do not contain any metal Fe. The

reason invoked here is that although reducing enough to allow in theory Fe saturation from silicate, the primitive solar nebula exhibited a very low pressure (10^{-5} bar) at which, the communication of the redox potential from gas to silicate is extremely sluggish (several thousand of years). Therefore, the formation of Fe metal from silicate was only possible when the gas of the solar nebula was dense enough to reach pressures of ~ 10^{-2}-10^{-3} bar, which is virtually achievable by gravitational capture during planetary accretion (Fig. 3.4-2). The maximum gas pressure that a planet can concentrate by gravity is given by the hydrostatic equation and is a linear function of the pressure in the surrounding nebula, and an exponential function the size and the density of the planet. The HWIW reaction indicates that for a fixed ratio Fe/FeO (typical for each planets of the inner solar system), increasing the water content of the primary magma ocean increases the hydrogen fugacity (Fig. 3.4-2). The hydrogen fugacities buffered by HWIW are of the order of 1000 bar if the primary magma ocean contained 0.5 wt.% of water. The Earth, given its size and density, would have been able to maintain such atmospheric pressure if surrounded by a solar nebula at 10^{-5} bar. In contrast, Mercury and Mars, being much smaller, were at maximum able to retain an atmosphere of 4.10^{-2}bar, equivalent to maximum magma ocean water contents of only a few ppm.

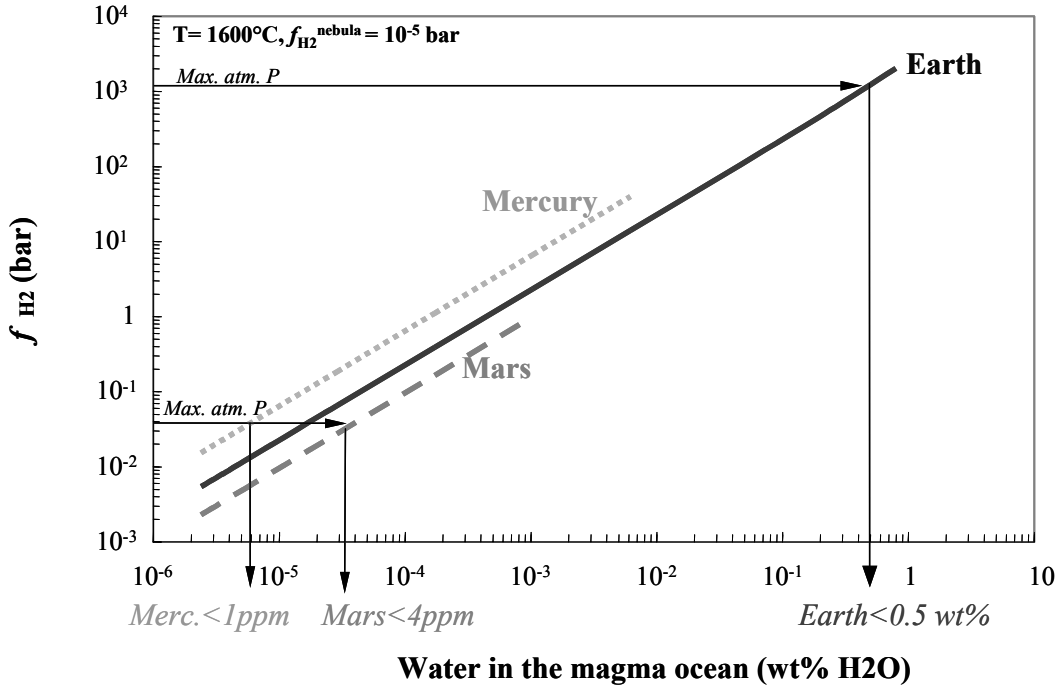

Fig. 3.4-2: Hydrogen fugacities buffered by HWIW as a function of the water content dissolved in the primitive magma ocean of Mercury, Earth and Mars. Maximum pressures attained in the atmospheres of the planets during accretion are indicated.

Whether the Earth accreted wet or not is a critical issue subject to significant controversy. A further implication of the formation of Fe by H_2 oxidation is that that the primordial water

content of the Earth could have been derive from H_2 of the solar nebula (Fig. 3.4-3). The counterintuitive consequence of this process is that reduced planetesimals and meteorites, in contrast to oxidized ones, are likely to have been the source of most of the available water in the solar system.

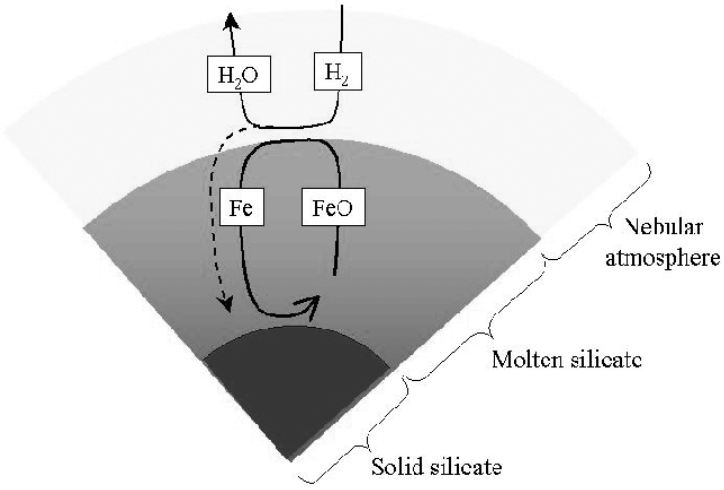

Fig. 3.4-3: Redox exchanges between the solar nebula and a molten planet. FeO is reduced into Fe by H_2. Part of the H_2O produced is dissolved in the magma ocean depending on the atmospheric pressure that the planet is capable of maintaining (see Fig. 3.4-2).

b. *Interconnectivity of liquid Fe-alloy in silicate perovskite at lower mantle conditions (H. Terasaki, D.C. Rubie, D.J. Frost and F. Langenhorst)*

An important aspect of planetary core formation is whether interconnectivity of liquid metal can occur in crystalline silicates. At the low Fe metal melt fractions that are relevant to efficient core/mantle separation, the occurrence of interconnectivity requires the dihedral angle between metal and crystals to be less than 60°. In a previous study (see Annual Report 2003) we have investigated the effect of oxygen and sulphur contents on the dihedral angle between Fe-S liquid and solid silicates (olivine and ringwoodite) up to 20 GPa. The observed dihedral angles decreased to 66° at high O and S fugacities. Shannon and Agee (Science, 280, 1059, 1998) reported that dihedral angles in mantle assemblages decrease from the 108° at upper mantle conditions to 71° at lower mantle conditions as a result of mineral phase transformations. Therefore, it may be possible for liquid metal to form an interconnected network at lower mantle conditions at high O and S fugacities. If liquid metal could have percolated through a solid lower mantle then this may help to explain the relatively rapid time scale reported for core formation.

We have investigated the effects of the FeO content of perovskite (Mg# = 0.84-1.00) on the dihedral angle up to 23.0-24.5 GPa and 2200-2223 K. This range of compositions should be

applicable to the lower mantles of both Earth and Mars, with the Martian mantle being at the more Fe-rich extreme. Experiments were performed using 1200 and 5000 tonne multianvil presses. An $Fe_{61}S_{39}$ liquid composition was employed. 10/4 and 18/8 type assemblies with $LaCrO_3$ furnaces were employed. Graphite was used as the capsule material. Experimental durations were from 5 to 7 hours. Sample textures were observed using scanning and transmitted electron microscopy. The Fe^{2+}/Fe^{3+} ratio in silicate perovskite was also measured using electron energy-loss spectroscopy combined with TEM.

Measured dihedral angles decrease (101°-79°) with increasing FeO content in the perovskite phase as shown in Fig. 3.4-4. This tendency is in good agreement with our previous dihedral angle results for olivine and ringwoodite where the increasing FeO content of the silicate was related to an increase in the oxygen fugacity and consequently an increase in the measured oxygen content of the Fe-S liquid. It is the increasing oxygen content of the liquid which most likely reduces the dihedral angle. In contrast to olivine and ringwoodite experiments, however, as the FeO content of perovskite is increased the concentration of Fe in the Fe-S liquid also increases. As it is unlikely that S is lost from the liquid the only explanation is that FeO in the silicates is being reduced during the experiments. Such a phenomena has only been observed in experiments involving silicate perovskite. In experiments on olivine or ringwoodite generally the opposite effect is observed *i.e.* Fe in the liquid is oxidised during the experiment and the FeO content of the silicates increases. The Fe^{3+} concentration in perovskite, measured using electron energy loss spectroscopy, is relatively high (> 20 % of total Fe) and increases with perovskite FeO content. One possible explanation is that the high affinity of perovskite for Fe^{3+} drives a disproportionation reaction where Fe^{3+} is obtained from the reduction of FeO to metallic Fe. Thus disproportionation may increase the Fe content of the Fe-S liquid.

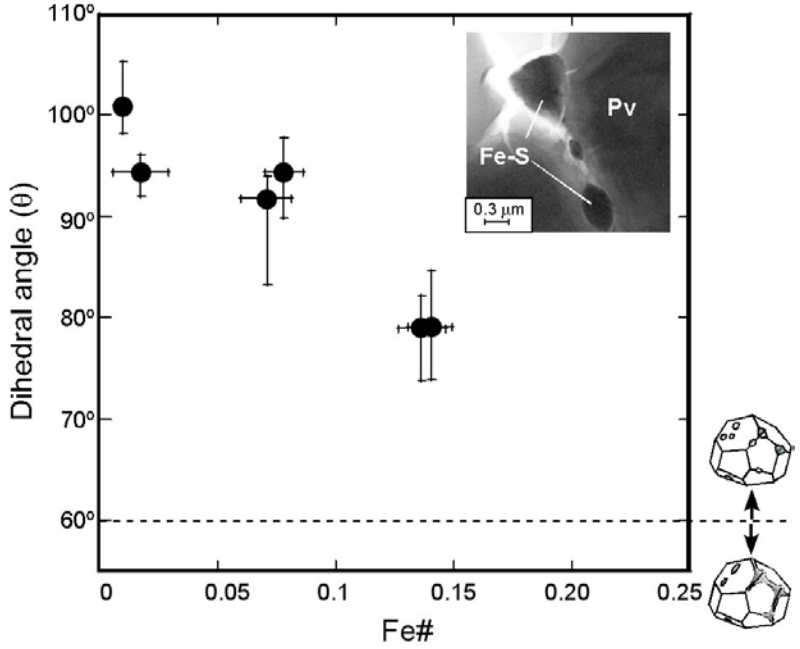

Fig. 3.4-4: Dihedral angles between silicate perovskite and Fe-S melt (initially $Fe_{61}S_{39}$) as a function of the perovskite Fe# (=FeO/{FeO+MgO} as a molar ratio). The dashed line is the wetting boundary of 60°. The inset is a TEM image of Fe-S melt pockets from the experiment at 23 GPa and 2223 K.

There is no significant difference between dihedral angles observed in perovskite assemblages and olivine and ringwoodite assemblages. The dihedral angle is, therefore, still higher than the critical value of 60° at conditions compatible with the top of the Earth's lower mantle. The base of the Martian mantle is at approximately 25 GPa so our results suggest that dihedral angles will be higher than 60° over the entire range of conditions encompassed by the Martian mantle.

c. *The influence of Si on dihedral angles between liquid Fe-Si alloy and forsterite (U. Mann, D.J. Frost and D.C. Rubie)*

The silicon concentration of the Earth's mantle is significantly lower than in chondritic meteorites and a good explanation for this would be that Si was extracted into the core during accretion. Si readily forms alloys with Fe and is suitably abundant to explain the complete outer core apparent density deficit of 10 %. However, Si extraction into core-forming liquids would have required quite reducing conditions, conditions that would have also significantly depleted the silicate phases of the Earth's mantle in iron and nickel. A way around this apparent redox paradox would be if accretion occurred at variable redox conditions. If quite reducing conditions prevailed during early core formation then significant Si could have been extracted into the core along with much of the mantle's Fe and Ni. During later stages of accretion of more oxidized material Si would not be extracted into the core and Fe and Ni would remain in the Earth's mantle. Such a process of early extraction of Fe-Si liquids would have been aided if the solubility of Si influences the wetting characteristics of core-forming liquids in a solid silicate assemblage. Specifically, if the creation of an Fe-Si alloy lowers the dihedral angle between Fe liquid and silicate minerals to below the critical connection boundary of 60° then this would have allowed porous flow to assist early core formation. In order to investigate the effects of Si on the dihedral angles between Fe-rich liquid and a silicate assemblage, in this instance forsterite, we have performed a series of high-pressure experiments at 5 GPa and 1750-1850 °C.

High-pressure experiments were carried out using the 500 tonne multianvil apparatus and an 18/11 assembly. Graphite capsules were employed with some attempts made using MgO capsules. $Fe_{91}Si_9$ and $Fe_{83}Si_{17}$ alloys were used for experiments on Si in conjunction with forsterite. Experiments were performed for between 7 and 72 hours. Imaging and chemical analyses were carried out using a SEM/EDX and an electron microprobe. In initial experiments where Fe-bearing silicates were employed the low redox conditions resulted in the formation of tiny metallic Fe droplets that pinned grain boundaries and inhibited textural equilibration. In subsequent experiments forsterite was used and run times of up to 72 hours were employed to ensure that an equilibrated texture was achieved. In experiments in MgO capsules oxidation of Si metal occurred over the time scales of the experiments. In graphite capsules this oxidation was minimized except at the highest temperatures (1850 °C) where Si was also lost from the metal phase.

The texture of a typical experiment is shown in Fig. 3.4-5. In normal back-scattered electron images forsterite grain boundaries cannot be seen, the dark lines in Fig. 3.4-5a are only cracks. Orientation contrast (OC) images, however, clearly show Fe-Si alloys at well-equilibrated forsterite triple junctions. True dihedral angles between forsterite and the Fe-rich liquid, determined from numerous apparent dihedral angle measurements, are 112° for $Fe_{91}Si_9$ and 107° for $Fe_{83}Si_{17}$. There is clearly very little effect of Si on interfacial energies between liquid Fe and forsterite at these conditions. Porous flow of core forming liquid through the solid silicate mantles of early relatively reduced planetary bodies is therefore unlikely.

a) **b)**

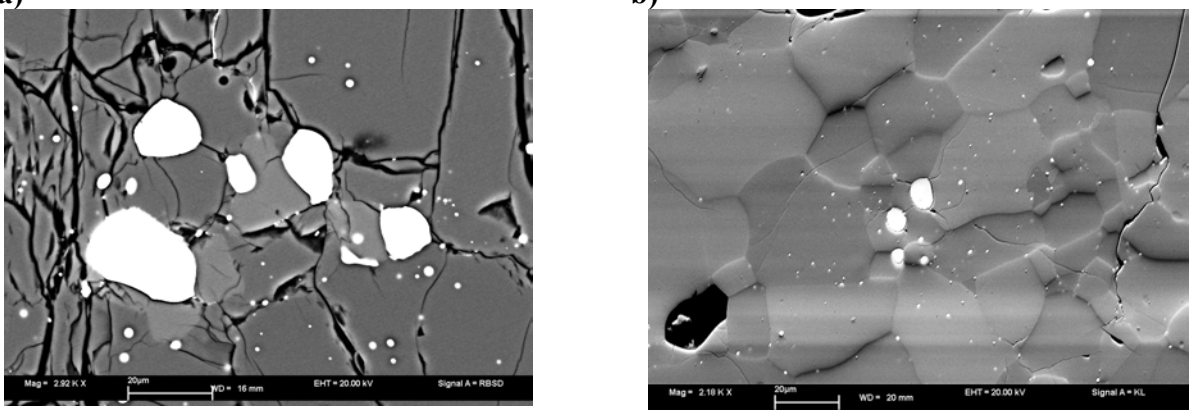

Fig. 3.4-5: **a)** Sample textures from back-scattered electron images of forsterite with Fe-Si melt pockets at 5 GPa and 1750 °C. K. Some lighter gains of enstatite can be seen adjacent to some melt pockets. **b)** Orientation contrast (OC) image of Fe-Si metal at well equilibrated forsterite grain boundaries.

d. *Oxygen partitioning between magnesiowüstite and liquid Fe-rich metal at high pressure and high temperature (Y. Asahara, D.J. Frost and D.C. Rubie)*

Oxygen is a candidate for being a light element in the Earth's core. The phase diagram of the Fe-FeO system has been investigated up to 16 GPa but the high temperature portion of this diagram is poorly determined. There is immiscibility between Fe and FeO-rich liquids, which is temperature dependent. Rapid exsolution of FeO from liquid Fe occurs during quenching, making the interpretation of the quenched metal FeO contents very difficult. In this study, we are investigating the partitioning behaviour of oxygen in the Fe-FeO-MgO system in order to understand oxygen solubility in molten iron at high pressures and temperatures.

Oxygen partitioning experiments have been conducted at 15-24 GPa and 2200-2900 °C with a multianvil apparatus. The starting material was a mixture of Fe metal powder and Fe_2O_3 oxide powder with a composition that is 95 wt.% Fe- 5 wt.% O. We used MgO single crystals as sample containers. Temperatures were monitored with a W3%Re-W25%Re thermocouple in experiments below 2400 °C, and above 2400 °C, temperature was estimated using a

temperature-power relation. Figure 3.4-6 shows a backscattered electron image of a representative run product at 24 GPa and 2900 °C. Quenched liquids consisted of O-rich blobs and dendrites in an Fe-rich matrix. During the experiment FeO from the metal liquid reacts with the MgO capsule to produce a magnesiowüstite rim on the capsule wall. Chemical analyses were conducted on each of the phases, *i.e.*, blobs and matrix and the magnesiowüstite at the interface with the metallic liquid, using an electron microprobe. The fractions of the FeO-rich blobs and matrix were determined from backscattered electron images using the image analysis software Image J. We assumed the area fractions of the blobs and the matrix are proportional to their respective volume fractions. The composition of the bulk liquid metal was estimated by integrating the compositions of the blobs and the matrix metal, based on their volume fractions.

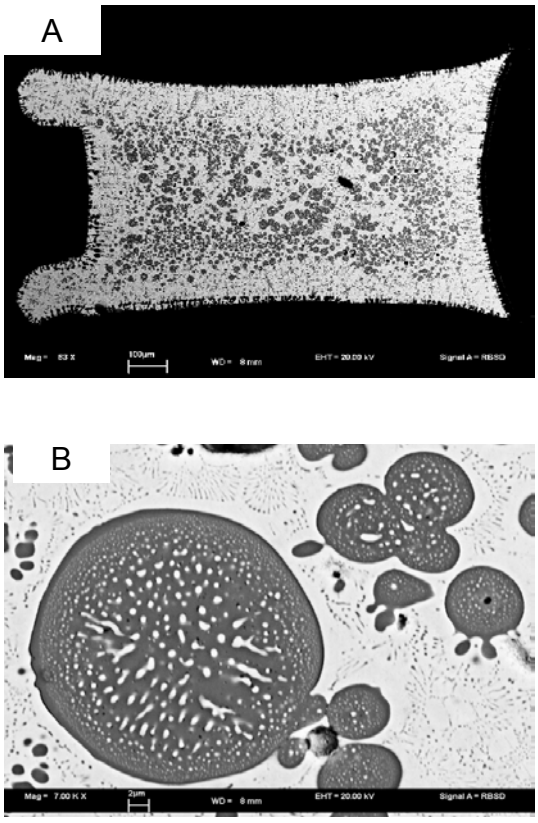

Fig. 3.4-6: backscattered electron image of a run product at 24 GPa and 2900 °C: **A:** an entire image of a quenched metallic liquid; **B:** an expanded image of O-rich blobs.

Our preliminary results indicate that the partition coefficient, Kd (= $X^{met}_{O}X^{met}_{Fe}/X^{mw}_{FeO}$; where X^{met}_{O}, X^{met}_{Fe}, X^{mw}_{FeO} are the mole fractions of oxygen in metal, Fe in metal and FeO in magnesiowüstite respectively), may increase with both increasing pressure and temperature (Fig. 3.4-7). The pressure effect seems to be inconsistent with previous studies on oxygen partitioning between magnesiowüstite and liquid Fe-Ni alloy (O´Neill *et al.*, JGR, 103, B6, 12239, 1998; Rubie *et al.*, Nature, 2473, 2004). However, previous phase diagram studies on the Fe-FeO system have suggested that oxygen solubility in liquid iron increases with increasing pressure and the present results are consistent with these studies. The compositional difference might cause the different pressure effect. Differences might also be

due to the higher oxygen fugacity employed in this study. Though more experiments over a wider pressure range are required to clarify the pressure effect on the oxygen solubility of molten iron, the present results might suggest that effects of pressure are different depending on the activity of FeO in molten iron and in molten Fe-Ni alloy, or that *Kd* varies as a function of the oxygen content of the metal.

a)

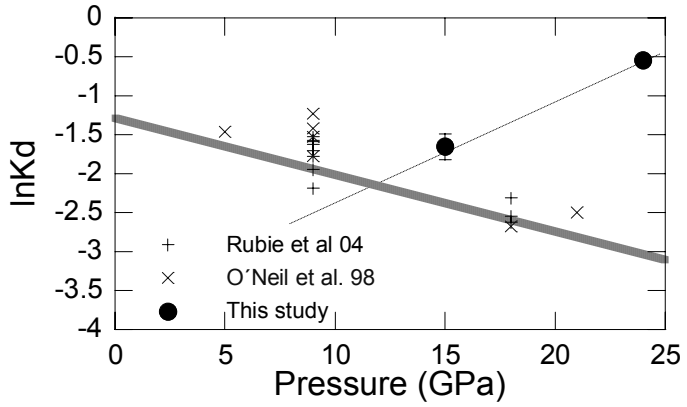

b)

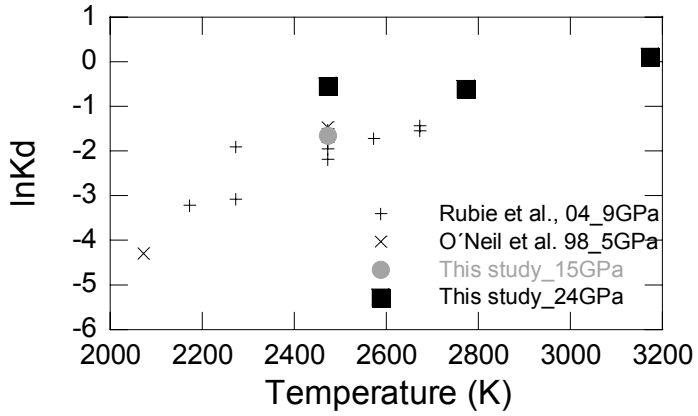

Fig. 3.4-7: (a) Pressure dependence of ln *Kd* at 2473 K: This study was performed in the Fe-FeO-MgO system while those of Rubie *et al.* (2004) and O´Neill *et al.* (1998) were perfromed in the Fe-Ni-FeO-MgO system. The grey bold line and the dashed line show the pressure dependence of ln *Kd* in the Fe-Ni-MgO system, and in the Fe-FeO-MgO system, respectively. (b) The temperature dependence of ln *Kd* at various pressures.

e. *Iron-magnesium alloying at conditions of Earth's core (L.S. Dubrovinsky and N.A. Dubrovinskaia, in collaboration with W.A. Crichton/Grenoble and I. Abrikosov/Linköping)*

The composition of the Earth's outer core is a crucial geochemical parameter for understanding the evolution and current dynamics of our planet. Since it was recognized that the liquid metallic outer core is about 10 % less dense than pure iron, different elements lighter than iron, including Si, S, O, C, and H, have been proposed as possible components in Earth's core. A combination of experimental, theoretical and geochemical considerations, however, suggests that it is unlikely that any one of these elements accounts for the entire density deficit.

In order to be considered as an important component of Earth's outer core, an element lighter than iron must be geochemically abundant, must alloy readily with iron, and must partition preferably into liquid rather than solid iron. Magnesium is among the lightest of all the metals, and also the fourth most abundant element on Earth. The complete Mg-Fe phase diagram has not yet been determined. At ambient pressure the maximum solid solubility of Fe in Mg is 0.00041 at.% Fe, and the Mg concentration at the eutectic point is estimated to be less than 0.008 at.%. Below 1273 K the solubility of Mg in Fe is below the detection limit, while the maximum solid solubility of Mg in δ-Fe is approximately 0.25 at.% Mg at the monotectic temperature. There is clear evidence that magnesium and iron do not mix in the liquid state at ambient pressure.

We have demonstrated in experiments performed in a large-volume apparatus that at moderate pressure of about 20 GPa more than 4 at.% of magnesium can dissolve in molten iron. Moreover, theoretical calculations predict that the mixing enthalpy of disordered Fe-rich hexagonal close packed (*hcp*) Fe-Mg alloys changes sign at about 100 GPa. This means that already at zero temperature there is a transition from the tendency towards phase separation between Fe and Mg at low pressure to the tendency towards alloying at higher pressure. With increasing temperature the tendency towards alloying increases further due to the entropy contribution.

In order to check these theoretical predictions, we tested if Fe- 4.1 at.% Mg alloy synthesized in a multianvil experiment at 20 GPa will be stable at conditions of Earth's core. At ambient conditions Fe- 4.1 at.% Mg alloy has a body-centered cubic (bcc) structure but under compression in a NaCl or MgO pressure medium at 10 to 13 GPa it transforms to a new phase with an hcp structure (Fig. 3.4-5). No further transformation was observed on compression to 135(5) GPa at ambient temperature. Laser-heating of the Fe- 4.1 at.% Mg alloy in NaCl pressure medium at 125(5) GPa and 3200 (200) K does not affect the diffraction pattern of hcp-structured alloy (Fig. 3.4-8) and no sign of decomposition or chemical reaction was detected in the material quenched to ambient conditions.

Metal alloying experiments in the diamond anvil cell are difficult to perform – external electrical heating does not supply high enough temperatures, while laser heating cannot provide a homogeneous heating environment for a mixture of metals at high pressures. We heated a thin layer of a magnesium foil internally by attaching it to iron electrodes compressed within either a MgO or NaCl pressure medium. By slowly increasing the electrical current passing through the magnesium foil, we first melted the magnesium and then by increasing the temperature further the iron was also melted and the electrical connection was eventually broken. Temperatures were measured spectroradiometrically, as in laser-heating experiments. The materials were kept at the highest temperatures reached for between 20 seconds and one minute. After quenched to ambient conditions, the samples were polished and studied with SEM and X-ray microprobe. Unfortunately, in up to a dozen experiments the samples were either lost or droplets of the molten metal were too small for

quantitative analysis and consequently only a few of the samples were acceptable for further study. At 25(2) GPa and 2300(100) °C we found that 4.2(5) at.% Mg dissolved in the liquid iron, in agreement with results of multianvil experiments. Figure 3.4-9 shows a backscattering electron image of a metallic droplet of about 3.5 μm in diameter found in the quenched sample after the experiment at 89(3) GPa and 3400(200) °C. On average, the droplet contains 7.8(5) at.% Mg. Note that the droplet contains small exsolved blobs in the quenched liquid metal, and the region around the margin is free of these blobs. This observation suggests that on quenching the margin crystallized first and became enriched with iron as magnesium preferably partitioned into the central liquid region. At conditions close to the Earth's core-mantle boundary we found that more than 10 at.% Mg could be dissolve in liquid iron.

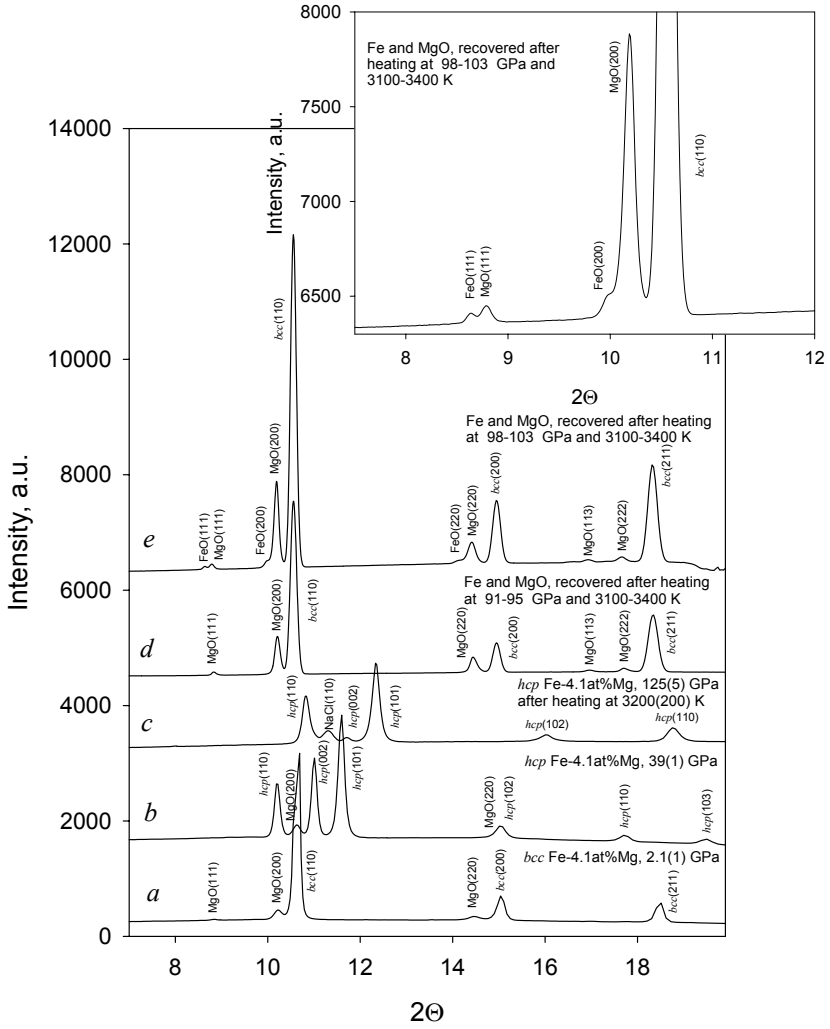

Fig. 3.4-8: Diffraction patterns collected on compression of Fe-4.1 at.% Mg alloy (a) compressed in a MgO pressure medium at room temperature and 2.1(1) GPa and (b) 39(1) GPa. (c) Fe-4.1 at.%. Mg alloy in a NaCl pressure medium after heating to 3200(2)K at 125(5) GPa. (d) a pure iron and MgO mixture after heating to 3100-3400 K at 91-95 GPa and (e) a similar assemblage heated to 3100-3400 K at 98-103 GPa. Insert shows enlarge portion of the curve (e). bcc and hcp denote the cubic body centred and hexagonal closed packed structured phases of pure iron or iron-magnesium alloy.

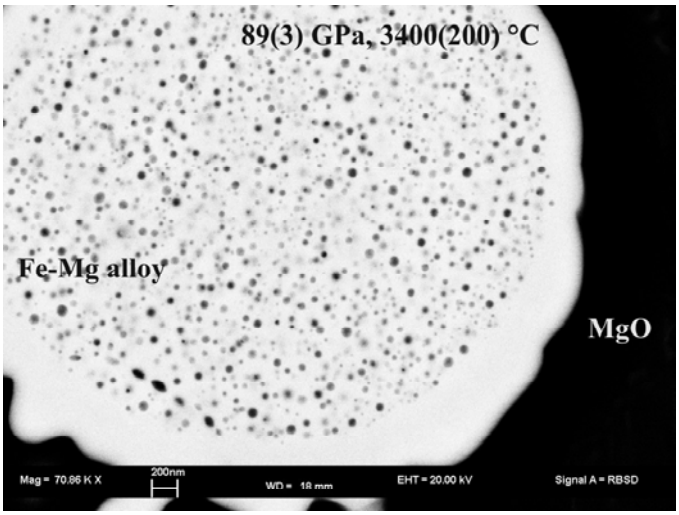

Fig. 3.4-9: Back-scattering electron image of the metal droplet in the sample recovered after experiment in internally electrically heated diamond anvil cell at 89(3) GPa and 3400(200) °C. In average, droplet contains 7.8(5) at.% Mg.

f. *Ab initio high-pressure alloying of iron and potassium: Implications for the Earth's core (K.K.M. Lee and R. Jeanloz/Berkley; G. Steinle-Neumann)*

The possible presence of potassium in the Earth's core is an old debate stemming from discrepant values of K/U (potassium/uranium) ratios as measured in chondrites and terrestrial rocks. The radioactive decay of the long-lived radioactive isotope ^{40}K (half-life ~ 1.25 billion years) in the core could be an important source of energy for the geodynamo and mantle dynamics.

Here we test experimental results that suggest iron (Fe) can alloy with K at sufficiently high pressures (*i.e.*, above the pressure-induced s $\rightarrow$ d electronic transition). To verify the plausibility of the formation of an Fe-K alloy, we have used the Vienna *ab-initio* simulation package (VASP), a density functional theory based method, to evaluate the ground-state energetics of hcp Fe-K alloy supercells with varying K abundance and position *i.e.* substituted for Fe, interstitial octachedral, or interstitial tetrahedral. We used supercells to study substitution and interstitial behaviour. A potassium atom was substituted on an hcp lattice site with 32, 48, and 96 Fe atoms over a wide compressional range, and incorporated interstitially on the tetrahedral and octahedral sites for the 96 atom supercell at two volumes, corresponding to ambient pressure and at a compression of $V/V_0 = 0.7$. We found that substitution is energetically favored at both volumes, with the energy difference increasing with compression. Consequently we focused on the substitutional incorporation mechanism in the supercells as discussed above.

Using these computations we can confirm that K and Fe can form an alloy at high pressure and the alloy is energetically favored over the pure elements. In agreement with previous

high-pressure diamond anvil cell experiments we find that the incorporation of K into Fe causes the hcp structure to expand nonlinearly with pressure and concentration. The resulting energy-volume relations have been fit with a third-order finite-strain expression (Birch-Murnaghan equation of state) from which equation of state parameters are obtained. We can then use the volume deviations given by the equations of state of these hcp potassium-iron alloys from the pure hcp iron equation of state to constrain the potassium content in the experiments (Fig. 3.4-10).

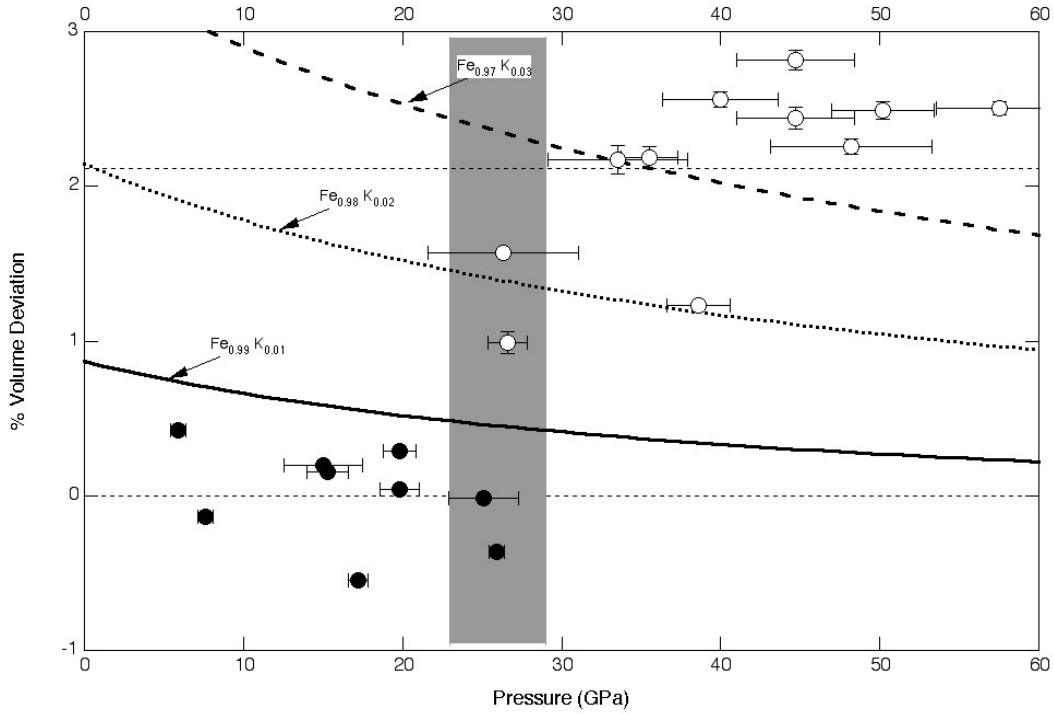

Fig. 3.4-10: Percent volume difference, 100*(V($Fe_{(1-x)}K_x$)-V(Fe))/V(Fe), vs. pressure. Curves are labeled for the different K concentrations: $Fe_{0.99}K_{0.01}$ ($Fe_{95}K_1$, solid), $Fe_{0.98}K_{0.02}$ ($Fe_{48}K_1$, dotted), $Fe_{0.97}K_{0.03}$ ($Fe_{32}K_1$, dashed). Filled (empty) circles show experimental data for unalloyed (alloyed) $Fe_{(1-x)}K_x$ [*Lee and Jeanloz*, 2003]. The bold vertical shaded area centered at 26 (± 3) GPa indicates the empirical alloying pressure.

g. *The influence of pressure and temperature on the metal/silicate partition behaviour of Ni and Co: Implications for planetary differentiation processes (P. Kegler and H. Palme/Köln; A. Holzheid/Münster, D.C. Rubie and D.J. Frost)*

The formation of an iron-rich metallic core is one of the most significant events in the history of the terrestrial planets. An important key for understanding core formation processes in planetary bodies is precise knowledge of the partitioning behaviour of Ni and Co between liquid metal and silicate at elevated temperatures and pressures. In recent years a number of studies have focussed on this topic. There are, however, quite extreme variations in the experimentally determined metal/silicate partition coefficients ($D^{met/sil}$) for these metals. In

order to clarify these variations we have undertaken a reinvestigation of the metal/silicate partitioning behaviour of Ni and Co at high pressures and high temperatures.

Partition coefficients were experimentally investigated at pressures between 1 atm. and 25 GPa and at temperatures between 1300 and 2300 °C. The experiments were performed using vertical gas mixing furnaces at the University of Köln (1 atm), piston cylinder apparatus at the University of Münster and the Bayerisches Geoinstitut (0.3-3.5 GPa), and multianvil presses at the Bayerisches Geoinstitut (3.5-25 GPa). In all experiments $Fe_{54}Ni_{29}Co_{17}$ alloys were equilibrated with silicate liquids of basaltic composition. At lower pressures and temperatures (*i.e.* 1 atm - 2.5 GPa, 1300-1440 °C) the silicate starting material was inserted into crucibles made of the alloy of interest. Liquid silicate coexisted with solid alloy in these experiments. Single crystal MgO crucibles were used as containers for the silicate and metal phases at pressures above 2.5 GPa at temperatures between 1460 and 2300 °C where liquid silicate equilibrated with liquid metal (Fig. 3.4-11). The silicate and metal phases in all experimental charges were analyzed using an electron microprobe.

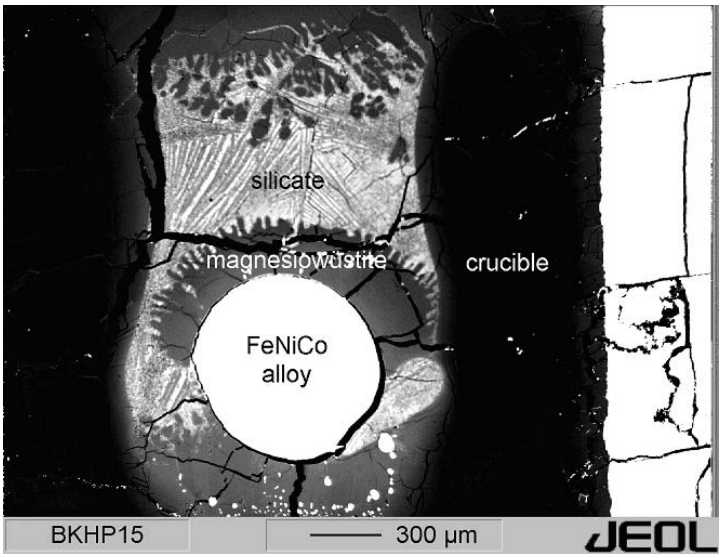

Fig. 3.4-11: A back-scattered electron image of a high-pressure run product (2000 °C, 10 GPa, 35 minutes run duration). During the experiment a rim of magnesiowüstite is formed by the reaction of MgO from the capsule with Fe from the silicate and alloy.

Preliminary results indicate two pressure regimes for the Ni-Fe and Co-Fe exchange partition coefficients, $K_D^{Ni\text{-}Fe}$ and $K_D^{Co\text{-}Fe}$. The oxygen fugacity independent exchange partition coefficient $K_D^{M\text{-}Fe}$ (M: Ni or Co) is defined as:

$$K_D^{M-Fe} = \frac{D_M^{met-sil}}{D_{Fe}^{met-sil}}$$

At pressures below about 5 GPa the pressure and temperature dependences of $K_D^{Ni\text{-}Fe}$ and $K_D^{Co\text{-}Fe}$ are more pronounced than at pressures above 5 GPa (Fig. 3.4-12). A possible reason

for this change is a change in the coordination number of Ni and Co in silicate melts at about the same pressure. As a consequence of the pressure and temperature dependences $K_D^{Ni\text{-}Fe}$ and $K_D^{Co\text{-}Fe}$ cannot be regressed with a single linear fit as assumed by Li and Agee (Nature, 381, 686, 1996), who predicted a crossover of the K_D's for Ni and Co at a pressure of approximately 30 GPa. Using the pressure dependences determined from the data shown in Fig. 3.4-12 this crossover will not occur within the pressure regime of the Earth's mantle. This has important consequences for models of core formation and the accretion history of the Earth as it implies that the broadly chondritic Ni/Co ratio of the Earth's mantle is not an artefact of high-pressure core/mantle equilibration. Possible explanations of the present Ni and Co concentrations in the Earth's mantle could be inhomogeneous accretion (a change in the oxidation state of accreting material with time) or inefficient core formation (oxidized remnants of core forming metal in the mantle).

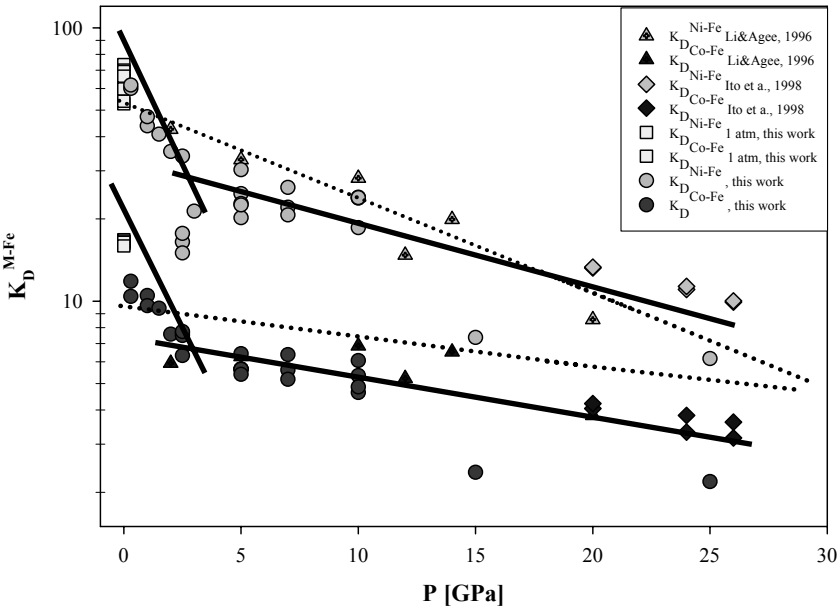

Fig. 3.4-12: $K_D^{Ni\text{-}Fe}$ and $K_D^{Co\text{-}Fe}$ as a function of pressure. All data are recalculated to 2000 °C using the experimentally determined temperature dependence. The dotted lines show the pressure dependence assumed by Li & Agee (1996), the solid lines are the pressure dependences of this study. The data of Li & Agee and Ito *et al.* (AGU Monograph, 101, 215, 1998) are included in these regressions.

h. *Element partition coefficients between metallic liquid and silicate liquid at high pressures obtained from laser heated diamond anvil cell experiments (Y. Asahara, L.S. Dubrovinsky, D.C. Rubie, F. Langenhorst and D.J. Frost, in collaboration with E. Ohtani and T. Kondo/ Tohoku)*

The aim of this study is to clarify the partitioning behaviour of siderophile and light elements between metallic and silicate liquids up to 60 GPa. It has been suggested that moderately

siderophile element abundances (*e.g.*, Ni, Co) in Earth's upper mantle were established by liquid metal-liquid silicate equilibrium at the base of a terrestrial magma ocean at depths in the range 700-1500 km corresponding to pressures of 30-60 GPa. In order to evaluate the importance of high-pressure core mantle equilibration, it is crucial to perform partitioning experiments in the range 30-60 GPa where currently there is still relatively little experimental data. Here we report the preliminary results of melting experiments on a carbonaceous chondrite composition using a laser-heated diamond anvil cell.

A powdered sample of the Allende meteorite, mixed with metallic Fe (weight ratio 7:3), was sintered at 20 GPa and 1600 °C for 1 hour using a multianvil press. A pellet with a thickness of 30 μm was made from the recovered sample and used as a starting material for laser heated diamond anvil cell experiments. Argon was used as the pressure medium. We conducted melting experiments at 26, 40, and 60 GPa, and temperatures in the range 2300-3000 °C. A sample recovered after the experiment at 26 GPa and 2400 °C is shown in Fig. 3.4-13. Metallic spherules large enough for microprobe analysis were not observed in run products from experiments performed at 40 and 60 GPa. Electron microprobe analysis could be conducted, however, on a sample recovered from 26 GPa.

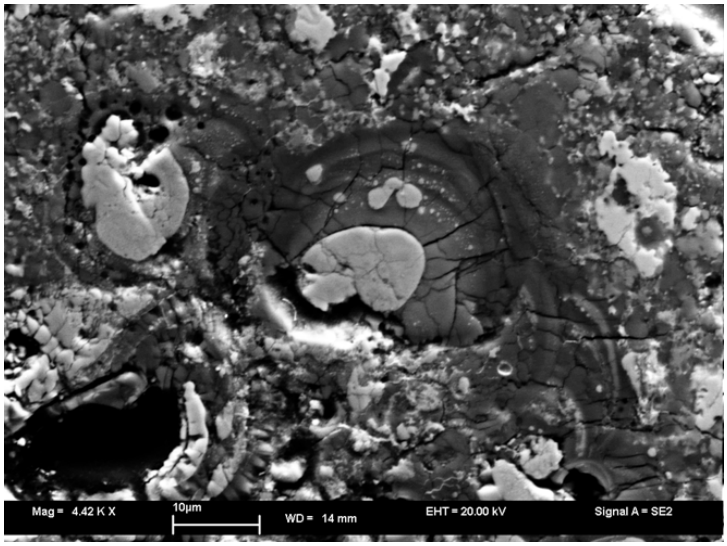

Fig. 3.4-13: Secondary electron image of a run product recovered from 26 GPa and 2400 °C: The central region was melted using the laser, which now consists of quenched silicate liquid and metallic spherules.

Exchange partition coefficients ($Kd(i/Fe)^{\text{metal liq. /silicate liq}}$) obtained from this experiment are shown in Fig. 3.4-14 [$Kd(i/Fe)^{A/B} = ([X_i]^A/[X_{Fe}]^B)/([X_i]^A/[X_{Fe}]^B)$, where $[Xi]^A$ is the mole fraction of element, i, in phase A, i = S, Ni, Co, O]. The partition coefficients obtained using the electron microprobe are in reasonable agreement with similar results obtained on Allende meteorite at similar conditions using a multianvil apparatus (Agee *et al.*, JGR, 100, B9, 17725, 1995; Asahara *et al.*, PEPI, 143, 421, 2004).

We also performed chemical analyses of the recovered sample using a TEM. Heterogeneity in the sample, however, complicated the determination of the average melt composition. The region of quenched silicate liquid indicated in Fig. 3.4-13 actually consists of majorite- and magnesiowüstite-quench crystals that are too large for an average composition, representative of the bulk silicate liquid, to be obtained. Experiments in simpler systems may well be more suitable for diamond anvil cell partitioning experiments that are to be analyzed using a TEM.

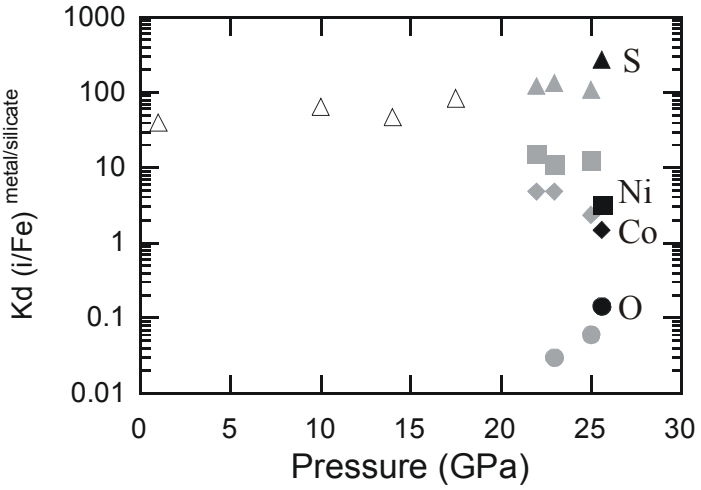

Fig. 3.4-14: Partition coefficients between metallic liquid and silicate liquid as a function of pressure; open triangles (△), and open squares (□), are partition coefficients for S and Ni reported by Agee *et al.* (1995); solid triangles (▲), and solid squares (■), solid diamonds (♦), solid circles (●) are partition coefficients for S, Ni, Co, and O respectively from multianvil experiments reported in Asahara *et al.* (2004) (grey), and this study (black).

i. *Melting relations and element partitioning in peridotite and chondrite compositions at lower mantle conditions (C. Liebske, D.J. Frost and D.C. Rubie)*

Knowledge of the melting relations of typical bulk mantle or potentially primordial Earth compositions, such as peridotites and chondrites, is essential in order to test the likelihood of early large-scale chemical differentiation in a global magma ocean. We have performed a series of high-pressure melting experiments at 25-26 GPa and 2100-2300 °C on synthetic peridotite and chondrite compositions with varying Mg/Si and Fe/Mg ratios using a multianvil apparatus. Mg/Si ratios in the starting materials varied, at constant Fe/Mg ratio, from peridotitic (molar Mg/Si =1.26) over CI chondritic (Mg/Si =1.05) to a composition corresponding to enstatite chondrites (EC, Mg/Si= 0.80). Peridotite and CI-chondrite-like materials have also been studied with variable Fe/Mg ratios.

It is clear from the recovered experimental charges that thermal gradients, which are unavoidable in high-pressure multianvil experiments, led to the segregation of the silicate

melt to the hottest part of the sample and the creation of zones of solid phases. It is believed that these zones broadly reflect the crystallisation sequence with decreasing temperature down the thermal gradient. At ~ 26 GPa, we observe a change in crystallisation sequence from ferropericlase (Fp) as the first crystallising liquidus phase followed down temperature by Fp plus Mg-silicate perovskite (MgPv) (abbreviated as Liq-[Fp]-[Fp+MgPv]) in the peridotite compositions to Liq – [MgPv]-[MgPv+Fp] for CI-chondritic compositions, independent of the Fe/Mg ratio. The first phase crystallising from a EC composition is stishovite (St) followed by [St+MgPv]. The differences in liquidus phase relations can be qualitatively described using a simple phase diagram in the system MgO-SiO_2 as it is shown in Fig. 3.4-15. Depending on the position of particular bulk compositions relative to the location of the eutectic on the MgO-SiO_2 join, different liquidus phases will be stable.

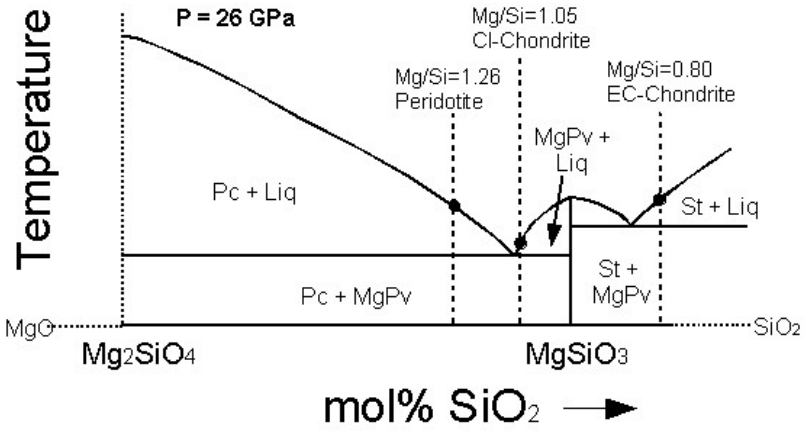

Fig. 3.4-15: Potential MgO-SiO_2 phase diagram at 26 GPa inferred from melting relations in complex multi-component systems. The dashed vertical lines indicate different bulk compositions and their intersection with the liquidus defines the liquidus phase. The observed crystallisation sequences indicate a eutectic-like composition between peridotite and CI-chondrites.

Mineral/melt partition coefficients D_i ($C_i^{mineral}/C_i^{melt}$) for major and minor elements have been determined from element concentrations measured by electron microprobe analysis. We observe a strong correlation between the MgPv/melt partition coefficients of Mg and Si (D_{Mg}, D_{Si}) and the Mg/Si ratio of the residual melt, such that D_{Mg} decreases and D_{Si} increases with increasing Mg/Si ratio of the liquid as it is shown in Fig. 3.4-16.

An attractive aspect of crystal fractionation of MgPv from a deep magma ocean is that this could have raised the Mg/Si ratio of the residual liquid that formed the primitive upper mantle (PUM) and therefore explain the difference in Mg/Si ratio between the Earth's upper mantle and the array of chondritic compositions from which the Earth likely formed. However, as shown in Fig. 3.4-16, D_{Mg} and D_{Si} actually crossover at Mg/Si ratios in the range of CI

chondrites, such that Si is less effectively fractionated by MgPv crystallisation relative to Mg with decreasing bulk Mg/Si ratio. Thus, the present day Mg/Si ratio of the primitive upper mantle cannot be a result of MgPv fractionation from an initially (CI-) chondritic magma ocean.

For an enstatite chondrite (EC) magma ocean at lower mantle conditions our results indicate that stishovite would be the liquidus phase (Fig. 3.4-15) and fractional crystallisation of stishovite into the lower mantle would very rapidly raise the Mg/Si ratio of the residual liquid. Stishovite fractionation raises an interesting possibility because it would probably not disturb chondritic rare earth element ratios in the residual liquid. However, the residual liquid would quite rapidly leave the compositional range where stishovite is on the liquidus and MgPv would again become the liquidus phase. Fractionation of MgPv at these compositions would drive the Mg/Si ratio of the residual liquid down. It is, therefore, not possible to obtain the current upper mantle bulk composition from an initial enstatite chondrite mantle by either stishovite or MgPv crystal fractionation into the lower mantle.

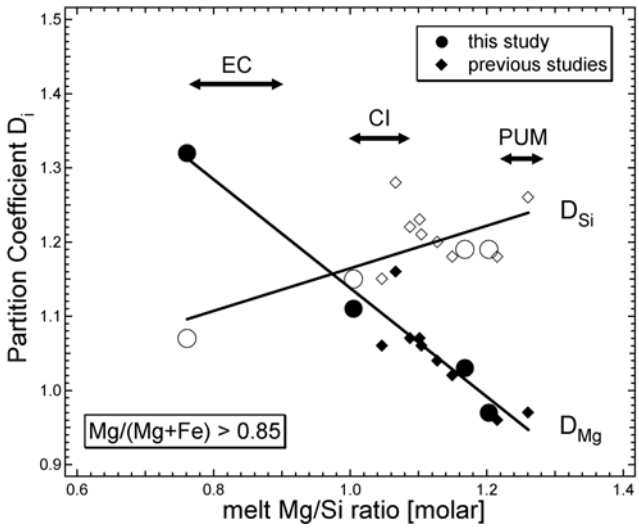

Fig. 3.4-16: Magnesium silicate perovskite (MgPv)/melt partition coefficients for Mg and Si as a function of Mg/Si ratios of the residual melts for Mg/(Mg+Fe) ratios greater than 0.85. Data from this and previous studies are shown. Arrows denoted as EC, CI and PUM indicate compositional ranges of enstatite- and CI chondrites and the primitive upper mantle, respectively.

j. *Iron isotope fractionation and its relation to oxygen fugacity in mantle minerals (H. Williams/Zurich and C.A. McCammon, in collaboration with A.H. Peslier/Houston; A.N. Halliday, N. Teutsch, S. Levasseur and J.-P. Burg/Zurich)*

The stable isotope geochemistry of iron has been the focus of intense interest in the recent past. While iron isotope applications are well known in low temperature chemistry, particularly in paleosediments, iron isotopes may also have considerable potential as tracers of

planetary formation and differentiation processes. In particular, there are indications from the literature of links between iron isotope fractionation and oxygen fugacity. Since oxygen fugacity exerts a fundamental influence on numerous and diverse processes in the mantle (*e.g.* melting, volatile speciation, and the evolution of the atmosphere), and there are only limited methods for determining mantle oxygen fugacity, we made a study of mantle xenoliths that combined determination of iron isotopic compositions with oxygen fugacity measurements to assess the potential use of iron isotopes as tracers of changes in iron oxidation state and mantle oxygen fugacity.

We chose a range of well-characterised mantle xenoliths from sub-arc, continental margin and intraplate (continental garnet and spinel-facies) tectonic settings to evaluate the effects of mineralogy, melting and mantle oxidation state on iron isotope fractionation. We used multiple collector inductively coupled plasma mass spectrometry to determine iron isotopic compositions of individual minerals and the bulk rock assemblages, and Mössbauer spectroscopy to determine $Fe^{3+}/\Sigma Fe$ of individual minerals. Coupled with the olivine-orthopyroxene-spinel oxygen barometer, these values were used to derive oxygen fugacities for the equilibrium assemblages.

We found a negative correlation between oxygen fugacity and iron isotopic composition (recorded as $\delta^{57/54}Fe$) for bulk rock, spinel and clinopyroxene (Fig. 3.4-17). There is also a corresponding correlation between iron isotopic composition and chemical indices of melt extraction. The results are readily explained if variations in mineral and bulk-rock $\delta^{57/54}Fe$ are caused by melt-extraction processes accompanied by changes in mantle oxygen fugacity. Large differences in the $\delta^{57/54}Fe$ values of garnet and spinel peridotites are likely caused by the contrasting behaviour of Fe^{3+} during melting in the spinel and garnet facies.

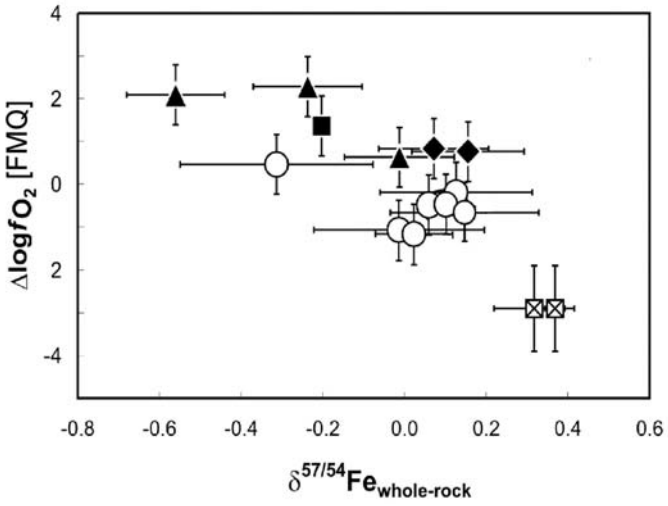

Fig. 3.4-17: Variation of relative oxygen fugacity with bulk rock iron isotopic composition for mantle peridotites from different tectonic environments (solid symbols: spinel-facies dunites, harzburgites and olivine clinopyroxenites from the sub-arc mantle; open circles: spinel lherzolites from the sub-continental mantle; squares with crosses: garnet websterites from the sub-continental mantle).

k. *The formation of $CaSiO_3$ perovskite from complex garnet compositions at transition zone and lower mantle conditions (A. Saikia, D.J. Frost and D.C. Rubie)*

At mid transition zone conditions the mantle's entire CaO budget is stored in majoritic garnet. Above approximately 15 GPa, however, the solubility of CaO in garnet starts to decrease with increasing pressure and CaO-saturated garnet starts to exsolve $CaSiO_3$ perovskite. From the lower part of the transition zone onward the amount of $CaSiO_3$ perovskite gradually increases as the solubility of CaO in garnet decreases, until garnet is virtually CaO-free. Throughout the lower mantle $CaSiO_3$ perovskite is the dominant CaO-bearing mineral. What is quite interesting is that $CaSiO_3$ perovskite formation from garnet in both peridotitic and basaltic compositions occurs at approximately the same pressure, even though basaltic compositions contain almost double the amount of CaO. This must mean that garnet CaO solubility is dependent on some variable other than just pressure. The most likely explanation is that the solubility of CaO in garnet, and consequently the pressure dependence of $CaSiO_3$ perovksite formation, also depends on the Al/Si ratio of garnet *i.e.* the proportion of the majorite component in garnet. It has been recently proposed that the formation of $CaSiO_3$ perovskite, although occurring over a significant pressure interval, could cause a weak seismic discontinuity. The conditions over which this reaction occurs are poorly constrained, however, and the effects of varying the complex chemical composition of garnet cannot be rigorously assessed from the existing data.

In this study we aim to determine the solubility of $CaSiO_3$ in garnet as a function of pressure, temperature, and composition. The amount of coexisting $CaSiO_3$ perovskite for any given bulk composition can be calculated at any relevant pressure and temperature from such data. With this aim in mind we have chosen four starting compositions with varying proportions of the majorite garnet component. If we consider the end member $Mg_3Al_2Si_3O_{12}$-$Mg_4Si_4O_{12}$ garnet-majorite join then peridotitic majorites at mid transition zone conditions have approximately 0.7 Al formula units while basaltic garnets have approximately 1.4. We prepared CaO-free garnet compositions with varying Al/Si ratios along this join with a fixed Fe/(Mg+Fe) ratio of 0.08. These glass starting compositions were reduced in a CO_2/H_2 gas mixing furnace at 700 °C and 2 log units above the iron-wüstite oxygen buffer. Mossbauer spectra after reduction showed virtually no Fe^{3+} in the reduced glass powders. The garnet compositions were mixed with excess $CaSiO_3$ wollastonite in a 1:2 ratio.

Experiments were carried out in a multianvil press using 10/5 and 10/4 assemblies between 15 to 26 GPa and temperatures in the range of 1200 to 1800 °C. Re multi-chamber capsules were employed such that several compositions with varying majorite garnet contents could be run in the same experiment. To calibrate the pressure in each experiment we also added an $(Mg,Fe)_2SiO_4$ composition to one of the sample chambers. From the distribution of Fe and Mg between phases crystallising in this system it is possible to make relatively precise estimates of the pressure.

During the experiment, the glass and $CaSiO_3$ compositions crystallise rapidly as garnet and perovskite respectively and $CaSiO_3$ dissolves into the garnet phase. In experiments performed at 1400 °C for up to one day, equilibration of garnet and $CaSiO_3$ was relatively sluggish and significant zoning was observed in the recovered garnets. After one day at 1600 °C, however, garnets with relatively homogenous CaO contents were recovered (Fig. 3.4-18).

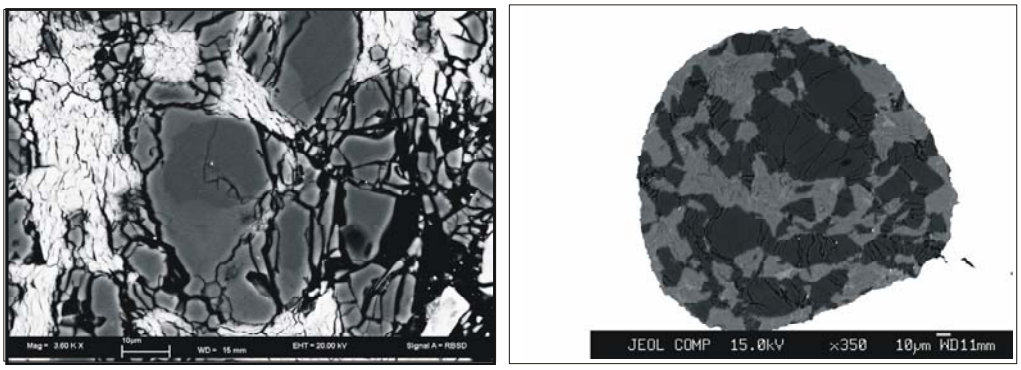

Fig. 3.4-18: Left: A recovered sample from 1400 °C showing light $CaSiO_3$ perovskite surrounding darker garnet grains. Significant zoning of the garnet grains can be seen due to the incomplete reaction with $CaSiO_3$. Right: A similar sample from 1600 °C where zoning is no longer apparent (SEM-BSE images).

Figure 3.4-19 summarises the preliminary results at 1600 °C. As the Al_2O_3 content of garnet increases, *i.e.* the majorite component decreases, so the CaO content increases. Pressure decreases the overall CaO solubility and slightly reduces the Al_2O_3 dependence. Both these effects (*i.e.* pressure and majorite content) can be related to a reduction in the garnet unit cell,

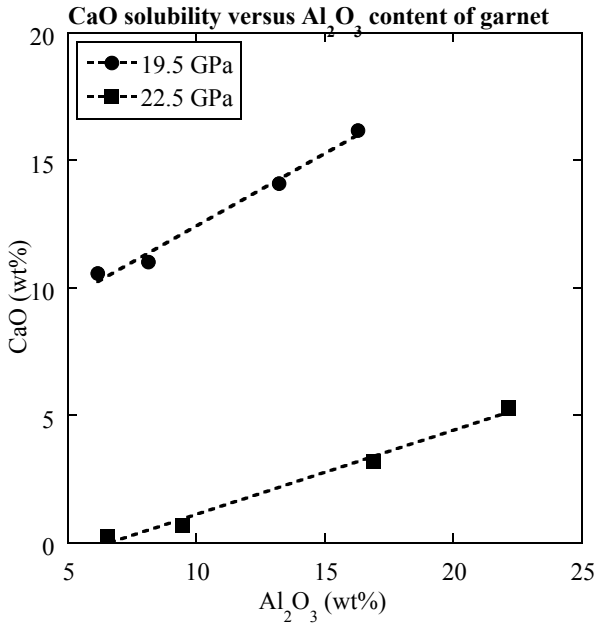

Fig. 3.4-19: The dependence of garnet CaO solubility on Al_2O_3 content at 19.5 and 22.5 GPa and 1600 °C. As the majorite component of garnet increases (*i.e.* lower Al_2O_3) so the solubility of CaO in garnet is reduced.

which makes garnet a less favourable environment for the relatively large Ca ion. The next step will be to reverse these experiments by employing Ca-bearing majorite garnet starting compositions. Effects of varying iron content will also be examined. With these results along with current estimates of physical properties of these phases we will be able to produce a mineralogical model for the transition zone and determine aggregate velocity and density profiles.

l. *Experimental tests of the transition zone 'water filter' hypothesis (B.J. Wood and J. Wade/ Bristol; D.J. Frost)*

Bercovici and Karato (Nature 425, 39-44, 2003) have recently proposed a radical new model to explain the chemical and isotopic differences between mid ocean ridge basalts (MORB) and oceanic island basalts (OIB). The 'classical' geochemical explanation has been that MORB come from an upper mantle which has been depleted in the incompatible elements (including noble gases and H_2O) by an old melting event which lead to development of the crust. OIB, on the other hand, were considered to come from plumes rising from 'primitive' lower mantle which is relatively undegassed and undepleted by prior melting events. The new hypothesis starts from the experimental evidence that H_2O is much more soluble (10 times) in $(Mg,Fe)_2SiO_4$ wadsleyite and ringwoodite, the major minerals of the transition zone, than in the principal upper mantle mineral olivine and the lower mantle equivalents perovskite plus magnesiowüstite. This implies that the transition zone may, based on cosmochemical estimates of H_2O content of the Earth, contain somewhere between 0.2 and 2 % H_2O. The subduction of material into the transition zone forces a slow passive return flow of transition zone material into the upper mantle. As this material crosses the 410 km discontinuity, and wadsleyite transforms to olivine, Bercovici and Karato argue that the water content, which is well below saturation in wadsleyite, is above the saturation level in the upper mantle olivine-bearing assemblage. They suggest that the supersaturation causes low-temperature melting of the passively upwelling mantle and generates a thin layer of dense melt 'perched' on the 410 km discontinuity. The melt, about 0.5 % of the total volume, should strip a large fraction of the incompatible trace elements out of the mantle traversing this zone. Thus, argue Bercovici and Karato, the upper mantle source of MORB becomes depleted and relatively homogeneous in composition by passing through a thin zone of melting at 410 km.

This new idea on the origin of the depleted upper mantle is testable because the partitioning of incompatible elements between melt and the minerals stable at 410 km must be consistent with observed depletions of these elements in the upper mantle. In order to make such a test, we performed experiments on model mantle compositions at pressures and temperatures corresponding closely to those at the 410 km discontinuity, 14-16 GPa and 1400-1600 °C respectively. Starting materials were fine-grained oxide mixtures which were doped with a suite of trace elements in the form of ICP-MS solutions. The mixtures were dried and heated under reducing conditions to break down residual nitrates. About 10 % water was added to the

mixtures in the form of magnesium hydroxide. Experiments were performed in the multianvil apparatus using welded Pt-capsules which were lined with Re foil to minimise iron-loss. The hydrous silicate melt (containing about 20 % H_2O) was found to quench to a crystalline mat. A suite of experiments performed on compositions of different Mg/Si ratios has produced majorite, wadsleyite, olivine, pyroxene and anhydrous phase B with crystal sizes in the 30-70 micron range. These (and the quenched melts) have been analysed for major elements with the electron microprobe and preliminary trace element data have been obtained by Laser-Ablation ICP-MS. The latter indicate that the crystal-solid partitioning *patterns* are similar to those measured at low pressures under anhydrous conditions. Majorite, for example exhibits a strong preference for the heavy over the light REE. Absolute partition coefficients (D=concentration in crystal/concentration in melt) are, however, much lower than previous low pressure anhydrous data. REE partition coefficients in garnet are about a factor of 5 lower while those in olivine and orthopyroxene are a factor of 10 lower than obtained in low-pressure experiments.

3.5 Geodynamics

Geophysical observations, including seismology and the study of the gravitational field of the Earth, provide an ever better resolved picture of physical properties in the interior of our planet. Hypotheses on the dynamic state of the Earth's mantle can now be tested by integrating computations on the viscous flow in the mantle and the current understanding of relevant physical properties of Earth materials at conditions of high pressure and temperature. While most of the high-pressure research at the Bayerisches Geoinstitut is focused on the latter aspect of deep Earth geophysics, geodynamics provides a critical link to observational geophysics (and geochemistry), and such studies are increasingly incorporating such information in models of mantle flow.

In the past year some aspects of mineral physics have been integrated into geodynamic computations. In one contribution the viscosity structure of the Earth's mantle is examined by integrating observations from the geoid, average heat flux data, seismic travel time anomalies, and mineral physics. In a second contribution the influence of latent heat release across phase transitions on the topography of the respective seismic discontinuities in the mantle has been studied, as well as on dynamic topography on the Earth's surface.

a. *Models of viscous flow in the Earth's mantle with constraints from mineral physics and surface observations (B. Steinberger, in collaboration with A. Calderwood/Vancouver)*

Modeling the geoid has been a widely used and successful approach in constraining flow and viscosity in the Earth's mantle. However details of the viscosity structure cannot be tightly constrained with this approach. Here, radial viscosity variations in 4-5 mantle layers (lithosphere, upper mantle, 1-2 layers transition zone, lower mantle) are computed with the aid of independent mineral physics results. A density model is obtained by converting s-wave anomalies from seismic tomography to density anomalies. Assuming both are of thermal origin, conversion factors are computed based on mineral physics results. From the density and viscosity model, a model of mantle flow, and the resulting geoid and radial heat flux profile is computed. Absolute viscosity values in the mantle layers are determined by optimizing the fit to the geoid, while at the same time requiring that the model yields a sensible radial heat flux profile: We minimize the value of P-VR whereby VR is geoid variance reduction and P mainly penalizes if the computed advected radial heat flux profile exceeds reduced surface heat flux (surface heat flux minus heat production in crust) at some depth. Typically, optimized models do not exceed this value by more than about 20 %. Because viscosity values also have to satisfy a "Haskell average" from postglacial rebound there are only 3-4 free parameters in the optimization. Viscosity profiles obtained show a characteristic hump in the lower mantle, with maximum viscosities of about 10^{23} Pas just above the D" layer – about 1000 times the lowest viscosities in the upper mantle. The

viscosity contrast is at least 10 times higher that what is inferred when a constant lower mantle viscosity is assumed. The geoid variance reduction obtained is up to about 80 % – similar to previous results. However, because of the use of mineral physics constraints, a rather small number of free model parameters is required, and at the same time, a reasonable heat flux profile is obtained. Results are best when the lowest viscosities occur in the transition zone. When viscosity is lowest below the lithosphere, variance reduction is about 70 %. Best results were obtained with a viscous lithosphere with a few times10^{22} Pas and a free surface, *i.e.* continuously varying and not-plate-like surface velocities (Fig. 3.5-1). The optimized models yield a CMB excess ellipticity several times higher than observed, possibly indicating that radial stresses are partly compensated within the lowermost mantle, due to chemical variations and/or a phase boundary, thus reducing CMB topography. Within the parameter space investigated, no models could be found that simultaneously give a good fit to the geoid and CMB excess ellipticity, and a reasonable heat flux profile.

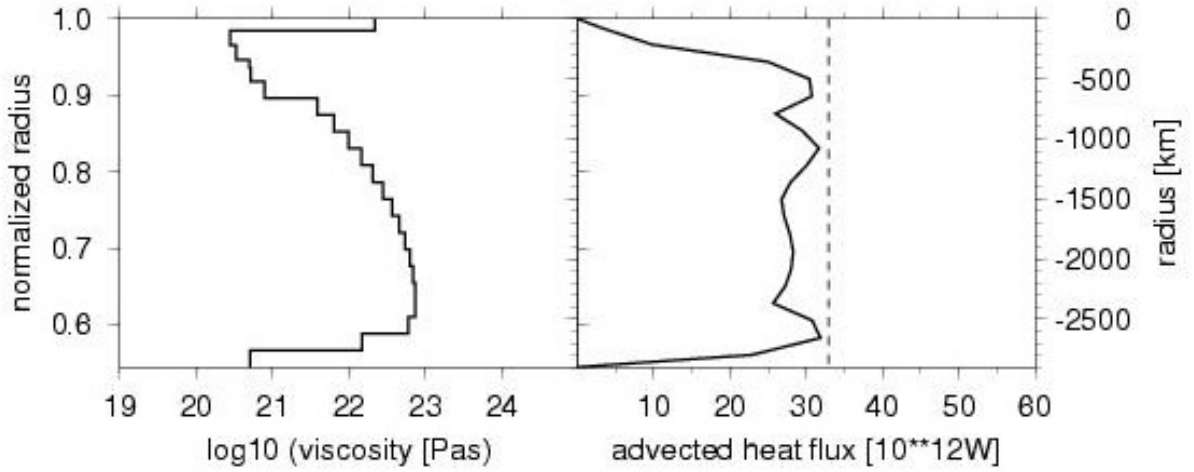

Fig. 3.5-1: Viscosity (left) and heat flux (right) profile for the preferred model, with geoid variance reduction 75 %. Also shown (dashed line) is the reduced surface heat flux 33 TW.

b. *Effect of latent heat release at phase boundaries on flow in the Earth's mantle, phase boundary topography and dynamic topography at the Earth's surface (B. Steinberger)*

Seismic velocity anomalies seen in mantle tomographic models are frequently assumed to be of thermal origin. Under this assumption they can be converted to temperature anomalies and hence be used to predict equilibrium phase boundary topography. However, the prediction correlates rather poorly with phase boundary topography observed with seismology. Furthermore, mantle flow models based on the thermal density anomalies inferred from seismic tomography can be used to predict dynamic surface topography. This prediction depends on a variety of further assumptions, such as viscosity structure. However, regardless of these assumptions, there is no good global agreement with *observed* dynamic surface

topography (*i.e.*, observed topography, minus effect of crustal isostasy, minus thermal effect of ocean floor cooling). Thus, further effects need to be considered in order to better understand surface and phase boundary topography.

Here we study how the effects of latent heat of transformation on both the 410 and 660 km discontinuities change the predictions of phase boundary and dynamic surface topography. This approach is implemented in a model of global mantle temperature and flow with an iterative procedure, and a model of the phase boundary deflection and its deviation from equilibrium. In particular, it is found that the advection of phase boundaries due to latent heat effects reduces the amplitude of predicted dynamic surface topography, which is too large compared to observation-based models, by several hundred meters.

Even without the latent heat effect, correlations between predictions and observation-based models of phase boundary topography and dynamic topography are almost always positive, giving a strong indication that both phase boundary topography and seismic velocity variations are at least partly related to lateral temperature variations. These temperature variations give rise to mantle flow that causes at least part of the surface dynamic topography. Including latent heat effects, the correlations between predictions and observation-based models almost always increase, and root mean square amplitudes of predictions get closer to the observation-based values, indicating that this effect also plays a role in the Earth. However, the fact that correlations remain rather low, and that the latent heat effect is not sufficient to eliminate the misfit between predicted and observation-based root mean square amplitude of the 660 km seismic discontinuity and dynamic topography may indicate that other physical mechanisms not considered here also play a role (Fig. 3.5-2).

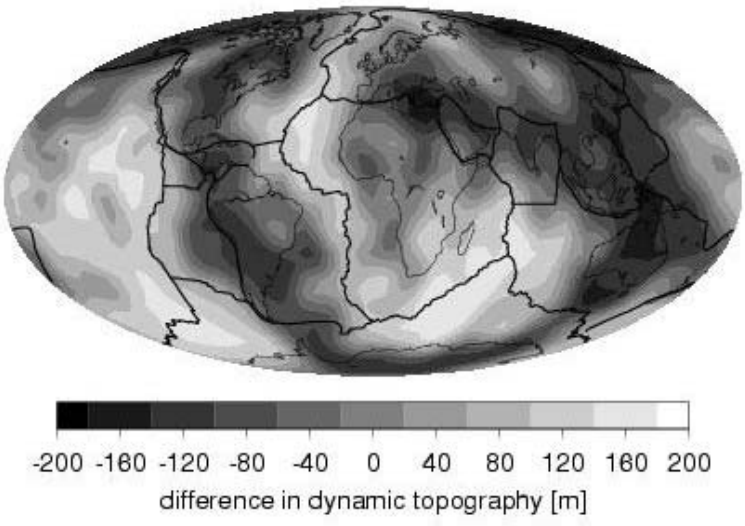

Fig. 3.5-2: Dynamic topography prediction without latent heat effect minus prediction with consideration of latent heat effect at phase boundaries.

3.6 Metamorphism at Different Time Scales

Metamorphic rocks make up about 85 % of the Earth by volume and almost all of these are formed in lower part of the crust and mantle as a result of tectonic processes like subduction at plate boundaries, crustal thickening in mountain ranges, rifting during creation of plate boundaries, and by mantle circulation in the Earth's interior. Metamorphic rocks are formed from preexisting rocks that are subjected to a new set of conditions imposed in these tectonic environments. Their formation involves physical and chemical changes in the solid state. Physical changes are produced by deformation and the formation of new minerals and chemical changes result from continuous and discontinuous metamorphic reactions that create new stable minerals and/or compositions of minerals.

During their formation in different tectonic environments, metamorphic rocks record information in two general areas. The first area includes insights into the tectonic setting and processes including, for example, the conditions under which they are formed, which are determined by studying the mineral assemblages, the rheologic properties of the crust and mantle by determining how the stable minerals deform, and the rates of processes that are obtained by dating metamorphic minerals. The second area includes insights into the process of metamorphism including, for example, the nucleation and growth of metamorphic minerals and the role of deformation and fluids in enhancing rates of metamorphic reactions. The contributions in this section fall into both of these areas and give new insights into tectonic and metamorphic processes. These include experimental constraints on the stability of high-pressure mineral assemblages and an experimental study on the role of deformation in enhancing metamorphic reactions.

a. *Experimental phase relationships for kyanite-eclogites in the CMAS and CMASH systems (M.P. Terry, G.D. Bromiley, E. Krogh Ravna/Tromsø, P. Robinson/Trondheim and J. Liu)*

Knowledge of the pressure and temperature conditions at which metamorphic rocks were formed has played a very important role in helping to understanding tectonic processes. Accurate determination of these conditions has been particularly challenging in crustal eclogites derived from basaltic compositions in HP and UHP terrains. To better constrain pressure and temperature, we are conducting an experimental study of the phase relationships in the CMAS systems with a specific focus on the discontinuous reaction

2 garnet (py50) + 2 coesite (Quartz) = 3 kyanite + 3 diopside (**1**)

This reaction has a moderate pressure in the coesite stability field and strong temperature dependence in quartz stability field (Fig. 3.6-1).

All phases were synthesized between 1000 and 1100 °C at 3.5 GPa for 48 hours using oxide powders except garnet, which was synthesized from a glass seeded with garnet. The

compositions were characterized using the electron microprobe and X-ray diffraction to determine unit cell dimensions. The Ca/(Ca+Mg) ratios for the starting compositions of garnet and clinopyroxene were 0.410 and 0.492. A stoichiometric mixture of the starting minerals that reflects reaction (1) was used in the experiments. The duration of each experiment was 96 hours and results were evaluated using X-ray diffraction and the electron microprobe.

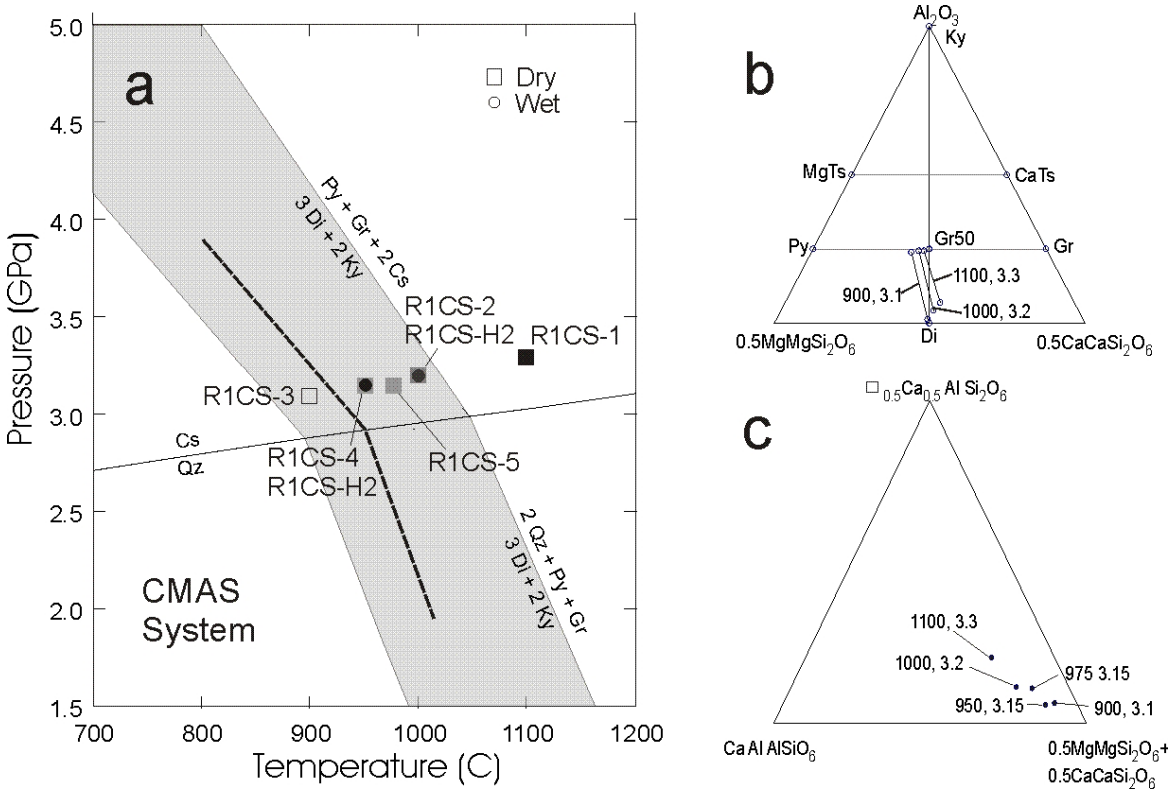

Fig. 3.6-1: a: Graph of experiments results and the range of P & T conditions where reaction (1) may occur based on commonly used thermodynamic data set and activity models (shaded region). The heavy dashed line the approximate position of reaction (1). b and c: Circles - water was added; squares - no water added; black symbol- garnet growth; gray symbol - inconclusive result; white symbol - Cpx growth.

Initial experiments to constrain the position of reaction (1) were carried out under dry conditions. Comparison of relative peak intensities in X-ray diffraction patterns between experiments at 900 and 1100 °C and the starting mixture indicate growth of clinopyroxene and garnet respectively. However, dry experiments at 1000, 950 and 975 °C are not as clear, probably due to a combination of slow reaction kinetics and being in close proximity to reaction (1). Even though the degree of reaction was not sufficient to conclusively constrain the reaction position, the results from all the dry experiments nicely document the Ca-tschermaks exchange ($CaAl_{-2}Si_{-1}$) between garnet and pyroxene (Fig. 3.6-1b) and the increase in the Ca-Eskola component ($\square_{0.5}Ca_{0.5}AlSi_2O_6$) in pyroxene with increasing T & P (Fig. 3.6-1c).

Due to the inconclusive results from comparison of relative peak heights in the X-ray diffraction patterns from starting material and experiments at 1000, 975, and 950 °C, water was added to the capsule to increase the amount of reaction. The addition of water at 1000 °C and 3.2 GPa resulted in the formation of two different assemblages in the capsule, diopside-zoisite-garnet-kyanite and garnet-kyanite (Fig. 3.6-2a, b, c). The modes of zoisite and diopside increase away from the boundary between the two assemblages, which may be interpreted as an increase in fluid activity towards the top of the capsule. Zoisite and diopside are stabilized by the discontinuous reaction.

18 Garnet (py = 0.385) + 12 Coesite + 6 H20 = 15 Diopside + 12 Zoisite (**2**).

The garnet-kyanite assemblage (Fig. 3.6-2b) is interpreted to have been formed at low activity of H_2O by reaction (1). Note that the presence of kyanite rather quartz might be attributed to a small majorite component, solution of Si into the fluid, or small error in the starting bulk composition. A similar experiment (water added to the capsule) was carried out 950 °C and preliminary analysis indicates similar results to those obtained at 1000 °C.

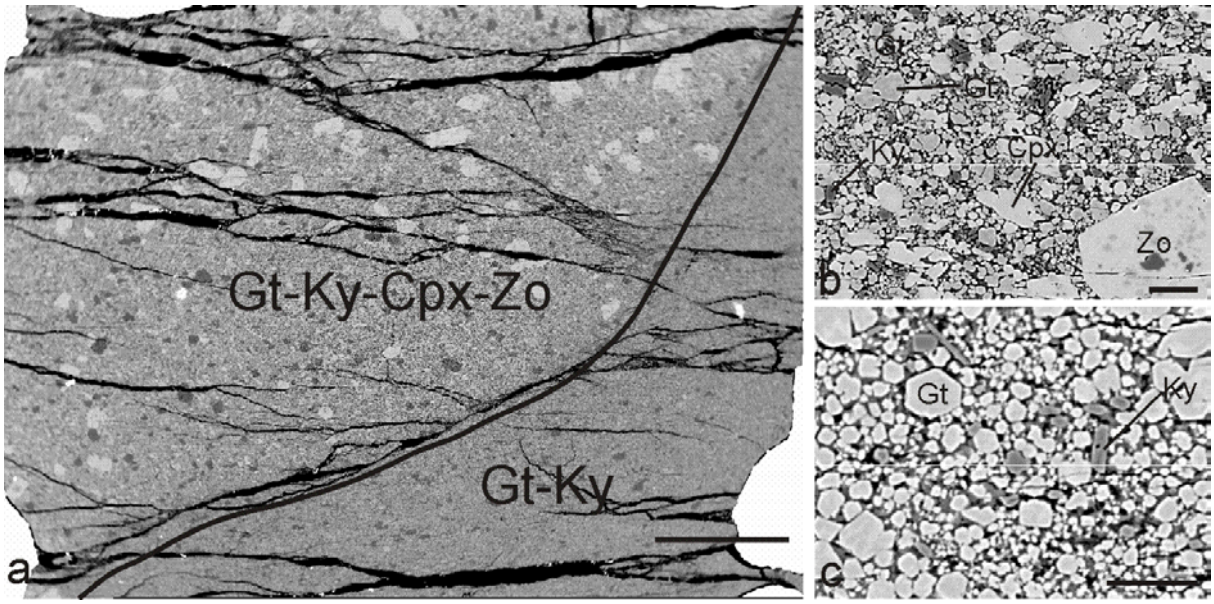

Fig. 3.6-2: Images of a polished section through the capsule (a) and the different mineral assemblages present (b, c). The conditions of this experiment were 1000 °C and 3.2 with water added to the capsule. Scale bars are 0.50 mm in (a) and 0.02 mm in (b) and (c).

Our results constrain reaction (1) to lie between 900 and 950 °C at 3.1 GPa. The dry experiments nicely illustrate the incorporation of garnet Ca-tschermaks and Ca-Eskola components into the pyroxene structure with increasing temperature. Results from this study and natural samples indicate that the end-member reaction for incorporation of the Ca-Eskola component has a negative slope and increases with both temperature and pressure.

b. *High-pressure phase equilibria an amphibole-bearing gabbro from an island arc tectonic setting: The case of Ustica Island (I. Di Carlo and M. Alletti/Palermo; G.D. Bromiley)*

In the Southern Tyrrehenian Sea, the occurrence of Na-alkaline lavas (Ustica) surrounded by calc-alkaline and K-alkaline magmas (Aeolian Islands, Aceste and Anchise seamounts) is still not fully understood, but is most commonly explained by a variable degree of interaction between oceanic slab-components and variably hydrated mantle peridotite. In this context, Ustica island volcanism represents a crucial point in understanding the mechanisms that led to a rather complicated compositional scenario. The Na-alkaline affinity of Ustica has an island arc geochemical signature (*e.g.* negative anomalies of some HFSE elements and positive correlation between $^{87}Sr/^{86}Sr$ and Th/Ta), despite its within-plate bulk rock character. Previous studies have suggested that amphibole could be an important phase in controlling the distribution of some trace elements in the sub-arc mantle. Kaersutitic amphibole has been found in some Ustica gabbroic cumulates. Here we experimentally investigate the stability of amphibole in alkaline lavas of Ustica island in T-P-fO_2-a_{H2O} space to determine constraints on the capacity of amphibole to influence trace element distribution.

The starting composition was a gabbro collected from Contrada Spalmatore, containing the assemblage labradoritic plagioclase ≥ kaersutite > clinopyroxene > olivine. Samples were fused two times at 1600 °C, and the composition of starting glasses was determined after each melting cycle, in order to check for any inhomogeneity and possible Na-loss. High-pressure annealing experiments were performed using a ¾" piston cylinder apparatus. Assemblies consisted of a tapered internal graphite resistance furnace surrounded by a Pyrex sleeve, with an outer cylinder of talc acting as a pressure-transmitting medium. Samples were loaded into $Au_{80}Pd_{20}$ or Au (for lower temperature experiments) capsules with variable amounts of water. Previous work has demonstrated that the use of $Au_{80}Pd_{20}$ or Au capsules minimises iron-loss from samples under high P-T conditions. Capsules were welded shut to prevent water-loss during the experiments, and were surrounded by pyrophyllite sleeves in the sample assemblies to minimize water loss due to H^+ diffusion through the capsule walls. Experiments were performed to determine the effects of variable temperature, pressure, and water content on phase relations. No attempt was made to directly control the fO_2. The fO_2 conditions were indirectly calculated using resulting mineralogical assemblages. Work focused on investigation of the temperature range 1040-950 °C with variable water contents (5 to 20 wt.%) and the pressure range 5 to 15 kb (to replicate upper mantle conditions). High water contents were chosen to promote amphibole nucleation in the experimental charges.

The experiments at 15 kb were performed at 1040 °C (19 wt.% and 9 wt.% H_2O)-1000 °C (19, 17 and 9 wt.% H_2O) and 950 °C (22 wt.% H_2O). In the experiments with higher water contents, the phase assemblage was amphibole (≈ 20 μm) + ilmenite-magnetite, with a small amount of glass around the amphibole at 1040 and 1000 °C (Fig. 3.6-3). The amphibole had a

ferro-pargasite composition: SiO_2=39.2 wt.%, Al_2O_3=15.5 wt.%, $Mg/(Mg+Fe^{2+})$=0.673, $Fe^{3+}/(Fe^{3+}+Al^{VI})$=0.360.

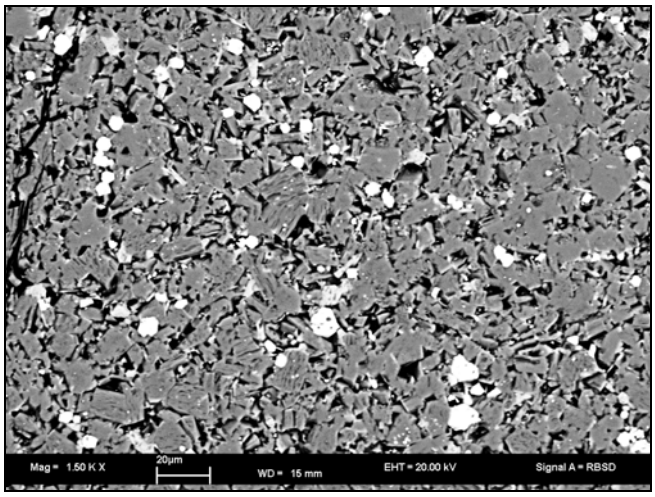

Fig. 3.6-3: Experiment at 1000 °C, 15kb, 19 wt.% H_2O inserted (SEM-BSE images).

In experiments with lower water contents (water undersaturated) at 1000 °C, the stable phase assemblage is clinopyroxene, glass and magnetite. At 950 °C, garnet joins amphibole, ilmenite/magnetite +/- glass (H_2O = 22 wt.%). Garnet also appears as an equilibrium phase in experiments at all pressure conditions with lower water contents. It should be noted that, to date, garnet has not been found in natural samples.

At 10 kb, the situation is the same, with amphibole and an opaque phase +/- glass as the equilibrium phase assemblage under water-rich conditions at higher temperature, and clinopyroxene, glass and magnetite in bulk compositions with < 8 wt.% water. Glass is normally more abundant in the water-poor experiments, when clinopyroxene is stable.

Only two experiments were performed at 5 kb at 1040 °C; in water-rich compositions (9.5 wt.%) olivine (Fo 87 %) is the liquidus phase. The experiment with 5.6 wt.% H_2O is rather inhomogeneous: in the central part olivine is stable with magnetite, but in the bottom and top parts amphibole is present with an opaque phase. In some of the run products, problems with interpretation rose due to inhomogeneity and possible chemical zoning. In several charges, phase assemblages differ in different parts of the capsule. Inhomogeneity in many of these runs can be interpreted in terms of varying water contents in different parts of the capsule, possible resulting from slight temperature gradients across the length of the capsules. Therefore, fluid-enriched and fluid-depleted parts of some experimental charges can be identified. This leads to problems with interpretation because bulk water contents for different parts of the capsule (and possibly also, to a lesser degree, bulk chemical compositions) are very difficult to accurately determine. However, such experiments can be used to give a semi-quantitative indication of the effects of variable water content on phase relations.

c. *A dynamic diffusion experiment: The role of deformation in enhancing metamorphic reactions (M.P. Terry, F. Heidelbach, M. Bystricky/Zurich and C. Holzapfel/Saarbrücken)*

Observations from natural samples and experiments indicate that deformation may enhance the rates of metamorphic reactions but detailed mechanisms are not well constrained. In this experiment, we examine the effects of deformation on a continuous exchange reaction between ferropericlase and periclase to provide insights into the interplay between metamorphic reactions and deformation.

In order to simulate simultaneous deformation with a continuous reaction, torsion experiments were used to produce a linear shear strain (gamma) gradient of approximately 0 in the center of a cylindrical sample that increases outward to the edge of the sample and approximates simple shear. (Fig. 3.6-4a). Two small cylinders of periclase (MgO) and ferropericlase ($Mg_{0.605}$ $Fe_{0.395}O$) jacketed in nickel were deformed by torsion using the Patterson deformation apparatus at ETH in Zurich (Fig. 3.6-4b). The conditions were 1300 ˚C, 300 MPa, and a shear strain rate $1.4x10^{-4}$ s^{-1} for 5.5 hours which gave a bulk strain of 2.7. However, all of the strain was partitioned into ferropericlase ($\gamma = 5.4$) while the MgO was not deformed at all (Fig. 3.6-4a).

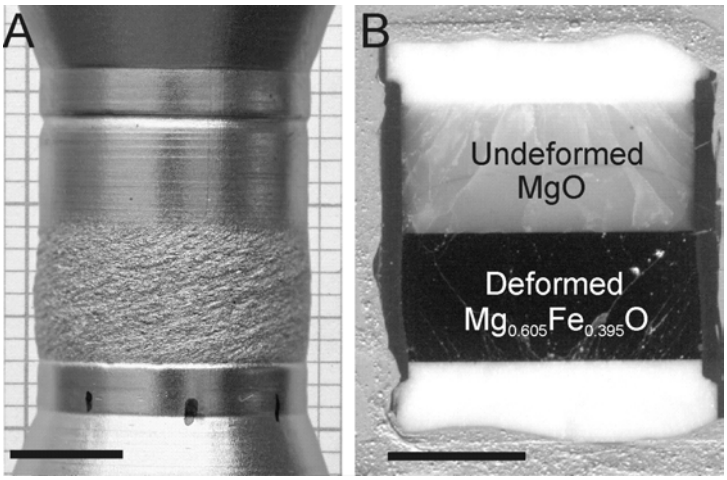

Fig. 3.6-4: a: Image of the Ni jacket that enclosed undeformed periclase (upper) and deformed ferropericlase (lower) indicating that stain is partitioned into the ferropericlase. b: Image of a vertical polished section through the interface between deformed periclase (upper) and deformed ferropericlase (lower). Scale bar in both images is 5 mm.

Composition mapping and quantitative traverses were made normal to the interface using the electron microprobe (Fig. 3.6-5). High-resolution composition maps were used to avoid diffusion of Ni from the jacket that surrounds the sample. The results indicate that diffusion is faster at the edge of the sample where shear strain is highest and slower in the center where stain is very low.

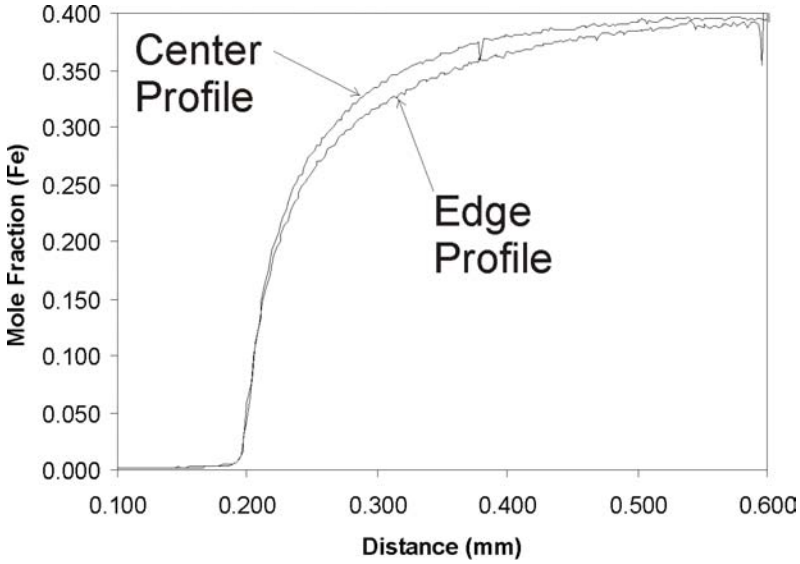

Fig. 3.6-5: Chemical profiles using a 2 μm step normal to the interface between ferropericlase and periclase at the edge and center of the sample.

Simulations of the chemical profiles from the edge and center profiles to were performed by using the composition-dependence

$$D = (D_{01} + D_{02} * X_{FeO}^{01:17}) \exp A * X_{FeO} \quad (\mathbf{1})$$

consistent with the expression given in previous studies for a similar composition range as investigated in this study. The simulation utilized a finite difference scheme with distance divided into steps of 1 μm, time divided into steps of 1 second, and a normalized concentration. Simulations of the center profile agree well by using Eq. 1, whereas some slight inconsistencies exist for the profile at the edge where shear strain is the highest. The diffusion coeffcients derived at the center and the edge of the diffusion couple deviate by a factor of 1.2 to 1.4 between $X_{FeO} = 0.1$ and 0.3.

Two possible explanations are being considered for faster diffusion on the edge of the sample. The first is a gradient in fO_2 from the center to the edge. This would cause a gradient in Fe^{3+} and an increase in the number of point defects in the ferropericlase structure that would allow faster diffusion. In this experiment, a Ni-NiO buffer was used and previous studies of olivine by other workers indicate that these point defects equilibrate rapidly and a significant gradient is unlikely. The second is deformation which is our preferred explanation currently under investigation. Previous investigations show that ferropericlase deforms by dislocation creep under these conditions; possible explanations for the relationships are an increase in dislocation density or a change in the larger scale microstructure such as an increase in grain boundary area caused by grain size reduction.

3.7 Fluids and their Interaction with Melts and Minerals

The Earth would be rather different in the absence of fluids. Apart from the lack of an ocean, without which there probably would be no life, the processes which take place on the surface of the Earth and within its interior would be either absent or quite altered. Fluids have been present since the early part of the Earth's history, and occur from the crust to the core. The ocean may represent only a small fraction of the water stored within the Earth, since minerals which have been normally thought to be dry (or nominally anhydrous) can in fact incorporate large quantities of hydrogen. This means that water cycled from the oceans and atmosphere into the mantle by subduction can reside in the interior for long periods of time. Since dissolved hydrogen can have significant effects on the physical and chemical properties of the Earth's mantle, a crucial first step is to characterise the nature and quantity of hydrogen incorporation into mantle phases.

Fluids are a critical component in the formation of many mineral resources that occur on and within the Earth. One of the more rare, yet highly prized resources – diamonds – are also formed by the action of fluids, yet many details of their formation remain unclear. The study of natural diamonds provides constraints on the chemistry of the fluids from which they formed, while complementary studies of synthetic diamonds help to model the processes of their formation.

a. *Investigation of H related defects in synthetic rutile using neutron irradiation and vibrational spectroscopy coupled with in situ annealing in controlled atmospheres (G.D. Bromiley, A.A. Shiryaev and F. Gaillard, in collaboration with N.N. Dogadkin/Moscow)*

Most of the phases thought to constitute the Earth's mantle, despite being nominally anhydrous, can contain trace amounts of hydrogen (100s to 1000s ppm H_2O by weight). Hydrogen is incorporated in such phases as isolated hydroxyl groups or as clusters of hydroxyl groups, usually associated with other point defects such as substitutional impurities, cation vacancies or oxygen vacancies. Techniques such as vibrational spectroscopy, NMR spectroscopy, SIMS and neutron diffraction allow us to constrain H concentrations and H positions in certain phases, and from this, to propose possible H incorporation mechanisms. However, our understanding of the reasons for and consequences of H incorporation in minerals would be greatly improved if we could use another complementary technique to provide direct information on coupling of H with other defects (*i.e.* defect clustering) and the relative stability of H-related defects and defect clusters under different conditions. In order to provide this information, we have been performing several series of experiments using neutron irradiation and post-irradiation annealing to investigate H incorporation in synthetic rutile.

Synthetic reduced rutile (TiO_{2-x}), grown under water-saturated conditions at 2.0 GPa, 1100 °C, was bombarded with high energy neutrons with a flux of 3 x 10^{16} n^0/cm^2 at a nuclear

reactor facility (in collaboration with N.N. Dogadkin, Institute of Geochemistry and Analytical Chemistry, Russian Academy of Sciences, Moscow). Before irradiation, crystalline defects in synthetic, reduced rutile can be considered in terms of Ti interstitials ($Ti_i^{\cdots}$), reduced Ti on the main cation (octahedral) site (Ti_{Ti}'), oxygen vacancies ($V_O^{\cdot\cdot}$) and interstitial hydrogen ($H_i^{\cdot}$). The main result of neutron irradiation of oxides and silicates is production of oxygen vacancies, sometimes coupled with valency changes on cation sites. With synthetic, reduced rutile, irradiation results in an increase in the number of $V_O^{\cdot\cdot}$ coupled with a reduction in the amount of optical absorption (crystals change colour from dark blue to light blue to colourless during irradiation) as demonstrated in Fig. 3.7-1. This change in colour is consistent with a model where optical absorption is due to e^- sharing between a Ti cation on the main octahedral site and an adjacent interstitial Ti cation (*i.e.* $Ti^{3+}Ti^{4+}$ intervalence charge transfer). Production of $V_O^{\cdot\cdot}$ in the irradiated rutile leads to a marked reduction in the affinity of the structure for Ti interstitials; thereby leading to a reduction in the amount of optical absorption. It had previously been suggested that optical absorption in reduced rutile was due to electron trapping at oxygen vacancies. This is, however, completely inconsistent with the effects of neutron irradiation. In Figure 3.7-1 it can also been seen that irradiation leads to a marked reduction in the amount of $H_i^{\cdot}$. This can also be related to an increase in the number of $V_O^{\cdot\cdot}$ in the irradiated sample, leading to a reduction in the affinity of the structure for interstitial H.

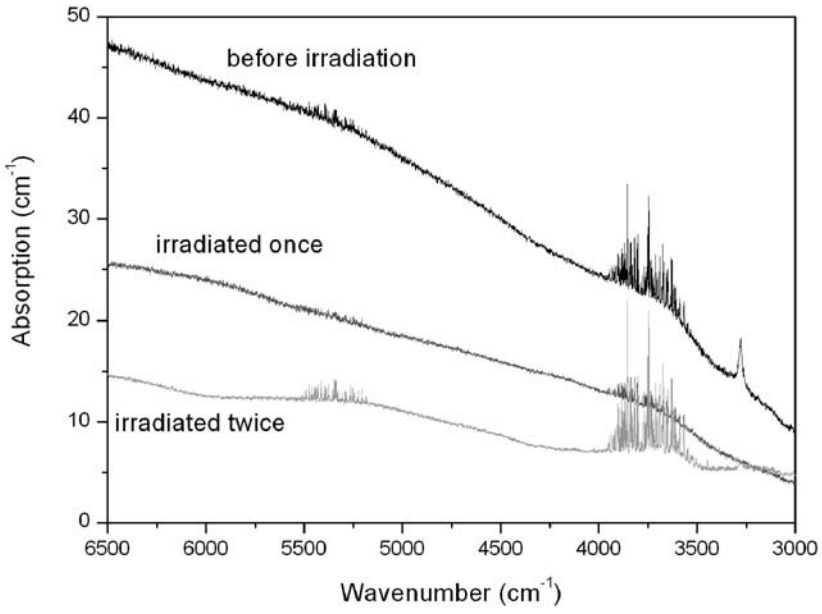

Fig. 3.7-1: NIR spectra obtained from synthetic, reduced rutile before irradiation (top), after irradiation (middle), and after two episodes of irradiation (bottom). Before irradiation, reduced rutile crystals are dark blue due to broad absorption over the optical part of the spectrum. This absorption extends into the near infrared part of the spectrum as can be seen from the steep background on the NIR spectrum. The slope of the NIR spectrum therefore provides a measure of the amount of optical absorption. Sharp absorption bands around 3279 cm^{-1} are OH stretching bands, implying the presence of structurally-incorporated H. Both the amount of optical absorption and the amount of interstitial H decrease during the irradiation process.

By heating irradiated samples under different conditions, it is possible to anneal out different types of crystalline defects, and therefore, to determine which types of defect are related to H incorporation. In order to test this, we used a small heating stage to anneal samples under controlled atmospheres. This heating stage can be coupled to a standard IR spectrometer and microscope to allow series of time resolved measurements to be made. Figure 3.7-2 shows a series of spectra obtained from a single crystal of irradiated rutile annealed in Ar-2% H_2 at 500 °C. By performing several experiments under a range of conditions we can demonstrate that (1) the main OH band in rutile spectra (3279 cm^{-1}) is due to $H_i^{\cdot}$ decoupled from other defects; (2) that at least two other H incorporation mechanisms operate in reduced rutile, one of which is probably related to Ti_{Ti}'; (3) that H affinity in the rutile structure is strongly reduced by the presence of $V_O^{\cdot\cdot}$; (4) that H affinity in the rutile structure is slightly reduced by the presence of other interstitial cations; (5) that e^- trapping may operate in heavily irradiated rutile, resulting in a slight yellow colour (*i.e.* some optical absorption); and (6) that H solubility in rutile is strongly P and fH_2 dependent.

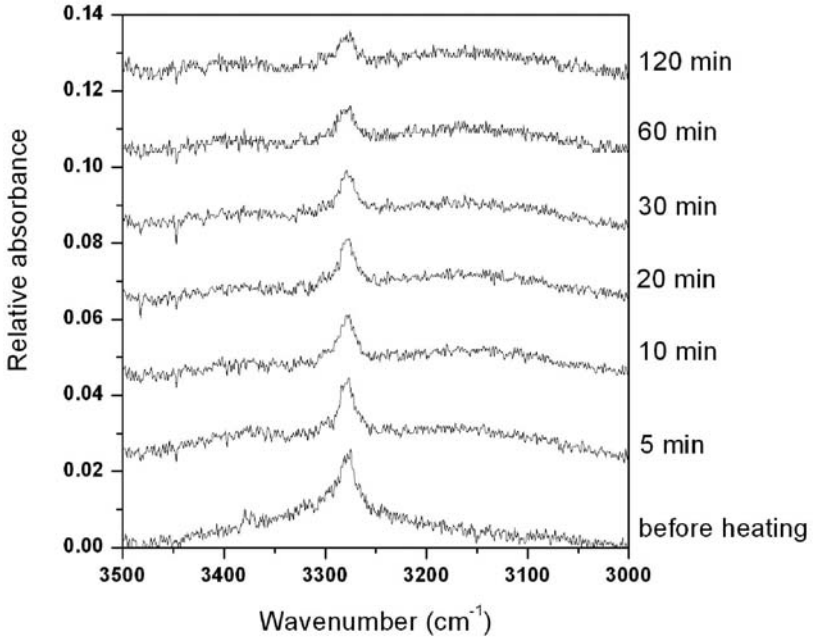

Fig. 3.7-2: NIR spectra obtained from a single crystal of irradiated, reduced rutile before and after annealing in Ar-2% H_2 for increasing amounts of time (offset vertically). During annealing, interstitial H is rapidly lost, as noted by a decrease in the height of the OH stretching band at 3279 cm^{-1}; however, no colour change in the crystal was observed, implying no concurrent loss of $Ti_i^{\cdot\cdot\cdot\cdot}$.

By performing this study, we have demonstrated that it is possible to use neutron irradiation as a complimentary technique to provide additional information on H incorporation in minerals. The great advantage of doing this is that it is possible to study small samples (crystal sizes down to a few tens of microns) typically produced in high-pressure experiments, and to provide direct information on how H is coupled to other types of crystalline defects.

b. *Hydrogen and minor element incorporation in synthetic rutile (G.D. Bromiley)*

Rutile is the most common, naturally occurring form of titanium oxide (TiO_2), and is found as an accessory mineral in many igneous and metamorphic rocks. Because rutile has a range of useful industrial applications, its defect structures, electrical and optical properties have been the subject of a considerable amount of research. Rutile has a simple tetragonal structure, and shows a high affinity for H incorporation. Therefore, rutile provides a useful model for considering some of the detailed aspects of H incorporation in nominally anhydrous minerals (NAMs) at high pressure.

In one series of experiments, we synthesised rutile with increasing Fe_2O_3 contents under water-saturated conditions at high pressure. Figure 3.7-3 shows NIR spectra obtained from single crystals of rutile as a function of increasing Fe content. Several interesting features are observed. With increasing Fe content, the slope of the background on the NIR spectra decreases. This slope is due to the broad optical absorption characteristic of reduced (TiO_{2-x}) rutile, which extends into the NIR part of the spectrum. Our neutron irradiation study of rutile has demonstrated that this absorption is due to $Ti^{3+}Ti^{4+}$ intervalence charge-transfer, that is, electron sharing between adjacent octahedral (Ti_{Ti}) and interstitial ($Ti_i^{\cdots}$) cations. The effect of Fe substitution in rutile is to lower the amount of absorption and by inference, to decrease the amount of interstitial Ti. This effect can be explained in terms of the fO_2 conditions imposed by the bulk composition. Presumably, Fe^{3+} substitutes into the rutile structure either via a coupled substitution mechanism involving Fe substitution onto both octahedral (*i.e.* Fe_{Ti}') and interstitial sites ($Fe_i^{\cdots}$), or Fe substitution onto the octahedral site is charge-balanced by oxygen vacancies ($V_O^{\cdot\cdot}$). The presence of excess ilmenite in run products implies that, in the latter case, Fe substitution in Fe-rich systems can be defined by the equation

$$2Fe^{2+}TiO_3 + \tfrac{1}{2}O_2 = Fe_2O_3 + 2TiO_2. \qquad [1]$$

This implies a change in oxidation state of Fe in the system. The equilibrium described in equation [1] would effectively control fO_2. However, in Fe-poor systems the presence of $Ti_i^{\cdots}$ implies reduction of TiO_2 during the experiments:

$$2Ti^{4+}O_2 = Ti^{3+}{}_2O_3 + \tfrac{1}{2}O_2. \qquad [2]$$

TiO_2 reduction implies more reducing conditions than in Fe-rich systems. We have observed that Fe_2O_3 solubility in rutile is dependent upon the Fe content of the starting mix, such that in Fe-poor systems, Fe_2O_3 solubility is lower. From equation [1] we can see that low Fe contents in rutile are also consistent with more reducing conditions. Changes in Fe oxidation state during the experiments effectively increase fO_2, thereby increasing Fe_2O_3 solubility and decreasing TiO_2 reduction. The effects of Fe content of the bulk composition on Fe solubility in rutile cannot be explained if Fe is incorporated in rutile via a coupled substitution mechanism. Therefore, our results effectively demonstrate that Fe^{3+} substitutes for Ti^{4+} in rutile, and is charge balanced by ($V_O^{\cdot\cdot}$).

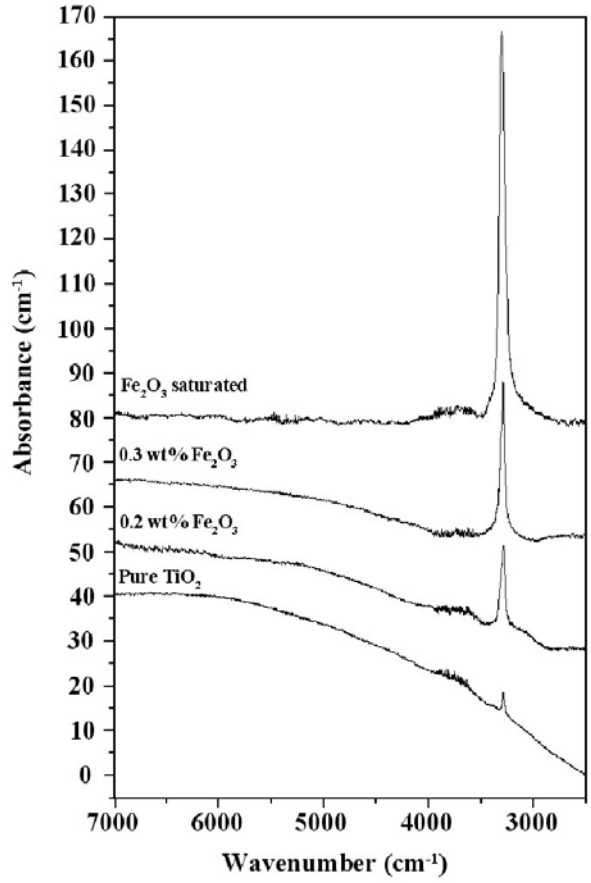

Fig. 3.7-3: Polarised NIR spectra (*E* // *c* axis) obtained from rutile doped with increasing amounts of Fe_2O_3, synthesised under water-saturated conditions at 2.0 GPa, 1100 °C. A horizontal baseline over the spectral range shown has been subtracted. Spectra are offset vertically with increasing iron content for clarity.

In Figure 3.7-3 it can also be seen that all rutile spectra contain sharp OH absorption bands around 3500-3000 cm^{-1}, implying the presence of structurally incorporated H. Figure 3.7-4 shows an enlargement of part of the NIR spectra to highlight this region. Spectra obtained from Fe-free rutile contain one OH absorption band at 3279 cm^{-1}. Presumably, H incorporation ($H_i^{\cdot}$) is charge-balanced by Ti reduction (Ti_{Ti}'), although our neutron irradiation study has demonstrated that these defects are decoupled. All Fe-bearing samples contain an additional absorption band at 3295 cm^{-1}. We have synthesized a number of rutile samples containing various trivalent and divalent cations, and we are able to demonstrate that additional absorption bands are due to $H_i^{\cdot}$ coupled with lower valance cation substitutions onto the octahedral site (in the case of Fe-bearing rutile this is Fe_{Ti}'). Neutron diffraction experiments have shown that H is located just off of a shared O-O edge in the rutile structure, close to a (½ ½ 0) position. Presumably, $H_i^{\cdot}$ sits on one of the O-O edges about one of the main octahedral sites containing a substitutional impurity, forming the defect cluster (M_{Ti}' - $H_i^{\cdot}$). This appears to be the main H incorporation mechanism in synthetic, lower-valency cation doped rutile. However, we also observe that NIR spectra from all samples still contain a small band at 3279 cm^{-1}, implying that in all samples some of the $H_i^{\cdot}$ remains decoupled. This is likely to have considerable implications for H mobility and electrical conductivity in rutile at elevated temperature, because this H could move rapidly through the crystal structure. Interestingly, comparison of IR spectra from synthetic and natural rutile appears to suggest

that in natural rutiles, most of the interstitial H remains decoupled from substitutional impurities. This could have important implications for how we consider H incorporation and mobility in other NAMs, particularly stishovite, which is isostructural with rutile.

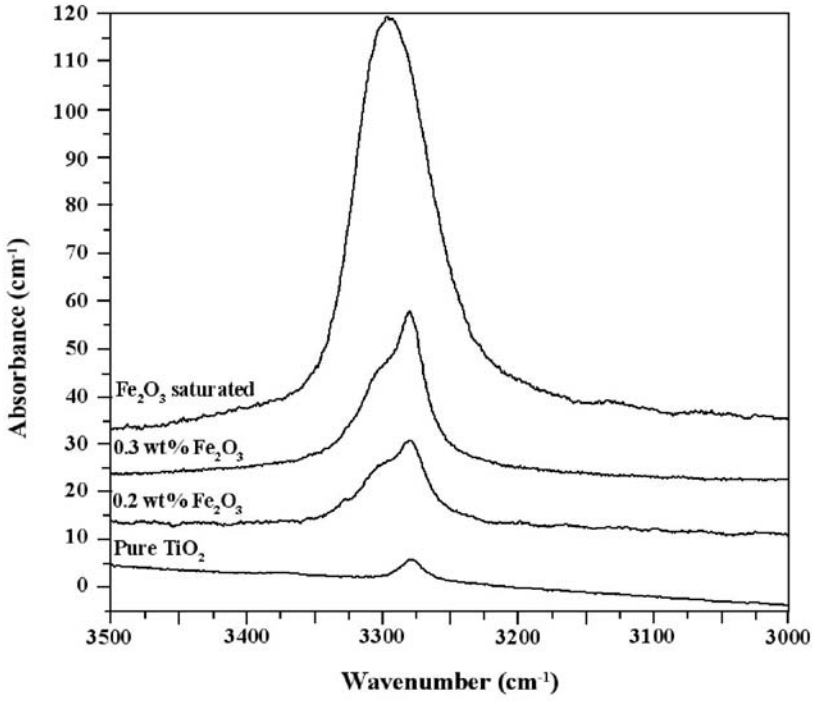

Fig. 3.7-4: OH stretching region of the NIR spectra shown in Fig. 3.7-3 (vertical offset rescaled).

c. *Hydration of olivine near the Earth's transition zone (J.R. Smyth, D.J. Frost, G.D. Bromiley and F. Nestola)*

Olivine is the most abundant mineral phase in most models of the upper mantle, so hydrogen uptake by olivine has been a major subject of investigation. Although nominally anhydrous, natural olivines can contain up to about 240 ppm (by weight) (ppmw) H_2O, they typically contain 100 ppmw or less. Olivines synthesized at pressures up to 13 GPa may contain considerably more, with up to 3500 ppmw H_2O reported in olivine at 12 GPa and 1100 °C in equilibrium with enstatite, and up to 9000 ppmw H_2O in forsterite synthesized at 12 GPa and 1100 °C in silica deficient compositions. Hydrogen in these amounts, if present in the Earth, would constitute a significant fraction of the total water budget of the planet. Even trace amounts of hydrogen can have a major effect on some physical properties such as deformation strength and electrical conductivity. In order to better quantify and understand the solubility of H in olivine at pressures near the 410 km discontinuity, we have undertaken a series of experiments to synthesize hydrous olivines under various conditions of silica activity and to characterize the effects on the crystal structure, FTIR spectra, and isothermal compressibility.

Olivines of approximate composition Fo_{95} and Fo_{100} were synthesized under hydrous conditions coexisting with clinohumite (silica undersaturated) and clinoenstatite (silica excess) in experiments at 12 GPa and 1250 ºC in the 5000-ton multianvil press. Synthesis experiments were carried out in multiple capsule experiments in which two 1.5 mm-diameter inner capsules containing the different compositions were placed inside a 3.5 mm-diameter outer capsule packed with brucite to maintain H activity. Heating time in each experiment was approximately five hours. The capsules were opened and liquid water was released on opening the outer capsule. The grain size of the run products ranged up to 300 μm. Phases were identified by Raman spectroscopy, X-ray powder diffraction and X-ray single crystal diffraction. The low silica-activity capsules contained olivine plus hydroxyl clinohumite; whereas the high silica activity capsules contained olivine plus clinoenstatite. Single crystals were oriented by X-ray diffraction and faceted grains prepared for infrared spectroscopy.

Polarized FTIR spectra indicate H_2O contents up to 8900 ppmw in olivines coexisting with clinohumite and up to 5000 ppmw in samples coexisting with clinoenstatite and melt under these conditions. Polarized IR spectra in the three principal optical directions for a pure magnesian sample equilibrated with clinohumite are shown in Fig. 3.7-5. The integrated absorbance of this specimen indicates approximately 8900 ppmw H_2O. The unit cell parameters of the hydrous specimens were determined to high precision using the Huber four-circle single-crystal diffractometer. We observe a significant expansion of the unit cell with hydration. The unit cell volume of an anhydrous synthetic forsterite is 290.109(17) $Å^3$; whereas the pure magnesian sample with 8900 ppmw H_2O has a cell volume of 290.503(19) $Å^3$. This gives an estimated unit cell volume of the hypothetical $Mg_2H_4O_4$ of 301.6$Å^3$ if all of the H is in the tetrahedral site as in hydrogarnet. The crystal structures of the samples were refined from single-crystal X-ray diffraction data. The silica activity appears to have a major effect on the hydration mechanism, with tetrahedral vacancies dominating in silica undersaturated samples and octahedral vacancies, principally in *M*2, dominating in silica-excess conditions. The silicon vacancies are seen as both decreased X-ray scattering from the Si site and volume expansion of the tetrahedral site. A simultaneous compression experiment to 7.1 GPa was conducted for the two sample at approximate composition Fo_{95}. The hydrous olivines are measurably more compressible than anhydrous olivine. The refined bulk modulus for the more hydrous sample (~ 8000 ppmw H_2O) is K_0 = 120 ± 1.5 GPa with K' = 7 compared to K_0 = 122 ±1.2 with K' = 6 for the less hydrous sample (~ 5000 ppmw H_2O). This compares to K_0 = 128 with K' = 5 for anhydrous olivine. The compression curves are compared in Fig. 3.7-6, which also clearly shows the excess volume of hydration relative to the volume effect of compression.

Olivine, the most abundant mineral of the upper mantle, is therefore a major potential reservoir for H in the Earth's interior. If fully saturated, the olivine phase of the upper mantle could hold more water than the entire hydrosphere. The increasing solubility of H in olivine with pressure indicates that olivine may serve as a major conduit by which H can be transported into the Transition Zone by subduction. Also, the compatibility of H in the mantle may increase by two orders of magnitude on an increase of pressure to 12 GPa.

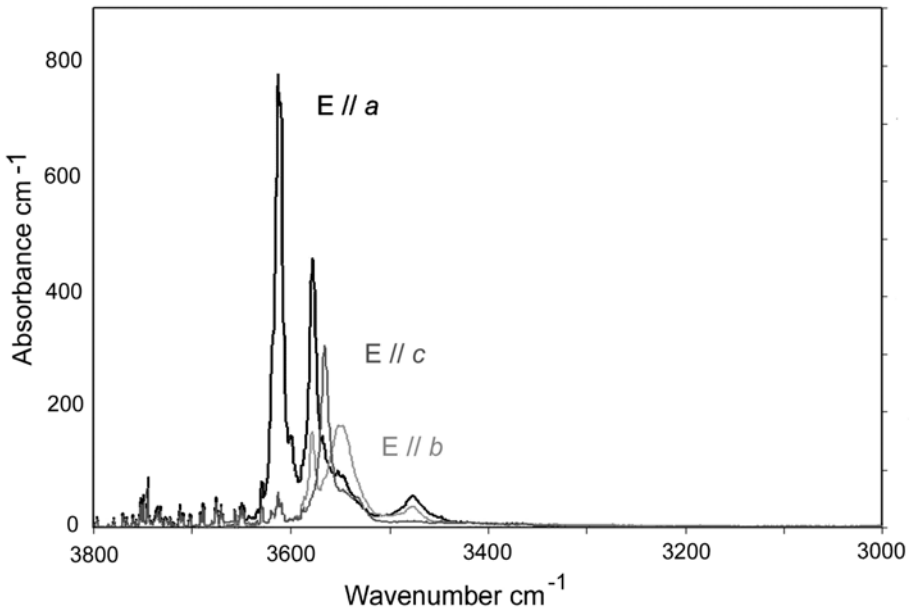

Fig. 3.7-5: Polarized infrared absorption spectra of hydrous forsterite equilibrated with clinohumite and melt at 12 GPa and 1250 °C (run SZ0408A). The sample contains approximately 8900 ppmw H_2O.

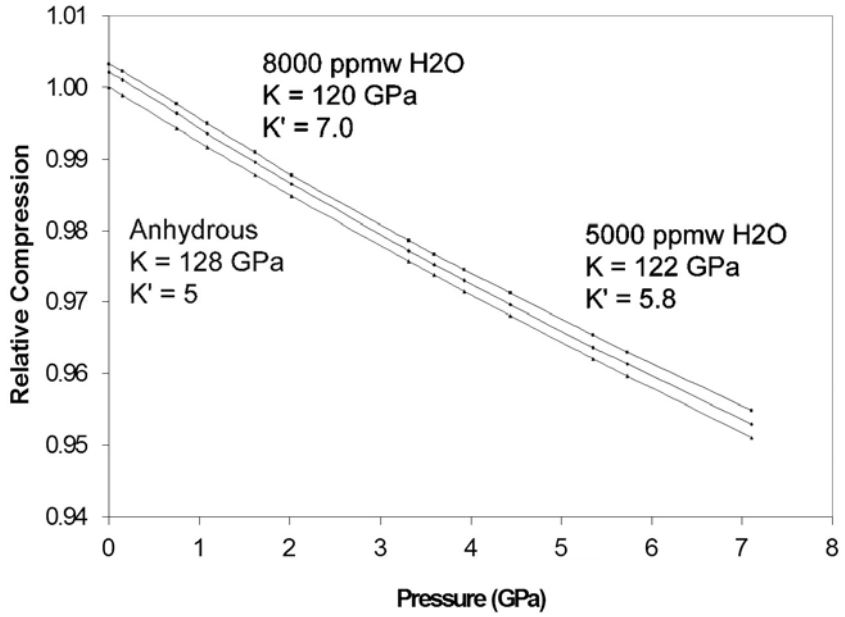

Fig. 3.7-6: Volume compression curves for Fo_{95} olivine containing ~ 8000 ppmw H_2O (top), 5000 ppmw H_2O (middle), and a calculated curve for anhydrous Fo95 composition (bottom). The volume compressions are plotted relative to the anhydrous, zero-pressure volume for Fo_{95} olivine. The hydrous samples are more compressible at low pressures, but become less compressible at higher pressures as *K*' increases with H content. Hydrous samples will be less dense than the anhydrous samples throughout the pressure range.

d. *Effect of temperature and pressure on water solubility in wadsleyite (S. Demouchy, E. Deloule/Nancy, D.J. Frost and H. Keppler/Tübingen)*

During the last decade, many studies have shown that minerals of the Earth's mantle can contain water-derived species. The minerals from the transition zone (TZ), particularly wadsleyite, can incorporate up to a few weight percent of water. Previous experimental studies indicate that the maximum solubility of water in wadsleyite may vary as a function of pressure and temperature. The aim of this study is to investigate rigorously the potential effect of temperature and pressure on the water solubility of iron-free wadsleyite. Samples were synthesized using a 1000t multianvil press at BGI, Bayreuth. One series of experiments were performed at a fixed pressure of 15 GPa and at various temperatures, and in a second series the temperature was fixed at 1200 °C and pressure was varied from 13 to 18 GPa. The starting material was a mixture of oxides and hydroxide powders yielding Mg_2SiO_4 + 5wt H_2O. The water content was quantified using SIMS IMS 1270 at CRPG, Nancy.

Results show that at 15 GPa, the water concentration decreases significantly with increasing temperature from 3 wt.% H_2O at 900 °C down to 1 wt.% H_2O at 1400 °C (Fig. 3.7-7a); the corresponding wadsleyite Mg/Si ratios increase from 1.79 to 1.93 over this temperature range. This effect appears to be largely due to changes in the water activity in the coexisting fluid, which becomes more silicate-rich at high temperature. The partition coefficient of water between wadsleyite and coexisting fluid is nearly independent of temperature. No significant effect of pressure on the water solubility was observed at a constant temperature of 1200 °C (~ 2.5 wt.% H_2O) (Fig. 3.7-7b). The Mg/Si ratio is stable at 1.82 ± 0.02. These results confirm the previous substitution mechanism proposed with Mg = 2H and suggest a strong decrease of the water partition coefficient between wadsleyite and ringwoodite with temperature.

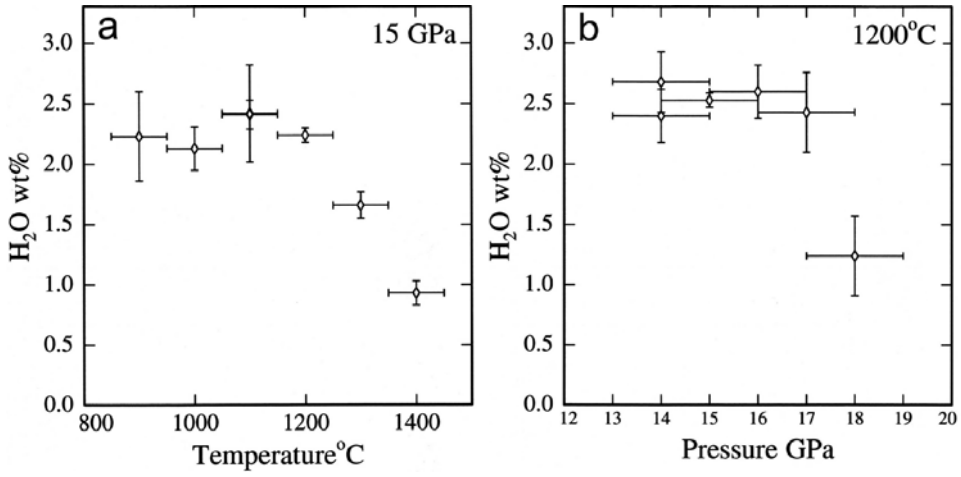

Fig. 3.7-7: (a) Water content of hydrous wadsleyite as a function of the temperature at a constant pressure of 15 GPa; (b) Water content of hydrous wadsleyite as a function of pressure at a constant temperature of 1200 °C. The water content of the sample at 18 GPa is highly uncertain because only one SIMS measurement could be performed on the sample.

e. *Influence of microstructure on nitrogen diffusion in diamonds (A.A. Shiryaev, D.J. Frost and F. Langenhorst, in collaboration with N. Johner/Karlsruhe)*

Diamond is a material of interest from both a fundamental and applied point of view. The dominant and most studied impurity is nitrogen, which is present in synthetic and natural diamonds in concentrations up to several thousand ppm. Nitrogen is considered to be incorporated into the diamond lattice as single substitutional atoms (so-called C-defects), while annealing leads to nitrogen diffusion and formation of more complex defects such as nitrogen pairs (A-defects) and complexes 4N+V (B-defects). The process of more complex defect formation is called "nitrogen aggregation", and several important investigations of the process kinetics have been performed, but discrepancies between values of activation energy of diffusion and other parameters still exist. In geosciences the degree of nitrogen aggregation is used for estimation of the time-temperature history of diamond storage in the mantle. However the results are often unrealistic, *e.g.* the mantle residence time of some diamonds extracted from the N aggregation behaviour is longer than the age of the Earth. It seems, therefore, that there may be physical processes that can enhance nitrogen diffusion, such as plastic deformation.

In our work we investigated the relationship between the microstructure of diamond and nitrogen diffusion. Two approaches were used to address this question. The first involved a comparison of nitrogen aggregation state in synthetic diamonds annealed in a multianvil apparatus under two different conditions: (a) under strong deformation using a mixture of hard silicates, and (b) under quasi-hydrostatic conditions using MgO as a pressure medium. The second approach involved examination of natural diamonds that were non-uniformly stressed due to mineral inclusions. In both approaches the spatial distribution of optically-active nitrogen defects was measured with infrared (IR) spectroscopy and compared with the distribution of lattice stresses and dislocations. Projection Synchrotron X-ray topography (XRT) at ANKA (Karlsruhe) on the FLUO-TOPO beamline and transmission electron microscopy (TEM) were used as methods to reveal the distribution of dislocations and other extended defects.

Before the multianvil experiments the synthetic diamonds were of high crystalline quality as revealed by XRT. Dislocation bundles, stacking faults and some other defects are clearly visible (Fig. 3.7-8a). Natural diamonds are on average more deformed and only a few of them gave high quality topographs. Annealing and compression of synthetic diamonds in "soft" MgO did not create a high density of extended defects. However, the crystalline quality became poor through annealing in MgO and individual extended defects are not resolvable. XRT permits to distinguish between strongly and moderately deformed parts of the samples. Annealing and compression in hard silicates produces severe deformation, which is comparable to heavily deformed natural diamonds.

The IR study of the nitrogen aggregation process in deformed diamonds yielded unexpected results: the nitrogen aggregation rate under deformation is slower than in reference samples.

In order to explain this behaviour we studied our samples using TEM, and found that the microstructure of annealed diamonds differs depending on the pressure medium. Annealing in MgO does not disturb the lattice significantly (dislocation density is low), annealing in hard silicates produces numerous microtwins and stacking faults (Fig. 3.7-8b) and annealing in SiC or in diamond powders creates a heterogeneous distribution of dislocations (Fig. 3.7-8c). It is known that vacancies accelerate nitrogen diffusion. Therefore, a low concentration of available vacancies would slow down the diffusion rate. A plausible explanation for the slow diffusion in deformed diamond is that mechanical stacking faults and microtwins created during annealing in hard silicates serve as sinks for vacancies.

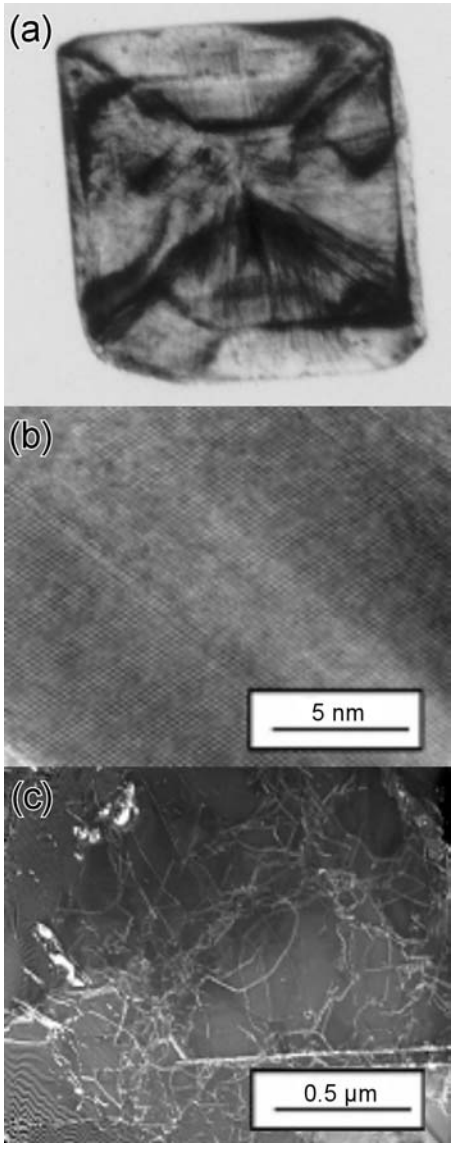

Fig. 3.7-8a: X-ray topograph of synthetic diamond prior to HPHT treatment. Reflection (1 $\bar{1}$ 3), exposure time 0.1 sec. The width of the diamond is approximately 3 mm.

Fig. 3.7-8b: HRTEM photograph of stacking fault and microtwins in diamond deformed in a silicate mixture.

Fig. 3.7-8c: TEM photograph of dislocations and stacking faults in diamond deformed in SiC.

Simultaneously, we are investigating natural diamonds with mineral inclusions, where inclusions are surrounded by stress fields. The distribution of different nitrogen defects was monitored using an IR spectrometer equipped with a Focal Plane Array detector – a state-of the-art technology permitting very fast visualization of IR-active defects. First results indicate

that degree of nitrogen aggregation is indeed higher in the stressed domains. Therefore, comparison of our experimental results with observations on natural samples suggests that the microstructure of diamonds is an important factor for the diffusion behaviour. Zones of high dislocation density seem to accelerate nitrogen diffusion; whereas numerous stacking faults and microtwins separating almost perfect crystalline domains inhibit diffusion.

f. *Hydrogen diffusion in diamonds (A.A. Shiryaev and F. Gaillard, in collaboration with D. Grambole/Rossendorf)*

According to mass-spectrometric studies and nuclear probes, hydrogen could be present in diamonds in concentrations up to 7000 atomic ppm (at.ppm). It is known that the surface of diamond has a high affinity for hydrogen. However, its position in the crystalline lattice, mode of incorporation, correlation with other impurities, diffusivity and many other properties are still poorly understood. In order to better constrain hydrogen behaviour we are performing an investigation of hydrogen diffusion in natural and synthetic monocrystalline diamonds in their as-received states and after exposure to gaseous hydrogen. Besides infrared spectroscopy we are using Elastic Recoil Detection Analysis (ERDA) (FZ Rossendorf) which is an ideal tool to study hydrogen concentration and diffusion. The use of micro-ERDA set up with a beam size of 200×350 microns allows investigation of spatial inhomogeneities in hydrogen distribution. To the best of our knowledge this is the first detailed study of hydrogen diffusion in representative sets of diamonds of different types.

Natural and synthetic diamonds with variable concentrations (0-2000 at.ppm) and different types of nitrogen point defects were annealed at 1173 K in an $Ar+H_2$ mixture for times ranging from 2 to 72 hours. In nearly all samples studied, hydrogen concentrations were close to the detection limit of the technique, *i.e.* < 200 at.ppm. Hydrogen diffusivity in diamond at our experimental conditions is surprisingly slow: at depths larger than 30-50 nm, only a background signal was observed. Deep (~ 200 nm) penetration of large quantities of hydrogen was found in only one case, but it could be related to cracks and other visible imperfections at the analysis spot. At the same time radiation-induced loss of hydrogen was observed for some samples. Evaluation of radiation-assisted hydrogen diffusion is now underway.

No obvious correlation between H diffusivity and optically-active nitrogen defects was found. Moreover, the absolute concentration of hydrogen given by ERDA does not correspond to H-related optical features: while ERDA showed the presence of hydrogen in all samples, only two of the samples showed minor infrared absorption by H-related defects. This observation indicates that a significant fraction of hydrogen is present in an optically-inactive form.

Our study provides information regarding diamond growth in nature. Since H concentration in natural diamonds could be quite high, it is important to establish the source of this impurity. We have shown that hydrogen diffusion in diamonds is low, at least when H is in molecular

form. It is known that the surface of diamond has a high affinity for hydrogen. Apparently, the major fraction of hydrogen is trapped during diamond growth, and its concentration does not change significantly during subsequent mantle storage. There is some evidence, although indirect, that in diamond hydrogen diffusion in molecular form is very slow; whereas in atomic form hydrogen could be more mobile. Direct experimental verification of this possibility and investigation of growth sector variations in H concentration are underway.

g. *Complex study of microinclusions and fluids in fibrous diamonds (A.A. Shiryaev, in collaboration with D. Zedgenizov/Novosibirsk; O. Navon and E. Israeli/Jerusalem; E. Hauri/ Washington DC)*

Despite extensive efforts, the genesis of natural diamonds is still a matter of debate. We lack a clear physical model of diamond growth and chemistry of the growth medium, and even the source of carbon is unknown. One of the promising methods to understand the chemistry of the growth medium is the investigation of inclusions in diamond. Due to the chemical and physical inertness of the diamond matrix, many of these inclusions remain intact and permit reconstruction of the composition of the growth medium. Inclusions in diamond provide important information on the environment in which diamonds crystallize. A specific subclass of natural diamonds – fibrous diamonds – trap fluids, and thus provide unique information about fluids from the upper mantle and contribute to our understanding of diamond growth conditions.

In this study we applied several complementary local techniques for a comprehensive investigation of microinclusions (1-2 microns in size) with regard to chemistry and phase composition, and carbon and nitrogen isotopes within fibrous diamonds from different locations. This approach permitted us to monitor the evolution and changes of fluids and isotopes during different growth steps. Similar to previous investigations of fibrous diamonds, we observed numerous infrared (IR) absorption bands due to minerals residing in the microinclusions. It is interesting to note that the mineral species in fibrous diamonds from different world deposits (Africa, Canada, Yakutia, Brasil) are broadly similar: phosphates (*e.g.*, apatite), carbonates (probably ankerite), and silicates are among the most common minerals. Shifts of quartz and CO_2 absorption bands indicate that the inclusions are under confining pressures in the range 1.5-2.5 GPa. A common feature of the IR spectra of many fibrous diamonds is the absorption ascribed to a silicate melt phase (around 1000 and 1100 cm^{-1}). Chemical analysis of individual microinclusions indicates mixing between hydrous-silicic and carbonatitic fluids/melts.

A remarkable feature of fibrous diamonds is that microinclusions also contain CO_2 and different water solutions and ice polymorphs. To obtain detailed information about these fluids we performed IR measurements in a temperature range from -80° to 450 °C. These data are currently being analysed, but from a preliminary inspection it is immediately evident that

fluid compositions differ from one sample to another. In many spectra sharp lines in the region of OH valence vibrations are observed, indicating that minerals in inclusions contain OH groups. Possibly, some of the observed lines are related to OH groups in talc and/or serpentine. Interestingly, nitrogen concentrations determined from IR absorption spectra closely correspond to values obtained using Secondary Ion Mass Spectrometry (SIMS). This suggests that the nitrogen content of fluid microinclusions is low.

Point-by-point measurements of nitrogen and carbon isotopic compositions of the diamond matrix were made by SIMS. As a general observation we found that while the central parts of all samples can have widely different carbon isotopic compositions, the periphery is essentially similar for all the stones. Another important result is that in the majority of cases, nitrogen behaviour is uncorrelated with carbon. Apart from differences in isotopic composition of different growth zones, we observed progressive enrichment in heavy isotopes towards the rims of the diamonds. At least two explanations could be proposed: a) in the diamonds studied, growth and nitrogen incorporation were governed by kinetics with preferential incorporation of light isotopes into the growing crystals in *a closed system*; and b) the growth volume became progressively more oxidised. Of course, both mechanisms could act simultaneously and do not exclude each other. Progressive oxidation in the case of some of the diamonds is supported by evolution of the chemical composition of microinclusions. It is notable that in some cases the evolution could be observed even within a single growth zone as revealed by cathodoluminescence.

3.8 Physics and Chemistry of Melts and Magmas

The chemical evolution of the Earth has occurred primarily through the generation of magma (partially-molten rock) by melting at depth, transport of the magma and its subsequent crystallization. Experimental studies of magmatic processes, through investigations of both melting/crystallization relationships and the physical and chemical properties of melts and magmas, are therefore essential for understanding how the chemistry and structure of the Earth have evolved in the past and how they continue to do so at the present time.

Magmatic processes played a major role during the very early history of the Earth and other terrestrial planets. During accretion from the solar nebula, the impacts of small asteroid-size bodies (planetesimals) on the early Earth likely caused temperatures to become so high that the planet melted on a global scale, thus producing a "magma ocean". In addition, it is likely that the Moon formed as a result of a giant impact when the Earth collided with a body approximately the size of Mars. This event alone is likely to have formed a magma ocean that may have been as deep as 1500-2000 km or more. The formation of a magma ocean during the early history of the Earth allowed early chemical differentiation to take place. First, molten Fe-rich metal was able to separate easily from silicate melt and sink gravitationally to form the Earth's core. Second, crystallization of the silicate melt may have resulted in chemical differentiation through the separation (by sinking or floating) of crystals. The dynamics of magma ocean convection, cooling and crystallization depend on the transport properties of silicate liquid at high pressures. Two contributions in this section describe the results of investigations of transport properties (viscosity and diffusion) of peridotite liquid at pressures up to 16 GPa and 2500 K.

Investigations of the properties of magma are essential for understanding the nature and products of volcanic eruptions that occur at the present time. Such studies are therefore important for predicting the nature of volcanism – for example, whether eruptions are likely to be explosive. A key factor in this respect concerns the rate at which dissolved volatiles (*e.g.* water and carbon dioxide) can be exsolved during magma ascent. Disequilibrium degassing, as described below for Vesuvuis magmas, can play an important role in this respect. In addition to differentiation by crystallization, the chemical composition of magmas can evolve through contamination by the rocks through which they are erupted. It is shown that reaction of magmas with limestones and marbles of the continental crust controls compositions of calc-alkaline rocks from Italy. Such reaction also explains large emissions of carbon dioxide that have been observed around Italian volcanoes.

An important geophysical method for recognizing the presence of magma at depth in the Earth's crust involves electrical conductivity measurements. In order to interpret such field measurements, laboratory investigations of the electrical conductivity of magma as a function of composition and extent of crystallization are required. Such data are presented below for basaltic magmas and emphasis is placed of the importance of the composition of the residual

liquid during the crystallization process. In a further contribution, laboratory measurements are used to show that magma may be present at the present time below the Tibetan plateau.

The final contribution in this section is concerned with the role of iron in controlling the structure and chemical/physical properties of silicate liquids. Here, quenched glasses have been studied because spectroscopic measurements on liquids are difficult or impossible.

a. *Viscosity of peridotite liquid at high pressure (C. Liebske, B. Schmickler, H. Terasaki and D.C. Rubie, in collaboration with A. Suzuki and R. Ando/Sendai, K. Funakoshi/Hyogo and B.T. Poe/Rome)*

Models for the accretion of the Earth include a period of substantial melting of the planet and the formation of a deep magma ocean as a result of bombardment of planetesimals and at least one giant (moon-forming) impact. The viscosity of molten mantle as a function of depth is a crucial parameter in modelling the fluid dynamical properties of a magma ocean.

The viscosity of peridotite liquid, as a likely magma ocean constituent, has been investigated by *in situ* falling sphere viscometry on beamline BL04B1 at SPring-8 synchrotron radiation facility in Japan. The experimental procedure has been described in detail in the 2003 Annual Report (p. 136). In this study we extended the conditions of the experimental investigation to pressures and temperatures of 13 GPa and 2500 K. The experimental viscosity data show that viscosity increases as a function of pressure up to 9 GPa, but decreases again between 9 and 13 GPa. Recent viscosity measurements on peridotite liquid performed at one atmosphere at temperatures ranging from the glass-transition to above the liquidus (Dingwell *et al.* 2004, EPSL, 226, 127) were used to constrain viscosity as a function of pressure and temperature.

We use a non-Arrhenian Vogel-Fulcher-Tamman (VFT) equation, which has been modified to account for the effect of pressure, to parameterise all available viscosity data for peridotite liquid such that

$$\log \eta = A_{VFT} + \frac{B_{VFT} + C(P)}{T - T_0}$$

with the pressure dependent term being expressed as

$$C(P) = C_1 P + C_2 P^2 + C_3 P^3$$

where A_{VFT}, B_{VFT}, and T_0 are constants. A_{VFT} represents the viscosity η at infinite temperature, B_{VFT} corresponds to an energy barrier of viscous flow and T_0 can be regarded as the temperature at infinite viscosity. $C(P)$ is an empirical relation, in which C_1, C_2 and C_3 are constants, that describes the pressure dependence of viscosity. Analysis of one-atmosphere viscosity data of silicate liquids over a wide range of chemical compositions and

temperatures, from above the liquidus to the glass-transition, indicate that A_{VFT} may be constrained by a single value of -4.3 (± 0.7) (Russell *et al.* 2003, Am Mineral. 88, 1390), which physically corresponds to a high temperature limit of viscosity. Fitting the above VFT equation to all available viscosity data for peridotite liquid over pressure and temperature ranges from 0.1 MPa to 13 GPa and 1000-2500 K with A_{VFT}= -4.3 reproduces experimental values to within 0.08 log-units on average with a maximum deviation of 0.23 log-units. Experimentally determined viscosities of this study and fits to the data are shown in Fig. 3.8-1. Given the wide range of experimental conditions and considering the pressure and temperature uncertainties in falling sphere viscometry, this represents an excellent fit to the data.

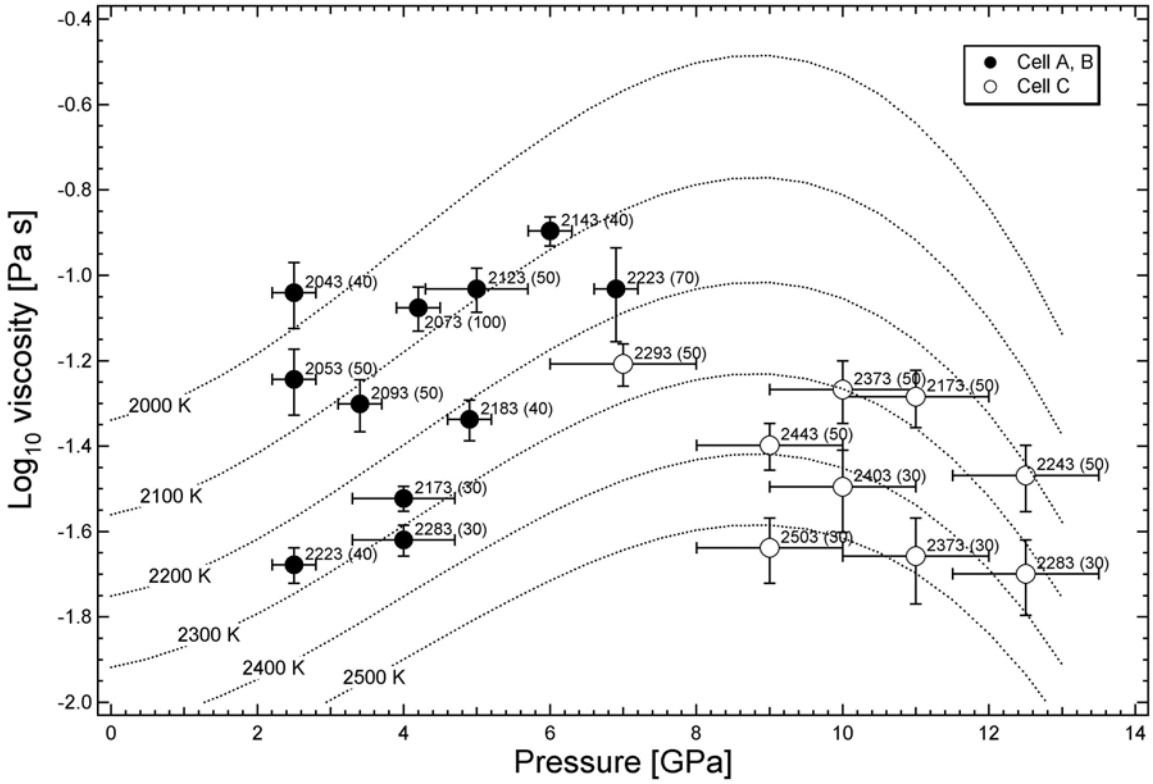

Fig. 3.8-1: Experimentally determined viscosities from this study as a function of pressure. Dotted lines are isotherms calculated from the modified VFT Equation. Filled and open circles represent results obtained from different multianvil pressure cells. Experimental data are reproduced by the fit to within an average deviation of 0.08 log units. Numbers adjacent to data points are experimental run temperatures and their uncertainties.

The presented expression for peridotite liquid viscosity can be used to calculate magma ocean viscosities along an adiabat. Assuming a magma ocean depth of 1800 km, as has been previously suggested, we calculate the viscosity to be on the order of 3 mPa s and conclude that it changes by less than half an order of magnitude to a depth of 400 km (13 GPa). This value is extremely low and is close to the viscosity of water at ambient conditions (~ 1 mPa

s). Unfortunately, the current model cannot be used to extrapolate viscosities to pressures greater than 13 GPa, because of the empirical nature of the fitted pressure dependence.

b. *Diffusion in peridotite liquid at high pressure (B. Schmickler, D.C. Rubie and C. Liebske, in collaboration with C. Holzapfel/Saarbrücken)*

As discussed in the previous contribution, the early Earth is likely to have melted to a large extent due to the conversion of kinetic energy to heat during the accretion of planetesimals, thus resulting in the formation of a deep terrestrial magma ocean. The transport properties of such a global magma body would have profoundly influenced convection dynamics and crystallization processes, and hence would have controlled the early chemical differentiation of the Earth. High-pressure viscosity and diffusivity data for magma-ocean liquids are therefore crucial for modelling the large-scale differentiation processes that determined the formation of the Earth's metallic core and early crystallization of the mantle. For these reasons, we focused on the effect of pressure on diffusivity and viscous flow in peridotite liquid, which is the most likely constituent of a primordial magma ocean. Both chemical-diffusion and self-diffusion experiments have been performed up to 23 GPa and 2573 K using a multianvil apparatus. The diffusion coefficients of network formers (*e.g.* Si and O) and network modifiers in peridotite liquid were determined from analysed diffusion profiles. Viscosities, calculated from oxygen and silicon self-diffusion coefficients using the Eyring equation, were compared to direct viscosity data determined by falling-sphere viscometry (see contribution above by Liebske, *et al.*) up to 13 GPa. This approach is used to establish the Eyring relation as a transport model for peridotite liquid and to provide insights into the dynamics of melt structures and the nature of diffusing species.

Our results show that oxygen and silicon self-diffusion coefficients are identical, within error, over the range of experimental P-T conditions, while diffusion coefficients for the network modifiers, Mg and Ca, are always faster than the network-former diffusivities. Chemical diffusion rates for Co and Ni are orders of magnitude faster than the rates of self-diffusion of the network formers. At 2100 °C, self-diffusivities of Si and O decrease with increasing pressure up to 9-10 GPa (Fig. 3.8-2), which is consistent with the trend observed in the viscosity data (Fig. 3.8-1). In the pressure range 9 to 18 GPa (experiments up to 23 GPa are not yet analysed) the diffusivity of Si and O appears to increase again. Activation volumes for self-diffusion are approximately 3 (± 1) cm^3/mol in the pressure range up to 9 GPa and about -2 cm^3/mol in the pressure range 9-16 GPa. Activation energies for self-diffusion are approximately 200 (±120) kJ/mol for pressures up to 9 GPa and 180 (±100) kJ/mol in the range of 9-16 GPa. While the self-diffusivity of Mg appears to remain unaffected by pressure, Co, Ni and Ca diffusion coefficients decrease with pressure up to 9 GPa. The observation that Mg and Ca diffusion coefficients show different behaviour with increasing pressure implies that these network modifiers occupy different sites.

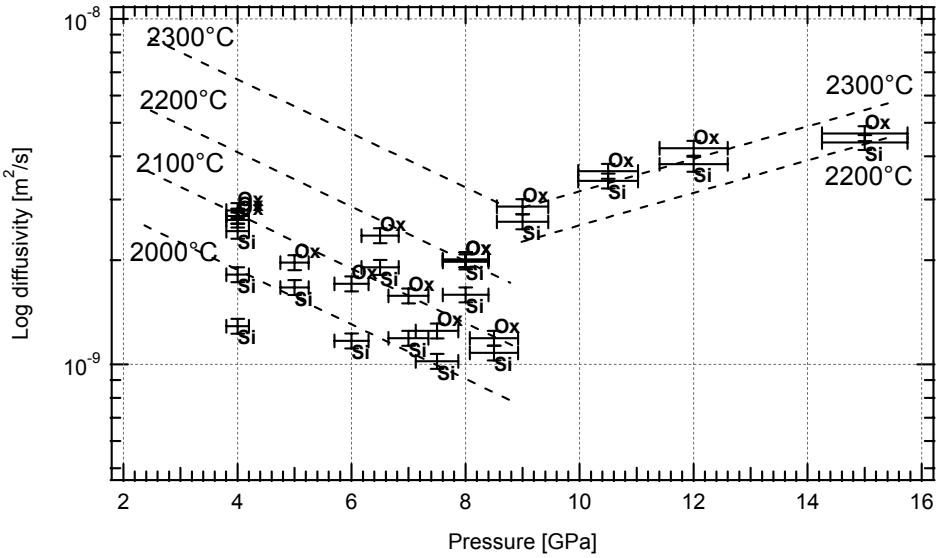

Fig. 3.8-2: Oxygen and silicon self-diffusion coefficients in peridotite liquid decrease with pressure up to 9 Gpa, but increase again in the pressure range 9-16 GPa.

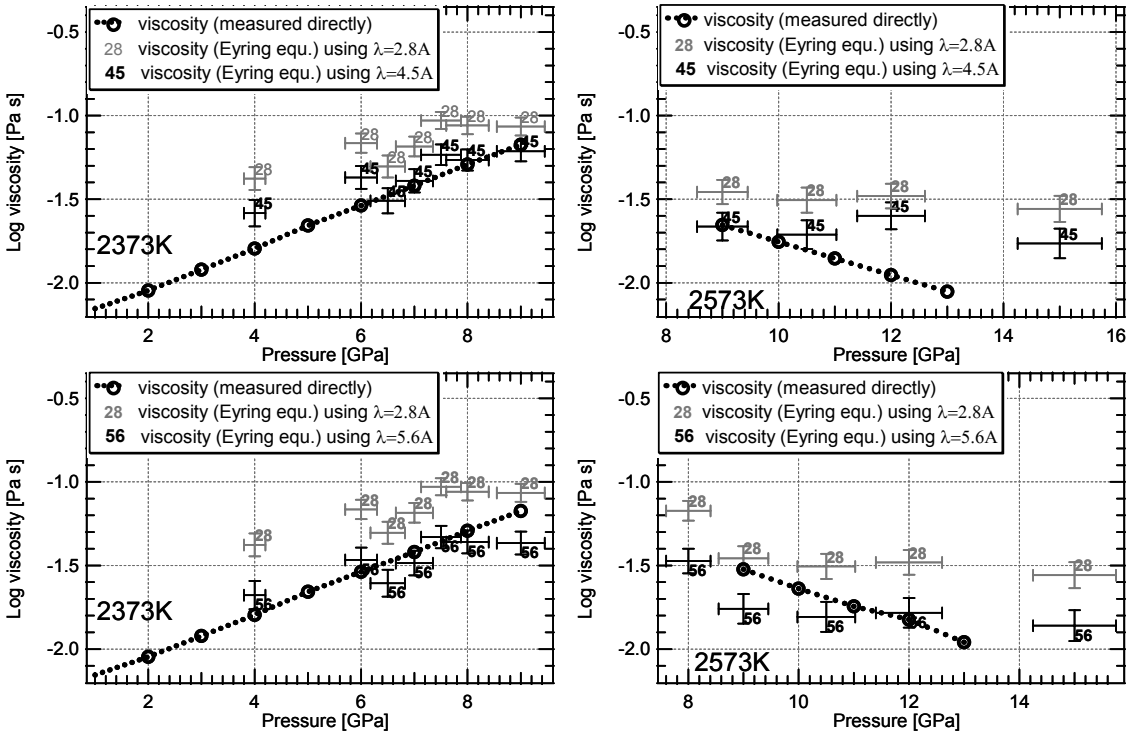

Fig. 3.8-3: Viscosities calculated from O and Si self-diffusion coefficients using the Eyring relation for translation distances of 2.8 and 5.6 Å. Viscosities determined directly by falling-sphere viscometry are shown for comparison. Eyring-derived viscosities calculated with a translation distance of 2.8 Å (the size of an oxygen anion) are significantly higher than the measured viscosities. More consistent values are obtained when using a translation distance of 4.5-5.6 Å, which suggests that the network diffusing species has molecular characteristics and could be a SiO_4^{4-} anion.

The change in the activation volume at 9-10 GPa observed in both diffusivity and viscosity data for depolymerised liquids provides the first insights into possible structural changes in peridotite liquid with increasing pressure, which might involve the formation of high-coordinated species above 9 GPa. Because spectroscopic data are lacking, activation volumes and activation energies are the only parameters to which the properties and structures of depolymerised melts can be related at present. The similarity of Si and O self-diffusion coefficients, with activation energies and activation volumes that are identical within the uncertainties, implies a cooperative diffusion mechanism for these species, most likely involving the formation and disassociation of a high-coordinated species. Considering the relatively low activation energies for silicon and oxygen, a feasible mechanism would be the diffusion of SiO_4^{4-} anions, which does not require breaking any Si-O bonds and allows silicon and oxygen to diffuse together. The application of the Eyring equation, which relates diffusivity to viscosity, also indicates the translation distance (λ) to be about twice the size of an oxygen anion (2 x 2.8 Å, see Fig. 3.8-3), and hence suggests a molecular nature of the network diffusing species. However, further investigations are still required to clarify the extent of the structural rearrangements that occur during decompression in depolymerised silicate liquids.

c. *Towards an experimental reconstruction of the dynamics of degassing during the ascent of Vesuvius magmas (G. Iacono Marziano and F. Gaillard, in collaboration with B.C. Schmidt/Göttingen)*

The exsolution of dissolved volatiles during magma decompression provides a major driving force for magma ascent and, in particular, the volatile degassing behaviour determines the explosive nature of related volcanic eruptions. Therefore knowing the mechanisms of volatile degassing is essential for understanding eruption dynamics.

This research is an extension of the project "Equilibrium and disequilibrium degassing of a phonolitic melt simulated by decompression experiments" (see Annual Report 2003), in which we investigated if equilibrium could be maintained during the degassing of a phonolitic melt. This previous study suggested that deviations from equilibrium can occur at high decompression rates (high magma ascent rates). In the present research we emphasize the occurrence of delayed degassing during magma ascent and the factors that can control it, and attempt to simulate the degassing behaviour of Vesuvius phonolitic magmas. In particular we investigate the effects of temperature and of CO_2 dissolution in the melt, given that Vesuvius phonolites are CO_2-rich and have eruptive temperatures of 800-900 °C (150-200 °C less than the experimental temperature we used in the earlier experiments).

As in the previous project, the investigated composition was the phonolite of the 79AD Vesuvius plinian eruption and the fluid phase consisted of pure H_2O and a H_2O+CO_2 mixture (X_{H2O}=0.5). The decompression experiments were performed in vertically-operating TZM

pressure vessels in the pressure range 20-200 MPa. H_2O and CO_2 concentrations in the quenched glasses were determined by infrared spectroscopy (NIR and MIR) and by electron microprobe analysis.

Experiments involving pure H_2O were decompressed to low pressures (10 or 20 MPa) at fast rates (5 and 1.7 MPa/s) and show that high water over-saturations can be released rapidly at pressures < 50 MPa (1.5 km depth). Figure 3.8-4 shows the disequilibrium degassing path for a decompression rate of 1.7 MPa/s, compared to the equilibrium one. Low-pressure exsolution results in a large expansion of the magma: this is because the molar volume of water is larger in the fluid phase than in the melt, with the difference increasing substantially with decreasing pressure (one order of magnitude at 50 MPa, two orders of magnitudes at 10 MPa). The consequence is an upward acceleration of the magma that results in sudden fragmentation.

The main effects of decreasing temperature on the degassing of water are a decrease in the diffusion rate of H_2O in the melt and an increase in the melt viscosity; these factors control the nucleation and growth of bubbles during decompression. The experiments carried out at 950 °C, otherwise under the same conditions as the experiments performed at 1050 °C, reveal different bubble nucleation behaviour: homogeneous nucleation is triggered in the melt also at a decompression rate of 0.17 MPa/s. Measurements of water contents in these samples are in progress.

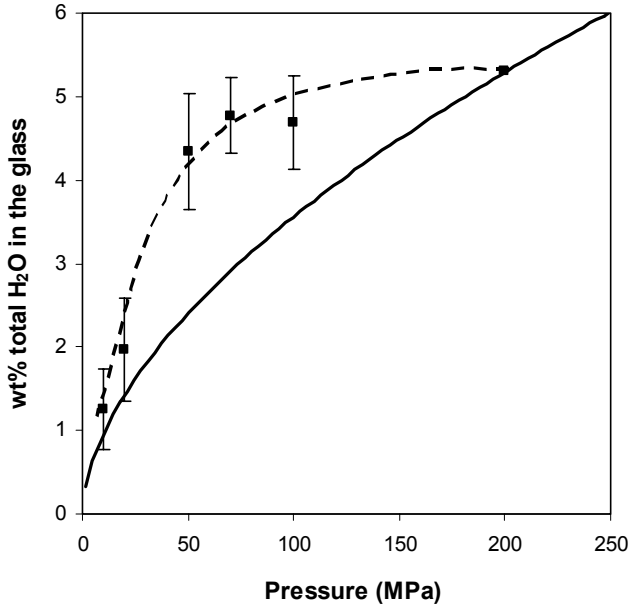

Fig 3.8-4: Disequilibrium degassing path for a decompression rate of 1.7 MPa/s (pure H_2O experiments at 1050 °C). The symbols represent the average water content of the glasses at the final pressure at which the decompression experiments were quenched; the initial pressure was always 200 MPa. The error bars indicate the standard deviation of the analyses, reflecting the inhomogeneous distribution of water in the glasses. The dashed line shows the trend of the data (disequilibrium degassing path), while the solid line shows the equilibrium degassing path, based on solubility experiments.

At 50 MPa the experiments involving a mixed H_2O-CO_2 fluid phase show a higher degree of water oversaturation than the pure H_2O experiments, indicating that the presence of CO_2 delays the exsolution of water. Semi-quantitative analyses of CO_3^{2-} groups dissolved in the quenched glasses show disequilibrium degassing behaviour also for CO_2. Once again the experiments conducted at 20 MPa reveal almost complete degassing. In this case the explosivity of the process is higher than in the case of pure H_2O and is a consequence of the larger amount of exsolving volatiles and the lower exsolution pressure (which results in higher expansion).

These results demonstrate how the dissolution of CO_2 in phonolitic magma can increase the explosive potential of the magma itself and thus controls the nature of the related eruption.

d. *Understanding the origin of calc-alkaline and silica-undersaturated magmas and the source of massive CO_2 emissions in Italy (G. Iacono Marziano and F. Gaillard, in collaboration with D. Dolfi/Rome)*

Volcanism in Italy is extremely variable in terms of the chemistry of erupted products and the geological settings of the different volcanoes. Italian volcanoes produce magmas that lie along a potassium-rich *calcalkaline* magmatic trend (shoshonitic) ranging from relatively primitive basalts (Stromboli, K-rich basalt) to more evolved lavas, and ultimately rhyolites (Vulcano Island). Additionally, some volcanoes, typically the famous Mount Vesuvius, produced magmas lying along silica-*undersaturated* trends characterized by tephrite and phonolite end-members (Fig. 3.8-5). To interpret this volcanic variability, a model involving a compositionally-heterogeneous mantle, at depth, has been the most popular explanation. However, Italian volcanoes present some common features, such as a global enrichment of erupted rocks in potassium and some large CO_2 emissions (Italy contributes 20 % of the global CO_2 naturally emitted by the Earth's volcanoes). This study aims at finding a common source for the "calk-alkaline" and the "undersaturated" trends by showing experimentally that primitive basaltic magma evolves to tephritic magma as the result of interaction with carbonates, a dominant component of the continental crust in Italy.

The *calcalkaline* series is characterized by early and massive crystallization of olivine from hydrous magma leading to a progressive enrichment of the residual liquid in silica and alkalis (Fig. 3.8-5). Classically, the differentiation of *calcalkaline* basalt leads to andesite and could also produce rhyolite magma. This trend is generally observed in Italian islands, far from any continental crust. When passing through the continental carbonate crust, the magma tends to become silica-*undersaturated*: in addition to becoming poorer in silica it becomes extremely alkali rich.

We performed experiments in which basalt from Stromboli was mixed with Carrara marble in various proportions (0, 5, 10, 20 wt.%) at high temperature and variable pressures (0.1 to 40

MPa). The results obtained indicate that the mixing of basalt with carbonate produces a liquid low in silica and high in alkalis that matches the chemical characteristics of tephrite liquid. The carbonate breaks down and liberates CaO into the silicate liquid and CO_2 mainly into the coexisting fluid phase. The CaO in the liquid destabilizes olivine, which is normally the liquidus phase, and promotes massive crystallization of Ca-rich pyroxenes (containing ~ 20-24 wt.% CaO). Such Ca-rich pyroxenes have been observed in tephrite lavas on Mount Vesuvius. As the silica content of pyroxene is, in contrast to olivine, higher than the silica content of the residual liquid, the carbonate-basalt mixing leads to the formation of a silica-poor residual liquid. The degree of mixing correlates with the degree of silica under-saturation and alkali-enrichment. Interestingly, most of the CO_2 derived from the breakdown of carbonate cannot be dissolved in the magma because of its low solubility in comparison to the solubility of water. First, this offers a source for the large emissions of CO_2 that have been measured around Italian volcanoes. Second, the large amounts of liberated CO_2 forms bubbles that temporarily coexist in the magma, which dramatically affects the eruptive dynamics of the system. Some primitive magmas of Vesuvius have been shown recently to be in equilibrium with a fluid composed of 90 % CO_2 and 10 % H_2O.

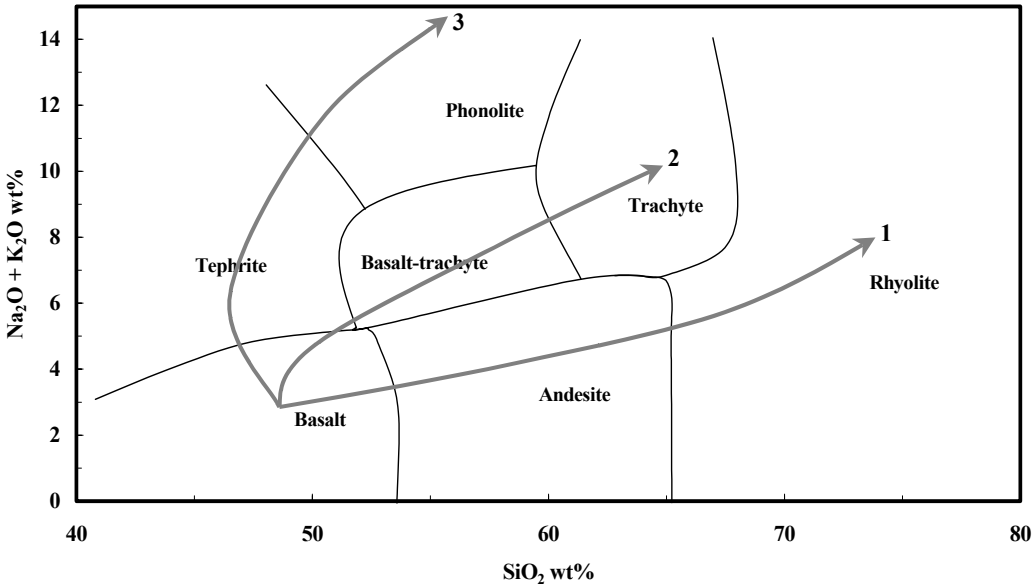

Fig. 3.8-5: Simplified diagram of total alkalis plotted against silica concentration showing the different magmatic evolution paths. 1: Calc-alkaline, 2: Shoshonite, 3: Silica undersaturated. Mixing basalt with carbonate results in either the shoshonite or silica-undersaturated trend, depending on the amount of carbonate added.

The genetic model we propose here probably applies in other regions where silica-undersaturated magmas are produced. For example, carbonatitic magmas (molten carbonates) are produced in conjunction with silica-undersaturated series in the African rift valley. A generalization of our model would imply that the global volcanic CO_2 flux into the Earth's atmosphere is strongly affected by silica-undersaturated magma production.

e. *The electrical conductivity of magma during crystallization is controlled by the residual liquid composition (F. Gaillard and G. Iacono Marziano)*

Magnetotelluric surveys have revealed many regions within the Earth's interior showing anomalously high electrical conductivities that are often attributed, on the basis of independent geological and experimental constraints, to the presence of magmas stored within the Earth. The electrical signature of these magmatic reservoirs, collected at the surface, could be used to infer the maturity reached by the magma, at depth, in terms of volatile abundances, temperature and crystal content, if appropriate laboratory studies are available. Most terrestrial magmas are composed of silicate liquid plus a fraction of crystals ranging from 0 to 80 %, where the liquid phase is the dominant conductor and the solid crystals can be regarded as insulators. The issue addressed here is to elucidate the extent of a decrease in conductivity associated with the partial crystallization of magma.

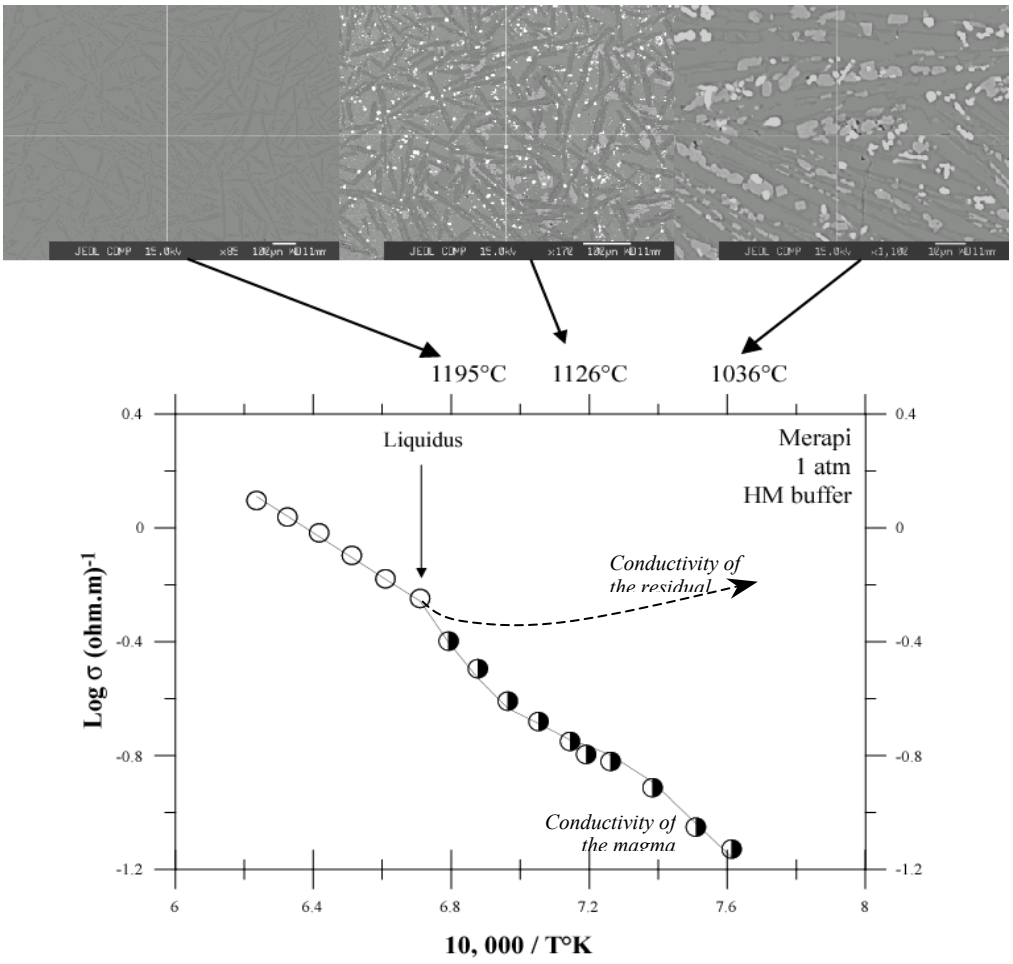

Fig. 3.8-6: Change in electrical conductivity of basalt (from the Merapi volcano) as a function of temperature and crystallization. Open symbols are results obtained above the liquidus temperature. Half-open symbols show measurements on partially crystallized samples. SEM pictures of partially crystallized samples are shown at the top (from left to right, 20, 50, 80 % of crystallization). The dashed line shows the electrical conductivity of the residual liquid.

The electrical conductivity of a basaltic magma as a function of crystallization has been investigated experimentally in the temperature range 1350-1036 °C. Large samples of silicate melt containing a range of contents of homogeneously distributed crystals were synthesized in a gas-mixing 1 atm furnace. These samples were analyzed by electron microprobe and the proportion of phases was determined as a function of temperature. Depending on temperature, the phase assembages included silicate liquid, +/- plagioclase, +/- pyroxene, +/- Fe-Ti oxides. The crystal content varied from 0 to 80 wt.%. In response to partial crystallization, the residual liquid underwent changes in composition evolving from basalt to andesite to dacite. The electrical conductivity of the partially crystallized basaltic samples was measured. In addition, measurements were conducted above the liquidus temperature on melt compositions matching the residual liquids observed at different sub-liquidus temperatures. These supplemental electrical measurements allow us to discriminate between the effects of crystal content and changes in liquid composition associated with partial crystallization (Fig. 3.8-6). We have proposed model to calculate the changes in conductivity associated with partial crystallization of magma. This model shows how the composition of the residual liquid is critical and explains previous difficulties in finding a robust model for describing the electrical behaviour of crystal + liquid systems. These findings reveal that we need a comprehensive model to predict the conductivity of molten silicate as a function of chemical composition.

f. *Evidence for present-day growth of leucogranite plutons in Tibet (F. Gaillard, in collaboration with B. Scaillet and M. Pichavant/Orléans)*

Several geophysical surveys carried out in southern Tibet have revealed the presence of regions ("bright spots") at 15-20 km depth that correspond to zones of seismic attenuation and high electrical conductivity that are correlated with high heat flow at the surface. It has been shown that the electrical signatures of such zones are consistent with the conductivity of anhydrous partially-molten granulites at ~ 1075 °C. Therefore, the bright spots have been interpreted to indicate the presence at depth of magmas intruding in a manner analogous to the intrusion, during the Miocene, of leucogranite plutons now exposed to the south in the High Himalayan range. However, independent petrological and geochemical studies have shown that the Himalayan leucogranites were generated at temperatures lower than 850 °C, which is 325 °C lower than the temperature estimated from the geophysical measurements in Tibet. The interpretation of the electrical signature of extremely water-rich granites is reevaluated here in the light of the first experimental constraints on electrical conductivity of hydrous granitic melts and we are able to show a perfect agreement between petrological, geochemical and geophysical data.

Geochemical and petrological studies revealed that Himalayan Leucogranites were probably derived from the partial melting of underlying metapelites at a pressure of 600-700 MPa, via dehydration melting of muscovite (Fig. 3.8-7a). After coalescence and upward migration, these granitic magmas were emplaced in the middle crust at a depth equivalent to a pressure of 400 MPa and then cooled, thus initiating their crystallization (Fig. 3.8-7a). The

temperature-crystal content-water content of the residual liquid, as constrained previously (Fig. 3.8-7a, b), was used to calculate the electrical conductivity changes during the emplacement and cooling of these leucogranites (Fig. 3.8-7c).

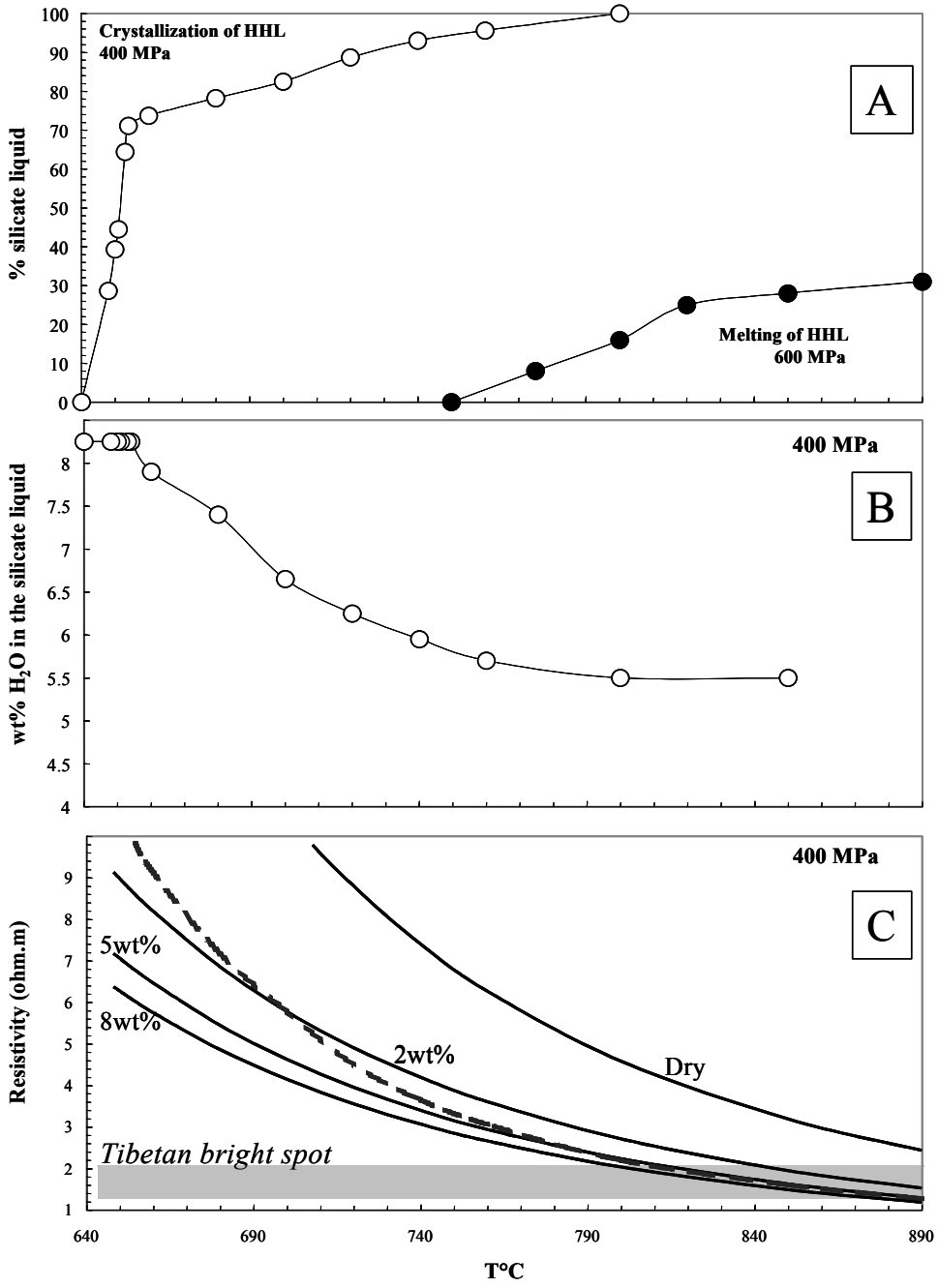

Fig. 3.8-7: A) Relation between melt fraction and temperature for the melting (closed symbols) and the crystallization (open symbols) of leucogranite. B) Relation between water content of the residual liquid and temperature during partial crystallization of leucogranite. C) Changes in electrical resistivity associated with crystallization of leucogranites at 400 MPa (dashed line). Solid lines show the electrical resistivity of liquids with different water contents. The electrical resistivity corresponding to the Tibetan bright spot is shown to match the electrical characteristics of leucogranite at near-liquidus conditions.

The results reveal a perfect agreement between the geophysical electrical signature of the anomalous regions below Tibet and the electrical resistivity of leucogranites as expected during their conditions of emplacement at 400 MPa. We therefore provide very strong evidence that the geophysical anomolies below the Tibetan plateau are the result of leucogranite plutons which are being emplacement in a manner similar to the Himalayan Miocene leucogranites that are now exposed in the south of the High Himalayan range. This work shows that the geophysical signature of rocks at depth can be interpreted based on relevant experimental data but this has to be accomplished within an appropriate petrological framework.

g. *Short-range structure of iron in anorthite-diopside glass (C.A. McCammon, in collaboration with H. O'Neill, A. Berry and S. Campbell/Canberra; K. Jayasuriya/Kelaniya)*

Iron is the dominant transition element in natural glasses and melts; hence an understanding of its structural behaviour is of primary importance for knowledge of physical properties such as density and viscosity, chemical properties such as redox behaviour, and dynamic processes such as magma generation and volcanism. Mössbauer spectroscopy provides a measure of the short-range structure of iron in glass, as well as a quantitative determination of $Fe^{3+}/\Sigma Fe$, which can provide information on the temperature-fO_2 history of natural magmas. However Mössbauer spectra reflect site-to-site distortions of iron coordination polyhedra which complicate spectral analysis. Various approaches have been suggested, and while $Fe^{3+}/\Sigma Fe$ is relatively independent of the fitting method, the hyperfine parameters that relate to the short-range structure of iron are generally not. We therefore undertook a study of a well-characterised suite of glasses in order to develop a fitting approach that could be applied over a wide range of iron compositions (including both Fe^{2+} and Fe^{3+}), with the goal of characterising the effect of oxygen fugacity and glass composition on the short-range structure of iron in these glasses.

The glasses comprised two series: (1) 1 wt.% $^{57}Fe_2O_3$ added to $An_{42}Di_{58}$ (nominally corresponding to the eutectic composition) and equilibrated at 1409 °C over a range of oxygen fugacities from $fO_2 \sim 10^5$ bars ($Fe^{3+}/\Sigma Fe=1$) to 10^{-13} bars ($Fe^{3+}/\Sigma Fe=0$); and (2) increasing amounts of Fe_2O_3 (2, 4, 7, 10, 20 or 30 wt.%) added to the same $An_{42}Di_{58}$ starting composition and equilibrated at 1409 °C and three different oxygen fugacities (10^0, 10^{-4} and 10^{-7} bars). We used an extended Voigt-based fitting analysis with two-dimensional distributions of isomer shift and quadrupole splitting to fit the Mössbauer data, coupled with one-dimensional distributions of hyperfine magnetic fields to account for magnetic relaxation effects that are present in glasses with low iron concentration. Preliminary results for glasses with 1 wt.% Fe_2O_3 show that derived $Fe^{3+}/\Sigma Fe$ values are consistent with predictions from thermodynamics (Fig. 3.8-8a). Fe^{2+} absorption requires a minimum of two quadrupole splitting distributions to fit the data, suggesting the presence of more than one coordination environment. There is no observable effect of Fe^{3+} concentration on the centre shifts of Fe^{2+}

and Fe^{3+} absorption, suggesting negligible change in local structure (Fig. 3.8-8b). To investigate the effect of the choice of fitting model on this conclusion, particularly for spectra with higher iron concentrations where line overlap is greater, the concept of mean centre shift is being developed as an unbiased means of assessing changes in the spectra with composition variables. The goal is to provide more information on the structural state of iron and hence into the physical and chemical properties of the corresponding silicate melts.

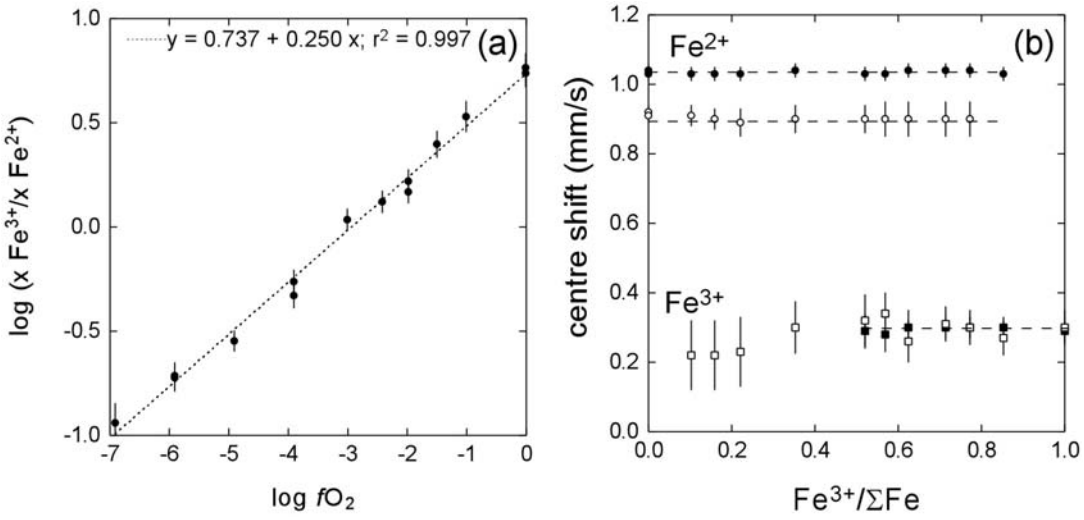

Fig. 3.8-8: (a) Effect of oxygen fugacity on relative Fe^{3+} concentration derived from Mössbauer spectra for glasses containing 1 wt.% Fe_2O_3. The slope agrees exactly with predictions from the equation $Fe^{2+}O + ¼ O_2 = Fe^{3+}O_{1.5}$; (b) Effect of Fe^{3+} concentration on centre shift of glasses containing 1 wt.% Fe_2O_3 derived from Mössbauer data. Fe^{2+} absorption was fitted to two quadrupole splitting distributions (solid and open circles) while Fe^{3+} absorption was fitted to one magnetic field distribution (open squares) and one quadrupole splitting distribution (closed squares).

3.9 Materials Science

High-pressure/high-temperature research is more involved in the development of new materials than ever before, which places BGI in a strong position within the research field. Projects cover a wide range of materials, from simple metals to complex compounds. The properties of Ce, Pr, Ge and Sn and their alloys change at high pressure and temperature, which opens possibilities for synthesis of new materials with unique and useful properties. Superhard materials continue to be a focus of research, and use of the 5000-tonne multianvil press at BGI has enabled synthesis of a new composite superhard semiconducting material made of intergrown boron carbide and heavily B-doped diamond. Devices made from such materials have the potential to function at temperatures where conventional Si-based electronics fail. Oxides have been studied with both experimental and theoretical methods as a means of optimising their use in a wide range of technological applications. High-pressure synthesis of double perovskites has provided insight into the physics of cation disorder and the origin of remarkable properties such as colossal magnetoresistance. Layered zirconium phosphate and phosphonates provide a large toolkit for the preparation of tailor-made compounds, with structures and reactivities that can be fine-tuned for many applications.

a. *Stability of the high-pressure monoclinic phases in Ce and Pr metals: Comparative diffraction study and phenomenological theory (A.Yu. Kuznetsov and L.S. Dubrovinsky, in collaboration with V.P. Dmitriev, O. Bandilet, P. Bouvier, D. Machon and H.-P. Weber/ Grenoble)*

Rare earth metals exhibit pronounced systematics in their crystal structures as a function of the atomic number across the lanthanides series or with increasing pressure. It is well established that the electron transfer in valence shells induces a characteristic hcp→9R→dhcp→fcc→dist. fcc sequence of reconstructive phase transitions in lanthanides observed in high-pressure experiments. However, knowledge about another typical sequence of phase transformations, dist. fcc→ hp3/monoclinic → α-*U*/bct, with some features commonly attributed to phenomena from *f* electrons, is more limited.

The structural similarity reported for the high-pressure monoclinic and α-*U* polymorph modifications of Pr and Ce motivated us to study more thoroughly the evolution of the above phases as a function of pressure. The presence of monoclinic and/or α-*U* phases in the phase diagram of Pr and Ce can be comprehensively accounted for in the framework of a phenomenological theory, showing that specific strain/stress conditions induced in the material, for example, by thermo-mechanical treatment, promote metastable phases in Pr and Ce metals in agreement with the experimental results.

Small chips of polycrystalline Ce and Pr with a purity of 99.9 % (GoodFellow) were studied in an externally heated diamond anvil cell (DAC) by angle-dispersive X-ray diffraction techniques.

The experiments with Ce samples, loaded with and without silicon oil, have resulted in the well known sequence of phase transitions (Fig. 3.9-1a). A mixture of dhcp ($P6_3/mmc$, Z=4) and fcc ($Fm\bar{3}m$, Z=1) phases of Ce was transformed into a pure fcc phase, γ, in the DAC after loading and slight compression. The γ-to-α (fcc-fcc′) isostructural phase transition occurs in Ce in the pressure range 0.6-1.0 GPa. The α-Ce phase then transforms to the monoclinic α′′-Ce phase ($C2/m$, Z=2) starting from 5.3 GPa. Further pressure increase results, at P=12.5 GPa, in the appearance of weak diffraction peaks of the body centered tetragonal (bct) structure ($I4/mmm$, Z=1). The pressure range of the transformation from the α′′-Ce to the bct-Ce extends to 17.7 GPa.

In order to induce in Ce a transition to the α-*U*-type phase we carried out high-pressure diffraction measurements at elevated temperature. Compression of Ce at 473 K results, at 1.5 GPa, in the volume-collapsed transition from the γ-Ce phase to the α-Ce one. The single α phase of Ce was stable up to 4 GPa. The image taken at 6 GPa revealed several very intense spots at 2θ values expected for the α-*U* phase. The compression of the sample up to 10 GPa induced a gradual distortion of the intense spot from the α-*U* phase of Ce into the inhomogeneous diffraction rings.

The diffraction experiments on Pr disclose the sequence of pressure-induced phases, dhcp (Pr-I)-fcc (Pr-II)-dist. fcc (Pr-III). The diffraction peaks from the fcc structure appear at about 5.0 GPa. A two-phase mixture was observed up to 7.7 GPa, where the dhcp-to-fcc phase transformation was completed. The appearance of superlattice reflections characteristic for the rhombohedral phase was clearly seen at 8.1 GPa. The rhombohedral dist. fcc phase ($R\bar{3}m$, Z=8) is considered usually as stable up to about 20 GPa, above which the transition to the "collapsed" α-*U* phase occurs (P_{tr}=25 GPa in our experiments). However, we have found that diffraction patterns can be satisfactorily fitted to the corresponding rhombohedral structure only up to about 12 GPa. A systematic and increasing misfit of simulated and experimental diffraction patterns was observed with pressure increasing above 12 GPa. An important argument for the existence of a phase transition at P ≅ 10 GPa is provided by the equation of state of Pr plotted in Fig. 3.9-1b. One notes, in Fig. 3.9-1b, an evident singularity at P ≅ 10 GPa in the atomic volume dependence plotted versus pressure. The existence of different compressibilities is a clear indication of a structural change. This result led us to propose the new phase of Pr in the pressure range 12-25 GPa with the monoclinic structure belonging to the $C2/m$ space group and the unit cell lattice parameters: a_m=10.984(2) Å, b_m=6.3810(2) Å, c_m=6.275(3) Å and β=126.12(1)°. The Pr atoms occupy two fourfold positions and one general eightfold position with the atomic positional parameters: $4(i)_1$: (0.7149, 0, 0.2666), $4(i)_2$: (0.2338, 0, 0.2680) and 8(j): (-0.0107, 0.7589, 0.2655). At variance with the rhombohedral structure, the above monoclinic one, Pr-VII, gives good reliability indices (R_{wp}=0.0383, goodness of fit equal to 1.62).

The question arises as to the existence or the absence of an analogy between monoclinic phases observed in Ce and Pr metals. The monoclinic phase of Ce can be considered as a

collapsed structure with itinerant 4*f* electrons. An important indication on the *f*-electron state in Pr is provided by an evident change of the Pr structure compressibility at the dist. fcc-to-monoclinic transition (Fig. 3.9-1b). The almost continuous character of the latter and the preceding fcc-dist.fcc transformation does not allow one to conclude that there is an interatomic nature of such a change, but speaks in favor of the electronic shell modification, which transforms the "compressibility" of the atom itself. One notes the identical values of the bulk modulus, B_0, of monoclinic Ce (B_0=30.7 GPa) and Pr (B_0=30.5 GPa) metals, both differing remarkably from that of the γ-Ce (B_0=24.4 GPa) and fcc Pr-II (B_0=25.1 GPa) structures. Such an analogy in the "elastic" properties of the Ce and Pr atoms in their monoclinic phases leads us to attribute the monoclinic Pr-VII structure to one with already itinerant 4*f* electrons but not to a "precollapsed" structure.

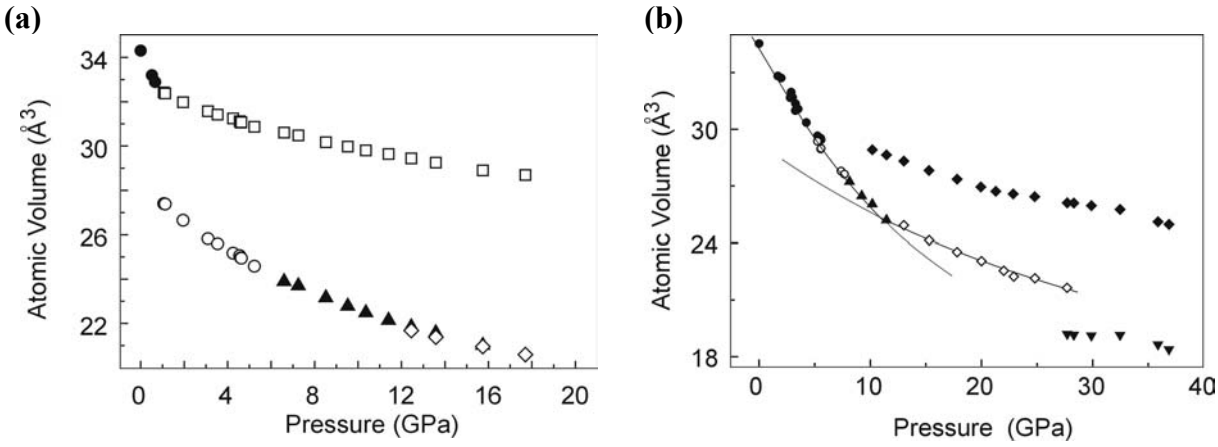

Fig 3.9-1: (a) Atomic volume of Ce metal as a function of increasing pressure. Solid circles- cubic γ-Ce; open circles- cubic α-Ce; triangles- monoclinic α″-Ce; diamonds- tetragonal Ce; squares, CeO. (b) Atomic volume of Pr metal as a function of increasing pressure: solid circles- dhcp; open circles- fcc; triangles- rhombohedral; diamonds- monoclinic; inverted triangles- α-*U*; solid diamonds- PrO.

The existence of an analogy in the corresponding atomistic mechanisms of the transformations in Pr and Ce can be shown in the framework of phenomenological Landau approach. The observed low symmetry monoclinic, orthorhombic and rhombohedral structures can be deduced from the parent fcc phase following a standard procedure of a group-theoretical analysis. Effective Landau free energy expressed in terms of the order parameters for the latter transformations results in equilibrium phase diagrams which are compatible with the experimentally observed features in the phase diagrams of Ce and Pr. In particular, special sensitivity of the α″-α-*U* phase boundary with respect to external effects in the phase diagram of Ce can be accounted by the elastic field shifts of the stability limits of the above phases. The analysis of the order-parameter genesis from the bcc parent phase shows that α″ and α-*U* phases of Ce are the originally equivalent domains of the same

orthorhombic phase. The α′′-Ce – to – α-*U* structure transformation appears, therefore, as a type of switching of domains. In case of Pr, a calculated partial phase diagram is compatible with the whole phase diagram including the melting curve. The transition line predicted for the fcc(Pr-II) - to - α-*U*(Pr-IV) transformation and extrapolated to higher temperatures and pressures intercepts the experimentally determined melting curve close to the triple point melt-fcc-α-*U* suggested from experiments on high-pressure melting of Pr.

b. *The search for novel semiconducting and intermetallic alloys at high pressures and temperatures (C. Guillaume, G. Serghiou, C. Jeffree and N. Odling/Edinburgh; D.J Frost)*

In this work we are investigating the formation of new alloys comprised of group IV elements (C-Si-Ge-Sn) using high pressures and temperatures. While silicon itself is the most important material in the semiconductor industry, it is an inefficient light emitter because it has an indirect band gap. Novel group IV alloys on the other hand could have tunable direct band gaps and lattice constants that would allow for efficient fabrication of electronic and optoelectronic devices. Theoretical calculations indicate that novel group IV compositions (containing tin) and structures (clathrates) are direct gap semiconductors. The ambient pressure phase diagram of tin shows that the solubility of this element in group IV alloys is negligible. It is the purpose here to change the reactivity of these elements at high densities leading to synthesis of alloys that cannot be made under conventional conditions. This work will allow us to both markedly extend current experimental studies and structural systematics which are largely limited to the ambient temperature high pressure behaviour of group IV elements, as well as to possibly synthesize new technologically important alloys.

(a) **(b)**

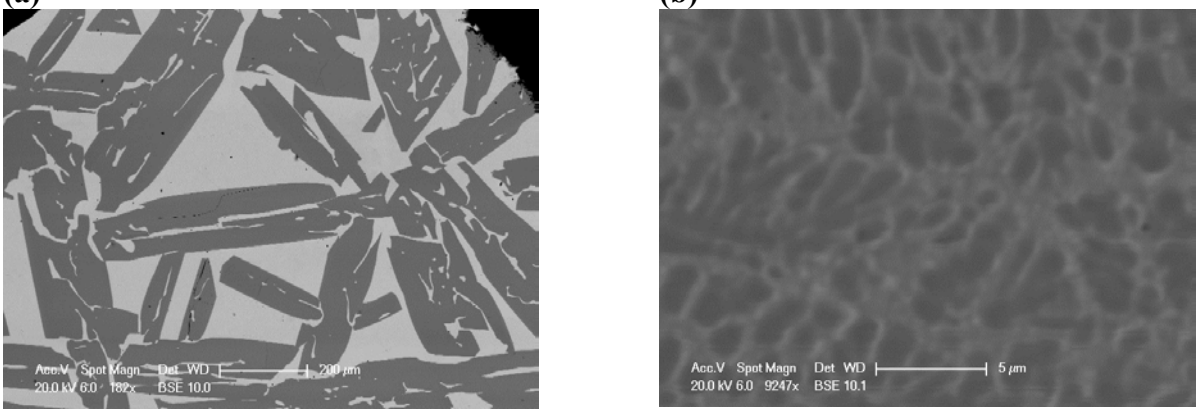

Fig. 3.9-2: Scanning electron microscopy images in backscattering mode of **a)** a recovered sample after heating an intimate mixture of Ge and Sn at ambient pressure and 1500 K for 2 hours in an inert gas atmosphere. The dark regions are pure Ge and the bright regions are pure Sn; **b)** intimate mixture of Ge and Sn heated at 1500 K and 24 GPa for 5 minutes. Both the dark and bright regions contain Ge and Sn with the dark regions containing more Ge and the bright regions containing more Sn.

We have performed numerous experiments on mixtures of Ge and Sn both at ambient and at varying conditions of high pressure and temperature using both piston cylinder and multianvil as well as laser-heated diamond anvil cell devices. Five multianvil experiments on liquid Ge and Sn mixtures were performed at the Bayerisches Geoinstitut using the 1200 tonne press. Experiments were performed between 7 and 24 GPa at 1500 K using 18/11, 10/5 and 10/4 assemblies. Ge and Sn mixtures were encapsulated in Re and Al_2O_3 capsules. Escape of the liquid metal in initial experiments was prevented by using double Re capsules. Experiments were heated for between 5 and 30 minutes. Samples have been characterised using spectroscopic, diffraction, and scanning electron microscopy methods. We find, consistent with previous work, that no reaction between Ge and Sn takes place at ambient pressure using melt-quenching techniques, and further, that this is also the case up to a pressure of 3 GPa and 1500 K. In this pressure and temperature regime, clear boundaries demarcate pure germanium from the pure tin regions (Fig. 3.9-2a). Preliminary results of analyses of experiments from 24 GPa (Fig. 3.9-2b) and 1500K indicate that at these higher pressures sharp boundaries between Ge and Sn apparently cease to exist. Extensive energy dispersive X-ray analysis has revealed both Ge and Sn at each spot examined in the sample (Fig. 3.9-2b) and it appears that some degree of solid solution has occurred between the Ge and Sn at these conditions. Zone axis electron diffraction patterns taken from several of the crystallites synthesized at higher pressure exhibit patterns that could not be indexed with any of the known ambient or dense Ge or Sn structures. Further investigation of the recovered samples is underway.

c. *Nanocrystalline diamond synthesized from C_{60} (N.A. Dubrovinskaia, L.S. Dubrovinsky, F. Langenhorst, S.D. Jacobsen/Washington DC and C. Liebske)*

Since the first artificial diamonds were manufactured in the mid 1950's, various methods (ranging from direct solid-state transformation of graphite under static or shock pressure to chemical-vapour deposition) for diamond and DLC (diamond like carbon) synthesis under variable pressure and temperature conditions have been explored, resulting in materials with properties approaching those of natural diamonds. Ultrafine diamonds with grain sizes of 5-10 nm were synthesised by explosives and may display excellent properties as surface coating for metals. Polycrystalline cubic diamond synthesised by direct conversion of graphite at static high pressures and temperatures is ultrahard. Compression of fullerene C_{60} under non-hydrostatic pressures to 25-30 GPa at room temperature has resulted in direct transformation to diamond, probably with small crystallite sizes, but the amount of synthesized material was insufficient for detailed characterisation of the structure or mechanical properties and the reproducibility of such experiments has come under scrutiny. Numerous nanocluster-based phases with presumably 3D-polymerized fullerite structures have been synthesized from C_{60} and carbon single-wall nanotubes at pressures above 13 GPa and temperatures above 800 K. These new materials show impressive mechanical properties and some of them appeared to be harder than diamond. However, subsequent studies did not confirm the exceptional hardness of fullerites.

In course of the systematic studies of direct transformation of low-density carbon materials into diamond, we synthesized nanocrystalline diamond using C_{60} as a starting material. The new material has a number of unusual and potentially important properties.

We conducted a series of experiments in 1200- and 5000- tonne multianvil presses, using powdered graphite, amorphous carbon, C_{60}, and natural diamond as starting materials. The samples were contained in a Pt capsule to avoid undesirable reactions with carbon. The C_{60} sample compressed at room temperature to 20 GPa came out as a black non-transparent brittle cylinder. X-ray diffraction and Raman spectroscopy show, in good agreement with previous observations, that fullerene preserves its structure (lattice parameter of the cubic cell reduced from 14.041(3) Å for pristine material to 13.856(3) Å for the product phase) after high-pressure treatment. All carbon phases processed at simultaneous high pressures and temperatures transformed to transparent (in the case of amorphous carbon, graphite, and C_{60}) or semi-transparent (when diamond powder was used) materials. Samples obtained from powdered diamond and amorphous carbon are slightly grey in colour, while materials obtained from graphite and C_{60} are yellowish. SEM and ATEM studies show that at the conditions of our experiments, platinum did not react with carbon, the samples were not contaminated and contained only pure carbon. X-ray powder diffraction patterns of all recovered samples are dominated by reflections from diamond (Fig. 3.9-3), however, materials synthesized at temperatures below 2600 K from amorphous carbon, graphite, and diamond exhibit several additional small reflections at ~2.19 Å, 1.92 Å, and 1.50 Å (Fig. 3.9-3). These reflections correspond to lonsdaleite (2H diamond polytype) and could result from either a small amount of this phase or disorder of the diamond structure along [111]. X-ray and electron diffraction patterns from the samples synthesized from C_{60} contain (in addition to the diamond-structure reflections at 2.0497, 1.2552, and 1.0705 Å) diffraction lines at 2.141, 1.9195, 1.6292, 1.3670, 1.1578, and 1.0519 Å (Fig 3.9-3). All these lines can be indexed in the framework of a hexagonal unit cell with lattice parameters a = 2.510(1) Å and c = 12.301(3) Å. Such diffraction data are thus consistent with theoretically predicted 6H diamond-like polytype.

TEM images, as well as estimation from the broadening of X-ray diffraction lines by the Williamson-Hall method, show that bulk samples of diamond obtained at P=20 GPa and T=2300 K from C_{60} consist of crystallites of 5 to 12 nm. Additional synthesis experiments indicate that nanocrystalline diamond forms independent of the cooling rate. Due to the very small grain size of the nanocrystalline material, high-resolution TEM (HRTEM) images were difficult to achieve, but where possible, HRTEM images show that the nano-crystalline diamond synthesised from C_{60} has an ideal structure, free of stacking faults or other defects (Fig. 3.9-4). The EELS spectra are also perfectly compatible with the diamond structure (Fig. 3.9-5) and suggest that sp^3 hybridization prevails even across the numerous grain boundaries.
Hardness measurements of superhard materials like diamond or DLC are problematic, because the measurements are based on the assumption that the tested material plastically deforms. Obviously, the hardness of the indenter should exceed the hardness of the tested

material and this requirement limited our ability to measure the hardness of synthesized nano-diamond. It is known, for example, that the hardness of the (111) face of the type IIa diamond ("hardest" diamond face) so far has not been measured, because it is not possible to make an indentation on this face. In our case, a tip of the diamond of a Vickers-type indenter does not make any scratches or indentations on the surfaces of nano-diamonds at loads up to 500 g. Even using SEM we can not see the mark of indentor. So, we conclude that nanodiamond material is at least as hard as usual bulk diamond.

A bulk sample of nanocrystalline cubic diamond with crystallite sizes of 5-12 nm was synthesised from fullerene C_{60}. Its properties were studied using X-ray diffraction, Raman, IR spectroscopy, and HRTEM. It was found that the material has a unique Raman spectrum different from that of usual diamond, and the thermal stability of nano-diamond produced from C_{60} is at least 300 K higher than that of normal diamond. Such properties of the new material could relate to the small dimensions and sharp size distribution of crystallites (5-12 nm).

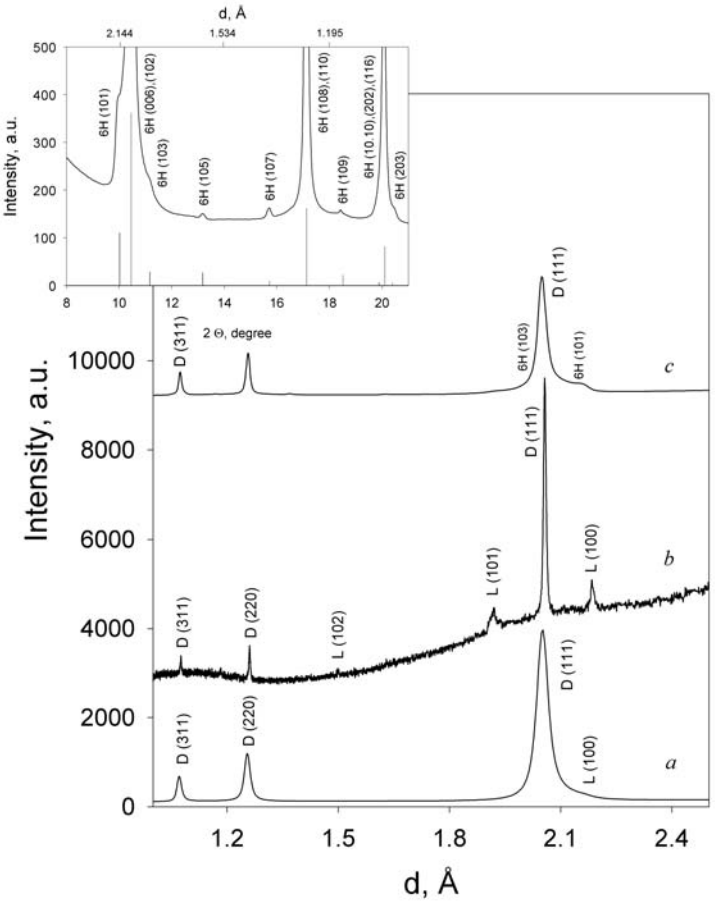

Fig. 3.9-3: Examples of diffraction patterns of carbon materials synthesized (a) from graphite at 24 GPa and 2400 K, (b) from natural diamond at 20 GPa and 2300 K, and (c) from C_{60} at 20 GPa and 2300 K ("D" for diamond reflections, "L" for lonsdaleite (or 2H diamond polytype), "6H" for 6H diamond polytype). Insert shows enlarged plot of pattern *c* with vertical bars corresponding to the position and intensities of the diffraction lines of 6H polytype of diamond.

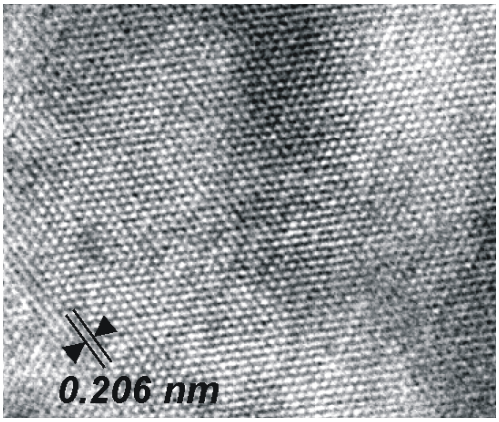

Fig. 3.9-4: HRTEM image shows that individual crystallites, which comprised the bulk of the nano-crystalline sample synthesised from C_{60}, have the ideal diamond structure, free of stacking faults or other defects.

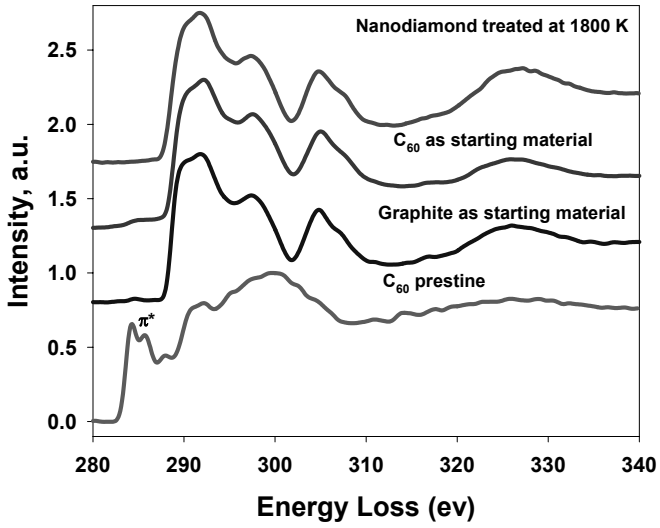

Fig. 3.9-5: The EELS spectra from ptestine C_{60} (bottom); from polycrystalline diamond obtained from graphite at 20 GPa and 2300 K; from the nanocrystalline diamond produced by direct conversion of C_{60} at the same conditions. Spectrum of the nanodiamond sample (top) treated at 1800 K in forming gas atmosphere does not shoe any sign of sp^2- bonded carbon.

d. *In situ study of C_{60} polymerisation (A. Talyzin/Umeå and L.S. Dubrovinsky)*

At high-pressure and high-temperature conditions (HPHT) C_{60} is known to undergo polymerisation. Below 9 GPa and 900 K several kinds of one- and two-dimensional polymeric phases have been obtained: orthorhombic (linear chains), tetragonal (planar with four connections per molecule) and rhombohedral (with six connections per molecule). One- and two-dimensional polymeric phases are well characterized by different techniques

including Raman spectroscopy and XRD. Three-dimensionally polymerized superhard fullerites have been claimed to exist at pressures above 12-13 GPa and temperatures above 800 K.

Most of the previous studies were performed *ex situ* after cooling the sample and release of pressure. Using externally heated diamond anvil cell designed at BGI, we performed during last years extensive studies of the P-T diagram of C_{60} using *in situ* Raman spectroscopy and XRD. Very recently it was proposed that pre-synthesized polymeric phases of C_{60} (tetragonal and rhombohedral) can be used as a precursor for synthesis of three dimensional polymers. First, we pressurized tetragonal and rhombohedral polymers at room temperature up to ~ 30 GPa in quasi-hydrostatic pressure medium or without any pressure transmitting medium. These experiments have not confirmed literature reports about direct transformation of tetragonal phase into a new three-dimensionally polymerized fullerite. In the another experiments the pressure region where 3D polymerization is expected (about 13 GPa and 800 K) was approached using unusual P-T path. Typically, 3D polymeric phases were attempted for synthesis using first pressure increase and heating on the second step. In our studies we used isothermal pressure path at 800 K. At these conditions C_{60} is already transformed into a two-dimensionally polymerized phases at ambient pressure. The aim of experiments was to check if these two dimensional polymers (tetragonal in one experiment and rhombohedral in second) can be transformed into a three-dimensional phase by linking polymeric planes. It could be that such synthesis would result in much better ordering of 3D polymers, which were always observed to be almost amorphous and very difficult for characterization.

Our experiments revealed very strong difference in behaviour of two-dimensional polymers upon isothermal compression at 800 K. As it can be seen in Fig. 3.9-6, tetragonal phase exhibited unusual stability in the P-T region where 3D polymerization is believed to occur. This could be explained by relative orientation of C_{60} molecules in tetragonal polymers which prevent them from formation of inter-planar links.

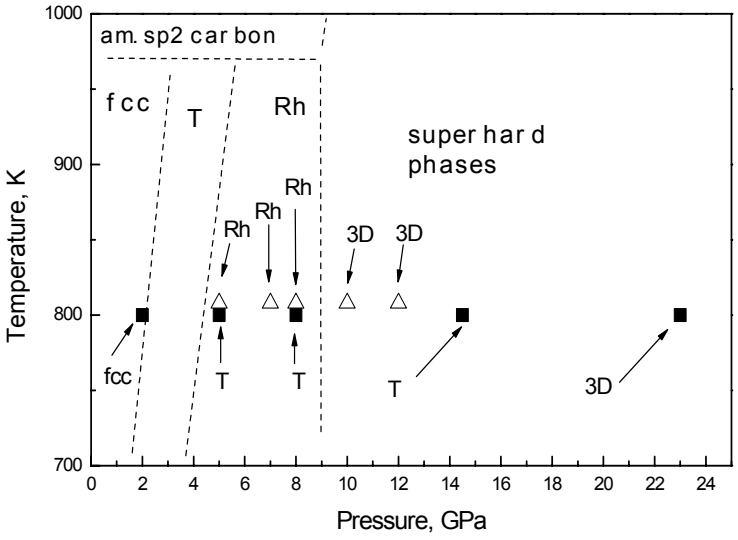

Fig. 3.9-6: Phases observed during *in situ* isothermal pressurizing experiments with tetragonal (black squares) and rhombohedral (open triangles) phases as starting materials. Dashed lines mark P-T diagram known from experiments performed using isobaric heating at different pressures.

e. *Synthesis of magnetic carbon in piston-cylinder apparatus (T. Makarova, A. Dzwilewski and A. Talyzin/Umeå; G.D. Bromiley and L.S. Dubrovinsky)*

As it was recently reported, a specially treated pure carbon samples- polymerized fullerenes, show a permanent magnetization with a Curie temperature of about 500 K. The rhombohedral two-dimensional polymer formed under high pressure and high temperatures is stable under normal conditions.The experimental observation of ferromagnetic domains in large impurity-free areas of the samples excludes the possibility of that a contamination accounts for the observed behaviour.

The research project "Magnetic carbon" conducted in collaboration with BGI includes both experimental and theoretical studies of the recently discovered magnetic phases of carbon. The goal of the project is the identification of the physical mechanisms which drive the magnetic or superconducting transitions in pure carbon, and development of methods to control reproducible manufacturing of the materials based on carbon and its mixtures.

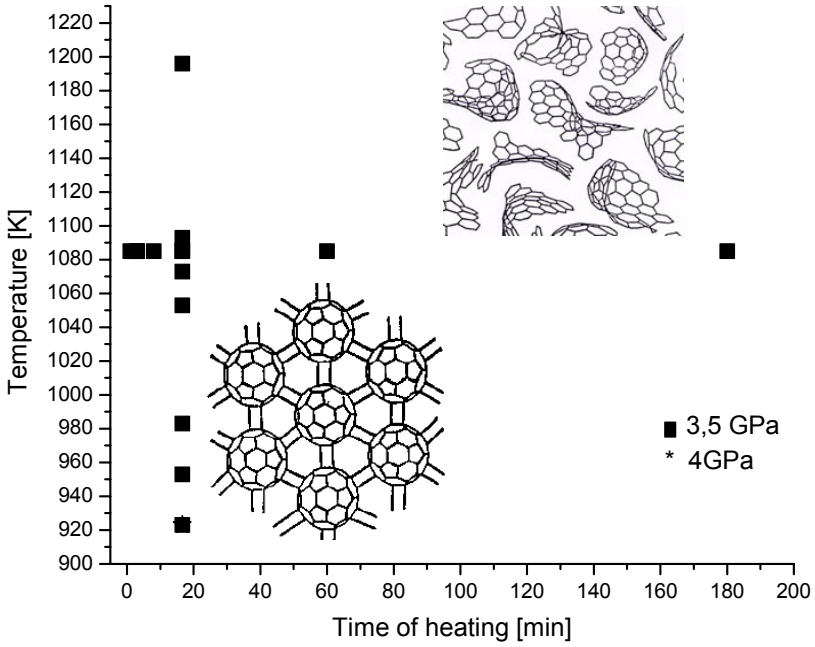

Figure 3.9-7: Synthesis conditions for samples preparedusing piston-cylinder

Ferromagnetic phase appears at the boundary between polymerized fullerenes (Fig. 3.9-7, lower inset) and graphitic carbon (Fig. 3.9-7, upper inset). For a given pressure, this boundary is determined by the temperature and time of preparation.

Synthesis of the samples was performed at different P-T-t conditions using BGI facilities (piston-cylinder system), while structural and magnetic characterizations were conducted at Umeå University.

Two sets of samples were synthesized at 3.5 GPa (Fig. 3.9-7). The first set of samples was prepared using heating time of 1000 s at the different temperatures within the 920-1200 K range and the second set of samples was produced using different heating time at the pressure 3.5 GPa and temperature of 1085 K. The temperature for the second set of samples was chosen close to the phase transition point from polymeric fullerite into an amorphous hard carbon which forms due to collapse of C_{60} cage structure. According to powder XRD and Raman spectra recorded from the first set of samples this phase transformation occurs at very narrow temperature interval between 1073 and 1085K. The second set of samples showed that time of the heating is also a very important synthesis parameter. A Shorter heating time (60-480 sec) results in synthesis of mostly polymeric C_{60}, while longer heating time lead to collapse of fullerenes into a hard carbon phase. Magnetic microscopy studies of these samples proved that some of the synthesized samples are, in fact, ferromagnetic (Fig. 3.9-8). Currently the work is under way to correlate magnetic properties with some particular structural features of studied samples.

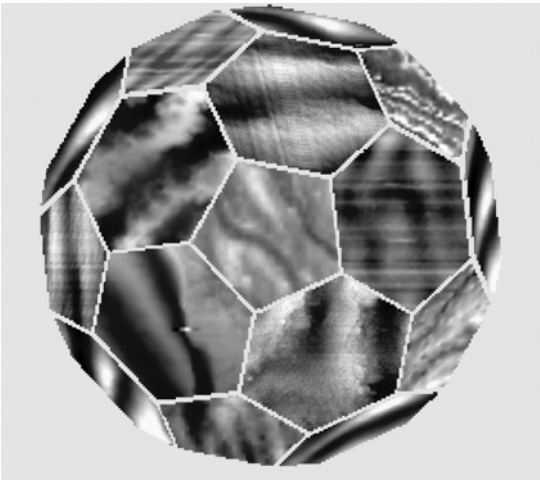

Fig. 3.9-8: Ferromagnetic domains in fullerene C_{60} (collage). Magnetic microscopy images were obtained from the sample synthesized in BGI.

f. *New superhard semiconducting composite B-C material (V. Solozhenko/Paris, N.A. Dubrovinskaia and L.S. Dubrovinsky)*

Pure diamond is a perfect electrical insulator. But, like silicon, it can be turned into a semiconductor by adding traces of boron or nitrogen. Significant progress in the doping of diamond by boron was achieved by microwave plasma chemical-vapour deposition (CVD). Using different substrate materials, different temperatures of deposition, and varying components of chemical mixture as well as C/B ratio, both single-crystal and polycrystalline diamond films with boron concentration up to 2×10^{21} [B] cm^{-3} (or about 1.2 at.% B) can be produced. When transition metals are used as solvents, synthesis of the B-doped bulk diamond is possible in large-volume apparatuses. However, the concentration of boron in such bulk samples is lower (less 1 at.%) than in CVD-synthesized diamond films. Here we

have made an attempt to combine the two technologies and synthesize B-doped diamond by direct conversion of CVD-produced graphite-like BC_3 (g-BC_3) at high pressures and temperatures.

As starting materials in different experiments we used pure graphite (99.99 %, Goodfellow Inc.), B_4C (99.99 %, Goodfellow Inc.), and graphite-like BC_3 synthesized by thermal CVD.

High-pressure experiments up to 20 GPa were performed using a two-stage 6-8 type large-volume multianvil system with a 5000-tonne press. The sample assembly consisted of a MgO (+5 wt.% Cr_2O_3) octahedron with 18 mm edge length containing a $LaCrO_3$ heater. The octahedron was compressed using 54-mm tungsten carbide anvils with a truncation edge length of 11 mm and pyrophyllite gaskets. The sample was placed into BN capsule of a cylindrical shape with a sample chamber of 2 mm in diameter and 3 mm height. Sample temperature was monitored by a W3%Re-W25%Re thermocouple located axially with respect to the heater and with a junction close to the BN capsule. The pressure and temperature uncertainties were estimated to be 1 GPa and 50 K, respectively. Samples were gradually compressed to the desired pressure at ambient temperature, and then the temperature was stepwise increased (with a heating rate of about 100 K/min) up to the desired value. Duration of heating varied from several minutes to one hour. The samples were quenched by switching off the power and then slowly decompressed. Upon completion of an experiment, the capsule was carefully removed and the sample was mechanically cleaned of cubic BN. Samples came out as well-sintered cylinders of about 1.8 mm in diameter and 3 mm in height.

SEM images of a fresh untreated surface (Fig. 3.9-9) show a dense matrix with inclusions of crystals of a submicron size. Detailed analysis reveals the presence of two types of crystals – with flat "tablet" and predominantly octahedral shape. The resolution of energy-dispersive detector of the LEO-1530 scanning electron microscope is not sufficient for quantitative chemical analysis of B-C compounds. However, qualitative elemental analysis allows the conclusion that the octahedral crystals and the matrix contain low amounts of boron, while the "tablet" crystals are enriched with boron. Microprobe analysis of the biggest flat crystals show that they have B_4C composition, while the area almost free from the crystals ("dense matrix") contains 1.8(1) at.% B (20 data points over the 5×5 μm^2 area). Octahedral crystals are significantly smaller than the electron beam, and their reliable quantitative chemical analysis was not possible, but qualitatively the chemical composition of the matrix and octahedral crystals is the same.

Figure 3.9-10 shows diffraction patterns of the samples recovered after experiments with different starting materials at 20 GPa and 2300 K.

The resistivity of the composite material synthesized from graphite-like BC_3 is $2.45(2)\times10^{-3}$ $\Omega\cdot m$ at 295 K. This value is typical for semiconducting materials. Temperature dependence of the resistance was measured by four-probe method in the 200-600 K range. In the temperature interval under study, the resistance changes exponentially and the corresponding activation

energy is 0.35(1) eV. It should be noted that the resistance decreases with temperature as it is expected for classical semiconductors.

Originally graphite-like BC_3 is soft like pristine graphite. After treatment at high pressures and temperatures it transforms to a very hard ceramic. Polishing of the material was very difficult even with a diamond paste. Attempts to indent the polished sample by Vickers indenter with loads lower than 10 N failed. It means that the sample belongs to the clase of superhard materials, which do not show an imprint even under relatively high loads. With the 10-N load we could get an imprint and estimate the hardness on the level of 88(3) GPa. Higher loads (above 10 N) resulted in the formation of cracks. Since the indenter is much larger than the grains of the composite material, the obtained hardness value can not be attributed to individual phases (diamond and B_4C), but is a characteristic of the material as a whole.

A bulk composite material has been synthesized from graphite-like BC_3 at 20 GPa and 2300 K using a multianvil press in the form of well-sintered 8-mm^3 cylinders. The material consists of intergrown boron carbide B_4C and boron-doped diamond with 1.8 at.% B.. The material exhibits semiconducting behaviour and has a hardness comparable with that of single-crystal diamond. Synthesis of composite ceramics with a hardness approaching that of diamond suggests that new superhard materials could be not only among monophases. Combination of semiconducting properties and extreme hardness makes the synthesised material potentially important for precision (for example, electroerosion) machining, electrochemical, and electronic (high-power, high-frequency) applications.

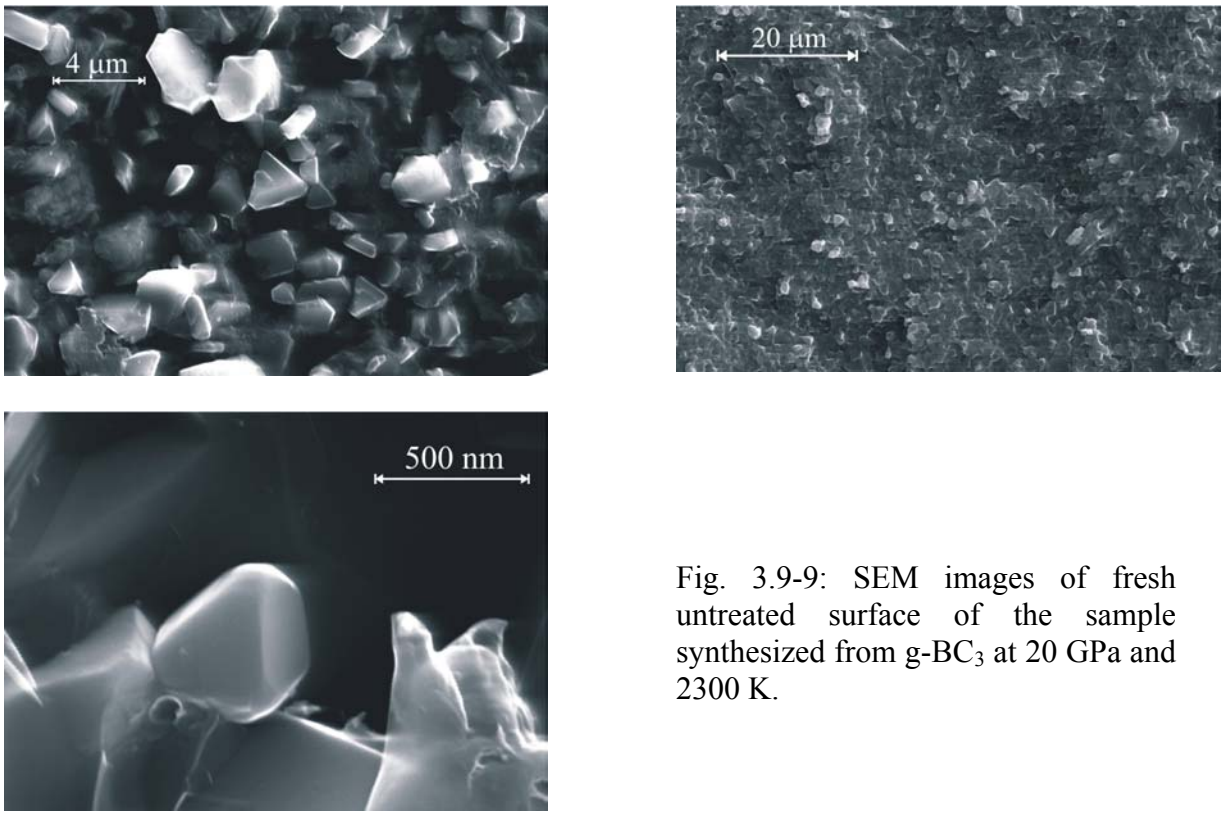

Fig. 3.9-9: SEM images of fresh untreated surface of the sample synthesized from g-BC_3 at 20 GPa and 2300 K.

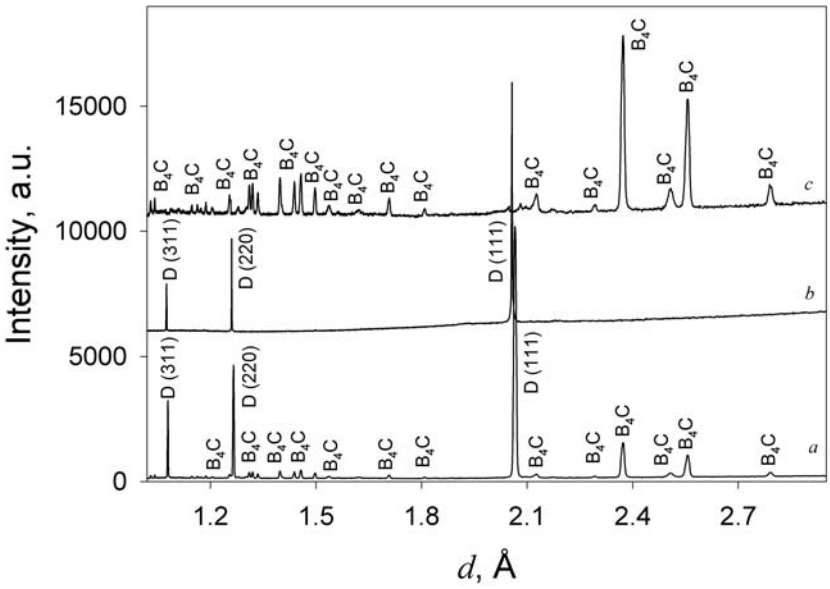

Fig. 3.9-10: X-ray diffraction patterns of the samples synthesized at 20 GPa and 2300 K from g-BC_3 (*a*), graphite (*b*), and B_4C (*c*) (D is for diamond reflections).

g. *High-pressure synthesis of a new orthorhombic phase of chromium dioxide by in situ laser heating (A.Yu. Kuznetsov, L.S. Dubrovinsky, I.Yu. Kantor and A.P. Kantor)*

Chromium dioxide is a well-known half-metallic ferromagnet typified by the property that *d* electrons with spin-up polarization occupy partially filled bands that crosses the Fermi level, whereas the Fermi level lies in a gap between valence and conduction bands for spin-down electrons. Such a situation has the consequence that there should be a 100 % spin polarization of the *d* electrons, which agrees with the reflection spectroscopy and magnetic measurement of CrO_2. These unusual transition metal oxides properties open perspectives for technological application of CrO_2 in spin-based electronic devices and has motivated numerous theoretical and experimental studies on chromium dioxide. In particular, band structure calculations have shown that peculiar ferromagnetic metal behaviour of CrO_2 can be ascribed to a non-ideal octahedral oxygen coordination of each Cr atom (four equatorial Cr-O distances are slightly larger than two apical) in the rutile structure of CrO_2 (space group $P4_2/mnm$, two formula units per unit cell). This distortion of CrO_6 octahedra results in energy and band width splitting of the t_{2g} *d* electronic states. Some of them are localized and completely occupied by one majority spin electron – others provide dispersing *d* bands. The latter *d* states are strongly hybridized with oxygen 2*p* bands and form a narrow conduction band which crosses the Fermi level. A mechanism similar to double-exchange spin coupling aligns the spins of conduction electrons parallel to the spins of localized *d* electrons, thus explaining a ferromagnetic spin alignment in CrO_2.

In the above mechanism of spin polarization an essential role is attributed to a local oxygen environment of chromium in the structure of chromium dioxide. One may expect that a compression of CrO_2 will substantially modify the configuration of CrO_6 octahedra in

analogy, for example with TiO_2, SnO_2, GeO_2, RuO_2, SiO_2 and MnO_2. The possibility of a polymorphic transformation of CrO_2 also can not be excluded. Such changes in the CrO_2 structure could produce noticeable alterations in electrical and magnetic properties of CrO_2.

A chromium sample was loaded into a diamond anvil cell (DAC) with a condensed mixture of high purity oxygen (99.999 %) and nitrogen (99.99 %) gases. The X-ray diffraction pattern of a Cr-O_2-N_2 mixture compressed to 30 GPa before laser heating was dominated by the diffraction lines from a body-centered cubic (BCC) phase of Cr and a mixture of ε-O_2 and ε-N_2 phases. After the laser heating of Cr-O_2-N_2 mixture, the crystal structures of the quenched products produced the diffraction pattern shown in Fig. 3.9-11a. All observed strong peaks could be indexed in the orthorhombic lattice with the space group *Pnnm* and the unit cell lattice parameters: a=4.4156(2) Å, b=4.2527(3) Å and c= 2.8790(2) Å. Additional weak features in the diffraction pattern in Fig. 3.9-11a fit well to the orthorhombic structure (space group $P2_1cn$) of $NO^+NO_3^-$ ionic crystal with the lattice parameters: a=5.6259(3) Å, b=7.3016(6) Å and c=6.1808(5) Å. Texture and preferred orientation effects precluded a full

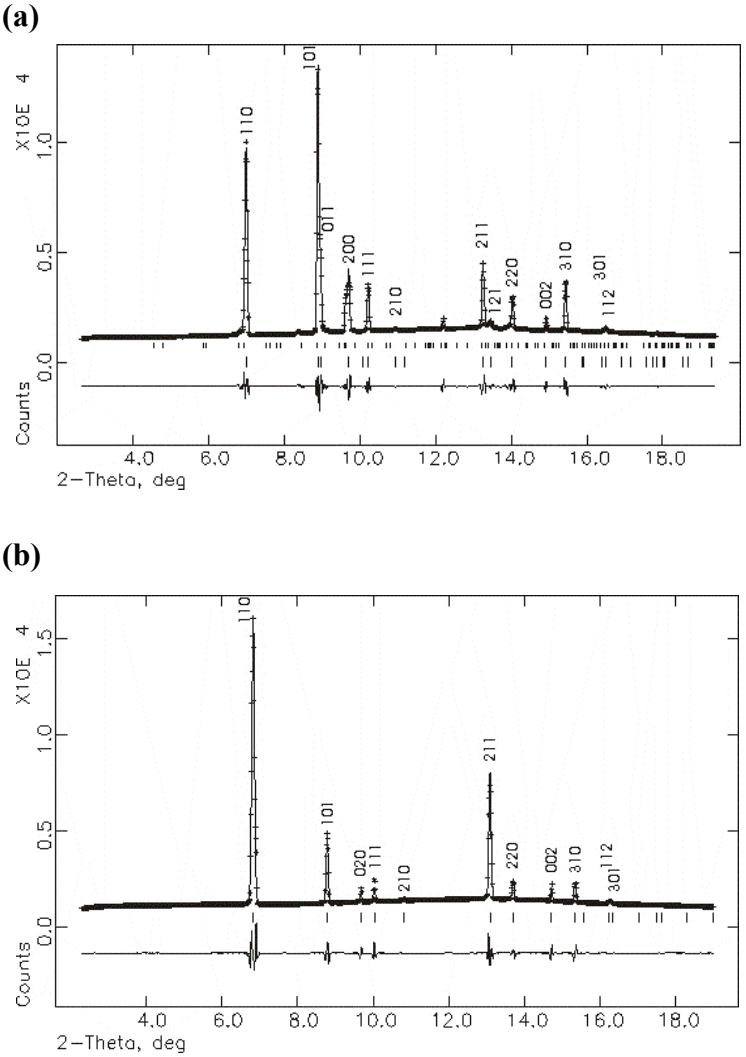

Fig. 3.9-11: Experimental (crosses) and calculated (solid lines, GSAS, Le Bail fit) diffraction patterns. (a) Orthorhombic phase of CrO_2 after laser heating, P=22 GPa, T=RT. Orthorhombic phase of $NO^+NO_3^-$ accounts for additional weak features in the diffraction pattern; (b) Tetragonal phase of CrO_2 after laser heating and decompression to 2 GPa, T=RT.

structural refinement, nevertheless a Le Bail fit provided a good description of the observed diffraction pattern in terms of the orthorhombic phase of CrO_2 and the orthorhombic phase of $NO^+NO_3^-$. The former phase represents an orthorhombic distortion of the known rutile-type tetragonal phase of CrO_2 showing a consistency with the Bragg reflections splitting rule: the *hkl* diffraction lines of the tetragonal phase with $h \neq k$ should split in the orthorhombic phase, whereas the *hhl* lines should not. A subsequent sample pressure release to 2 GPa confirmed this orthorhombic distortion of the rutile-type CrO_2 at higher pressures resulted in the diffraction pattern of Fig. 3.9-11b. The known tetragonal structure of CrO_2 explained almost all features in the obtained diffraction pattern. A comparison of Figs. 3.9-11a and 3.8-11b shows that characteristic for the rutile – to – $CaCl_2$ phase transition splitting of (101) and (211) reflections in orthorhombic phase vanishes on decompression of the sample. This result provides strong evidence that the rutile-type CrO_2 undergoes a pressure-induced phase transition to the $CaCl_2$ structure, common to many others AB_2 compounds.

The evidenced by X-ray diffraction experiments rutile to $CaCl_2$-type structural phase transition in CrO_2 provided a confirmation in the Raman spectroscopy studies with Cr-O_2 mixture (Fig. 3.9-12).

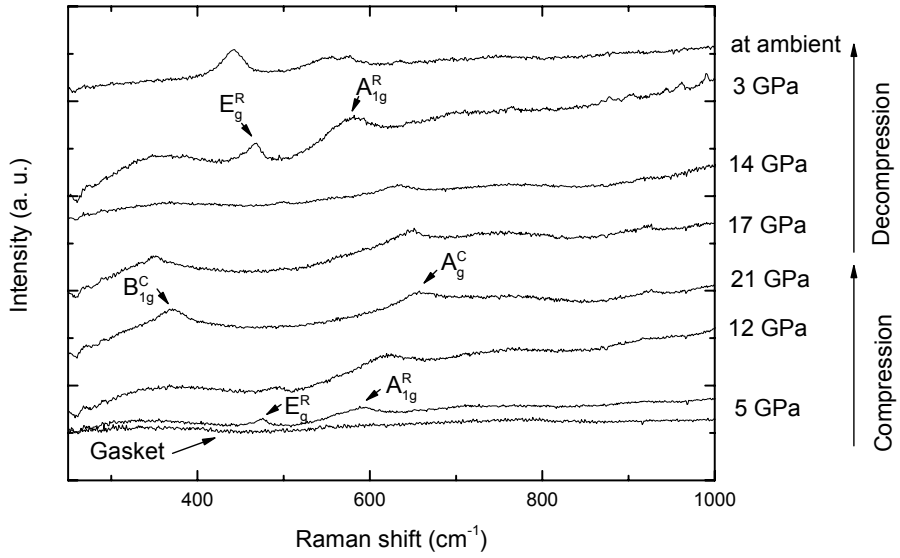

Fig. 3.9-12: Pressure evolution of the Raman spectra of Cr+O_2 reaction products quenched from 2000 K at 14 GPa, showing the evidence for rutile-type – to – a $CaCl_2$-type structural phase transition in CrO_2. The respective Raman active modes of CrO_2 with the rutile-type structure (superscript "R") and with $CaCl_2$-type structure (superscript "C") are identified.

In summary, orthorhombic $CaCl_2$-structured phase of CrO_2 has been synthesized by a direct combustion process between Cr and O_2 reactant's in a diamond anvil cell at 35 GPa using laser heating. Addition of nitrogen into the reactants environment substantially facilitated the

synthesis of CrO_2. High-pressure synchrotron X-ray diffraction and Raman spectroscopy measurements of quenched to ambient temperature CrO_2 evidenced a tetragonal (rutile-type structure) to orthorhombic ($CaCl_2$-type structure) phase transition at about 15 GPa.

h. *Cubic TiO_2 polymorphs as potential light absorbers in solar-energy conversion (M. Mattesini, J. Souza de Almeida and R. Ahuja/Uppsala; L.S. Dubrovinsky and N.A. Dubrovinskaia)*

The most abundant forms of TiO_2 (rutile and anatase) are largely used as antireflection coatings for solar cells and more in general in the development of photo-electrodes for photochemical energy-conversion processes. The ideal material for high-efficiency photo-electrodes must satisfy several specific requirements in terms of semiconducting and electrochemical properties. The optimal band gap for high-performance photo-electrodes has been fixed to ~ 2 eV. Unfortunately, up to now high corrosion-resistant materials with such a band gap were not yet identified. Another very important requirement is imposed by the potential of the photo-excited electron in the semiconductor. Very often, when trying to reduce the value of E_g in metal oxides (such as ZnO and Fe_2O_3), this potential becomes more positive than the potential needed to split H_2O into H_2 and O_2. The overall effect is therefore to make the reaction of water reduction thermodynamically unfavourable at ambient conditions. The recent discovery of a novel titania high-pressure polymorphs has opened a great expectation toward the possibility to synthesize new high-pressure TiO_2 forms with smaller band gaps and to quench them at room conditions for practicable applications. Particular attention is here given to the high-pressure cubic phases of TiO_2.

The electronic structure properties of the cubic TiO_2 polymorphs (fluorite and pyrite) were theoretically investigated by means of *ab initio* calculations. Figure 3.9-13a shows the calculated density of states (DOS) at the equilibrium geometry for TiO_2 in the fluorite structure. The valence band (VB) density of states at -17.2 eV is composed predominantly of oxygen 2*s* orbitals with a small amount of mixing of the Ti *s* and *p* states. At the top of the VB, in the region between -7.5 eV and 0 eV, the O 2 *p* states hybridize mostly with the Ti 3 *d* orbitals and to a less extent with an admixture of *s* and *p* states. The bottom of the conduction band (CB), just above the Fermi level (E_F), is primarily determined by the unoccupied Ti *d* states and the O orbitals with *p* character. Finally, the higher portion of the CB (from 10 eV to 20 eV) consists mostly of hybridized *s* and *p* states of both titanium and oxygen atoms.

The VB DOS for the pyrite phase is very similar to the one calculated for the fluorite-type phase. However, two small changes have been found in the calculated energy window. The first one is related to a certain contraction of the higher valence bands, which slightly increases the localization of the Ti *d* and O *p* states. The full bandwidth has been computed to be 1.5 eV smaller than for the fluorite system. We attribute this electronic effect to the presence of two rather long Ti-O bond distances (2.83 Å) in the inner shell of the pyrite structure. The second modification simply relates to the high-energy shift (~ 0.6 eV) of the oxygen 2 *s* states.

Figure 3.9-13b shows the computed self-consistent band structure for the TiO_2 fluorite polymorph. This phase has a direct LDA band gap of 1.80 eV at the symmetry point *X* and an indirect gap of 1.04 eV, with the top of the valence band being at the point *X* and the bottom of the conduction band at Γ. For the pyrite phase we found a minimum direct band gap of 1.81 eV at Γ and an indirect gap ($\Gamma \rightarrow L$) of 1.44 eV. Both phases can be defined as *indirect semiconductors*, which means that the lowest-energy transition from the valence to conduction bands involves a change in the crystal momentum. Employing the same calculational scheme we have estimated for rutile a direct band gap at the Γ point of 1.86 eV. As one would have anticipated, the calculated LDA gap is much lower than the experimental value of 3.0 eV. Such an underestimation amounts generally to 30-50 % of the experimental band gaps (38 % in the case of rutile) and can be attributed to the ground-state formalism of the density functional theory.

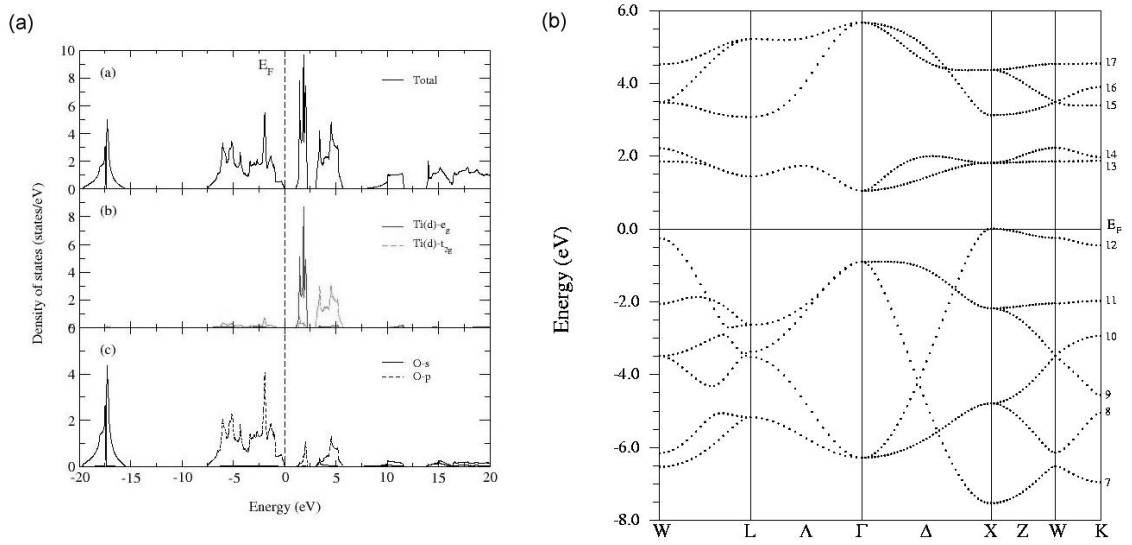

Fig. 3.9-13: (*a*) Calculated density of states for the fluorite structured TiO_2 phase. Insert (a) shows the total density of states, while (b) and (c) illustrate the partial DOS of titanium and oxygen, respectively. The splitting of the Ti-*d* states due to the O_h symmetry is clearly shown in insert (b). (*b*) Band structure of fluorite structured TiO_2 phase.

The optical properties have been evaluated through the frequency-dependent complex dielectric tensor, $\varepsilon(\omega)=\varepsilon_1(\omega)+i\varepsilon_2(\omega)$, employing the self-consistent APW+lo method and the dipole approximation. The fundamental absorption edge for fluorite occurs at 1.80 eV, resulting from transitions between the topmost VB and the bottom of the CB along the *X* direction. The other absorptive transitions correspond essentially to the electronic transitions from the set of occupied oxygen *p* states to the empty bands with Ti *d* character.

In the cubic titanium dioxide forms the band gaps close only slightly with respect to the rutile phase. For the fluorite and pyrite the calculated band gap narrowing only amounts to 0.06 eV

and 0.05 eV, respectively. Nonetheless, the main advantage in employing cubic TiO_2 phases as electrodes is related to an efficient use of those optical transitions that take place at energies close to the fundamental absorption. In the wavelength range between 400 nm and 500 nm both fluorite- and pyrite-structured TiO_2 phase present absorptions that are significantly more intense than rutile and nitrogen-doped anatase system [$TiO_{(2-x)}N_x$]. This behaviour has been attributed to the presence of a considerable amount of localized Ti *d* states at the bottom of the CB, which are determined by the local cubic symmetry. It is worth to note that both cubic TiO_2 forms present active wavelengths very close to the main peak of the solar irradiation energy (~ 460 nm), thus providing the possibility to capture a considerable amount of energy from the sunlight available in the Earth's atmosphere. Another important aspect is related to the fact that the two cubic polymorphs are pure crystalline materials. A large part of the problem arising from the photo-excited electron-hole recombination found in doped TiO_2 systems [such as $TiO_{(2-x)}N_x$] will therefore be absent.

i. *Amorphization of cuprite, Cu_2O, due to chemical decomposition under high pressure (V.V. Sinitsyn and E.G. Ponyatovsky/Chernogolovka; V.P. Dmitriev, D. Machon and H.-P. Weber/ Grenoble; L.S. Dubrovinsky)*

One of the topical fields in present high-pressure research is the study of amorphization occurring in initially crystalline substances. More than a hundred substances have been found to undergo solid-state amorphization (SSA) due to an appropriate thermobaric treatment. Normally, SSA is observed in substances with two polymorphous modifications of considerably different density in their equilibrium *T-P* phase diagrams. Therefore, SSA is often considered as an intermediate stage of a "frozen" polymorphic transition. Another SSA mechanism was proposed, namely that SSA resulted from slow decomposition of a chemically pure initial crystalline phase into two crystalline phases of other composition. Typical compounds where this effect is assumed include hydroxides such as $Ca(OH)_2$ and $Ni(OH)_2$, rare earth molybdates as well as many minerals that are Earth-core and mantle components and have complex chemical formulas. Unquestionably, a clarification of the physical processes of SSA and of mineral formation in the Earth's interior is important. An experimental study of the transition sequence *pure crystalline compound* $\rightarrow$ *amorphous state* $\rightarrow$ *crystalline products of decomposition* has so far not been carried out *in situ*, and this study where we report on the first experimental observation of amorphization due to decomposition under pressure fills this gap.

To study the process experimentally, we chose cuprous oxide, Cu_2O. The structural studies were performed at the Swiss-Norwegian beam lines (BM1A) at the European Synchrotron Radiation Facility (ESRF, Grenoble, France) by angle-dispersive diffraction techniques using monochromatic radiation (λ = 0.7109Å).

In the experiment, pressure was increased to 30 GPa at room temperature in steps of about 10 GPa. Around 11 GPa, we observed a phase transition to a hexagonal phase II described

earlier. A further increase in pressure to 21 GPa resulted in a new diffraction pattern, indicative of a phase transition to a new crystalline modification, phase III. This phase remained on further pressure increase to 30 GPa, the maximum pressure applied. At a pressure of 30 GPa, the sample was heated to 400 °C in steps of 20 to 40 °C, and diffraction patterns were measured at each step. Figure 3.9-14 shows representative diffraction patterns collected upon heating. Heating results in strong broadening of all phase III reflections, with two broad haloes observed at a temperature of about 140 °C (curve 2 in Fig. 3.9-14). The haloes indicate sample amorphization; note that the maxima of the haloes lie at positions different than the positions of the strongest reflections of the hexagonal phase III. It can therefore be assumed that the short-range order of the amorphous phase differs from that of phase III. Further increase in temperature leads to a gradual increase of the intensity of the first maximum while its width decreases. At temperatures of 240 to 260 °C and above, the second maximum splits into two broad peaks with nearly the same intensities (Fig. 3.9-14, curve 3). The emergence of peaks of lower intensity indicates the onset of the recrystallization process. An estimation of the grain size from the half-width of the first maximum gives a value of about 6.5 nm, which is characteristic of the nanocrystalline state. The diffraction pattern demonstrates only quantitative changes in the temperature range of 240 to ~ 350 °C, that is, decreasing width of the sample reflections and their increase in intensity with respect to the lines of gold. The widths of the sample and gold reflections become comparable at $T = 400$ °C (Fig. 3.9-14, curve 4), evidence that the recrystallization process is complete. The diffraction pattern remained the same upon cooling to room temperature followed by decompression, but for the shift of all X-ray lines. The X-ray analysis at atmospheric pressure demonstrated that the recrystallized mixture consisted of CuO and Cu. Positions of the copper and copper oxide peaks after cooling the high-pressure cell are indicated in Fig. 3.9-14 curve 5 (pressure increased to $P = 33$ GPa at the cooling run).

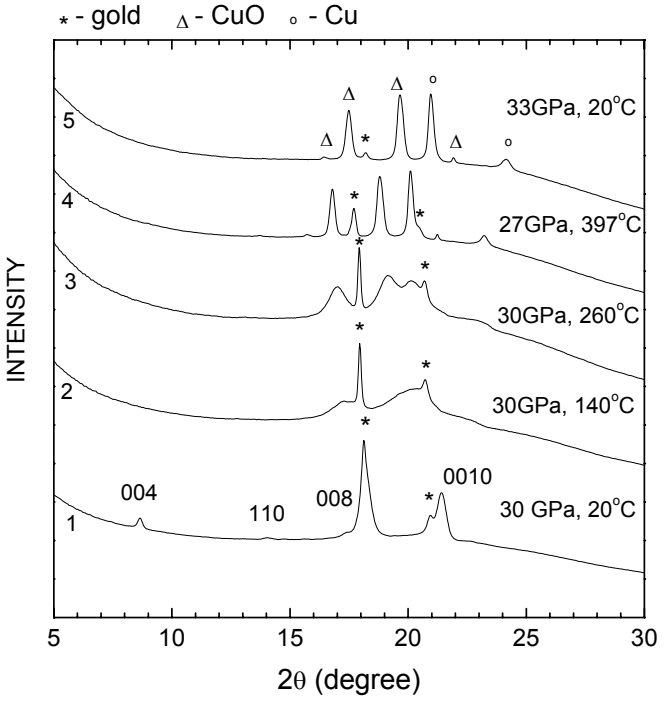

Fig. 3.9-14: The diffraction patterns of Cu_2O at P≈30 GPa and different temperatures.

So, the following sequence of the phase transformations is observed in Cu_2O in the present experiment at a pressure of 30 GPa during heating:

hexagonal phase $\xrightarrow{140°C}$ *amorphous state* $\xrightarrow{260°C}$ *nanocrystalline state* CuO + Cu $\xrightarrow{400°C}$ *crystalline* CuO + Cu *mixture*

The present structural data are the first experimental evidence of solid state amorphization under high pressure as an intermediate stage of the high-pressure decomposition of complex compounds.

j. *High-pressure synthesis of new compositions in the Li-Ni-Al-O system (E. Shinova, E. Zhecheva and R. Stoyanova/Sofia; G.D. Bromiley and T. Boffa Ballaran)*

Since the launch in 1990 of the first commercial lithium-ion battery based on a $LiCoO_2$-electrode, a new research topic in materials science has rapidly grown. This topic is devoted to the synthesis of new materials for more efficient lithium-insertion electrodes. Lithium nickel oxides ($LiNiO_2$) with layered crystal structures belong to the main family of insertion compositions in which reversible oxidation/reduction of the nickel ions takes place in the course of electrochemical lithium intercalation/deintercalation.

The general aim of this research program is the preparation and the structural characterization of new compositions in the Li-Ni-Al-O system. For the preparation of new $Li[Li_xNi_{1-x}]O_2$ and $LiAl_yNi_{1-y}O_2$ oxides, we have considered a synthetic procedure involving solid-state reaction under high-pressure in an oxygen-rich atmosphere with the intention to stabilize both Li^+, Ni^{3+} and Al^{3+} ions in the nickel layers. To the best of our knowledge, there is no data on the formation of solid solutions between "Li_2NiO_3-$LiNiO_2$-$LiAlO_2$"

The first part of the present project is aimed at a detailed crystal chemistry study of the solid solutions of trigonal $LiNiO_2$ with monoclinic Li_2NiO_3. In order to stabilize Ni^{3+} ions, lithium-nickelates were prepared using a starting mixture of Li_2O_2 and NiO. Synthesis experiments were performed using a piston-cylinder type apparatus with a reaction temperature of 700 °C and pressure of 3 GPa. Under these conditions, thermal decomposition of Li_2O_2 produces an oxygen-rich atmosphere inside the sample volume, which is sustained for the duration of the experiment, in addition to providing Li_2O for solid-state reaction with the NiO.

By varying the Li to Ni ratio in the precursor mixture, we have obtained new layered compositions $Li[Li_xNi_{1-x}]O_2$ in the range $0 \le x \le 1/3$ (Fig. 3.9-15). When the initial Li to Ni ratio varies between 1.05 to 1.2, non-stoichiometric lithium nickelates, $Li_{1-\delta}Ni_{1+\delta}O_2$, are obtained. In this case, the crystal structure of $LiNiO_2$ is composed of pure NiO_2-layers and the extra Ni ions occupy the LiO_2-layers. Nearly-stoichiometric $LiNiO_2$ oxide with δ=0.014 is prepared for a Li-to-Ni ratio in the precursor mixture of 1.1. The incorporation of Li in the NiO_2-layers occurs when the Li to Ni ratio is higher than 1.2 (Fig. 3.9-15). The structural

parameters of lithium-rich oxides become quite different from that of the well-known trigonal $LiNiO_2$. This means that Li_xNi_{1-x}-O bond lengths decreases, indicating the partial oxidation of Ni^{3+} to Ni^{4+} upon high-pressure synthesis (Fig. 3.9-16). The observed changes in the Li_xNi_{1-x}-O bond lengths coincide with corresponding changes in the mean Li-O bond length.

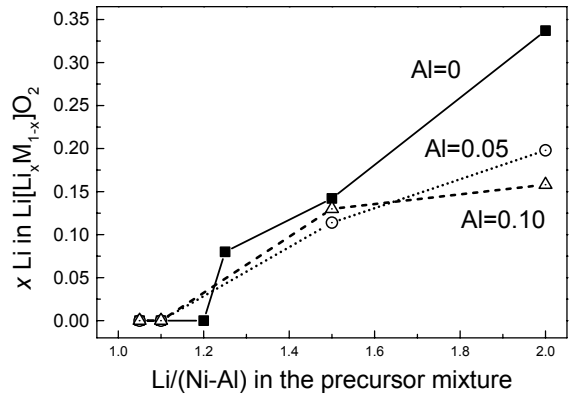

Fig. 3.9-15: Li amount in the mixed $[Li_x(Ni\text{-}Al)_{1-x}]O_2$-layers (determined from the Rietveld analysis of the XRD patterns) versus Li to (Ni-Al) ratio in the precursor mixture.

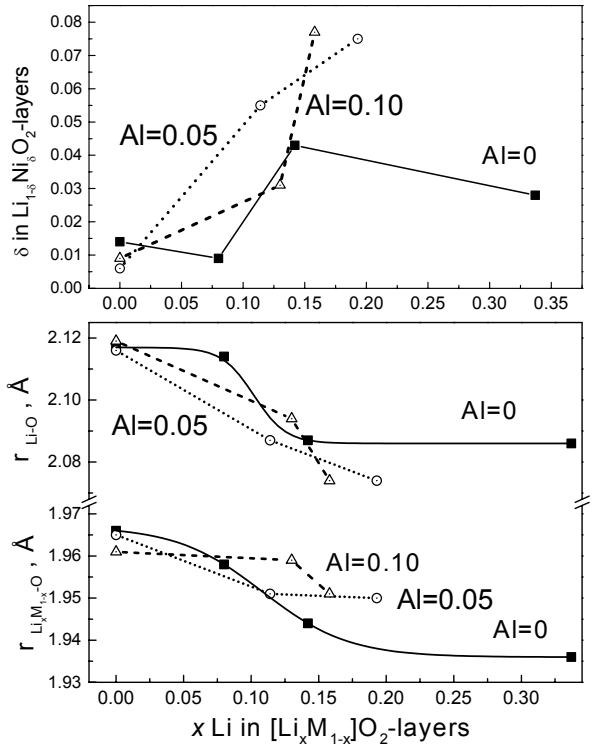

Fig. 3.9-16: Mean Li_xM_{1-x}-O and Li-O bond lengths, as well as the amount of cationic mixing between the layers, δ, versus Li amount in the mixed $[Li_xM_{1-x}]O_2$-layers.

High-pressure synthesis in oxygen atmosphere yields Al substituted $LiNiO_2$ compositions. When $Li/(Ni_{1-y}+Al_y) \leq 1.1$, layered $[Li_{1-\delta}Ni_\delta][Ni_{1-y}Al_y]O_2$ oxides isostructural to $LiNiO_2$ are formed, where Al substitutes for Ni in the NiO_2-layers. In this case, small Al additives (5 mol.%) reduce the Ni occupancy in the LiO_2-layers (Fig. 3.9-15), indicating stabilization of the layered crystal structure by Al. When the Li-to- (Ni+Al) ratio in the precursor is higher than 1.1, the incorporation of extra Li ions in the $Ni_{1-y}Al_yO_2$-layers takes place, leading to the

formation of $[Li_{1-\delta}Ni_{\delta}][Li_xNi_{1-\delta-x-y}Al_y]O_2$ solid solutions. However, the amount of Li in the mixed Ni-Al layers is lower than that in pure nickel layers (Fig. 3.9-15). In addition, there is a strong cationic mixing for Al containing oxides (Fig. 3.9-16).

k. *HP synthesis of $(AA'_3)Mn_4O_{12}$ mixed-valence double perovskites (A. Prodi, E. Gilioli, F. Licci, F. Bolzoni, M. Marezio and A.Gauzzi/Parma; F. Gaillard, G.D. Bromiley, T. Boffa Ballaran and F. Nestola)*

The search for novel materials with advanced electronic and magnetic properties at HP-HT conditions has proved to be very fruitful for discovering new complex oxides, such as Hg-based superconductors, and (Sr,Ca,Ba)CuO infinite layer compounds.

The family of $(AA'_3)Mn_4O_{12}$ (metastable) high-pressure phases possess a cubic perovskite-like structure consisting of a network of corner-sharing MnO_6 octahedra with $a^+a^+a^+$ tilt system and doubled lattice parameters. The peculiarity of their crystal framework lies in the presence of a A' Jahn-Teller ion (Mn^{3+} or Cu^{2+}) in a unique coordination that occupies the cuboctahedral site of the simple perovskite in an ordered 1:3 fashion (Fig. 3.9-17). This appears to grant great compositional flexibility to the structure and enables it to host either mono-, di-, trivalent or tetravalent cations in the A site, thus allowing the mixed valence of the octahedrally coordinated Mn to be tailored without introducing chemical disorder. This, on the contrary, is intrinsically associated to chemical doping in solid solutions.

The study of "doping-free" $(AA'_3)Mn_4O_{12}$ can therefore provide important clues for understanding the physics of disordered $A_{1-x}A'_xMnO_3$ perovskites, whose rich phase diagrams and remarkable properties (such as orbital ordering and colossal magnetoresistance) are thought to depend strongly on inhomogeneities and phase coexistence at the nanoscopic level. Indeed, we have shown that the analogy holds for $(NaMn_3)Mn_4O_{12}$ (Mn^{3+}:Mn^{4+}=1:1 on the octahedral site), which exhibits the distinctive charge-spin-orbital ordering phenomena usually observed in "half-doped manganites", such as $La_{0.5}Ca_{0.5}MnO_3$.

Nevertheless, the challenge that has to be faced when trying to characterize subtle details of the structure/properties relations in materials of such compositional complexity requires a deep comprehension of the high-pressure chemistry of these systems.

We have explored the PT condition of stability of several $(AA'_3)Mn_4O_{12}$ compounds (in particular, the Na-Mn-O phase diagram) by means of hydrothermal experiments (up to 5 kbars and 800 °C), piston cylinder and multianvil experiments (up to 80 kbars and 800 °C), with the aim of understanding the pressure effects in material synthesis and improve the synthesis design.

While mild hydrothermal condition are sufficient to synthesize the $ACu_3Mn_4O_{12}$ series, HP-HT are necessary for AMn_7O_{12}, suggesting that the role of pressure in phase formation is to

stabilize the unique coordination of the A' Jahn-Teller cation and that the two series with Mn^{3+} and Cu^{2+} are expected to have markedly different electronic structures, which could give a key to the interpretation of the physical properties observed.

Several strategies aimed at single crystal growth were attempted, including long hydrothermal runs, slow cooling in piston cylinder and multianvil experiments and recrystallization of bulk powders.

In order to obtain precious hints on how to guide the crystal growth, the recrystallization process was investigated *in situ* in hydrothermal conditions inside electrically heated DACs. Crystal up to 100 μm were obtained and characterized by means of single crystal X-ray diffraction.

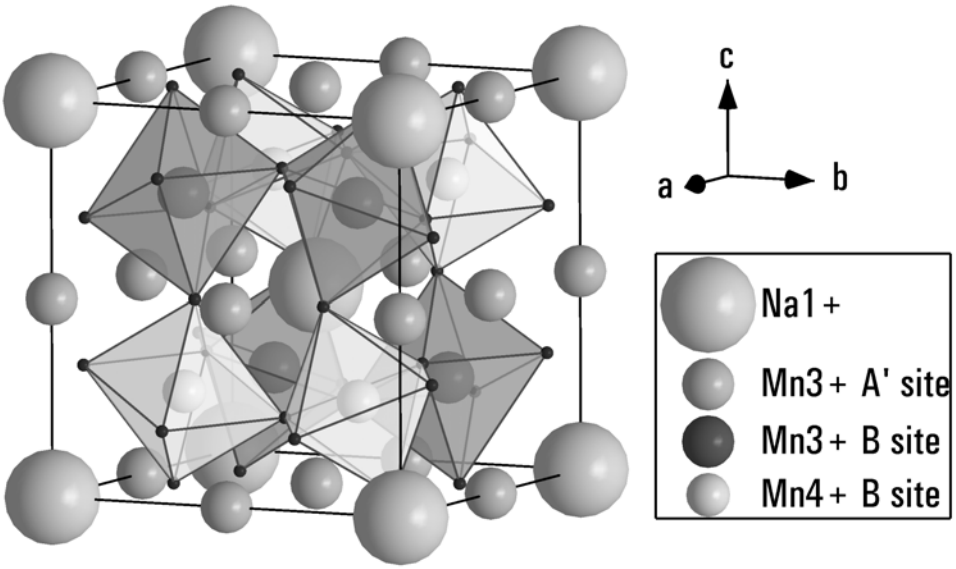

Fig. 3.9-17: Crystal structure of $(NaMn_3)Mn_4O_{12}$: the octahedral site hosts the Mn in mixed valence state, while the A' site, occupied by Jahn-Teller ions, is shown at the center of the squares representing the first coordination shell, each linking the corners of four neighbouring octahedra.

I. *Structural homologies in benzylamino-N,N bis methylphosphonic acid and its layered zirconium derivative (G.D. Gatta, in collaboration with R. Vivani and F. Costantino/Perugia)*

Layered zirconium phosphate and phosphonates have been widely investigated because they provide the materials chemist with a large toolkit for the preparation of tailor made compounds, with structure and reactivity that can be tuned for application in many fields, such as molecular and ionic recognition, catalysis, protonic conduction and so on. They are easily obtained as low-dimensional, especially layered, solids having different structures, corresponding to different chemical behaviours. They are generally very insoluble

compounds. This feature, although attractive for many potential applications, makes it difficult to deduce their structural characteristics.

We recently reported the synthesis and characterization of a series of zirconium phosphonates whose structures were solved by XRPD methods using a conventional X-ray source (Cu*K*α radiation). In this work the structure of a phosphonic acid with formula $(H_2O_3PCH_2)_2NCH_2C_6H_5$ (**1**) and of its Zr fluoride derivative (**2**) with formula $ZrF(O_3PCH_2)_2NHCH_2C_6H_5$ have been reported. The structure of **1** was solved by single crystal X-ray diffraction data while the structure of **2** was solved using the X-ray powder diffraction methods. Structure solution for compound **2** was performed using the "Reverse Monte Carlo" method implemented in the FOX program. The program is able to optimise a structural model described by the use of building blocks defined in terms of their internal coordinates, such as bond lengths, bond angles, and dihedral angles. Trial structures were generated using the "Parallel Tempering" algorithm. The structure was described using one ZrO_5F octahedron and one di-phosphonate molecule as building blocks. Benzyl ring lengths and angles were not optimised. All other dihedral angles were left to change freely. In short (about one million trials, 20 min.), the program found a stable configuration, with a connectivity similar to that previously observed in analogous systems, and a sufficiently low R_{wp} value (0.12). The model was then refined with the GSAS software.

Compound **1** crystallizes in the monoclinic system, $P2_1$ space groups with the cell parameters: a = 6.990(3) Å, b = 5.635(2) Å, c = 15.551(6) Å, β = 92.930(3)° and the molecules are packed with an interesting supramolecular arrangement. PO_3H_2 groups from adjacent molecular layers face each other and create a strongly polar region while the benzyl groups of adjacent molecular layers are interdigitated in a herringbone close packed arrangement, and define a non-polar layered region as shown in Fig. 3.9-18a. This structural character can also be found for the compound **2**: it crystallizes in orthorhombic system, *Pbca* space group with the cell parameters a = 8.9429(2) Å, b = 9.1746(2) Å, c = 31.5654(7) Å and its structure is made of corner sharing ZrO_5F octahedra and O_3PC tetrahedral (Fig. 3.9-18b). Zr octahedra are placed in two parallel planes about 4 Å apart. Pairs of phosphonate tetrahedra, facing the same side of the layers, belong to the same diphosphonate moiety, and are bridged together by the benzylamino group, via the nitrogen atom. The two phosphonate groups of each diphosphonic unit are crystallographically and chemically non-equivalent, since one of them is triply connected to three zirconium atoms, while the second one is connected by only two zirconium atoms. The third P-OH group points toward the nitrogen atom of an adjacent diphosphonic group. The N(12)···O(9)#5 distance (#5 = 1.5-x, 0.5+y, z) is only 2.48(1) Å, indicating that a strong hydrogen bond is present between them, or more probable, that the amino group is protonated by the phosphonate, as found in the pure diphosphonic acid structure, and in other similar systems.

In this layer framework the large free area potentially available for each organic group is doubly occupied by two interdigitated moieties. Future investigation will be devoted to finding out whether the whole space could be recovered to accommodate larger functional groups.

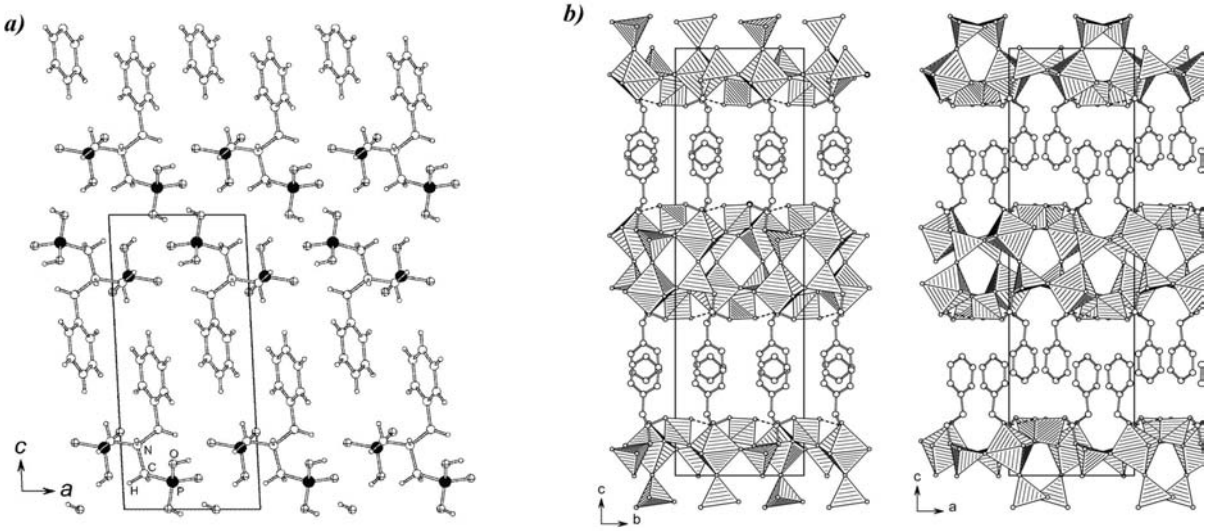

Fig. 3.9-18: *a)* Schematic view of the structure of **1** along the *b* axis; *b)* A portion of the structure of **2**, viewed along the *a* axis (left) and the *b* axis (right). Hydrogen bonds between N(12) and O(9) are represented as dashed lines.

3.10 Methodological developments

To develop novel experimental techniques and to explore their potentials is a fascinating scientific challenge, which can sometimes provide unexpected pioneering results. Such innovative efforts are necessary to eventually achieve a fundamental break-through and to be at the forefront in a certain scientific discipline. Therefore it is important to spare neither the effort nor the expense associated with time-consuming developments.

Bayerisches Geoinstitut currently has a number of high-pressure facilities and analytical techniques for *in situ* and *ex situ* micro-analysis (Raman, IR and Mössbauer spectroscopy, electrical conductivity measurements, microprobe, high-resolution ATEM, etc.). However, conventional X-ray facilities were not capable for *in situ* diffraction studies in DAC in the megabar pressure range. While the synchrotron technique is ideally suited for such work, there are a number of difficulties in combining the synchrotron operation with other requirements. Many phase transitions, in particular in complex systems, require chemical transport over distances of several microns (*e.g.* decomposition reactions). These processes are thermally activated, but rather slow due to the low diffusivities in the high-pressure phases. Reliable results can, therefore, only be achieved by extended run durations (up to 12 hours or more per PT-step). Furthermore, such studies require intermittent use of other measuring techniques (such as Mössbauer, Raman, IR, electrical conductivity) which are available in Bayreuth, but not at synchrotrons. The newly installed high-brilliance X-ray system at BGI is aimed to provide an in-house facility for diffraction studies in the megabar pressure range.

Progress in the development of the methodology of complex studies at high pressure and temperature is presented by two contributions describing (1) the system for high-pressure/ high-temperature Mössbauer studies and (2) simultaneous X-ray diffraction and electrical resistivity combined measurements on metals. As usual, we also present recent developments in the field of Nuclear Magnetic Resonance (NMR) techniques.

a. *High-brilliance X-ray system for high-pressure in-house research (L.S. Dubrovinsky, N.A. Dubrovinskaia, G.D. Gatta and F. Nestola)*

The newly installed X-ray system at BGI consists of the three major components (Fig. 3.10-1): a RIGAKU FR-D high-brilliance source, an OSMIC Inc. Confocal Max-Flux optics, and a SMART APEX 4K CCD area detector.

An FR-D high-brilliance X-ray Mo rotating anode generator operates at loads of up to 3.3 kW. The initial beam spot has an elliptical shape with the FWHM vertical axis of about 200 μm and horizontal axis of about 100 μm. The initial beam is further focused by confocal CMF optics. Utilizing constructive interference as in Bragg diffraction, thin film multilayers reflect X-rays at larger angles than total reflection mirrors, yielding a larger capture angle and thus

larger flux. A significant advantage of multilayer mirrors is their capability to act as a natural band-pass filter, automatically monochromatizing the beam, thereby providing higher intensity with much lower background. Custom made collimating and focusing 100 mm long mirrors are realized by curving the mirror surfaces into parabolic shapes. A two-dimensional reflection system is realized by using two mirrors in a "side-by-side" Kirkpatrick-Baez scheme. Each mirror independently reflects X-rays in one of the two perpendicular directions. With "side-by-side" scheme both mirrors of Confocal Max-Flux optics are manually positioned in order to optimize the performance parameters including flux, spectrum, and divergence. In order to enhance the system application for DACs, CMF optics is designed for focusing on the sample plane that provides the round beam with the FWHM diameter of about 40 μm. SMART APEX CCD detector with large 62 mm 4K chip provides unit demagnification and sensitivity of ≈170 electrons per photon.

Fig. 3.10-1: High-brilliance X-ray system for high-pressure in-house research.

Although the high-brilliance X-ray system was not specially designed for single-crystal studies, it appeared to be capable for collecting the data from single crystals as well. The garnet used for testing the high-brilliance X-ray system is from the same synthesis run described in Ohashi *et al.* (1995, Acta Cryst. C51, 2213-2215) and has the composition $Co_3Al_2Si_3O_{12}$. It is a violet gem quality single-crystal, with a very high transparency and sharp extinction (space group $Ia\bar{3}d$). A test performed using a 4-circles Huber diffractometer did not show evidence of twinning and gave the following unit-cell parameter: a = 11.4610(4) Å in very good agreement with the published data (a = 11.4603(2) Å). Using the high-brilliance X-ray system complete intensity data collection has been performed up to $2\theta_{max}$=56°. Weighted structural refinement was done using the SHELX-97 package. The refinement was performed starting from the coordinates published in Ohashi *et al.* (1995). The fractional atomic coordinates and the bond distances obtained by the refinement are within 1 or 2 standard deviations with respect to the published data and reported in Tables 1a and 1b.

	a/x	*b/y*	*c/z*	U_{eq}
Co	0.125	0	0.25	0.0130(8)
Co*	0.125	0	0.25	0.00904(5)
Al	0	0	0	0.0064(10)
Al*	0	0	0	0.00309(5)
Si	0.375	0	0.25	0.0070(10)
Si*	0.375	0	0.25	0.00384(9)
O	0.03359(13)	0.05112(14)	0.65284(13)	0.0114(8)
O*	0.03368(9)	0.05100(9)	0.65307(9)	0.0056(2)

Notes: * data from Ohashi *et al.* (1995)

Table 3.10-1a. Fractional atomic coordinates and equivalent isotropic displacement parameters ($Å^2$) for $Co_3Al_2Si_3O_{12}$ garnet.

	Present study	Ohashi *et al.* (1995)
Co-O×4	2.209(1)	2.210(1)
Co-O×4	2.332(1)	2.335(1)
Al-O×6	1.885(2)	1.889(1)
Si-O×4	1.636(1)	1.634(1)

Table 3.10-1b. Bond distances (Å) for $Co_3Al_2Si_3O_{12}$ garnet.

b. *Further developments in measuring Mössbauer spectra in the diamond anvil cell at high temperatures (I.Yu. Kantor, C.A. McCammon and L.S. Dubrovinsky)*

^{57}Fe Mössbauer spectroscopy is probably the most reliable technique to determine the valence, magnetic, and spin state of iron. An *in situ* Mössbauer spectroscopy study at ultrahigh pressures using the diamond anvil cell (DAC) can provide information on the electronic, structural and magnetic state of iron atoms at a pressure range encompassing the entire Earth's mantle and core. The addition of high temperature in the form of newly developed resistively heated DACs significantly enhances the relevance of the data.

There are two initial difficulties that restrict DAC Mössbauer spectroscopic studies at high temperatures. The first problem is that heating the cell over a relatively long time (tens of hours) causes heating of the source itself. We have solved this problem using a newly-developed platinum internal heater for the DAC (Fig. 3-10.2a). Using this new heater, the outer space remains relatively cold (about 50˚C), even when the temperature inside the DAC is about 650 K. Through the internal thermocouple that allows temperature measurements with accuracy better than ± 1˚C, we have found that the internal temperature remains constant over a long period of time. A second problem in conducting Mössbauer spectroscopic studies at high temperature is measuring the pressure at high temperature. During heating, the pressure in the DAC may change significantly, and it is important to monitor the pressure

during heating. We solved this problem with a long extension cord by moving the DAC from the Mössbauer drive (Fig. 3-10.2b) to the micro-Raman spectrometer for ruby fluorescence measurements without disconnecting the heater power supply, which allows a direct *in situ* pressure determination at high temperatures.

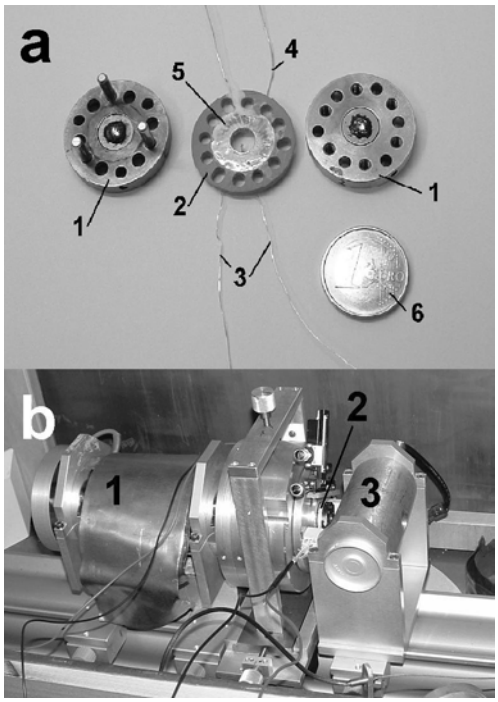

Fig. 3.10-2: New setup for high P,T Mössbauer measurements. (a) heating assembly: 1 – diamond anvil cell, 2 – ceramic (pyrophilite) heater, 3 – thermocouple, 4 – platinum wires, 5 – mica for electrical isolation, 6 – one Euro coin for scale; (b) heated DAC on Mössbauer spectrometer: 1 – source drive, 2 – heated DAC, 3 – detector.

As an example of high-pressure and high-temperature Mössbauer spectroscopic measurements we recorded Mössbauer spectra of $(Mg_{0.8}Fe_{0.2})O$ ferropericlase. At pressures higher than 55 GPa there is a change in the shape of the Mössbauer spectra that suggests a high-spin to low-spin transition of Fe^{2+}. We collected spectra at different pressures and temperatures up to 600 K and found that the proportion of low-spin Fe^{2+} is independent of temperature within experimental error (Fig. 3-10.3).

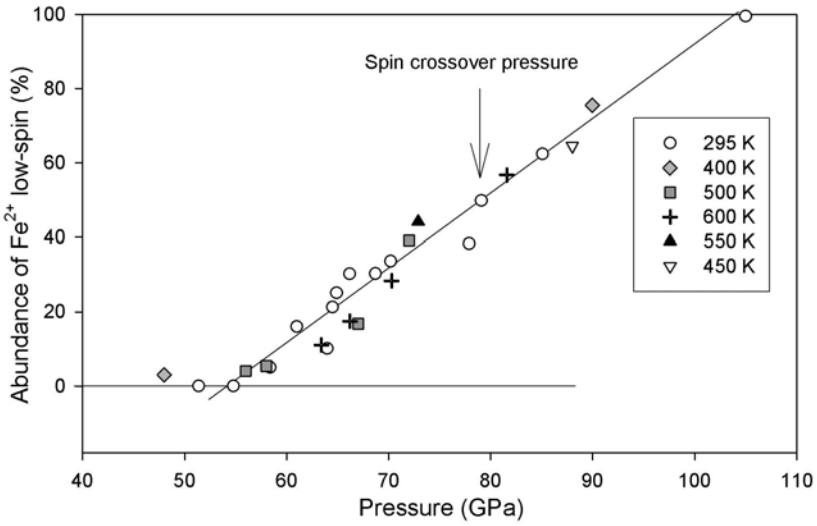

Fig. 3.10-3: Effect of pressure on the relative abundance of low-spin Fe^{2+} in $(Mg_{0.8}Fe_{0.2})O$. Within experimental error there appears to be no effect of temperature between 300 and 600 K on the relative abundance of low-spin Fe^{2+}.

c. *^{31}P chemical shielding tensor orientations for phosphorus sites in fourfold coordination (M. Bechmann and A. Sebald)*

The most common coordination pattern for phosphorus is fourfold coordination with the P atom located at the centre of an approximate tetrahedron. This is true for phosphorus in inorganic and organic phosphates as well as in organometallic compounds. Despite the large body of experimental ^{31}P solid-state NMR data available to date, very little is known about systematic patterns in the orientation of ^{31}P chemical shielding tensors for these most common molecular moieties. In contrast, some of the existing experimental data seems quite puzzling at a first glance and does not seem to be consistent. It is, however, often orientational parameters of (^{31}P) chemical shielding tensors that provide structural information.

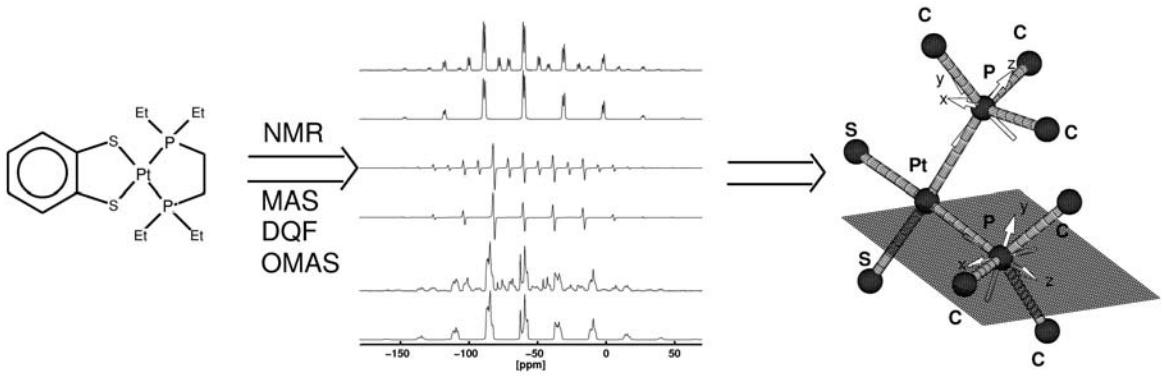

Fig. 3.10-5: A Pt(II)-phosphine complex and a selection of various experimental (upper traces) and best-fit simulated ^{31}P MAS NMR spectra. The spectral lineshapes encode the ^{31}P chemical shielding tensor orientations, these are also depicted in relation to the molecular frame.

With this situation in mind, we investigated the ^{31}P chemical shielding tensor orientations in two chemically very closely related Pt(II)-phosphine complexes both containing a square-planar P_2PtS_2 central moiety, by means of spectral lineshape analyses of various ^{31}P MAS NMR spectra obtained from polycrystalline powder samples of the two compounds (see Fig. 3.10-5 for some typical experimental and simulated ^{31}P NMR spectra of one of the two compounds, together with the resulting ^{31}P chemical shielding tensor orientation). For both compounds it was found that the direction of the *zz*-components of the ^{31}P chemical shielding tensors coincides approximately with the Pt-P bond directions. However, in one case this direction represents the *most* shielded component of the shielding tensor, whereas in the second compound the *zz*-component represents the *least* shielded component. The most common way of viewing shielding tensors is by defining their orientations with regard to the directions of chemical bonds. Here, this traditional way of viewing ^{31}P chemical shielding tensors leads to a seeming contradiction. In order to resolve this issue, we examined all known ^{31}P chemical shielding tensor orientations (mostly from ^{31}P single-crystal NMR) in the literature. From this search a clear picture emerges: the defining element for the ^{31}P chemical

shielding tensor orientation for phosphorus in fourfold coordination is an (idealised) local plane of symmetry containing the P atom and two of its directly neighboured elements. In all cases, the direction of one of the ^{31}P chemical shielding tensor components is found to be perpendicular to this (idealised) local plane. This finding also reveals the unifying picture behind the seemingly contradictory results for the two closely related Pt(II)-phosphine complexes: in both compounds, the direction of the intermediate shielding tensor component is oriented perpendicular to a (pseudo)plane defined by the P atom, the directly bonded Pt atom and one of the C atoms of the organic ligand (see Fig. 3.10-5).

4. Publications, Conference Presentations, Seminars

4.1 Publications (published)

Supplement to **2003** (papers published at the end of 2003):

O'NEILL, H.S.C.; POWNCEBY, M.; MCCAMMON, C.A. (2003): The magnesiowüstite: iron equilibrium and its implications for the activity-composition relations of $(Mg,Fe)_2SiO_4$ olivine solid solutions. Contributions to Mineralogy and Petrology 146, 308-325

2004

a) Refereed international journals

ABDU, Y.A.; ANNERSTEN, H.; DUBROVINSKY, L.S.; DUBROVINSKAIA, N.A. (2004): High-pressure Mössbauer studies on $Fe_{53}Ni_{47}$ alloy. Hyperfine Interactions 156 (1), 389-394

AHUJA, R.; DUBROVINSKY, L.S.; DUBROVINSKAIA, N.A.; OSORIO GUILLEN, J.M.; MATTESINI, M.; JOHANSSON, B.; LE BIHAN, T. (2004): Titanium metal at high pressure: Synchrotron experiments and *ab initio* calculations. Physical Review B 69, 184102

ALLWARDT, J.R.; SCHMIDT, B.C.; STEBBINS, J.F. (2004): Structural mechanisms of compression and decompression in high-pressure $K_2Si_4O_9$ glasses: An investigation utilizing Raman and NMR spectroscopy of high-pressure glasses and crystals. Chemical Geology 213, 137-151

AMAMI, M.; VAN SMAALEN, S.; BEN SALAH, A.; HELLUY, X.; SEBALD, A. (2004): Structural investigation of trimethylammonium tetrachloromercurate. Journal of Solid State Chemistry 177, 2961-2970

BECHMANN, M.; DUSOLD, S.; SEBALD, A.; SHUTTLEWORTH, W.A.; JAKEMAN, D.L.; MITCHELL, D.J.; EVANS, J.N.S. (2004): ^{13}C chemical shielding tensor orientations in a phosphoenolpyruvate moiety from ^{13}C rotational-resonance MAS NMR lineshapes. Solid State Sciences 6, 1097-1105

BIZZARRI, R.; AMBROSETTI, P.; ARGENTI, P.; GATTA, G.D.; BALDANZA, A. (2004): L'affioramento del Caio (Lago di Corbara, Orvieto, Italia Centrale) nell'ambito dell'evoluzione paleogeografica Plio-Pleistocenica della Valle del Tevere: evidenze sedimentologiche e stratigrafiche. Italian Journal of Quaternary Sciences 16(2), 241-255

BLÄß, U.W.; LANGENHORST, F.; BOFFA BALLARAN, T.; SEIFERT, F.; FROST, D.J.; MCCAMMON, C.A. (2004): A new oxygen deficient perovskite phase $Ca(Fe_{0.4}Si_{0.6})O_{2.8}$ and phase relations along the join $CaSiO_3$ - $CaFeO_{2.5}$ at transition zone conditions. Physics and Chemistry of Minerals 31, 52-65

BOFFA BALLARAN, T.; CARPENTER, M.A.; DOMENEGHETTI, M.C. (2004): Order parameter variation through the $C2/m$-$P2_1/m$ phase transition in cummingtonite. American Mineralogist 89, 1717-1727

BRAZHKIN, V.; DUBROVINSKAIA, N.A.; NICOL, M.; NOVIKOV, N.; RIEDEL, R.; SOLOZHENKO, V.L.; ZHAO, Y. (2004): What does "harder than diamond" mean? Nature Materials 3, No. 9, 576-577

BROMILEY, G.D.; KEPPLER, H. (2004): An experimental investigation of hydroxyl solubility in jadeite and Na-rich clinopyroxenes. Contributions to Mineralogy and Petrology 147(2), 189-200

BROMILEY, G.D.; HILAIRET, N.; MCCAMMON, C.A. (2004): Solubility of hydrogen and ferric iron in rutile and TiO_2 (II): Implications for phase assemblages during ultrahigh-pressure metamorphism and for the stability of silica polymorphs in the lower mantle. Geophysical Research Letters 31(4), L04610, doi: 10.1029/2004GL019430

BROMILEY, G.D.; KEPPLER, H.; MCCAMMON, C.A.; BROMILEY, F.A.; JACOBSEN, S.D. (2004): Hydrogen solubility and speciation in natural, gem-quality chromian diopside. American Mineralogist 89, 941-949

COMODI, P.; BERNARDI, M.; BENTIVOGLIO, A.; GATTA, G.D.; ZANAZZI P.F. (2004): Production and technology of Middle Age glazed ceramic from Saepinum territory (Italy): a multi-methodical approach. Archaeometry 46(3), 405-419

DMITRIEV, V.P.; KUZNETSOV, A.Yu.; BANDILET, O.; BOUVIER, P.; DUBROVINSKY, L.S.; MACHON, D.; WEBER, H.-P. (2004): Stability of the high-pressure monoclinic phases in Ce and Pr metals: Comparative diffraction study and phenomenological theory. Physical Review B 70, 014104

DOBSON, D.P.; JACOBSEN, S.D. (2004): The flux growth of magnesium silicate perovskite single crystals. American Mineralogist 89, 807-811

DU, L.-S.; ALLWARDT, J.R.; SCHMIDT, B.C.; STEBBINS, J.F. (2004): Pressure-induced structural changes in a borosilicate glass-forming liquid: boron coordination, non-bridging oxygens, and network ordering. Journal of Non-Crystalline Solids 337, 196-200

DUBROVINSKAIA, N.A.; DUBROVINSKY, L.S.; MCCAMMON, C.A. (2004): Iron-magnesium alloying at high pressures and temperatures. Journal of Physics: Condensed Matter 16, S1143-S1150

DUBROVINSKAIA, N.A.; DUBROVINSKY, L.S.; LANGENHORST, F.; JACOBSEN, S.D.; LIEBSKE, C. (2004): Nanocrystalline diamond synthesized from C_{60}. Diamond and Related Materials 14/1, 16-22

DUBROVINSKY, L.S.; DUBROVINSKAIA, N.A. (2004): High-pressure crystallography at elevated temperatures: experimental approach. – In: KATRUSIAK, A.; MCMILLAN, P. (Eds.): "High-pressure crystallography", NATO Science Series, II. Mathematics, Physics and Chemistry 140, Kluwer Academic Publishers, Dordrecht, Boston, London, 393- 410

DUBROVINSKY, L.S.; DUBROVINSKAIA, N.A. (2004): Angle-dispersive diffraction under non-hydrostatic stress in diamond anvil cells. Journal of Alloys and Compounds 375, 86-92

DUBROVINSKY, L.S.; DUBROVINSKAIA, N.A.; PRAKAPENKA, V.; SEIFERT, F.; LANGENHORST, F.; DMITRIEV, V.P.; WEBER, H.-P.; LE BIHAN, T. (2004): A class of new high-pressure silica polymorphs. Physics of the Earth and Planetary Interiors 143-144, 231-240

DUBROVINSKY, L.S.; DUBROVINSKAIA, N.A.; LANGENHORST, F.; DOBSON, D.P.; RUBIE, D.C.; GEßMANN, C.; LE BIHAN, T.; CRICHTON, W.A. (2004): Reaction of iron and silica at core-mantle boundary conditions. Physics of the Earth and Planetary Interiors 146, 243-247

EL GORESY, A.; DUBROVINSKY, L.S.; SHARP, T.G.; CHEN, M. (2004): Stishovite and post-stishovite polymorphs of silica in the Shergotty meteorite: their nature, petrographic settings versus theoretical predictions and relevance to Earth's mantle. Journal of Physics and Chemistry of Solids 65, 1597-1608

FROST, D.J.; LIEBSKE, C.; LANGENHORST, F.; MCCAMMON, C.A.; TRØNNES, R.; RUBIE, D.C. (2004): Experimental evidence for the existence of iron-rich metal in the Earth's lower mantle. Nature 428, 409-412

FROST, D.J.; POE, B.T.; TRØNNES, R.G.; LIEBSKE, C.; DUBA, A.; RUBIE, D.C. (2004): A new large-volume multianvil system. Physics of the Earth and Planetary Interiors 143-144, 507-514

GAILLARD F. (2004): Laboratory measurements of electrical conductivity of hydrous and dry silicic melt under pressure. Earth and Planetary Science Letters 218, 215-228

GAILLARD, F.; SCAILLET, B.; PICHAVANT, M. (2004): Evidence for present-day leucogranite pluton growth in Tibet. Geology 32, 801-805

GATTA, G.D.; BOFFA BALLARAN, T.; COMODI, P.; ZANAZZI, P.F. (2004): Isothermal equation of state and compressional behaviour of tetragonal edingtonite. American Mineralogist 89, 633-639

GATTA, G.D.; BOFFA BALLARAN, T. (2004): New insight into the crystal structure of orthorhombic edingtonite: evidence for a split Ba site. Mineralogical Magazine 68, 167-175

GATTA, G.D.; BOFFA BALLARAN, T.; COMODI, P.; ZANAZZI, P.F. (2004): Comparative compressibility and equation of state of orthorhombic and tetragonal edingtonite. Physics and Chemistry of Minerals 31, 288-298

GATTA, G.D.; WELLS, S.W. (2004): Rigid unit modes at high pressure: an explorative study of a fibrous zeolite like framework with EDI topology. Physics and Chemistry of Minerals 31, 465-474

HUBER, A.; HEUER, M.; FEHR, K.T.; BENTE, K.; SCHMIDBAUER, E.; BROMILEY, G.D. (2004): Characterisation of synthetic hedenbergite ($CaFeSi_2O_6$) – petedunnite ($CAZnSi_2O_6$) solid solution series by X-ray powder diffraction and ^{57}Fe Mössbauer spectroscopy. Physics and Chemistry of Minerals 31(2), 67-79

IEZZI, G.; DELLA VENTURA, G.; OBERTI, R.; CÁMARA, F.; HOLTZ, F. (2004): Synthesis and crystal-chemistry of $Na(NaMg)Mg_5Si_8O_{22}(OH)_2$, a $P2_1/m$ amphibole. American Mineralogist 89, 640-646

IEZZI, G.; CÁMARA, F.; DELLA VENTURA, G.; OBERTI, R.; PEDRAZZI, G.; ROBERT, J.-L. (2004): Synthesis, crystal structure and crystal chemistry of ferri-clinoholmquistite, □$Li_2Mg_3Fe^{3+}{}_2Si_8O_{22}(OH)_2$. Physics and Chemistry of Minerals 31, 375-385

JACOBSEN, S.D.; SMYTH, J.R.; SPETZLER, H.; HOLL, C.M.; FROST, D.J. (2004): Sound velocities and elastic constants of iron-bearing hydrous ringwoodite. Physics of the Earth and Planetary Interiors 143-144, 47-56

JACOBSEN, S.D.; SPETZLER, H.; REICHMANN, H.-J.; SMYTH, J.R. (2004): Shear waves in the diamond anvil cell reveal pressure-induced instability in (Mg,Fe)O. PNAS 101, No. 16, 5867-5871

KANTOR, I.Yu.; MCCAMMON, C.A.; DUBROVINSKY, L.S. (2004): Mössbauer spectroscopic study of pressure-induced magnetisation in wüstite (FeO). Journal of Alloys and Compounds 376, 5-8

KANTOR, A.P.; JACOBSEN, S.D.; KANTOR, I.Yu.; DUBROVINSKY, L.S.; MCCAMMON, C.A.; REICHMANN, H.-J.; GONCHARENKO, I.N. (2004): Pressure-induced magnetization in FeO: Evidence from elasticity and Mössbauer spectroscopy. Physical Review Letters 93, 215502

KAWAMOTO, T. (2004): Hydrous phase stability and partial melt chemistry in H_2O-saturated KLB-1 peridotite up to the uppermost lower mantle conditions. Physics of the Earth and Planetary Interiors 143-144, 387-395

LANGENHORST, F.; POIRIER, J.-P.; FROST, D.J. (2004): TEM observations of microscopic inclusions in synthetic diamond. Journal of Materials Science 39, 1865-1867

LEE, K.K.M.; STEINLE-NEUMANN, G.; JEANLOZ, R. (2004): *Ab-initio* high-pressure alloying of iron and potassium: Implications for the Earth's core. Geophysical Research Letters 31, L11603, doi: 10.1029/2004GL019839

LINNEN, R.L.; KEPPLER, H.; STERNER, S.M. (2004): *In situ* measurements of the H_2O:CO_2 ratio in fluid inclusions by infrared spectroscopy. The Canadian Mineralogist 42, 1275-1282

MALAVERGNE, V.; SIEBERT, J.; GUYOT, F.; GAUTRON, L.; COMBES, R.; HAMMOUDA, T.; BORENSZTAJN, S.; FROST, D.J.; MARTINEZ, I. (2004): Si in the core? New high-pressure and high-temperature experimental data. Geochimica et Cosmochimica Acta 68 (20), 4201-4211

MARSCHALL, H.; ERTL, A.; HUGHES, J.M.; MCCAMMON, C.A. (2004): Metamorphic Na- and OH-rich disordered dravite with tetrahedral boron, associated with omphacite, from Syros, Greece: chemistry and structure. European Journal of Mineralogy 16, 817-823

MASHKINA, E.; MCCAMMON, C.A.; SEIFERT, F. (2004): A Mössbauer study of oxygen vacancy and cation distribution in 6H-$BaTi_{1-x}Fe_xO_{3-x/2}$. Journal of Solid State Chemistry 177, 262-267

MATTESINI, M.; DE ALMEIDA, J.S.; DUBROVINSKY, L.S.; DUBROVINSKAIA, N.A.; JOHANSSON, B.; AHUJA, R. (2004): Cubic TiO_2 as a potential light absorber in solar-energy conversion. Physical Review B 70, 115101

MCCAMMON, C.A. (2004): Mössbauer spectroscopy: Applications. – In: BERAN, A.; LIBOWITSKY, E. (Eds.): "Spectroscopic Methods in Mineralogy", Eötvös University Press, Budapest, 369-398

MCCAMMON, C.A.; FROST, D.J.; SMYTH, J.R.; LAUSTSEN, H.M.S.; KAWAMOTO, T.; ROSS, N.L.; VAN AKEN, P.A. (2004): Oxidation state of iron in hydrous mantle phases: Implications for subduction and mantle oxygen fugacity. Physics of the Earth and Planetary Interiors 143-144, 157-169

MCCAMMON, C.A.; KOPYLOVA, M.G. (2004): A redox profile of the Slave mantle and oxygen fugacity control in the cratonic mantle. Contributions to Mineralogy and Petrology 148, 55-68

MCCAMMON, C.A.; LAUTERBACH, S.; SEIFERT, F.; LANGENHORST, F.; VAN AKEN, P.A. (2004): Iron oxidation state in lower mantle mineral assemblages: I. Empirical relations derived from high-pressure experiments. Earth and Planetary Science Letters 222, 435-449

MCCAMMON, C.A.; STACHEL, T.; HARRIS, J.W. (2004): Iron oxidation state in lower mantle mineral assemblages: II. Inclusions in diamonds from Kankan, Guinea. Earth and Planetary Science Letters 222, 423-434

MCENROE, S.A.; SKILBREI, J.R.; ROBINSON, P.; HEIDELBACH, F.; LANGENHORST, F.; BROWN, L.L. (2004): Magnetic anomalies, layered intrusions and Mars. Geophysical Research Letters 31, L19601, doi: 10.1029/2004GL020640

MCENROE, S.A.; LANGENHORST, F.; ROBINSON, P.; BROMILEY, G.D.; SHAW, C.S.J. (2004): What is magnetic in the lower crust? Earth and Planetary Science Letters 226(1-2), 175-192

MIYAJIMA, N.; LANGENHORST, F.; FROST, D.J.; YAGI, T. (2004): Electron channelling spectroscopy of iron in majoritic garnet and silicate perovskite using a transmission electron microscope. Physics of the Earth and Planetary Interiors 143-144, 601-609

MOLNAR, G.; KITAZAWA, T.; DUBROVINSKY, L.S.; MCGARVEY, J.; BOUSSEKSOU, A. (2004): Pressure tuning Raman spectroscopy of the spin crossover coordination polymer $Fe(C_5H_5N)_2[Ni(CN)_4]$. Journal of Physics: Condensed Matter 16, S1129 -S1136

NESTOLA, F.; TRIBAUDINO, M.; BOFFA BALLARAN, T. (2004): High-pressure behaviour, transformation and crystal structure of synthetic iron-free pigeonite. American Mineralogist 89, 189-196

NESTOLA, F.; BOFFA BALLARAN, T.; BENNA, P.; TRIBAUDINO, M.; BRUNO, E. (2004): High-pressure phase transitions in $Ca_{0.2}Sr_{0.8}Al_2Si_2O_8$ feldspar. American Mineralogist 89, 1474-1479

PARTZSCH, G.M.; LATTARD, D.; MCCAMMON, C.A. (2004): Mössbauer spectroscopic determination of Fe^{3+}/Fe^{2+} in synthetic basaltic glass: A test of empirical fO_2 equations under superliquidous and subliquidous conditions. Contributions to Mineralogy and Petrology 147, 565-580

PRAKAPENKA, V.B.; SHEN, G.Y.; DUBROVINSKY, L.S. (2004): Carbon transport in diamond anvil cell. High-Pressure High-Temperature 35/36, 127-151

PRAKAPENKA, V.P.; SHEN, G.Y.; DUBROVINSKY, L.S.; RIVERS, M.L.; SUTTON, S.R. (2004): High-pressure induced phase transformation of SiO_2 and GeO_2: difference and similarity. Journal of Physics and Chemistry of Solids 65, 1537-1545

PROYER, A.; DACHS, E.; MCCAMMON, C.A. (2004): Pitfalls in geothermometry of eclogites: Fe^{3+} and changes in the mineral chemistry of omphacite at ultrahigh pressures. Contributions to Mineralogy and Petrology 147, 305-318

RAVNA, E.J.K.; TERRY, M.P. (2004): Geothermobarometry of UHP and HP eclogites and schists – An evaluation of equilibria among garnet-clinopyroxene-kyanite-phengite-coesite/quartz. Journal of Metamorphic Geology 22, 579-592

RODEHORST, U.; CARPENTER, M.A.; BOFFA BALLARAN, T.; GEIGER, C.A. (2004): Local structural heterogeneity, mixing behaviour and saturation effects in the grossular-spessartine solid solution. Physics and Chemistry of Minerals 31, 387-404

RUBIE, D.C.; GESSMANN, C.K.; FROST, D.J. (2004): Partitioning of oxygen during core formation on the Earth and Mars. Nature 429, 58-61

RUBIE, D.C.; DUFFY, T.S.; OHTANI, E. (2004): Introduction: New developments in high pressure mineral physics and applications to the Earth's interior. Physics of the Earth and Planetary Interiors 143-144, 1-3

SCHMIDT, B.C.; GAILLARD, F.; SMITH, M.E. (2004): Characterisation of ^{17}O-enriched alumina from a new hydrothermal preparation. Solid State NMR 26, 197-202

SCHMIDT, B.C.; ZOTOV, N.; DUPREE, R. (2004): Structural implications of water and boron dissolution in albite glass. Journal of Non-Crystalline Solids 337, 207-219

SCHMIDT, B.C. (2004): Effect of boron on the water speciation in (alumino)silicate melts and glasses. Geochimica et Cosmochimica Acta 68, 5013-5025

SEISENBAEVA, G.A.; SUNDBERG, M.; NYGREN, M.; DUBROVINSKY, L.S.; KESSLER, V.G. (2004): Thermal decomposition of the methoxide complexes $MoO(OMe)_4$, $Re_4O_6(OMe)_{12}$ and $(Re_{1-x}Mo_x)O_6(OMe)_{12}$ ($0.24 \leq x \leq 0.55$). Materials Chemistry and Physics 87(1), 142-148

SHAW, C.S.J. (2004): The temporal evolution of three magmatic systems in the West Eifel volcanic field, Germany. Journal of Volcanology and Geothermal Research 131, 213-240

SMYTH, J.R.; HOLL, C.M., FROST, D.J.; JACOBSEN, S.D. (2004): High pressure crystal chemistry of hydrous ringwoodite and water in the Earth's interior. Physics of the Earth and Planetary Interiors 143-144, 271-278

SOLOZHENKO, V.L.; DUBROVINSKAIA, N.A., DUBROVINSKY; L.S. (2004): Synthesis of bulk superhard semiconducting B-C material. Applied Physics Letters 85, No. 9, 1508-1510

STEINLE-NEUMANN, G.; COHEN, R.E. (2004): Comment on 'On the importance of the free energy for elasticity under pressure'. Journal of Physics: Condensed Matter 16, 8783-8786

STEINLE-NEUMANN, G.; COHEN, R.E.; STIXRUDE, L. (2004): Magnetism in iron as a function of pressure. Journal of Physics: Condensed Matter 16, S1109-S1119

STEINLE-NEUMANN, G.; STIXRUDE, L.; COHEN, R.E. (2004): Magnetism in dense hexagonal iron. PNAS 101, No. 1, 33-36

STOYANOVA, R.; ZHECHEVA, E.; ALCÁNTARA, R.; TIRADO, J.L.; BROMILEY, G.D.; BROMILEY, F.A.; BOFFA BALLARAN, T. (2004): Layered solid solutions of $LiCo_{1-x}Ni_xO_2$ with α-$LiGaO_2$ obtained under high oxygen pressure. Journal of Materials Chemistry 14(3), 366-373

TALYZIN, A.V.; DUBROVINSKY, L.S. (2004): *In situ* Raman study of C_{60} polymerization during isothermal pressurizing at 800 K. Journal of Physics: Condensed Matter 16, 757-772

TALYZIN, A.V.; DUBROVINSKY, L.S. (2004): Pressure-induced phase transformations in tetragonal and rhombohedral C_{60} polymers. High Temperatures – High Pressures 35/36, 47-53

TERASAKI, H.; KATO, T.; FUNAKOSHI, K.; SUZUKI, A.; URAKAWA, S. (2004): Viscosity of liquid sulphur under high pressure. Journal of Physics: Condensed Matter 16, 1707-1714

TERRY, M.P.; HEIDELBACH, F. (2004): Superplasticity in garnet from eclogite facies shear zones in the Haram Gabbro, Haramsøya, Norway. Geology 32, 281-284

TERRY, M.P.; ROBINSON, P. (2004): Geometry of eclogite-facies structural features: Implications for production and exhumation of ultrahigh-pressure and high-pressure rocks, Western Gneiss Region, Norway. Tectonics 23, doi: 10.1029/2002TC001401

URAKAWA, S.; SOMEYA, K.; TERASAKI, H.; KATSURA, T.; YOKOSHI, S.; FUNAKOSHI, K.; UTSUMI, W.; KATAYAMA, Y.; SUEDA, Y.; IRIFUNE, T. (2004): Phase relations and equations of state for FeS at high pressures and high temperatures and implications to the internal structure of Mars. Physics of the Earth and Planetary Interior 143-144, 469-479

VIVANI, R.; COSTANTINO, F.; NOCCHETTI, M.; GATTA, G.D. (2004): Structural homologies in benzylamino-N,N-bis methylphosphonic acid and its layered zirconium derivative. Journal of Solid State Chemistry 177, 4013-4022

XU, Y.S.; SHANKLAND, T.J.; LINHARDT, S.; RUBIE, D.C.; LANGENHORST, F.; KLASINSKI K. (2004): Thermal diffusivity measurements of olivine, wadsleyite and ringwoodite to 20 GPa and 1100 °C. Physics of the Earth and Planetary Interiors 143/44, 321-336

WALTER, M.J.; NAKAMURA, E.; TRØNNES, R.G.; FROST, D.J. (2004): Experimental constraints on crystallization differentiation in a deep magma ocean. Geochimica et Cosmochimica Acta 68 (20), 4267-4284

WILLIAMS, H.M.; MCCAMMON, C.A.; PESLIER, A.H.; HALLIDAY, A.N.; TEUTSCH, N.; LEVASSEUR, S.; BURG, J.-P. (2004): Iron isotope fractionation and the oxygen fugacity of the mantle. Science 304, 1656-1659

b) Other publications and press reports

DEUTSCH, A.; LANGENHORST, F.; MASAITIS, V.L. (2004): A treasury in Sibiria. German Research, Special 2004, 66-71

LANGENHORST, F. (2004): Impaktkrater auf der Erde – Spuren des kosmischen Bombardements. GMIT Heft 1, 8-17

SEIFERT, F. (editor) (2004): From Crust to Core and Back – Geomaterials Research at Bayerisches Geoinstitut. Universität Bayreuth, 72 p

c) Monographs

RUBIE, D.C.; DUFFY, T.; OHTANI, E. (Guest Editors) (2004): High Pressure Mineral Physics and Applications to the Earth's Interior. Physics of the Earth and Planetary Interiors (special issue) 143-144, 616 pp

4.2 Publications (submitted, in press)

BECHMANN, M.; SEBALD, A.: MAS NMR with and without double-quantum filtration at and near the $n = 0$ rotational resonance condition. Journal of Magnetic Resonance (in press)

BECHMANN, M.; FOERSTER, H.; MAISEL, H.; SEBALD, A.: Double-quantum filtered 1H MAS NMR spectra. Solid State Nuclear Magnetic Resonance (in press)

BECHMANN, M.; DUSOLD, S.; GEIPEL, F.; SEBALD, A.; SELLMANN, D.: Magnitudes and orientations of 31P chemical shielding tensors in Pt(II)-phosphine complexes and other four-fold coordinated phosphorus sites. Journal of Physical Chemistry B (submitted)

BOTCHARNIKOV, R.; KOEPKE, J.; HOLTZ, F.; MCCAMMON, C.A.; WILKE, M.: The effect of water activity on the oxidation and structural state of Fe in a ferro-basaltic melt. Geochimica et Cosmochimica Acta (in press)

BROMILEY, G.D.; HILAIRET, N.: An investigation of hydrogen and minor element incorporation in synthetic rutile. Mineralogical Magazine, special edition on proton-mediated interactions in minerals (submitted)

CHAKHMOURADIAN, A.R.; MCCAMMON, C.A.; COOPER, M.A.: Schorlomite: A discussion of the crystal chemistry, formula, and inter-species boundaries. Physics and Chemistry of Minerals (in press)

CORGNE, A.; LIEBSKE, C.; WOOD, B.J.; FROST, D.J.; RUBIE, D.C.: Silicate perovskite-melt partitioning of trace elements and geochemical signature of a deep perovskitic reservoir. Geochimica et Cosmochimica Acta (in press)

COUVY, H.; FROST, D.J.; HEIDELBACH, F.; NYILAS, K.; UNGÁR, T.; MACKWELL, S.J.; CORDIER, P.: Shear deformation experiments of forsterite at 11 GPa – 1400 °C in the multianvil apparatus. European Journal of Mineralogy (in press)

DAHL, P.S.; HAMILTON, M.A.; TERRY, M.P.; FREI, R.; JERCINOVIC, M.J.; WILLIAMS, M.L.: Comparative geochronometry of monazite in metamorphic rocks from the eastern Wyoming province (USA), with implications for U-Th-Pb chemical dating by electron microprobe. American Mineralogist (in press)

DAHL, P.S.; TERRY, M.P.; HAMILTON, M.A.; JERCINOVIC, M.J.; WILLIAMS, M.L.; FOLAND, K.A.: *In situ* microchronometry of metamorphic monazite, with implications for dating polyphase deformation in the eastern Wyoming province (Black Hills, South Dakota, USA). American Mineralogist (submitted)

DELLA VENTURA, G.; IEZZI, G.; REDHAMMER, G.J.; HAWTHORNE, F.C.; SCAILLET, B.; NOVEMBRE, D.: Synthesis and crystal-chemistry of amphiboles along the magnesioriebeckite – magnesio-arfvedsonite series as a function of fO_2. American Mineralogist (in press)

DELLA VENTURA, G.; REDHAMMER, G.J.; IEZZI, G.; HAWTHORNE, F.C.; PAPIN, A.; ROBERT, J.-L.: A Mössbauer and FTIR study of synthetic amphiboles along the magnesioriebeckite – ferri-clinoholmquistite join. Physics and Chemistry of Minerals (in press)

DEMOUCHY, S.; DELOULE, E.; FROST, D.J.; KEPPLER, H.: Effect of temperature and pressure on water solubility in wadsleyite. American Mineralogist (submitted)

DMITRIEV, V.P.; DUBROVINSKY, L.S.; LE BIHAN, T.; BASHKIN, I.; KUZNETSOV, A.Yu.; PONYATOVSKY, E.; WEBER, H.-P.: Compressing TiZr: from the electron driven collapse to the phonon triggered expansion. Physical Review Letters (submitted)

DUBROVINSKAIA, N.A.; DUBROVINSKY, L.S.: Electrical heating in diamond anvil cells. Frontiers in High Pressure Research (in press)

DUBROVINSKY, L.S.; DUBROVINSKAIA, N.A.; KANTOR, I.Yu.; MCCAMMON, C.A.; CRICHTON, W.A.; URUSOV, V.: Decomposition of ferropericlase $(Mg_{0.80}Fe_{0.20})O$ at high pressures and temperatures. Journal of Alloys and Compounds (in press)

DUBROVINSKY, L.S.; DUBROVINSKAIA, N.A.; KANTOR, I.Yu.; ABRIKOSOV, I.; VITOS, L.; AHUJA, R.; CRICHTON, W.A.; SIMIONOVICI, A.; DMITRIEV, V.P.; PRAKAPENKA, V.B.; SHEN, G.: Iron-magnesium alloy in the Earth's core. Science (submitted)

DUBROVINSKY, L.S.; DUBROVINSKAIA, N.A.; KUZNETSOV, A.; KANTOR, I.Yu.: Chemistry at extreme conditions: Approaching the Earth's major interface. Frontiers in High Pressure Research (in press)

GAILLARD, F.; IACONO MARZIANO, G.: The electrical conductivity of magma in the course of crystallization is controlled by their residual liquid composition. Journal of Geophysical Research (submitted)

GATTA, G.D.; COMODI, P.; ZANAZZI, P.F.; BOFFA BALLARAN, T.: Anomalous elastic behaviour and high-pressure structural evolution of zeolite levyne. American Mineralogist (in press)

GATTA, G.D.; BOFFA BALLARAN, T.; IEZZI G.: High-pressure X-ray and Raman study of a Li-clinopyroxene: Influence of site-dimension on the elastic behaviour. Physics and Chemistry of Minerals (in press)

GATTA, G.D.: A comparative study of fibrous zeolites under pressure. European Journal of Mineralogy (submitted)

HACKER, B.R.; RUBIE, D.C.; KIRBY, S.H.; BOHLEN, S.R.: The calcite $\rightarrow$ aragonite transformation in low-Mg marble. Journal of Geophysical Research (submitted)

IEZZI, G.; GATTA, G.D.; KOCKELMANN, W.; DELLA VENTURA, G., RINALDI, R.; SCHÄFER, W.; PICCININI, M.; GAILLARD, F.: Low-T neutron powder-diffraction and synchrotron-radiation IR study of synthetic amphibole $Na(NaMg)Mg_5Si_8O_{22}(OH)_2$. American Mineralogist (in press)

IEZZI, G.; BOFFA BALLARAN, T.; MCCAMMON, C.A.; LANGENHORST, F.: The $CaGeO_3$-$Ca_3Fe_2Ge_3O_{12}$ garnet solid solution. Physics and Chemistry of Minerals (in press)

IEZZI, G.; DELLA VENTURA, G.; HAWTHORNE, F.C.; PEDRAZZI, G.; NOVEMBRE, D.; ROBERT, J.-L.: The (Mg,Fe^{2+}) substitution in ferri-clinoholmquistite, $\square Li_2(Mg,Fe^{2+})_3Fe^{3+}{}_2Si_8O_{22}(OH)_2$. European Journal of Mineralogy (submitted)

JACOBSEN, S.D.; DEMOUCHY, S.; FROST, D.J.; BOFFA BALLARAN, T.; KUNG, J.: A systematic study of OH in hydrous wadsleyite from polarized FTIR spectroscopy and single-crystal X-ray diffraction: oxygen sites for hydrogen storage in the Earth's interior. American Mineralogist (in press)

KANTOR, I.Yu.; DUBROVINSKY, L.S.; MCCAMMON, C.A.; KANTOR, A.P.; PASCARELLI, S.; AQUILANTI, G.; CRICHTON, W.A.; MATTESINI, M.; AHUJA, R.; ALMEIDA, V.; URUSOV, V.: Rhombohedral distortion of $Mg_{0.8}Fe_{0.2}O$ ferropericlase at high pressures. Physical Review B (submitted)

KONZETT, J.; YANG, H.; FROST, D.J.: Phase relations and stability of magnetoplumbite- and crichtonite-series phases under upper mantle P-T conditions: an experimental study to 15 GPa with implications for LILE-metasomatism in the lithospheric mantle. Journal of Petrology (in press)

LIEBSKE, C.; CORGNE, A.; FROST, D.J.; WOOD, B.J.; RUBIE, D.C.: Compositional effects on element partitioning between Mg-silicate perovskite and silicate melts. Contributions to Mineralogy and Petrology (in press)

MAINPRICE, D.; TOMMASI, A.; COUVY, H.; CORDIER, P.; FROST, D.J.: Pressure sensitivity of olivine slip systems: implications for the interpretation of seismic anisotropy of the Earth's upper mantle. Nature (in press)

MARTON, F.C.; SHANKLAND, T.J.; RUBIE, D.C.; XU, Y.: Effects of variable thermal conductivity on the mineralogy of subducting slabs and implications for mechanisms of deep earthquakes. Physics of the Earth and Planetary Interiors (in press)

MCCAMMON, C.A.: Mantle oxidation state and oxygen fugacity: Constraints on mantle chemistry, structure and dynamics. – In: Structure, Composition and Evolution of Earth's Mantle, American Geophysical Union, Washington DC (in press)

NESTOLA, F.; BOFFA BALLARAN, T.; TRIBAUDINO, M.; OHASHI, H.: Compressional behaviour of $CaNiSi_2O_6$ clinopyroxene: bulk modulus systematics and cation type in clinopyroxenes. Physics and Chemistry of Minerals (submitted)

O'NEILL, H.S.C.; BERRY, A.J.; MCCAMMON, C.A.; JAYASURIYA, K.D.; CAMPBELL, S.J.; FORAN, G.: A direct experimental determination of the effect of pressure on the Fe^{3+}/Fe^{2+} ratio of an anhydrous silicate melt to 3.0 GPa. American Mineralogist (submitted)

SANDBAKKEN, P.T.; LANGENHORST, F.; DYPVIK, H.: Shock metamorphism of quartz at the submarine Mjølnir impact crater, Barents sea. Meteoritics and Planetary Sciences (submitted)

SEIDEL, K.; ETZKORN, M.; SONNENBERG, L.; SEBALD, A.; BALDUS, M.: Studying 3D structure and dynamics by high-resolution solid-state NMR: Application to L-tyrosine-ethylester. Journal of Physical Chemistry B (submitted)

SKÁLA, R.; HÖRZ, F.; LANGENHORST, F.: Experimentally shock-loaded anhydrite: unit-cell dimensions, microstrain and domain size from X-ray powder diffraction. GSA Special Volume (in press)

SMYTH, J.R.; HOLL, C.M.; LANGENHORST, F.; LAUSTSEN, H.M.; ROSSMAN, G.R.; KLEPPE, A.; MCCAMMON, C.A.; KAWAMOTO, T.; VAN AKEN, P.A.: Crystal chemistry of wadsleyite II and water in the Earth's interior. Physics and Chemistry of Minerals (in press)

SUZUKI, A.; OHTANI, E.; TERASAKI, H.; FUNAKOSHI, K.: Viscosity of silicate melts in $CaMgSi_2O_6$-$NaAlSi_2O_6$ system at high pressure: Physics and Chemistry of Minerals (submitted)

SWAMY, V.; KUZNETSOV, A.Yu.; DUBROVINSKY, L.S.; CARUSO, R.A.; SHCHUKIN, D.G.; MUDDLE, B.C.: Finite-size and pressure effects on the Raman spectra of nanocrystalline anatase TiO_2. Physical Review B (submitted)

TALYZIN, A.V.; LANGENHORST, F.; DUBROVINSKAIA, N.A.; DUB, S.; DUBROVINSKY, L.S.: Structural characterisation of the "hard fullerite" phase obtained at 13 GPa and 830 K. Physical Review B (submitted)

TARANTINO, S.C.; GHIGNA, P.; MCCAMMON, C.A.; AMANTEA, R.; CARPENTER, M.A.: Local structural properties of $(Mn,Fe)Nb_2O_6$ from Mössbauer and X-ray absorption spectroscopy. Acta Crystallographica B (in press)

TERASAKI, H.; FROST, D.J.; RUBIE, D.C.; LANGENHORST, F.: The effect of oxygen and sulphur on the dihedral angle between Fe-O-S melt and silicate minerals at high pressure: Implications for Martian core formation. Earth and Planetary Science Letters (submitted)

TERRY, M.P.; HEIDELBACH, F.: Deformation-enhanced metamorphic reactions and the rheology of high-pressure shear zones in the Western Gneiss Region, Norway. Journal of Metamorphic Geology (submitted)

TIRONE, M.; GANGULY, J.; DOHMEN, R.; LANGENHORST, F.; HERVIG, R.; BECKER, H.-W.: Rare Earth diffusion kinetics in garnet: Experimental studies and applications. Geochimica et Cosmochimica Acta (in press)

TOMMASI, A.; MAINPRICE, D.; CORDIER, P.; THORAVAL, C.; COUVY, H.: Strain-induced seismic anisotropy of wadsleyite polycrystals and flow patterns in the mantle transition zone. Journal of Geophysical Research Solid Earth (in press)

TRIBAUDINO, M.; NESTOLA, F.; OHASHI, H.: High-temperature single crystal investigation in a clinopyroxene of composition $(Na_{0.5}Ca_{0.5})(Cr_{0.5}Mg_{0.5})Si_2O_6$. European Journal of Mineralogy (in press)

TRIBAUDINO, M.; BENNA, P.; NESTOLA, F.; MENEGHINI, C.; BRUNO, E.: Thermodynamic behaviour of the high-temperature P-1 / I-1 phase transition along the $CaAl_2Si_2O_8$ – $SrAl_2Si_2O_8$ join. Physics and Chemistry of Minerals (submitted)

TRIBAUDINO, M.; NESTOLA, F.; MENEGHINI, C.: The average structure of clinopyroxenes with intermediate Ca-content along the join diopside-enstatite. Canadian Mineralogist (submitted)

WILLIAMS, H.M.; PESLIER, A.H.; MCCAMMON, C.A.; HALLIDAY, A.N.; TEUTSCH, N.; LEVASSEUR, S.; BURG, J.-P.: Iron isotope fractionation in mantle minerals and the effects of partial melting and oxygen fugacity. Earth and Planetary Science Letters (in press)

WRIGHT, K.; BLANCHARD, M.; BRAITHWAITE, J.S.; CATLOW, C.R.A.; DEMOUCHY, S.; GATZEMEIER, A.; WALKER, A.M.: Simulation of H defects in the nominally anhydrous minerals of the Earth's upper mantle and transition zone. Special Issue of Mineralogical Magazine on "Proton mediated interaction in minerals" (submitted)

4.3 Presentations at scientific institutions and at congresses

AKBER-KNUTSON, S.; STEINLE-NEUMANN, G.: 13.-17.12.2004, AGU Fall Meeting, San Francisco, USA[*3]: "Aluminium incorporation in post-perovskite from first principles", EOS Trans. AGU, 85(47), Fall Meet. Suppl., Abstract MR22A-08, 2004

ALLWARDT, J.R.; STEBBINS, J.F.; SCHMIDT, B.C.; FROST, D.J.; WITHERS, A.C.; HIRSCHMANN, M.M.: 13.-17.12.2004, AGU Fall Meeting, San Francisco, USA[*3]: "Aluminium coordination and density in high-pressure aluminosilicate glasses: Significance for the structural changes and densification in basaltic magmas, EOS Trans. AGU, 85(47), Fall Meet. Suppl., Abstract V52A-01, 2004

BLÄß, U.W.; BOFFA BALLARAN, T.; FROST, D.J.; LANGENHORST, F.; MCCAMMON, C.A.; SEIFERT, F.; VAN AKEN, P.A.: 04.-07.04.2004, EMPG X, Frankfurt/M., Germany[*1]: "Exchange of silicon by trivalent cations of iron or aluminium in calcium silicate perovskite", Lithos 73, 1-2, Supplement 1, S10

BOFFA BALLARAN, T.; CARPENTER, M.A.: 05.-11.06.2004, Goldschmidt Conference, Copenhagen, Denmark[*2] *(invited)*: "Hard mode infrared spectroscopy applied to the study of solid solutions", Conference Supplement to Geochimica et Cosmochimica Acta, A78

BOFFA BALLARAN, T.: 26.-31.08.2004, 22nd European Crystallographic Meeting, Budapest, Hungary *(invited)*: "High-pressure behaviour of pyroxenes"

BOTCHARNIKOV, R.; KOEPKE, J.; HOLTZ, F.; MCCAMMON, C.A.; WILKE, M.: 04.-07.04.2004, EMPG X, Frankfurt/M., Germany[*1]: "The oxidation and structural state of Fe in hydrous ferrobasaltic melt", Lithos 73, 1-2, Supplement 1, S13

BROMILEY, G.D.; HILARET, N.; MCCAMMON, C.A.: 04.-07.04.2004, EMPG X, Frankfurt/M., Germany[*1]: "H and Fe^{3+} solubility in rutile and TiO_2 (II): Phase assemblages during UHP metamorphism and the role of silica polymorphs in the lower mantle", Lithos 73, 1-2, Supplement 1, S14

BROMILEY, G.D.; HILARET, N.; MCCAMMON, C.A.: 21.04.2004, Royal Institution meeting "H in oxides", London, U.K.: "H and Fe^{3+} incorporation in synthetic rutile and TiO_2 (II) up to 10 GPa"

BROMILEY, G.D.; HILARET, N.; MCCAMMON, C.A.: 05.-11.06.2004, Goldschmidt Conference, Copenhagen, Denmark[*2]: "H and Fe^{3+} solubility in rutile and TiO_2 (II): Effects on phase stability, and the role on silica polymorphs in the lower mantle", Conference Supplement to Geochimica et Cosmochimica Acta, A37

BROMILEY, F.A.; BOFFA BALLARAN, T.; ZHANG, M.; LANGENHORST, F.: 05.-11.06.2004, Goldschmidt Conference, Copenhagen, Denmark[*2]: "A macroscopic and microscopic investigation of the $MgCO_3$-$CdCO_3$ solid solution", Conference Supplement to Geochimica et Cosmochimica Acta, A87

BROMILEY, G.D.; HILAIRET, N. (2004): 13.-14.09.2004, University of Manchester, U.K.: "An investigation of H and minor element incorporation in synthetic rutile. Mineralogical Society meeting "Proton-mediated interactions in Minerals"

COMODI, P.; GATTA, G.D.; ZANAZZI, P.F.; BOFFA BALLARAN, T.: 26.-29.09.2004, XXXIV Nat. Congr. Italian Association of Crystallography, Rome, Italy: "Anomalous elastic behaviour and high-pressure structural evolution of zeolite levyne"

CORDIER, P.; COUVY, H.; RATERRON, P.; DURNICK, J.; MAINPRICE, D.; TOMMASI, A.: 13.-17.12.2004, AGU Fall Meeting, San Francisco, USA[*3] *(invited)*: "Pressure sensitivity of olivine slip systems: Evidence from high-pressure deformation experiments", EOS Trans. AGU, 85(47), Fall Meet. Suppl., Abstract T13D-03, 2004

COUVY, H.; TOMMASI, A.; MAINPRICE, D.; CORDIER, P.; FROST, D.J.; LANGENHORST, F.: 04.-07.04.2004, EMPG X, Frankfurt/M., Germany[*1]: "Deformation texture in wadsleyite and ringwoodite: Implications for the seismic anisotropy of the transition zone", Lithos 73, 1-2, Supplement 1, S20

COUVY, H.: 10.06.2004, Université Blaise Pascal, Laboratoire Magma et Volcan, Clermont-Ferrand, France: "Déformation des minéraux du manteau sous haute pression et haute température: implications pour l'anisotropie sismique du manteau"

COUVY, H.: 15.06.2004, Université Montpellier, Laboratoire de Tectonophysique, Montpellier, France: "Déformation des minéraux du manteau sous haute pression et haute température: implications pour l'anisotropie sismique du manteau"

DELLA VENTURA, G.; REDHAMMER, G.; IEZZI, G.: 20.-28.08.2004, 32nd International Geological Congress, Florence, Italy: "A Mössbauer and FTIR study of synthetic amphiboles along the magnesio-riebeckite – ferri-holmquistite join"

DELLA VENTURA, G.; IEZZI, G.; REDHAMMER, G.; SCAILLET, B.; NOVEMBRE, D.: 20.-28.08.2004, 32nd International Geological Congress, Florence, Italy: "The composition of magnesioriebeckitew as a function of fO_2: an experimental study"

DEMOUCHY, S.; DELOULE, E.; FROST, D.J.; KEPPLER, H.: 05.-11.06.2004, Goldschmidt Conference, Copenhagen, Denmark[*2]: "Effect of temperature and pressure on water solubility in wadsleyite", Conference Supplement to Geochimica et Cosmochimica Acta, A32

DEMOUCHY, S.; DELOULE, E.; FROST, D.J.; KEPPLER, H.: 11.-16.07.2004, 5th HYDROSPEC workshop, Stockholm, Sweden: "Effect of temperature and pressure on water solubility in wadsleyite"

DEMOUCHY, S.: 21.09.2004, Laboratoire Magma et Volcan, Clermont-Ferrand, France: "L'eau dans le manteau terrestre, Mobilite et solubilite de l'hydrogen dans l'olivine et la wadsleyite"

DOBSON, D.P.; MEREDITH, P.; HEIDELBACH, F.: 04.-07.04.2004, EMPG X, Frankfurt/M., Germany[*1]: "Aseismic remobilisation of faults during the olivine-wadsleyite transition", Lithos 73, 1-2, Supplement 1, S27

DUBROVINSKAIA, N.A.; DUBROVINSKY, L.S.: 01.-03.06.2004, III International Conference "Phase Transformations under High Pressure", HPP-2004, Chernogolovka, Moscow Region, Russia: "External electrical heating for the diamond anvil cell: implication for investigations of the structure and properties of the high-pressure phases"

DUBROVINSKAIA, N.A.: 27.07.2004, Vortrag des Monats, Kompetenzzentrum Neue Materialien Nordbayern GmbH, Bayreuth, Germany: "Novel superhard materials: synthesis at extreme conditions and characterization"

DUBROVINSKAIA, N.A.; DUBROVINSKY, L.S.: 20.-28.08.2004, 32nd International Geological Congress, Florence, Italy: "Melting curve and phase relations of water studied in externally heated diamond anvil cell"

DUBROVINSKY, L.S.; DUBROVINSKAIA, N.A.: 01.-03.06.2004, III International Conference "Phase Transformations under High Pressure", HPP-2004, Chernogolovka, Moscow Region, Russia: "Chemical reactions at extreme conditions: Approaching Earth major interface"

DUBROVINSKY, L.S.; DUBROVINSKAIA, N.A.; KANTOR, I.Yu.; CRICHTON, W.A.: 20.-28.08.2004, 32nd International Geological Congress, Florence, Italy: "Stability of magnesiowüstite in the lower mantle"

DUBROVINSKY, L.S.; DUBROVINSKAIA, N.A.; KANTOR, I.Yu.; CRICHTON, W.A.: 20.-28.08.2004, 32nd International Geological Congress, Florence, Italy: "Olivine in the lower mantle"

DUBROVINSKY, L.S.; DUBROVINSKAIA, N.A.: 26.-31.08.2004 22nd European Crystallographic Meeting, Budapest, Hungary: "Crystallography at extreme conditions: state of the art"

FROST, D.J.; LIEBSKE, C.; MCCAMMON, C.A.; LANGENHORST, F.; TRØNNES, R.G.; RUBIE, D.C.: 04.-07.04.2004, EMPG X, Frankfurt/M., Germany[*1]: "Experimental evidence for the existence of a metallic iron-rich phase in the Earth's mantle", Lithos 73, 1-2, Supplement 1, S38

FROST, D.J.; TRØNNES, R.G.; LIEBSKE, C.; LANGENHORST, F.; MCCAMMON, C.A.; RUBIE, D.C.: 05.-11.06.2004, Goldschmidt Conference, Copenhagen, Denmark[*2]: "The crystal chemistry of aluminous perovskite may cause precipitation of metallic Fe in the lower mantle", Conference Supplement to Geochimica et Cosmochimica Acta, A562

FROST, D.J.; LIEBSKE, C.; LANGENHORST, F.; MCCAMMON, C.A.; TRØNNES, R.G.; RUBIE, D.C.: 04.-09.07.2004, 9th Symposium on the Study of the Earth's Deep Interior, Garmisch-Partenkirchen, Germany: "The oxidation state of iron in the Earth's lower mantle"

FROST, D.J.: 14.-15.09.2004, 2nd Workshop "Interior – Early Evolution – Core Formation", Deutsche Forschungsgemeinschaft "Mars and the Terrestrial Planets", München, Germany: "The formation of metallic iron in planetary mantles"

FROST, D.J.: 12.11.2004, Oxford University, Department of Earth Sciences, Oxford, U.K.: "Ferric iron solubility in mantle minerals: Implications for the evolution of the Earth's redox state"

FROST, D.J.: 03.12.2004, Laboratoire Magma et Volcan, Clermont-Ferrand, France: "Mantle phase transformations and the sharpness of seismic discontinuities"

GAILLARD, F.: 09.03.2004, Laboratoire des Magmas et Volcans, Clermont-Ferrand, France: "Electrical conductivity of magma: From laboratory to field work in volcanic area"

GAILLARD, F.: 12.03.2004, Laboratoire de Géologie des Chaines Alpines, Grenoble, France: "Electrical conductivity as a probe of the Earth's interior: From laboratory to field"

GAILLARD, F.: 04.-07.04.2004, EMPG X, Frankfurt/M., Germany*1: "Electrical conductivity of crystallizing hydrous magma", Lithos 73, 1-2, Supplement 1, S41

GAILLARD, F: 24.-30.04.2004, 1st General Assembly of the European Geosciences Union, Nice, France: "Real time assessment of magma storage conditions by geophysical, petrological, and laboratory constraints", Geophysical Research Abstracts 6, Abstract 06138, 2004

GAILLARD, F.; SCHMIDT, B.C.; MCCAMMON, C.A.; PICHAVANT, M.; SCAILLET, B.; MACKWELL, S.J.: 20.-23.07.2004, Oxygen in the Terrestrial Planets, Santa Fe, USA: "Redox exchanges in hydrous magma: On the relationships between redox and water"

GATTA, G.D.; IEZZI, G.; BOFFA BALLARAN, T.: 04.-07.04.2004, EMPG X, Frankfurt/M., Germany*1: "Elastic behaviour of Mg-bearing ferri-spodumene", Lithos 73, 1-2, Supplement 1, S41

GATTA, G.D.; IEZZI, G.; BOFFA BALLARAN, T.: 20.-28.08.2004, 32nd International Geological Congress, Florence, Italy: "High-pressure X-ray and Raman study of a Li-clinopyroxene: Influence of site-dimension on the elastic behaviour"

GATTA, G.D.; BOFFA BALLARAN, T.: 20.-28.08.2004, 32nd International Geological Congress, Florence, Italy: "A systematic study of fibrous zeolites under pressure"

GATTA, G.D.: 26.-29.09.2004, XXXIV Nat. Congr. Italian Association of Crystallography, Rome, Italy: "High-pressure crystallography of natural microporous materials: experimental set-up and comparative crystal physics"

GLASMACHER, U.A.; LANG, M.; KEPPLER, H.; LANGENHORST, F.; NEUMANN, R.; SCHARDT, D.; TRAUTMANN, C.; WAGNER, G.A.: 04.-07.04.2004, EMPG X, Frankfurt/M., Germany*1: "Heavy-iron irradiation of solids at extreme pressures: Ion track formation and high-pressure phases", Lithos 73, 1-2, Supplement 1, S43

HEIDELBACH, F.: 02.03.2004, Bundesanstalt für Materialforschung, Berlin, Germany: "EBSD Anwendungen in polyphasen Gesteinen"

HEIDELBACH, F.: 04.-07.04.2004, EMPG X, Frankfurt/M., Germany*1: "The effect of large shear deformation on the fabric and the seismic anisotropy of polycrystalline magnesiowüstite", Lithos 73, 1-2, Supplement 1, S49

HIRT, A.M.; ROBINSON, P.; HEIDELBACH, F.; MCENROE, S.A.: 13.-17.12.2004, AGU Fall Meeting, San Francisco, USA[*3]: "Magnetic anisotropy of hemo-ilmenite single crystals: Testing the lamellar magnetism hypothesis", EOS Trans. AGU, 85(47), Fall Meet. Suppl., Abstract GP21A-0154, 2004

IEZZI, G.; BOFFA BALLARAN, T.; MCCAMMON, C.A.; LANGENHORST, F.: 20.-28.08.2004, 32nd International Geological Congress, Florence, Italy: "Crystal chemistry of cubic and tetragonal germanate garnets"

IEZZI, G.; GATTA, G.D.; KOCKELMANN, W.; DELLA VENTURA, G.; RINALDI, R.; SCHÄFER, W.; GAILLARD, F.: 20.-28.08.2004, 32nd International Geological Congress, Florence, Italy: "A $P2_1/m$ amphibole at low temperature (8 K): a neutron powder diffraction study"

IEZZI, G.; DELLA VENTURA, G.; PEDRAZZI, G.; HAWTHORNE, F.C.; NOVEMBRE, D.; ROBERT, J.-L.: 20.-28.08.2004, 32nd International Geological Congress, Florence, Italy: "Crystal-chemistry of synthetic (Mg,Fe^{2+})-ferri-clinoholmquistite"

IEZZI, G.; DELLA VENTURA, G.; CÁMARA, F.; OBERTI, R.; ROBERT, J.-L.: 20.-28.08.2004, 32nd International Geological Congress, Florence, Italy: "Li-bearing amphiboles: synthesis, stability and composition of clinoholmquistites"

JACOBSEN, S.D.; GILBERT, H.J.; BOFFA BALLARAN, T.; FROST, D.J.; DEMOUCHY, S.; HEMLEY, R.J.: 17.-21.05.2004, 2004 Joint Assembly, Montreal, Canada: "The effect of water on the $P2_1/c$ to $C2/c$ high-pressure phase transition in $MgSiO_3$-clinopyroxene: implications for the mantle X-discontinuity", EOS Trans. AGU, 85(17), Jt. Assem. Suppl., Abstract U53A-04, 2004

KANTOR, A.P.: 12.-15.04.2004, Lomonosov 2004, The International Conference of Students, Post Graduate Students and Young Scientists, Moscow, Russia: "Magnetic ordering of wüstite at about 5 GPa: elasticity measurements and Mössbauer spectroscopy"

KANTOR, A.P.: 20.-28.08.2004, 32nd International Geological Congress, Florence, Italy: "Pressure-induced magnetization in FeO: evidence from elasticity and Mössbauer spectroscopy"

KANTOR, I.Yu.: 12.-15.04.2004, Lomonosov 2004, The International Conference of Students, Post Graduate Students and Young Scientists, Moscow, Russia: "Symmetry-breaking transition in mantle composition ferropericlase at 35 GPa and 297 K"

KANTOR, I.Yu.: 20.-28.08.2004, 32nd International Geological Congress, Florence, Italy: "Rhombohedral distortion of $Mg_{0.8}Fe_{0.2}O$ ferropericlase at high pressure"

KEGLER, P.; HOLZHEID, A.; FROST, D.J.; RUBIE, D.C.; PALME, H.: 04.-07.04.2004, EMPG X, Frankfurt/M., Germany[*1]: "Reinvestigation of the metal/silicate partition behaviour of Ni and Co", Lithos 73, 1-2, Supplement 1, S55

KEGLER, P.; HOLZHEID, A.; RUBIE, D.C.; FROST, D.J.; PALME, H.: 19.-22.09.2004, 82. Jahrestagung der Deutschen Mineralogischen Gesellschaft, Karlsruhe, Germany: "Influence of pressure and temperature on metal/silicate partitioning of Ni and Co: Implications for planetary differentiation processes", Beihefte zum European Journal of Mineralogy 16, 65

LANGENHORST, F.: 16.01.2004, DFG-Rundgespräch, GeoForschungsZentrum Potsdam, Germany: "Potenzial von Mikrostrukturen in metamorphen Mineralen"

LANGENHORST, F.: 30.01.2004, Technische Universität Darmstadt, Germany: "Diamant und Perowskit: Kristalline Phasen an der Schnittstelle von Geo- und Materialwissenschaften"

LANGENHORST, F.: 10.02.2004, Institute for Solid State Physics, Tokyo, Japan: "Discovery of high-pressure phases in a Martian meteorite"

LANGENHORST, F.: 13.02.2004, University of Sendai, Tohoku, Japan: "Introduction to ATEM and applications to Earth interior"

LANGENHORST, F.: 16.02.2004, University of Sendai, Tohoku, Japan: "High-pressure minerals in shocked meteorites and terrestrial impact rocks: New insights from TEM"

LANGENHORST, F.: 17.02.2004, University of Sendai, Tohoku, Japan: "ATEM-EELS studies of diamond and diamond-structured BCN-compounds"

LANGENHORST, F.; POIRIER, J.-P.; DEUTSCH, A.; HORNEMANN, U.: 17.03.2004, Lunar and Planetary Science Conference, Houston, USA: "Experimental reproduction of shock veins in single-crystal minerals"

LANGENHORST, F.: 26.03.2004, La journée de Poirier, Université de Paris 6, Institut Physique du Globe, Paris, France: "A look into the nanoworld of high-pressure phases"

LANGENHORST, F.: 01.04.2004, PhD short course, Deutsche Mineralogische Gesellschaft, Universität Köln, Germany: "Impaktprozesse"

LANGENHORST, F.; DEUTSCH, A.; HORNEMANN, U.: 04.-07.04.2004, EMPG X, Frankfurt/M., Germany[*1]: "Experimental study on the shock behaviour of anhydrite", Lithos 73, 1-2, Supplement 1, S67

LANGENHORST, F.: 27.04.2004, Staatliche Naturhistorische Sammlungen Dresden, Museum für Mineralogie und Geologie, Dresden, Germany: "Diamanten in der Natur – Mikrostrukturelle Einblicke in ihre Genese"

LANGENHORST, F.: 14.06.2004, Westfälische Wilhelms-Universität Münster, Institut für Planetologie, Münster, Germany: "Impaktdiamanten und Hochdrucksilikate in Meteoriten"

LANGENHORST, F.: 19.07.2004, Naturwissenschaftliche Gesellschaft Bayreuth e.V., Universität Bayreuth, Germany: "Einschlagskrater auf der Erde – Zeugen kosmischer Katastrophen"

LANGENHORST, F.: 19.-22.09.2004, 82. Jahrestagung der Deutschen Mineralogischen Gesellschaft, Karlsruhe, Germany: "Ein Blick ins Erdinnere – TEM-Studien an Hochdruckphasen"

LANGENHORST, F.: 27.10.2004, Wismut-Kolloquium, Friedrich-Schiller-Universität Jena, Germany: "Auf Entdeckungsreise im Nanoraum – Phasenanalyse mit TEM"

LANGENHORST, F.: 08.11.2004, FAIR workshop, GSI Darmstadt, Germany: "Dynamic compression of minerals"

LEE, K.K.M.; STEINLE-NEUMANN, G.: 13.-17.12.2004, AGU Fall Meeting, San Francisco, USA[*3]: "High-pressure alloying of xenon and iron: 'Missing' Xe in the Earth's core?", EOS Trans. AGU, 85(47), Fall Meet. Suppl., Abstract MR41A-08, 2004

LIEBERMANN, R.C.; LANGENHORST, F.: 13.-17.12.2004, AGU Fall Meeting, San Francisco, USA[*3]: "Evolution, structure, and properties of the Earth's core I", EOS Trans. AGU, 85(47), Fall Meet. Suppl., Abstract MR41A, 2004

LIEBSKE, C.; CORGNE, A.; FROST, D.J.; WOOD, B.J.; MCCAMMON, C.A.; RUBIE, D.C.: 04.-07.04.2004, EMPG X, Frankfurt/M., Germany[*1]: "Effects of Al on Mg-silicate perovskite composition and trace element partitioning", Lithos 73, 1-2, Supplement 1, S70

LIEBSKE, C.; SCHMICKLER, B.; TERASAKI, H.; SUZUKI, A.; FUNAKOSHI, K.; ANDO, R.; POE, B.T.; RUBIE, D.C.: 04.-07.04.2004, EMPG X, Frankfurt/M., Germany[*1]: "Viscosity of pyrolite liquid at high pressure", Lithos 73, 1-2, Supplement 1, S70

LIEBSKE, C.; FROST, D.J.; RUBIE, D.C.: 10.09.2004, Institut für Mineralogie und Petrographie, ETH Zurich, Switzerland: "Mantle melting at high pressure: Experimental constraints on magma ocean differentiation"

MAINPRICE, D.; COUVY, H.; TOMMASI, A.; CORDIER, P.; FROST, D.J.: 07.-09.07.2004, 2nd International Conference on Texture and Anisotropy in Polycrystals, Metz, France: "The heritage of deformation texture during the olivine to wadsleyite phase transformation at high temperature and pressure"

MARTON, F.C.; BINA, C.R.: 05.-11.06.2004, Goldschmidt Conference, Copenhagen, Denmark[*2]: "Metastable phase transitions and latent heat release", Conference Supplement to Geochimica et Cosmochimica Acta, A92

MARTON, F.C.: 13.-17.12.2004, AGU Fall Meeting, San Francisco, USA[*3]: "Variable thermal conductivity, slab mineralogy, and subduction rates", EOS Trans. AGU, 85(47), Fall Meet. Suppl., Abstract T21B-0535, 2004

MCCAMMON, C.A.: 19.03.2004, Australian National University, Research School of Earth Sciences, Canberra, Australia: "What's so special about iron, or everything you ever wanted to know about oxidation state"

MCCAMMON, C.A.: 01.04.2004, Australian National University, Research School of Earth Sciences, Canberra, Australia: "Oxygen fugacity, diamonds and mantle dynamics"

MCCAMMON, C.A.: 16.04.2004, Australian Defence Force Academy, Department of Physics, Canberra, Australia: "Perovskite: where materials science and geophysics meet"

MCCAMMON, C.A.: 20.04.2004, Macquarie University, Department of Earth and Planetary Sciences, Sydney, Australia: "Oxygen fugacity, diamonds and mantle dynamics"

MCCAMMON, C.A.: 29.04.2004, Monash University, Department of Physics and Materials Engineering, Clayton, Australia: "Perovskite: where materials science and geophysics meet"

MCCAMMON, C.A.: 03.05.2004, Australian National University, Department of Earth and Marine Sciences, Canberra, Australia: "Diamonds are not forever: Constraints on their genesis and destruction"

MCCAMMON, C.A.: 04.05.2004, Australian Goethe Society, Canberra, Australia: "The Goethe-Humboldt connection and the Earth's interior"

MCCAMMON, C.A.: 07.05.2004, Australian National University, Research School of Earth Sciences, Canberra, Australia: "Perovskite: where materials science and geophysics meet"

MCCAMMON, C.A.: 30.08.-08.09.2004, 6th EMU School on "Spectroscopic Methods in Mineralogy", Vienna, Austria: "Mössbauer spectroscopy: Applications"

MCCAMMON, C.A.; O'NEILL, H.S.C.; BERRY, A.J.; JAYASURIYA, K.D.; CAMPBELL, S.J.: 04.-08.09.2004, 5th European Conference on Mineralogy and Spectroscopy, Vienna, Austria: "Short-range structure of iron in anorthite-diopside glass"

MCCAMMON, C.A.: 28.10.2004, Centre for Planetary Science, Copenhagen, Denmark: "Oxygen fugacity, diamonds and mantle dynamics"

MCCAMMON, C.A.: 04.11.2004, ETH, Department of Earth Sciences, Zurich, Switzerland: "Oxygen fugacity, diamonds and mantle dynamics"

MCCAMMON, C.A.: 06.12.2004, University of Oregon, Department of Geological Sciences, Eugene, USA: "Oxygen fugacity, diamonds and mantle dynamics"

MCCAMMON, C.A.: 13.-17.12.2004, AGU Fall Meeting, San Francisco, USA[*3] *(invited)*: "Mantle oxidation state and oxygen fugacity: Constraints on mantle chemistry, structure and dynamics", EOS Trans. AGU, 85(47), Fall Meet. Suppl., Abstract GP21C-02, 2004

MCENROE, S.A.; ROBINSON, P.; HARRISON, R.J.; LANGENHORST, F.: 13.-17.12.2004, AGU Fall Meeting, San Francisco, USA[*3] *(invited)*: "Lamellar magnetism: A new magnetic substructure?", EOS Trans. AGU, 85(47), Fall Meet. Suppl., Abstract V42A-01, 2004

NESTOLA, F.: 24.-27.10.2004, 1. Fränkisches Kristallographentreffen, Tüchersfeld/ Pottenstein, Germany: "High-pressure behaviour of Earth's crust and mantle silicate minerals"

NESTOLA, F.; BOFFA BALLARAN, T.; TRIBAUDINO, M.; OHASHI, H.: 32nd International Geological Congress, Florence, Italy: "Compressional behaviour of $CaNiSi_2O_6$"

NYILAS, K.; COUVY, H.; CORDIER, P.; UNGÁR, T.: 02.-05.09.2004, EPDIC9, Praha, Czech Republik: "The dislocation structure and crystallite size determined by X-ray line profile analysis in forsterite deformed at 11 GPa at 1400 °C", EPDIC9 proceedings

OBERTI, R.; QUARTIERI, S.; BAIOCCHI, M.; DALCONI, M.C.; BOSCHERINI, F.; DALCONI, C.M.; IEZZI, G.; ORLANDO A.: 20.-28.08.2004, 32nd International Geological Congress, Florence, Italy: "A multi-technique *in situ* investigation of site preference and local envinronment of scandium in garnets"

POE, B.T.; ROMANO, C.; KREIDIE, N.; MCCAMMON, C.A.: 04.-07.04.2004, EMPG X, Frankfurt/M., Germany[*1]: "The effect of Fe-Mg substitution on the electrical conductivity of pyrope ($Mg_3Al_2Si_3O_8$) – almandine ($Fe_3Al_2Si_3O_8$) garnets", Lithos 73, 1-2, Supplement 1, S89

POE, B.T.; ROMANO, C.; TERASAKI, H.; LIEBSKE, C.; RUBIE, D.C.; FUNAKOSHI, K.; SUZUKI, A.; OHTANI, E.: 05.-08.07.2004, XII Convegno Società Italiana di Luce di Sincrotrone, Camerino, Italy: "Structure and dynamics of silicate liquids at high pressure", Abstract volume

QUARTIERI, S.; DALCONI, M.C.; OBERTI, R.; BOSCHERINI, F.; IEZZI, G.; BAIOCCHI, M.: 05.-08.07.2004, XII Convegno Società Italiana di Luce di Sincrotrone, Camerino, Italy: "Incorporation and site preference of Sc in garnets: the join pyrope-grossular"

RINALDI, R.; GATTA, G.D.; KNIGHT, K.S.; ARTIOLI, G.; GEIGER, C.A.: 26.-29.09.2004, XXXIV Nat. Congr. Italian Association of Crystallography, Rome, Italy: "Thermoelastic and ordering behaviour in $CoMgSiO_4$ olivine: high-temperature *in situ* neutron powder diffraction study"

RUBIE, D.C.; COUVY, H.; FROST, D.J.; DURHAM, W.; WANG, Y.; CORDIER, P.: 04.-07.04.2004, EMPG X, Frankfurt/M., Germany[*1]: "Using the D-DIA to study changes in deformation mechanism in forsterite at high pressure", Lithos 73, 1-2, Supplement 1, S93

RUBIE, D.C.; GESSMANN, C.K.; FROST, D.J.: 20.-23.07.2004, Oxygen in the Terrestrial Planets, Santa Fe, USA: "Solubility of oxygen in liquid iron at high pressure and consequences for the early differentiation of Earth and Mars", Workshop Program and Abstracts, LPI Contribution No. 1203, 56

RUBIE, D.C.: 30.09.2004, Department of Earth and Atmospheric Sciences, Purdue University, USA: "Core formation in terrestrial planets"

SCHMICKLER, B.; RUBIE, D.C.; LIEBSKE, C.; POE, B.T.: 04.-07.04.2004, EMPG X, Frankfurt/M., Germany[*1]: "Diffusion of Si, O, Mg, Ca, Ni and Co in peridotite liquid at high pressures", Lithos 73, 1-2, Supplement 1, S98

SEBALD, A.: 10.05.2004, Universität Stuttgart, Institut für Physikalische Chemie, Stuttgart, Germany: "Virtual + real NMR spectrometer = quantitative structural information about solids"

SEBALD, A.: 06.-10.07.2004, XIIth School on Solid-State NMR, Zakopane, Poland: "MAS NMR spectra of spin systems composed of dipolar (re)coupled spin-1/2 nuclei"

SEBALD, A.: 22.07.2004, Universität Halle, Fachbereich Physik, Halle, Germany: "Virtuelles + reales NMR Spektrometer = quantitative Information an Feststoffen"

SEIFERT, F.: 08.09.2004, Department of Geology, Peking University, Beijing, China: "The mineralogy of the Earth's mantle: new insights into an old problem"

SEIFERT, F.: 08.09.2004, Department of Geology, Peking University, Beijing, China: "Crystal chemistry and properties of silicate perovskite, the Earth's most important mineral"

SEIFERT, F.: 12.09.2004, Institute of High Energy Physics (Beijing Synchrotron), Academia Sinica, Beijing, China: "The mineralogy of the Earth's mantle: new insights into an old problem"

SHINOVA, E.; ZHECHEVA, E.; STOYANOVA, R.; BROMILEY, G.D.; BOFFA BALLARAN, T.: 29.09.-01.10.2004, 5th National Conference of Chemistry, Sofia, Bulgaria: "New layered oxides $Li[Li_xNi_{1-x}]O_2$ as insertion electrodes for lithium-ion batteries"

SHINOVA, E.; ZHECHEVA, E.; STOYANOVA, R.; BROMILEY, G.D.; BOFFA BALLARAN, T.: November 2004, 4th Seminar on New Materials for Industry, Sofia, Bulgaria: "High-pressure synthesis of new compositions in the Li-Ni-Al-O system for cathode materials in lithium-ion batteries"

SHIRYAEV, A.A.: 13.02.2004, Introductory meeting for AvH fellows, Frankfurt, Germany: "Interaction of point and extended defects in diamond"

SHIRYAEV, A.A.: 15.07.2004, Martin-Luther University, Fachbereich Physik, Halle, Germany: "Defects in diamonds: Influence of deformation on diffusion and positron annihilation studies"

SHIRYAEV, A.A.; FROST, D.J.; LANGENHORST, F.: 09.-13.08.2004, 14th International Conference on Crystal Growth, Grenoble, France: "Experimental investigation of nitrogen diffusion in plastically deformed diamonds"

SHIRYAEV, A.A.; ZEDGENIZOV, D.: 04.-08.09.2004, 6th European Conference on Spectroscopy and Mineralogy, Vienna, Austria: "Optical studies of fluids in fibrous diamonds", Mitteilungen der Österreichischen Mineralogischen Gesellschaft 149, 91

SMYTH, J.R.; JACOBSEN, S.D.; HOLL, C.M.; FROST, D.J.; MANGHNANI, M.H.; AMULELE, G.; SHEN, G.: 17.-21.05.2004, 2004 Joint Assembly, Montreal, Canada: "Searching for Earth's lost oceans: A planetary odyssey in mineral physics", EOS Trans. AGU, 85(17), Jt. Assem. Suppl., Abstract U53A-03, 2004

SMYTH, J.R.; JACOBSEN, S.D.; HOLL, C.M.: 05.-11.06.2004, Goldschmidt Conference, Copenhagen, Denmark[*2]: "Detecting hydration in the Earth's interior", Conference Supplement to Geochimica et Cosmochimica Acta, A31

SMYTH, J.R.; FROST, D.J.; NESTOLA, F.: 13.-17.12.2004, AGU Fall Meeting, San Francisco, USA[*3]: "Hydration of olivine at 12 GPa", EOS Trans. AGU, 85(47), Fall Meet. Suppl., Abstract T32B-04, 2004

STEINLE-NEUMANN, G.: 01.04.2004, Carnegie Institution of Washington, Geophysical Laboratory, Washington DC, USA *(invited)*: "Hot core to cold subduction"

STEINLE-NEUMANN, G.: 05.05.2004, Max-Planck Institut für Chemie, Mainz, Germany *(invited)*: "Hot core, using mineral physics to understand Earth's deepest interior"

STEINLE-NEUMANN, G.; 28.09.2004, German Materials Research Society, Annual Meeting of the focus group 'mechanical properties at high temperature', Bayreuth, Germany *(invited)*: "Pressure, temperature, complexity – Materials research in the Earth sciences"

STEINLE-NEUMANN, G.: 26.-31.08.2004, 22nd European Crystallographic Meeting, Budapest, Hungary *(invited)*: "Squeezing magnets: implications for crystallography and geophysics

STEINLE-NEUMANN, G.: 04.-09.07.2004, 9th Symposium on the Study of the Earth's Deep Interior, Garmisch-Partenkirchen, Germany *(invited)*: "Combining computations and experiment to understand mineralogical processes in the Earth's interior", Book of Abstracts S1.2

STEINLE-NEUMANN, G.: 18.08.2004, GeoForschungsZentrum Potsdam, Germany *(invited)*: Hot core, using mineral physics to understand Earth's deepest interior"

STEINLE-NEUMANN, G.; DERA, P.; HYDE, R.: 19.-22.09.2004, 82. Jahrestagung der Deutschen Mineralogischen Gesellschaft, Karlsruhe, Germany: "Layer shift phase transition in kaolins under pressure", Beihefte zum European Journal of Mineralogy 16, 139

STEINLE-NEUMANN, G.: 30.10.2004, Kick-off meeting, International Graduate School 'THESIS', Department of Earth and Environmental Sciences, Ludwig Maximilians-Universität München, Bayrischzell, Germany *(invited)*: "Heating the core: does potassium do the job?"

STOYANOV, E.; LANGENHORST, F.; STEINLE-NEUMANN, G.: 19.-22.09.2004, 82. Jahrestagung der Deutschen Mineralogischen Gesellschaft, Karlsruhe, Germany: "Ti - $L_{2,3}$ and O-K electron energy loss near-edge structures of Ti_xO_y phases: fingerprints to the valence state of titanium", Beihefte zum European Journal of Mineralogy 16, 140

SUZUKI, A.; RUBIE, D.C.: 04.-07.04.2004, EMPG X, Frankfurt/M., Germany[*1]: "Thermal diffusivity of silicate glasses at high pressure", Lithos 73, 1-2, Supplement 1, S108

TERASAKI, H.; RUBIE, D.C.; FROST, D.J.: 04.-07.04.2004, EMPG X, Frankfurt/M., Germany[*1]: "The effect of oxygen content on the dihedral angle between Fe-S liquid and perovskite at lower mantle conditions", Lithos 73, 1-2, Supplement 1, S109

TERASAKI, H.; FROST, D.J.; LANGENHORST, F.; RUBIE, D.C.: 14.-15.09.2004, 2nd Workshop "Interior – Early Evolution – Core Formation", Deutsche Forschungs-gemeinschaft "Mars and the Terrestrial Planets", München, Germany: "Possibility of percolative core formation in planetary mantle"

TERASAKI, H.; FROST, D.J.; LANGENHORST, F.; RUBIE, D.C.: 13.-17.12.2004, AGU Fall Meeting, San Francisco, USA[*3]: "Interconnectivity of liquid Fe-alloy in planetary mantles", EOS Trans. AGU, 85(47), Fall Meet. Suppl., Abstract MR43A-0885, 2004

TERRY, M.P.; HEIDELBACH, F.: 05.-11.06.2004, Goldschmidt Conference, Copenhagen, Denmark[*2]: "Interplay between fluid infiltration, deformation, and diffusion during eclogitization in the Mte. Mucrone quartz diorite, Italy", Conference Supplement to Geochimica et Cosmochimica Acta, A182

TERRY, M.P.; ROBINSON, P.; KROGH, T.E.: 27.06.-01.07.2004, 17th International Basement Tectonics Association Conference, Oak Ridge, USA: "Effects of metamorphic and structural overprinting on Proterozoic basement during continental subduction and exhumation, Scandinavian Caledonides, Norway"

TERRY, M.P.; ROBINSON, P.; KROGH, T.E.: 06.-07.12.2004, Tectonic Studies Group Meeting 'Channel Flow, Ductile Extrusion and Exhumation of the Lower and Lower and Middle Crust', London, U.K.: "Evidence for a HP-UHP subduction and a crustal channels and their interaction during oblique continental collision, Scandinavian Caledonides, Norway", Program with Abstracts, Geological Society of London

WILLIAMS, H.M.; MCCAMMON, C.A.; PESLIER, A.H.; HALLIDAY, A.N.; TEUTSCH, N.; LEVASSEUR, S.; BURG, J.-P.: 05.-11.06.2004, Goldschmidt Conference, Copenhagen, Denmark[*2]: "Iron isotope fractionation and the oxygen fugacity of the mantle", Conference Supplement to Geochimica et Cosmochimica Acta, A563

WILLIAMS, H.M.; MCCAMMON, C.A.; PESLIER, A.H.; HALLIDAY, A.N.; LEVASSEUR, S.; TEUTSCH, N.; BURG, J.-P.: 13.-17.12.2004, AGU Fall Meeting, San Francisco, USA[*3] *(invited)*: "Iron isotope fractionation in mantle minerals and the effects of partial melting and oxygen fugacity", EOS Trans. AGU, 85(47), Fall Meet. Suppl., Abstract V42A-03, 2004

ZANAZZI, P.F.; COMODI, P.; GATTA, G.D.: 04.-07.04.2004, EMPG X, Frankfurt/M., Germany[*1]: "Structural behaviour of levyne at high pressure", Lithos 73, 1-2, Supplement 1, S123

[*1] **EMPG X: Tenth International Symposium on Experimental Mineralogy, Petrology and Geochemistry, 04.-07.04.2004, Frankfurt/Main, Germany – Lithos, Supplement to Volume 73, Nos. 1-2, 2004**

[*2] **Goldschmidt Geochemistry Conference, Processes in Geochemistry – Forces, Fluxes and Structure, 05.-11.06.2004, Copenhagen, Denmark – Conference Supplement to Geochimica et Cosmochimica Acta**

[*3] **AGU: American Geophysical Union Fall Meeting, 13.-17.12.2004, San Francisco, DC, USA – EOS Transactions, American Geophysical Union, 85(47), AGU Fall Meeting 2004 Supplement**

4.4 Lectures and seminars at Bayerisches Geoinstitut

AKAOGI, M.: 23.06.2004 "High-pressure transitions of some silicates and germinates, and energetics of ABO_3 perovskites"

AKBER-KNUTSON, S.: 02.09.2004 "Aluminium in a CMAS lower mantle assemblage"

ASAHARA, Y.: 31.03.2004 "Phase relations of a carbonaceous chondrite at lower mantle conditions"

AUZENDE, A.l.: 04.05.2004 "Evolution of serpentinite microstructures in convergent context: Effect of metamorphic grade and deformation"

BENEDETTI, L.-R.: 05.02.2004 "Structural and spectroscopic studies of fluid bromine in the laser-heated diamond cell"

BROMILEY, F.A.: 29.04.2004 "A microscopic and macroscopic investigation of the magnesite - otavite solid solution"

BROMILEY, G.D.: 17.09.2004 "H related defects in geomaterials: New experimental techniques and first results"

BUFFETT, B.: 01.07.2004 "Sediments at the top of the core"

BUNGE, H.-P.: 22.01.2004 "Mantle circulation models with variational data-assimilation: Inferring past mantle flow and structure from plate motion histories and seismic tomography"

DERA, P.: 21.04.2004 "Squeezing molecular glue, hydrous phases and hydrogen bonds at high pressure"

DOLEJŠ, D.: 14.10.2004 "Thermodynamics and phase equilibria of fluor silicate systems: Implications for the evolution of granitic magmas"

EL GORESY, A.: 17.06.2004 "New high-pressure assemblages in SNC (Martian) meteorites"

FUJINO, K.: 04.08.2004 "Stability, structure and cation solubility of silicate perovskites"

GRIEVE, R.A.F.: 04.11.2004 "Impact cratering record and early crustal evolution on Earth"

GUCSIK, A.: 04.03.2004 "Shock metamorphism of zircon in nature and experiment"

HOLTZMAN, B.: 28.04.2004 "Shearing melt out of the mantle: Self-organization of melt during deformation"

IGEL, H.: 15.07.2004 "Ground rotations: A new observable for seismology?"

JAHN, S.: 21.10.2004 "Transferable interaction potentials for oxides: Molecular dynamics simulation of solid and liquid alumina"

JUGO, P.J.: 18.11.2004 "Speciation and solubility of sulphur as a function of oxygen fugacity"

KURNOSOV, A.: 16.09.2004 "Clathrate hydrates at high pressures: Possible building materials for the Outer Solar System bodies"

LEE, K.K.M.: 11.03.2004 "High-pressure alloying of iron and potassium: Radioactivity in the Earth's core"

MATTESINI, M.: 02.11.2004 "High-pressure phases and their X-ray fingerprints: A theoretical characterization of novel polymorphs"

MILLITZER, B.: 07.09.2004 "Path integral simulations of hydrogen-helium mixtures in planet interiors"

MILSCH, H.: 04.08.2004 "Dehydration induced weakening and fault-slip in gypsum: Implications for the faulting process at intermediate depth"

MORGAN, W.J.: 05.08.2004 "Hotspots and horizontal flow in the asthenosphere"

OGANOV, A.: 07.12.2004 "Insights into Earth's mantle from *ab initio* calculations"

PIAZZONI, A.: 24.02.2004 "Relative sea level fluctuations induced by polar wander"

PRODI, A.: 11.11.2004 "$(AA'_3)Mn_4O_{12}$ mixed-valence double perovskites: a new playground for complex ordering phenomena"

RIGBY, M.: 13.05.2004 "Fluids, melts and metamorphism"

SHAW, C.: 01.04.2004 "The temporal evolution of three magmatic systems in the West Eifel volcanic field, Germany"

SHIRYAEV, A.A.: 17.09.2004 "Some new insights into growth of natural diamonds and their postgrowth history"

SMYTH, J.R.: 03.06.2004 "Water in the mantle: Geophysical and geochemical constraints"

STEINLE-NEUMANN, G.: 25.11.2004 "Potassium in the core?"

TERRY, M.P.: 29.01.2004 "Continental subduction and exhumation: Insight from field and laboratory study of high- and ultrahigh-pressure rocks"

TERRY, M.P.: 19.05.2004 "Toward a dynamic model for continental subduction and exhumation: Linking field observations to 3D thermal-mechanical models"

TRIBAUDINO, M.: 02.12.2004 "Transmission electron microscopy and X-ray diffraction: Complementary methods in the investigation of phase transitions in minerals"

VERNOOIJ, M.: 23.07.2004 "Shock metamorphism or tectonic deformation? A TEM investigation of planar features in quartz"

WALTE, N.: 16.09.2004 "The grain-scale distribution and behaviour of melt and fluid: An analogue approach"

WENZEL, M.: 26.02.2004 "Tharsis as a consequence of Mars' dichotomy and layered mantle"

WILLIAMS, H.: 24.06.2004 "Iron isotope fractionation and the oxygen fugacity of the mantle"

4.5 Conference organization

12.-17.9.2004, 3rd European Summer School "Solid-State NMR", Valencia, Spain (M. BECHMANN, A. SEBALD, T. BLASCO, A. BRINKMANN, S. CALDARELLI, M. LEVITT, T. VOSEGAARD)

03.-08.10.2004, International BaCaTec Summer School 2004, Nuclear Magnetic Resonance Spectroscopy of Biomolecular Complexes, Universität Bayreuth, Germany: "about... Solid-State NMR" (A. SEBALD)

24.-29.10.2004, 15th ISMAR Meeting, Jacksonville, Florida, USA: "Studying Molecular Structure and Dynamics Using Uniformly Labelled Compounds under Magic-Angle-Spinning Conditions" (O. ANDRONESI, G. ANGERSTEIN, S. BECKER, M. ETZKORN, A. LANGE, H. HEISE, C.E. HUGHES, A. SEBALD, K. SEIDEL, M. BALDUS)

13.-17.12.2004, American Geophysical Union Fall Meeting, San Francisco, USA: Special symposium "Evolution, Structure, and Properties of the Earth's core" in honour of Jean-Paul Poirier (R. LIEBERMANN, F. LANGENHORST)

13.-17.12.2004, American Geophysical Union Fall Meeting, San Francisco, USA: "Advances in Computational and Cyber Infrastructure in the Earth Sciences", special sessions SF31B, SF32A, SF31A (G. STEINLE-NEUMANN, H.-P. BUNGE, H. IGEL, T. JORDAN, R. KELLER, D. SEBER)

13.-17.12.2004, American Geophysical Union Fall Meeting, San Francisco, USA: Special session "The oxidation state of the mantle" (C.A. MCCAMMON, C.-T. LEE, A. WOODLAND)

5. Visiting scientists

5.1 Visiting scientists funded by the Bayerisches Geoinstitut

AKAOGI, M., Gakushuin University, Department of Chemistry, Tokyo, Japan: 20.-25.06.2004

AKBER-KNUTSON, S., California Institute of Technology, Seismological Laboratory, Pasadena, USA: 31.08.-09.09.2004

ASAHARA, Y., Tohoku University, Institute of Mineralogy, Petrology and Economic Geology, Sendai, Japan: 29.03.-04.04.2004

AUZENDE, A.l., CRMC-N, Marseille, France: 02.-05.05.2004

BENEDETTI, L.-R., Commisariat a l'Energie Atomique, Bruyères-le-Châtel, France: 04.-08.02.2004

BESSON-GIRARD, É., Observatoire Midi-Pyrénées, LMTG-Minéralogie, Toulouse, France: 02.-06.08.2004

BUFFETT, B., University of Chicago, The Department of the Geophysical Sciences, Chicago, USA: 01.-04.07.2004

BUNGE, H.-P., Ludwig-Maximilians Universität München, Institut für Geophysik, München, Germany: 22.01.2004

DERA, P., Carnegie Institution of Washington, Geophysical Laboratory, Washington DC, USA: 20.-22.04.2004

DOLEJŠ, D., McGill University, Department of Earth & Planetary Sciences, Montreal, Canada: 01.-03.09.2004

EBERT, E., TU Berlin, Germany, 03.06.2004, 15.07.2004

EL GORESY, A., Max-Planck-Institut für Chemie, Mainz, Germany: 15.-18.06.2004

GAVRILENKO, P., Moscow State University, Geological Faculty, Moscow, Russia: 08.-12.12.2004

GRIEVE, R.A.F., Geological Survey of Canada, Earth Sciences Sector, Ottawa, Canada: 03.-05.11.2004

GUCSIK, A., Okayama University, Japan: 01.-05.03.2004

HOLL, C., University of Colorado at Boulder, Geological Sciences, Boulder, USA: 23.02.-04.03.2004

JACOBSEN, S.D., Carnegie Institution of Washington, Geophysical Laboratory, Washington DC, USA: 26.03.-08.04.2004

JAHN, S., GeoForschungsZentrum Potsdam, Experimentelle Geochemie und Mineralphysik, Potsdam, Germany: 19.-22.10.2004

JUGO, P.J., Johann Wolfgang Goethe-Universität Frankfurt am Main, Institut für Mineralogie, Frankfurt/M., Germany: 18.-19.11.2004

KUDASHKINA, O., Würzburg, Germany: 02.08.2004

KURNOSOV, A., Nikolaev Institute of Inorganic Chemistry, Novosibirsk, Russia: 14.-17.09.2004

LEE, K.K.M., University of California, Department of Earth and Planetary Science, Berkeley, USA: 23.02.-12.03.2004

MANN, U., Universität Tübingen, Germany: 14.-16.07.2004

MECKLENBURGH, J., University of Manchester, Department of Earth Sciences, Manchester, U.K.: 21.-30.01.2004

MILITZER, B., Carnegie Institution of Washington, Geophysical Laboratory, Washington DC, USA: 06.-08.09.2004

MILSCH, H., Columbia University, Lamont-Doherty Earth Observatory, Palisades, USA: 02.-05.08.2004

MORGAN, W.J., Princeton University, Department of Geosciences, Princeton, USA: 05.-06.08.2004

MUNSHI, A.D., Indian Institute of Technology, Roorkee, India: 10.-15.10.2004

OGANOV, A., ETH Zurich, Laboratorium für Kristallographie, Zurich, Switzerland: 06.-08.12.2004

SAIKIA, A., University of Delhi, Department of Geology, Delhi, India: 12.-19.06.2004

SHAW, C., University of New Brunswick, Department of Geology, Fredericton, Canada: 31.03.-03.04.2004

SOLOZHENKO, V.L., Université Paris Nord, LPMTM-CNRS, Villetaneuse, France: 25.07.-02.08.2004

SWAMY, V., Monash University, School of Physics & Material Engineering, Victoria, Australia: 06.-08.06.2004

TAHER, S., Grenoble, France: 03.-07.08.2004

TRIBAUDINO, M., Università degli Studi di Torino, Dipartimento di Scienze Mineralogiche e Petrologiche, Torino, Italy: 01.-04.12.2004

URUSOV, V., Moscow State University, Department of Crystallography and Crystal Chemistry, Moscow, Russia: 01.-15.11.2004

WALTE, N., Universität Mainz, Institut für Geowissenschaften, Tektonophysik, Mainz, Germany: 15.-17.09.2004

WENZEL, M., University of California, Department of Earth and Planetary Science, Berkeley, USA: 25.01.-20.03.2004

WILLIAMS, H., ETH Zurich, Departement Erdwissenschaften, Zurich, Switzerland: 23.-25.06.2004

YING, L., Chinese Academy of Sciences, Institute of Geochemistry, Guiyang, China: 11.-17.10.2004

5.2 Visiting scientists supported by other externally funded BGI projects

ANGEL, R., Virginia Polytechnic Institute and State University, Crystallography Laboratory, Blacksburg, USA: 25.03.-04.04.2004 (AvH Sofja Kovalevskaja-Programm)

CHAMPALLIER, R., C.N.R.S., Institut des Sciences de la Terre d'Orléans, France: *"Experimental deformation of partially crystallized magmas and crystallization unter coaxial stress"*, 21.-31.01.2004 (EU "Access to Research Infrastructures" Programme)

DI CARLO, I., Università degli Studi di Palermo, Italy: *"The role of amphibole in trace elements partitioning in island arc tectonic settings (the case of Ustica Island)"*, 01.01.-16.03.2004 (EU Marie Curie Training Site)

PIAZZONI, A.S., Università degli Studi di Milano, Dipartimento di Scienze della Terra "Ardito Desio", Milano, Italy: *"Self-consistent mantle modelling using geodynamic mantle flow simulation and mineral physics"*, 01.06.-31.12.2004 (EU Marie Curie Training Site)

PISTORINO, M., Università degli Studi di Pavia, Dipartimento di Scienze della Terra, Pavia, Italy: *"Compressibility behaviour of the columbite-group minerals along the $FeNb_2O_6$ – $MnNb_2O_6$ solid solution"*, 15.04.-14.07.2004 (EU Marie Curie Training Site)

PRODI, A., Consiglio Nazionale delle Ricerche, Istituto Materiali per Elettronica e Magnetismo, Parma, Italy: *"Crystal growth of $(AA'_3)Mn_4O_{12}$ compounds"*, 01.09.-15.12.2004 (EU Marie Curie Training Site)

RIGBY, M., University of Manchester, Department of Earth Science, Manchester, U.K.: *"Cordierite as a fluid monitor during metamorphism and partial melting"*, 05.07.-04.10.2004 (EU Marie Curie Training Site)

SHINOVA, E., Bulgarian Academy of Sciences, Institute of General Inorganic Chemistry, Sofia, Bulgaria: *"High-pressure synthesis of new compositions in the Li-Ni-Al-O System"*, 26.04.-25.07.2004 (EU Marie Curie Training Site)

VERNOOIJ, M., ETH Zurich, Geologisches Institut, Zurich, Switzerland: *"Shock metamorphism or tectonic deformation? A TEM investigation of planar features in quartz"*, 03.05.-02.08.2004 (EU Marie Curie Training Site)

5.3 Visitors (externally funded)

AHUJA, R., Uppsala University, Department of Physics, Uppsala, Sweden: 01.-04.11.2004

ALLWARDT, J., Stanford University, Department of Geological and Environmental Sciences, Stanford, USA: 01.10.-17.11.2004

ALMEIDA, J., Uppsala University, Department of Physics, Uppsala, Sweden: 01.-05.11.2004

BESTMANN, M., Universität Wien, Institut für Geologische Wissenschaften, Vienna, Austria: 08.-13.04.2004

CARPENTER, M.A., University of Cambridge, Department of Earth Sciences, Cambridge, U.K.: 25.-27.03.2004

CORDIER, P., Université des Sciences et Technologies de Lille, Laboratoire de Structure et Propriétés de l'Etat Solide, Villeneuve d'Ascq, France: 19.04.-01.05.2004, 19.-31.07.2004

DOLLASE, W., University of California, Department of Earth and Space Sciences, Los Angeles, USA: 04.-29.10.2004

DZWILEWSKI, A., Umeå University, Umeå, Sweden: 26.06.-09.07.2004

EL GORESY, A., Max-Planck-Institut für Chemie, Mainz, Germany: 06.-08.10.2004

ERTEL-INGRISCH, W., Technische Universität Ilmenau, Germany: 13.-14.05.2004

GALADI-ENRIQUEZ, E., Johann Wolfgang Goethe-Universität Frankfurt am Main, Germany: 25.-29.10.2004

GROSS, T., Technische Universität Darmstadt, Fachbereich Materialwissenschaft, Darmstadt, Germany: 21.-24.06.2004

GUILLAUME, C., University of Edinburgh, School of Engineering and Electronics and Center for Materials Science, Edinburgh, U.K.: 21.-30.05.2004

HARTMANN, K., Technische Universität Ilmenau, Germany: 13.-14.05.2004

HOLTZMAN, B., University of Minnesota, Department of Geology and Geophysics, Minneapolis, USA: 20.-30.04.2004

HORVATH-BORDON, E., Technische Universität Darmstadt, Germany: 25.-29.10.2004

IEZZI, G., Università degli Studi di Chieti, Dipartimento di Scienze della Terra, Chieti, Italy: 25.06.-04.07.2004

KEGLER, P., Universität Köln, Germany: 26.01.-06.02.2004, 03.-19.05.2004

KESSLER, E., Universität Bochum, Institut für Geologie, Mineralogie & Geophysik, Bochum, Germany: 13.-15.04.2004

KOCI, L., Uppsala University, Department of Physics, Uppsala, Sweden: 02.-05.11.2004

KONZETT, J., Universität Innsbruck, Institut für Mineralogie und Petrographie, Innsbruck, Austria: 23.-28.02.2004

KWON, S., Uppsala University, Department of Physics, Uppsala, Sweden: 01.-05.11.2004

LAUTERBACH, S., Technische Universität Darmstadt, Fachgebiet Geomaterialwissenschaft, Darmstadt, Germany: 21.-25.07.2004

LOCHERER, T., Technische Universität Darmstadt, Fachbereich Materialwissenschaft, Darmstadt, Germany: 21.-24.06.2004, 25.-29.10.2004

MACHEK, M., Czech Academy of Science, Geophysical Institute, Prague, Czech Republik: 03.-04.05.2004

MATTESINI, M., Uppsala University, Department of Physics, Uppsala, Sweden: 01.-05.11.2004

MYSEN, B., Carnegie Institution of Washington, Geophysical Laboratory, Washington DC, USA: 03.-06.06.2004

NESTOLA, F., Università degli Studi di Torino, Dipartimento di Scienze Mineralogiche e Petrologiche, Torino, Italy: 27.01.-27.02.2004

NEUFELD, K., Universität Mainz, Institut für Geowissenschaften, Mainz, Germany: 26.-30.01.2004, 15.-19.03.2004. 05.-08.05.2004, 21.-24.07.2004, 05.-09.10.2004, 18.-19.11.2004

RIGBY, M., University of Manchester, Department of Earth Science, Manchester, U.K.: 05.-16.11.2004

SCHMITT, L., Technische Universität Darmstadt, Fachbereich Materialwissenschaft, Darmstadt, Germany: 22.04.2004

SCHNEIDER, C., Universität Bochum, Germany: 12.-30.07.2004

SCHWARZ, M., Technische Universität Darmstadt, Germany: 21.-24.06.2004

TALYZIN, A., Umeå University, Umeå, Sweden: 26.06.-09.07.2004

ULRICH, S., Czech Academy of Science, Geophysical Institute, Prague, Czech Republik: 03.05.2004

URAKAWA, S., Okayama University, Department of Earth Sciences, Okayama, Japan: 08.-09.04.2004

WADE, J., University of Bristol, Department of Earth Sciences, Bristol, U.K.: 04.-15.08.2004

WESTPHAL, T., Universität Bochum, Institut für Geologie, Mineralogie & Geophysik, Bochum, Germany: 13.-15.04.2004

WOOD, B.J., University of Bristol, Department of Earth Sciences, Bristol, U.K.: 04.-15.08.2004

YAGI, T., University of Tokyo, Institute for Solid State Physics, Tokyo, Japan: 26.-29.08.2004

6. Additional scientific activities

6.1 Patents

DUBROVINSKAIA, N.A.; DUBROVINSKY, L.S.; LANGENHORST, F.: Verfahren zur Herstellung von nanokristallinem stäbchenförmigem Diamant und Anwendungen dafür. Deutsche Patentanmeldung: 10 2004 026 976.9, 2. Juni 2004

6.2 Ph.D. theses

Bläß, U.: Austausch von Silizium durch die dreiwertigen Kationen von Eisen und Aluminium in $CaSiO_3$-Perowskiten: Mechanismen und Auswirkungen auf die Mineralogie der Übergangszone

Bromiley, F.: A macroscopic and microscopic investigation of the magnesite - otavite solid solution

Demouchy, S.: Water in the Earth's Interior: Thermodynamics and kinetics of hydrogen incorporation in olivine and wadsleyite

6.3 Honours and awards

Natalia DUBROVINSKAIA	invited Professor Fellowship for 1 month at "Institut Galilee" at the University of Paris for the research on advanced superhard materials
Leonid DUBROVINSKY	ESF grant for ESF Exploratory Workshop - Physical and Engineering Sciences (PESC) "Novel Superhard Materials", convened by Leonid Dubrovinsky (DE) and Natalia Dubrovinskaia (DE)
Giacomo Diego GATTA	is the winner of the 2004 prize of the Italian Association of Crystallography (A.I.C.) for the excellence and the novelty of his research and for his publications
Hans KEPPLER	Mineralogical Society of America Fellow
Falko LANGENHORST	was appointed as member of the Academia Europaea in September 2004
Falko LANGENHORST	has been offered a C4 professorship in *Geomaterial-wissenschaft* at the *Technische Universität Darmstadt*
Falko LANGENHORST	has been offered a C4 professorship in *Allgemeine und Angewandte Mineralogie* at the *Friedrich-Schiller-Universität Jena*
Catherine MCCAMMON	received the best speaker award at the 6th European Mineralogical Union School "Spectroscopic Methods in Mineralogy"

Friedrich SEIFERT	received in September 2004 the Abraham-Gottlob-Werner Medal of the German Mineralogical Society

6.4 Editorship of scientific journals

MCCAMMON, C.A.	Editor "Physics and Chemistry of Minerals"
RUBIE, D.C.	Editor-in-Chief, Physics of the Earth and Planetary Interiors
SEBALD, A.	Editorial Board of "Solid State Nuclear Magnetic Resonance"
SEIFERT, F.	Editorial Advisory Board of "Physics and Chemistry of Minerals"

6.5 Membership of scientific advisory bodies

LANGENHORST, F.	National representative of the Deutsche Mineralogische Gesellschaft within the European Mineralogical Union
MCCAMMON, C.A.	MSA Lecture Program Committee of the Mineralogical Society of America Advisory Board of "Mössbauer Information Exchange" International Advisory Board of the Mössbauer Effect Data Center
RUBIE, D.C.	AGU Mineral and Rock Physics Executive Committee Urey Medal Committee, European Association of Geochemistry Roebling Medal Committee, Mineralogical Society of America SPring-8 Beamline Review Committee (BL04B1)
SEBALD, A.	Chairperson of the German Magnetic Resonance Discussion Group, 2001-2004
SEIFERT, F.	Committee for Glaciology, Bavarian Academy of Sciences Forschungskollegium Mineralogie Mitglied des Kuratoriums des Geo-Zentrums an der KTB e. V. Academia Europaea, London Deutsche Akademie der Naturforscher Leopoldina, Halle (Senate 2003-2006) Bayerische Akademie der Wissenschaften, München Akademie der Wissenschaften, Göttingen

7. Scientific and Technical Personnel

Name		Position	Duration in 2004	Funding source
ASAHARA, Yuki	Dr.	Stipendiatin	from 17.05.	JSPS
AUDETAT, Andreas	Dr.	Wiss. Angestellter	from 01.12.	BGI
BECHMANN, Matthias	Dipl.-Phys.	Wiss. Angestellter		DFG[1]
BLÄß, Ulrich	Dipl.-Min.	Wiss. Angestellter	to 31.01.	DFG
BÖHM, Ulrich		Mechaniker		BGI
BÖSS, Wolfgang	RAR	Verwalt. Beamter		BGI
BOFFA BALLARAN, Tiziana	Dr.	Sofia Kovalevskaja-Preisträgerin	to 31.07.	AvH
		Akad. Rätin	from 01.08.	BGI
BROMILEY, Fiona	M.Phil.	Wiss. Angestellte	to 31.07.	AvH[2]
		Stipendiatin	from 01.08.	AvH[2]
BROMILEY, Geoffrey	Dr.	Wiss. Angestellter		BGI/VP
COUVY, Hélène	Dipl.-Geol.	Wiss. Angestellte	to 16.01.	BGI/VP
			from 17.01.	DFG
DOLEJŠ, David	Dr.	Wiss. Angestellter	from 01.10.	BGI/VP
DUBROVINSKAIA, Natalia	Dr.	Wiss. Angestellte	to 31.07.	BGI
			from 01.08.	BGI/VP
DUBROVINSKY, Leonid	PD Dr.	Akad. Oberrat		BGI
FISCHER, Heinz		Mechaniker		BGI
FROST, Daniel	Dr.	Akad. Oberrat		BGI
FUJINO, Kiyoshi	Prof. Dr.	Gastprofessor	11.06.-10.09.	DFG
GAILLARD, Fabrice	Dr.	Wiss. Angestellter		BGI/VP
GATTA, Giacomo Diego	Dr.	Wiss. Angestellter	to 14.04.	AvH[2]
			from 15.04.	BGI/VP
GOLLNER, Gertrud		Chem.-Techn. Assistentin		BGI
HEIDELBACH, Florian	Ph.D.	Wiss. Assistent		BGI
HERRMANNSDÖRFER, Georg		Mechaniker	to 31.07.	BGI
IACONO MARZIANO, Giada	Dipl.-Geol.	Wiss. Angestellte	from 01.10.	BGI/VP
KANTOR, Anastasia	Dipl.-Geol.	Wiss. Angestellte	to 31.01.	BGI/VP
			from 01.02.	DFG
KANTOR, Innokenty	Dipl.-Geol.	Wiss. Angestellter		DFG
KEPPLER, Hans	Prof. Dr.	Stellvertr. Leiter	from 01.12.	BGI
KEYSSNER, Stefan	Dr.	Akad. Oberrat		BGI
KISON-HERZING, Lydia		Sekretärin		BGI
KLASINSKI, Kurt	Dipl.-Ing. (FH)	Techn. Angestellter		BGI

KRAUßE, Detlef	Dipl.-Inform. (FH)	Techn. Angestellter		BGI
KRIEGL, Holger		Haustechniker		BGI
KUZNETSOV, Oleksii	Dr.	Wiss. Angestellter		BGI/VP
LANGENHORST, Falko	PD Dr.	Akad. Oberrat	to 09.12.	BGI
LEITNER, Oskar		Präparator		BGI
LIEBSKE, Christian	Dipl.-Min.	Wiss. Angestellter	to 30.11.	DFG
LINHARDT, Sven		Elektroniker		BGI
LIU, Jun	Dipl.-Min.	Stipendiatin		AvH[2]
MANN, Ute	Dipl.-Geol.	Wiss. Mitarbeiterin	from 15.10.	IGS[3]
MARTON, Fred	Dr.	Wiss. Angestellter	to 31.08.	BGI/VP
MCCAMMON, Catherine	Dr.	Akad. Oberrätin		BGI
NESTOLA, Fabrizio	Dr.	Forschungsstipendiat	from 01.04.	AvH
RAMMING, Gerd		Elektroniker		BGI
RAUSCH, Oliver		Mechaniker		BGI
RUBIE, David C.	Prof. Dr.	Stellvertr. Leiter		BGI
SAIKIA, Ashima	M.Sc. (Geol.)	Wiss. Mitarbeiterin	from 01.10.	IGS[3]
SCHMICKLER, Bettina	Dr.	Wiss. Angestellte	to 16.05.	EU
			from 17.05.	DFG
SCHULZE, Hubert		Präparator		BGI
SEBALD, Angelika	PD Dr.	Wiss. Angestellte		
SEIFERT, Friedrich	Prof. Dr.	Stellvertr. Leiter		BGI
SHIRYAEV, Andrei	Dr.	Forschungsstipendiat		AvH
SKÁLA, Roman	Dipl.-Geol.	Wiss. Angestellter	from 01.06.	DFG
SMYTH, Joseph	Prof. Dr.	Forschungspreisträger		AvH
STÄNDNER, Petra		Fremdsprachen-Sekretärin		BGI
STEINBERGER, Bernhard	Dr.	Wiss. Angestellter	01.04.-17.08.	DFG
STEINLE-NEUMANN, Gerd	Dr.	Juniorprofessor		BGI
STOYANOV, Emil	Dipl.-Chem.	Wiss. Angestellter	to 31.05.	BGI/VP
			from 01.06.	DFG
STRETTON, Iona	Dr.	Wiss. Assistentin	to 08.09.	BGI
TERASAKI, Hidenori	Dr.	Wiss. Angestellter	to 31.03.	DFG,
			to 31.03.	BGI/VP
		Stipendiat	01.04.-30.09.	JSPS
TERRY, Michael	Dr.	Wiss. Angestellter		BGI/VP
ÜBELHACK, Stefan		Mechaniker	from 01.11.	EU
WALTE, Nicolas	Dipl.-Geol.	Wiss. Angestellter	from 01.11.	BGI/VP

Abbreviations/explanations:

AvH	Alexander von Humboldt Foundation
BGI	Staff Position of Bayerisches Geoinstitut
BGI/VP	Visiting Scientists' Program of Bayerisches Geoinstitut
DFG	German Science Foundation
EU	European Union
IGS	International Graduate School
JSPS	Japanese Society for the Promotion of Science

[1] project granted to Prof. B. Wrackmeyer, Bayreuth

[2] Sofia Kovalevskaja-Preis

[3] International Graduate School under the Elitenetzwerk Bayern "Structure, Reactivity and Properties of Oxide Materials"

Index